Volume 96, Number 6, November–December 1991
Journal of Research of the National Institute of Standards and Technology

Contents

Articles

Conference Reports

Volume 96, Number 6, November–December 1991
Journal of Research of the National Institute of Standards and Technology

News Briefs

Volume 96, Number 6, November–December 1991
Journal of Research of the National Institute of Standards and Technology

Volume 96, Number 6, November-December 1991
Journal of Research of the National Institute of Standards and Technology

[J. Res. Natl. Inst. Stand. Technol. 96, 647 (1991)]

Results of a CCPR Intercomparison of Spectral Irradiance Measurements by National Laboratories

Volume 96 Number 6 November-December 1991

James H. Walker, Robert D. Saunders, John K. Jackson, and Klaus D. Mielenz

National Institute of Standards and Technology,
Gaithersburg, MD 20899, USA

An intercomparison of spectral irradiance measurements by 12 national laboratories has been carried out between 1987 and 1990. The intercomparison was conducted under the auspices of the Comité Consultatif de Photometrie et Radiometrie (CCPR) of the Comité International des Poids et Mesures, and the National Institute of Standards and Technology (NIST) served as the pilot laboratory. The spectral range of the intercomparison was 250 to 2400 nm and the transfer standards used were commercial tungsten-halogen lamps of two types. The world-wide consistency of the results (one standard deviation) was on the order of 1% in the visible spectral region and 2 to 4% in the ultraviolet and infrared portions of the spectrum. The intercomparison revealed no statistically significant differences between spectral-irradiance scales based on blackbody physics and absolute detector radiometry.

Key words: CCPR; intercomparison; national laboratories; radiometry; spectral irradiance; tungsten-halogen lamps.

Accepted: August 28, 1991

1. Overview

At the September 1986 Session of the Comité Consultatif de Photometrie et Radiometrie (CCPR) of the Comité International des Poids et Mesures [1], the delegates of the National Institute of Standards and Technology (NIST) proposed an intercomparison of the spectral-irradiance scales maintained and disseminated by national standards laboratories throughout the world. The proposal received wide support and the Radiometric Physics Division of NIST was appointed the pilot laboratory for the intercomparison. It was agreed that the intercomparison would cover the spectral region from 250 to 2400 nm, and that the following schedule would be adhered to:

1987/88—Invitation to participants, procurement of intercomparison lamps, lamp mounts, and alignment jigs.

1989/90—Initial calibration of a set of three lamps by each participant, calibration of all lamps by NIST, and repeat calibration of each set of lamps by the participants.

The intercomparison was to be "blind," in that the NIST results would not be revealed to the participants until their repeat calibrations had been completed.

A preliminary NIST report of the intercomparison was presented at the September 1990 Session of the CCPR [2]. The committee decided to allow no more "fine tuning" of data, and appointed a working party convened by NIST to prepare a final report in which the results of the intercomparison are presented in terms of the differences,

$$r = \frac{\text{Average of "before" and "after" measurements by participants}}{\text{NIST measurement}} - 1. \quad (1)$$

This value was multiplied by 100 to obtain the percent difference from NIST. It was noted that the quotients in Eq. (1) are reciprocal to the equivalent quotients used in the 1975 spectral-irradiance intercomparison coordinated by the Electrotechnical Laboratory (ETL) of Japan [3] and that in the latter intercomparison the final data were adjusted to show the differences of each participant (including ETL) from a "world mean" of zero.

2. Participants

Twelve national laboratories participated in the intercomparison.[1] They are listed below, with the names of the principal investigators assigned to the intercomparison given in parentheses.

CSIRO – Commonwealth Scientific and Industrial Research Organization, Division of Applied Physics, Lindfield, Australia (J. L. Gardner).

ETL – Electrotechnical Laboratory, Ibaraki, Japan (M. Nishi).

INM – Institut National de Metrologie du Conservatoire National des Arts et Metieres, Paris, France (J. Bastie).

IOM – Instituto de Optica Daza de Valdes, Madrid, Spain (A. Corrons).

NIM – National Institute of Metrology, Beijing, People's Republic of China (Chen Xiaju).

NIST – National Institute of Standards and Technology, Gaithersburg, MD, USA (J. H. Walker).

NPL – National Physical Laboratory, Teddington, Middlesex, UK (J. R. Moore).

DPT – Division of Production Technology, CSIR, Pretoria, South Africa (F. Hengstberger).

NRC – National Research Council, Ottawa, Canada (L. P. Boivin).

OMH – National Office of Measures, Budapest, Hungary (G. Deszi).

PTB – Physikalisch-Technische Bundesanstalt, Braunschweig, Federal Republic of Germany (J. Metzdorf)

VNIIOFI – All-Union Research Institute of Optical and Physical Measurements, Moscow, U.S.S.R. (V. I. Sapritsky).

3. Lamps

The lamp originally chosen for the intercomparison was a 770 W (14 A at 55 V dc) tungsten-bromine lamp that had been developed jointly by the National Physical Laboratory (NPL) and the General Electric Company (GEC) of the United Kingdom for use both as a standard of spectral irradiance and as a standard of illuminance at a correlated color temperature of 3000 K [4]).[2] The filament assembly of the lamp, consisting of six vertical tungsten coils arranged in a 16×24 mm plane, is enclosed in a fused-silica envelope filled with 304 kPa (3 atm) of nitrogen (equivalent to 1013 kPa (10 atm) when the lamp is operating). The lamp is equipped with a commercial 22 mm bi-pin base and is operated base down. Initial testing at the NPL had shown that the lamp required aging for 300 to 400 h on dc in order to achieve a stability in illuminance of no worse than 0.5% per 100 h of use. The lamp obeyed the inverse-square law for working distances greater than 200 mm. Its uniformity of field was found to be better than $\pm 0.5\%$ over an angular range of 5° subtended at the lamp in the direction of a horizontal axis through the center of, and perpendicular to, the filament plane.

NPL had agreed to select and deliver three of these NPL/GEC lamps for each participating laboratory. This was achieved in mid-1988, but unfortunately some of these lamps failed during the first round of measurements and replacements could no longer be obtained from GEC. In order to remedy this difficulty, NIST supplied several of its routinely issued spectral-irradiance standard lamps (General Electric Company (USA) FEL lamps) to

[1] Data submitted by the Amt fuer Standardisierung, Messwesen und Warenpruefung (ASMW) of the former German Democratic Republic were withdrawn after the unification of Germany.

[2] Certain commercial equipment, instruments, or materials are identified in this paper to specify adequately the experimental procedure. Such identification does not imply recommendation or endorsement by the National Institute of Standards and Technology, nor does it imply that the materials or equipment identified are necessarily the best available for the purpose.

those laboratories that had lost NPL/GEC lamps or wished to include the NIST/FEL lamp for other reasons.

A detailed description of the NIST/FEL lamp may be found in Ref. [5]. The lamp, rated at 1000 W, is a clear quartz envelope, tungsten-halogen lamp with a cylindrical coiled-coil filament of 8 mm diameter and 24 mm height. The lamp is modified to a 22 mm bi-pin base and is operated base down. The lamps are annealed at 120 V dc for 40 h (13% of its rated life), and then burnt in for 24 h under normal operating conditions (7.7 to 8.0 A at 106 to 112 V dc) to test their stability. Only lamps with changes less than 0.5% in 24 h at 655 nm are accepted. All lamps are tested for irradiance uniformity over a +1° range of rotation and tilt, and lamps exhibiting changes greater than 1% are rejected.

Schematic drawings of the NPL/GEC and NIST/FEL lamps are shown in Fig. 1. NIST supplied alignment jigs and detailed alignment instructions for each lamp type. The lamps were to be mounted vertically, base down, and measured at a distance of 500.0 mm between a specified reference plane and the aperture of the receiving instrument. The average spectral irradiances (in $\mu W/cm^2/nm$) produced by the lamps under these conditions are plotted in Fig. 2. From these data it was estimated that the approximate correlated color temperatures of the lamps were 2979 K for the NPL/GEC lamps and 3075 K for the NIST/FEL lamps.

The final count of lamps used in the intercomparison was 25 NPL/GEC lamps and 6 NIST/FEL lamps. Most participants contributed data for three lamps. Two laboratories (ETL, VNIIOFI) contributed data for two lamps.

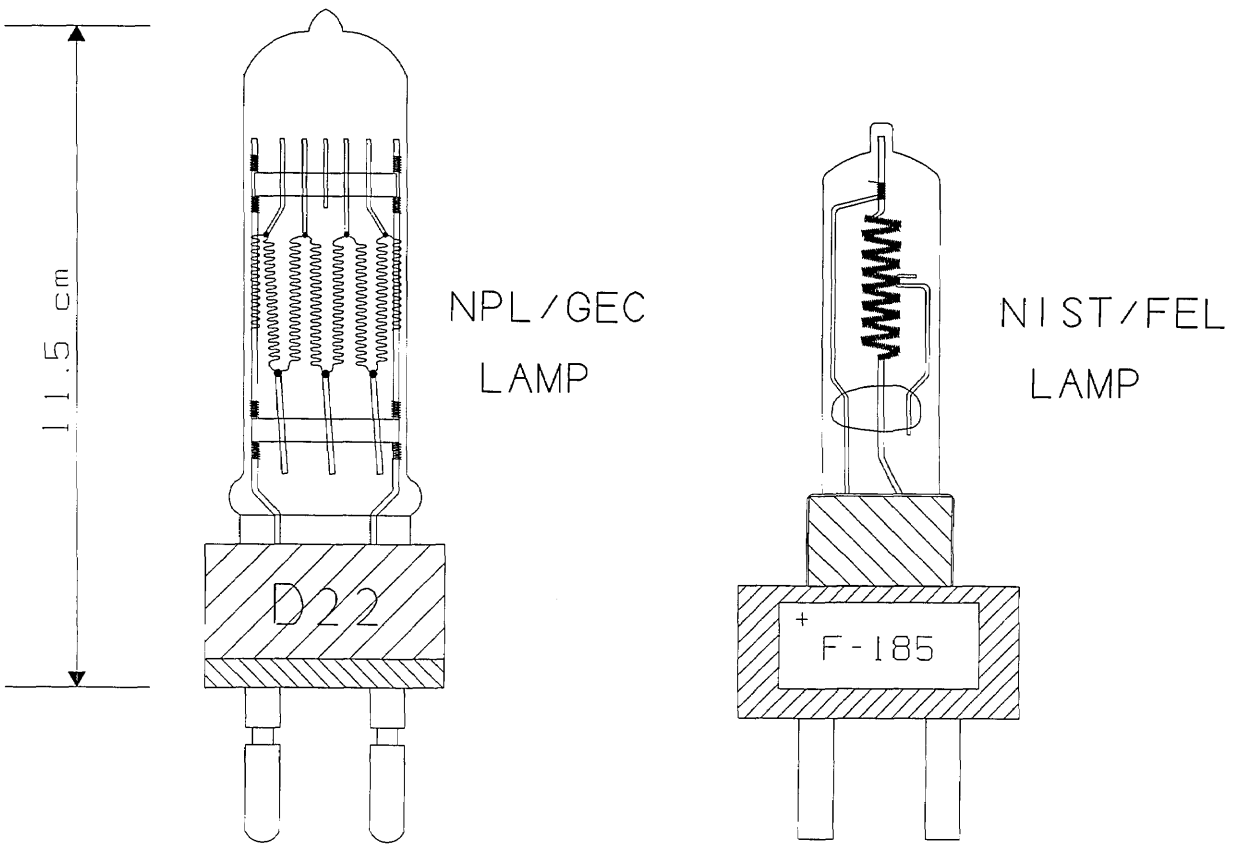

Figure 1. Lamps used in the spectral irradiance intercomparison.

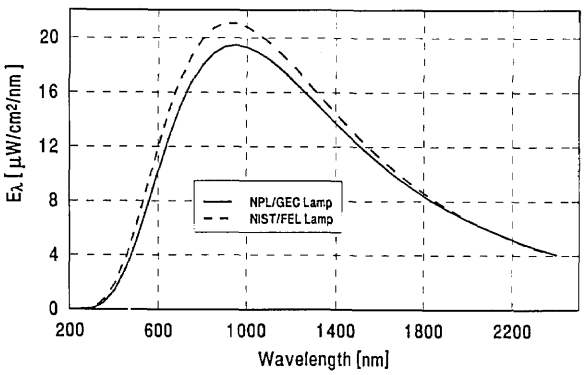

Figure 2. Average spectral irradiances of NPL/GEC and NIST/FEL lamps at a distance of 50 cm from lamp.

4. Measurement Procedures at Participating Laboratories

All lamps were operated at a constant current and their voltage was monitored. All the NPL/GEC lamps were operated at 14.000 A with a nominal voltage of about 55 V. The NIST/FEL lamps were operated at either 7.700, 7.800, or 7.900 A with nominal voltages of 106 to 109 V.

The information provided by the participating laboratories on the measurement methods used by them may be found in Appendix A of this paper. This information is summarized in Table 1, and the following points are worth emphasizing.

(a) Six laboratories (ETL, INM, NIM, NIST, PTB, VNIIOFI) had independently realized their spectral-irradiance scales by blackbody physics. All of these scales were stated to be consistent with the International Temperature Scale of 1990 [6] that was adopted during the intercomparison. Two scales (IOM, DPT) and the infrared portion of another (NRC from 700 nm upwards) had been independently realized by electrically calibrated radiometers. Two laboratories (CSIRO, NPL) reported that the 350 to 800 nm portions of their scales were based on relative spectral distributions derived from blackbodies, with absolute values assigned by photometric measurements. The NPL ultraviolet scale below 370 nm was based on synchrotron radiation. The NPL infrared scale from 900 nm upwards was based on provisional calculations using published data for the emissivity of tungsten because their new infrared scale was not completed in time for the intercomparison. The remaining scales (CSIRO below 350 nm and above 800 nm, NRC from 300 to 700 nm, OMH) were based on transfer standards provided by other national laboratories.

(b) Most laboratories contributed data over significant portions of the uv, visible, and near ir, but only five laboratories (CSIRO, ETL, NIM, NIST, PTB) covered the entire 250 to 2400 nm intercomparison range.

(c) All laboratories used medium-sized (0.25 to 1 m focal length) spectroradiometers. All used S-20 type photomultiplier tubes for measurements in the uv and visible. The detectors used in the infrared were Si and Ge photodiodes or PbS photoconductive cells, and several laboratories used two of these detectors.

(d) All laboratories performed the measurements using routine calibration methods and procedures. However, most laboratories performed the measurements using highly qualified staff and special care. Tests of wavelength accuracy, stray radiant energy, detector linearity and ambient temperature were performed as a routine matter.

All laboratories were requested to provide one standard deviation estimates of their measurement uncertainty, with random and systematic errors added in quadrature. These estimated uncertainties are listed in Table 2.

5. Measurement Procedure at NIST

The spectral irradiance measurements performed at NIST were made relative to the 1990 NIST scales of thermal radiometry [7] and are fully consistent with the ITS-90. Before and after spectral irradiance measurements on all intercomparison lamps were performed, once in September/October 1989 and again in April/May 1990, the NIST spectral irradiance scale was realized by calibrating a group of nine NIST/FEL transfer standards against a gold-point blackbody standard, using the measurement procedures described in Refs. [5] and [7]. All NIST measurements contributed to the intercomparison were derived by linear interpolations between these two scale realizations. The measurement setup used to compare the participants' intercomparison lamps to the NIST transfer standards is shown in Fig. 3. Each intercomparison lamp was measured against each of four NIST/FEL transfer standards, and the four spectral-irradiance values thus obtained for each lamp were averaged. The total burning time at NIST was on the order of 20 to 25 h for each lamp. A more detailed description of the NIST measurements may be found in Appendix A.

Table 1. Summary of measurement conditions at participants' laboratories

	CSIRO	ETL	INM	IOM	NIM	NIST	NPL	DPT	NRC	OMH	PTB	VNIIOFI
Sp Irr Scale												
Primary Std	AR/BB/CL[a]	BB	BB	AR	BB	BB	AR/BB	AR	AR/CL[c]	CL[d]	BB	BB
Trsf Std	TH	QB	CL[b]	TH	TH	TH	TH	None	None/TH	TH	DXW,FEL	BB
Lamps												
NPL/GEC	E14,E36	E20,(F15),F32	E25	E8,F24,F25	F6,F7,F8		(E23),E24	E15,E16,E17	E2,E3	E31,E32,F2	E9,E10,F28	D30,(D31),D32
NIST/FEL	(H146)[g],H148		F295,F296,(F297)				F287,F291		F176			
Comments												
Monochromator	double[h]	double	single	single[e]	double	double	double[f]	double	single[i]	double	double	double
Make	McPherson	JASCO	Jobin-Yvon	Jarrell-Ash	DMR	Cary	Jobin-Yvon	Jobin-Yvon	McPherson	Hilger-Watts	Cary	Jobin-Yvon
Type	grating	prism/grating	grating	grating	prism	prism/grating	grating	grating	grating	grating	prism/grating	grating
focal length	0.5 m	0.4 m	0.6 m	0.75 m	0.25 m	0.4 m	0.6 m	0.6 m	1 m	0.3m	0.4 m	0.64 m
f-number	7	6.8	5.6	6.5	10	8	5.7	5.7	8.7	6	8	5.7
UV-VIS Range	250–700	250–700	300–1000	350–800	250–800	250–800	300–800	400–700	300–700	280–900	250–800	270–800
BW @250 nm	2 nm	4 nm			3 nm	4.6 nm					6 nm	
400 nm	2	1.5	2 nm	1.8 nm	1.6	7.4	2 nm	2.2 nm	2 nm	4 nm	0.4	1.2 nm
700 nm	2	1.5	2	2.1	1.8	8.4	2	2.2	2	2.6	0.8	2.8
Detector	9558QB	R374	R546	9558QB	9659QB	9659Q	9558QA	R928	R758	9558QB	9558QB	PMT (two)[j]
Frequency	dc	1 kHz	dc	dc	800Hz	dc	dc	dc	dc	268Hz	dc	dc
Int time	3–10 s	300 ms	40 s	1 s	1 s	3–10 s	1 s	10 s	2.1 s	1–30 s	4 s	1 s
IR Range	700–2400	800–2400	1100–1700	800–2400	750–2500	900–2400	900–2400	700–1300	700-1600	1050-1600	800–2400	900-2400
BW @1050 nm	2 nm	10 nm	2 nm	7.2 nm	43 nm	7.2 nm	2 nm	1.8 nm		10.4 nm	2.4 nm	2.5 nm
1600 nm	8	10	4	14	65	6.8	2			10.4	11	5.2
2400 nm	8	10		14.4	88	5.2	4				9	4.8
Detector 1	Si UV800B	Si S2592	Si 10D	PbS	PbS	PbS	PbS	Si UV4448	ECR & filter	Si S1337	Ge E70	PbS
Frequency	dc	1 kHz	dc	141 Hz	800 Hz	78 Hz	200 Hz	dc	dc	268 Hz	133 Hz	510 Hz
Int time	3-10 s	300 ms	40 s	0.3 s	1 s	8–40 s	2.5 s	10 s	30 s	1–30 s	10 s	1 s
Detector 2	PbS	PbS P1026	Ge	n/a	n/a	n/a	n/a	Ge J16	n/a	PbS P2532	PbS H340	n/a
Frequency	300 Hz	1 kHz	10 Hz					32 Hz		268 Hz	133 Hz	
Int time	3–10 s	300 ms	40 s					10 s		1–30 s	25 s	
Tests Performed												
Wvlgth Acc	Hg lines	Hg and D2 lines	Hg lines and HeNe laser	Hg lines; Kr laser	Hg lines	Hg, Th lines	Hg, Cd lines <0.1 nm uncert	Hg and Cd lines	Hg, Cd lines	Hg, Cd, and Ne lines	Hg lines	Hg lines
Scat Light	cut-off f	cut-off f	bandpass f	cut-off f		no effect	cut-off f	backgrd sub	baffles	cut-off f	no effect	cut-off f
Det Lin	mult ap	not checked	light add	dbl beam	mult ap	dbl beam	dbl beam	dbl beam	checked 1979	dbl ap	$1/r^2$	mult ap
Amb Temp	21±.5	23±1	measured	measured	measured	23–25	22±1	22–24	24–26	23±1	23±1	measured

[a] 350–800 nm: tungsten tube cavity radiator at 2700 K and V(lambda) radiometer. 250–350 nm and 800–2400 nm: lamps from ETL.
[b] Spectral radiance lamps and luminous intensity lamps.
[c] 300–700 nm: lamps based on 1975 CIE intercomparison. 700–1600 nm: ECR.
[d] TH lamps from NIST.
[e] Used two monochromators: Jarrell-Ash used from 350–800 nm; Jobin-Yvon (double grating) used from 800–2400 nm with 0.25 m focal length and 3.5 f-number.
[f] Used two monochromators: Jobin-Yvon (double Czerny-Turner) used from 300–2400 nm; Hilger Uvisir (double prism Littrow) used from 300–800 nm.
[g] Parentheses around a lamp number indicates an excluded lamp.
[h] Double in UV-VIS. Single with prism predisperser in IR.
[i] Has prism predisperser.
[j] Two Soviet made PMTs: one for 280-600 nm, one for 600–900 nm.

Key to symbols in table:

AR	Absolute Radiometer	QB	Quartz Bromine lamps	Si Sxxxx	Hamamatsu Sxxxx silicon photodiode
BB	Blackbody	Ge J16	Judson J16 germanium photodiode	Si UVxxxx	EG&G UVxxxx silicon photodiode
CL	Calibrated lamps	Rxxx	Hamamatsu Rxxx photomultiplier tube	Ge E70	Electro Optical Systems GLN-050/E70 germanium photodiode
DX	DXW type lamps	xxxxQB	EMI xxxxQB photomultiplier tube	PbS H340	Santa Barbara Research Center H340 PbS-ITO detector
FEL	FEL type lamps	xxxxQ	EMI xxxxQ photomultiplier tube	PbS Pxxxx	Hamamatsu Pxxxx PbS photoconductive detector
TH	Tungsten Halogen lamps	Si 10D	UDT PIN 10D silicon photodiode		

Table 2. Grand-mean percent differences[a] from NIST and estimated one standard deviation uncertainties of participants' measurements

WL (nm)	NIST Unc (%)	CSIRO Grand mean	CSIRO Unc (%)	ETL Grand mean	ETL Unc (%)	INM Grand mean	INM Unc (%)	IOM Grand mean	IOM Unc (%)	NIM Grand mean	NIM Unc (%)	NPL Grand mean	NPL Unc (%)	DPT Grand mean	DPT Unc (%)	NRC Grand mean	NRC Unc (%)	OMH Grand mean	OMH Unc (%)	PTB Grand mean	PTB Unc (%)	VNIIOFI Grand mean	VNIIOFI Unc (%)
250	1.48	1.42	1.4	0.10	2.4					*12.69*[b]	3.9									1.77	6		
260	1.40	−0.04	1.4	0.92	2.4					*8.86*	3.8									0.42	4		
270	1.34	−0.44	1.3	0.96	2.4															−1.31	2.5	*4.47*	1.2
280	1.28	1.86	1.2	0.90	2.4					*6.10*	3.5							−2.21	3.0	−1.25	2	*4.58*	1.1
290	1.22	0.95	1.2	0.00	2.4													−1.46	2.8	−1.29	1.5	*4.53*	1.0
300	1.17	0.16	1.1	0.46	2.4			1.76	3	*4.07*	3.3	*−2.63*	1			−0.49	10	−1.40	2.5	−0.82	1.5	*4.05*	0.9
310	1.13	−0.03	1.1	−0.62	2.4							*−2.25*	1			−1.57	7	−1.52	2.4	−0.39	1.5	*3.68*	0.9
320	1.09	−0.05	1.1	−0.76	2.4	−2.50	2.1			2.82	3.1	*−2.12*	1			−2.85	6	−1.22	2.3	−0.08	1.5	*3.41*	0.9
330	1.06	0.07	1.1	−0.89	2.4	−0.31	1.9					−0.86	1			−3.86	5	−1.37	2.2	0.55	1.5	*3.60*	0.8
340	1.03	0.23	1.0	−1.04	2.4	0.23	0.8			2.43	2.9	−0.71	1			−3.86	4	−0.66	2.1	0.58	1.5	*3.57*	0.8
350	1.01	0.76	1.0	−0.77	2.4	0.64	0.4	0.39	3	1.94	2.9	−0.17	0.8			0.50	3	−0.82	2.0	0.52	1	*3.65*	0.7
400	0.92	−0.60	0.6	1.00	2.4	*1.53*	0.5	−0.51	2	0.71	2.3	0.67	0.5	1.14	1.1	1.15	2	0.79	2.0	0.57	0.8	*2.92*	0.6
450	0.84	−0.12	0.5	1.79	2.4	*1.26*	0.3	−0.18	2	0.37	2.2	0.66	0.4	0.99	1.1	2.26	2	−0.13	1.9	0.36	0.8	*2.52*	0.6
500	0.78	−0.02	0.4	1.07	1.4	*1.56*	0.3	−0.24	2	0.28	2.1	*1.14*	0.4	0.91	1	1.37	1.6	−0.42	1.8	−0.09	0.8	*2.14*	0.5
555	0.73			0.75	1.4	*1.76*	0.2	−0.35	2	−0.11	1.9	0.60	0.2			0.34	1.6			−0.25	0.8	*1.87*	0.5
600	0.70	0.15	0.4	0.16	1.4	*1.64*	0.3	−0.01	2	0.22	1.8	0.55	0.4	1.04	1	1.07	1.6	−0.39	1.7	−0.50	0.8	*1.59*	0.5
654.6	0.68			0.40	1.6			−0.43	2			−0.06	0.4			−0.07	1.6			−0.35	0.8	*1.22*	0.4
700	0.67	0.12	0.4	0.69	1.6	*1.40*	0.3	−0.21	2	−0.23	1.6	0.17	0.5	1.21	1	1.14	0.8	−0.32	1.8	−0.45	0.8	*1.06*	0.5
800	0.67	*−1.58*	0.8	−1.24	1.8	−0.25	0.3	−0.74	2	−0.51	1.6	−0.90	0.8	1.17	1	0.83	0.8	−0.31	1.9	−0.10	0.8	0.38	0.6
900	0.68	*−4.60*	1.1	*−4.56*	2.1	−0.12	0.3	−1.38	3	*−2.90*	1.6	*−3.65*	1	0.70	1.1	−0.08	0.8	−0.52	2.0	0.06	1	−0.42	0.7
1050	0.68	*−4.72*	1.1	*−5.04*	2.1			−1.04	3	1.28	1.7	*−5.52*	1.1	1.11	1.4	0.38	0.7	−0.11	2.5	1.15	1.5	−0.07	0.7
1150	0.67	*−4.63*	1.1	*−4.58*	2.0			−1.38	3	*3.59*	1.7	*−6.81*	1.2	1.13	1.5	0.41	0.7	−0.24	2.5	1.59	1.5	−0.20	0.7
1200	0.67	*−3.95*	1.1	*−4.13*	2.0			−1.24	3	*3.84*	1.7	*−7.23*	1.2	1.49	1.5	0.52	0.7	−0.29	2.5	*2.06*	1.5	−0.16	0.8
1300	0.67	*−3.23*	1.3	*−3.50*	2.0			−1.21	3	*4.13*	1.8	*−7.99*	1.2	*2.45*	1.6	0.68	0.7	−0.28	2.5	*2.33*	1.5	0.19	0.8
1540	0.75			*−3.41*	2.0			−1.01	3	*4.92*	1.2	*−10.9*	1.5			0.61	0.8			*3.52*	1.5	−0.26	0.8
1600	0.77	*−2.63*	1.3	*−4.02*	2.0			−1.99	3	*4.24*	1.2	*−12.2*	1.5			−0.24	0.8	−0.82	2.7	*2.64*	1.5	−1.19	0.9
1700	0.87	−0.91	1.3	*−2.75*	2.0			−1.08	3	*5.45*	1.2	*−12.1*	1.8							*3.55*	1.5	−0.33	0.9
2000	1.30	−0.27	1.4	−2.25	2.0			−0.54	3	*5.19*	1.1	*−15.6*	2							*2.97*	1.5	−0.98	1.0
2100	1.39	−2.08	1.4	*−3.80*	2.0			−2.15	3	*3.91*	1.1	*−17.8*	2							1.01	2.5	*−3.76*	1.0
2300	1.86	−0.42	1.4	−2.65	2.0			−1.26	3	*5.92*	1.2	*−18.8*	2.5							1.66	2.5	*−5.28*	1.1
2400	2.34	−1.13	1.4	−2.45	2.1			−1.49	3	*6.14*	1.2	*−19.2*	2.5							−1.34	2.5	*−4.73*	1.1

[a] The average of the differences of all the lamps for each laboratory.

[b] *Italics* indicates the grand-mean difference exceeds 1.1 times the combined Laboratory/NIST uncertainty associated with it.

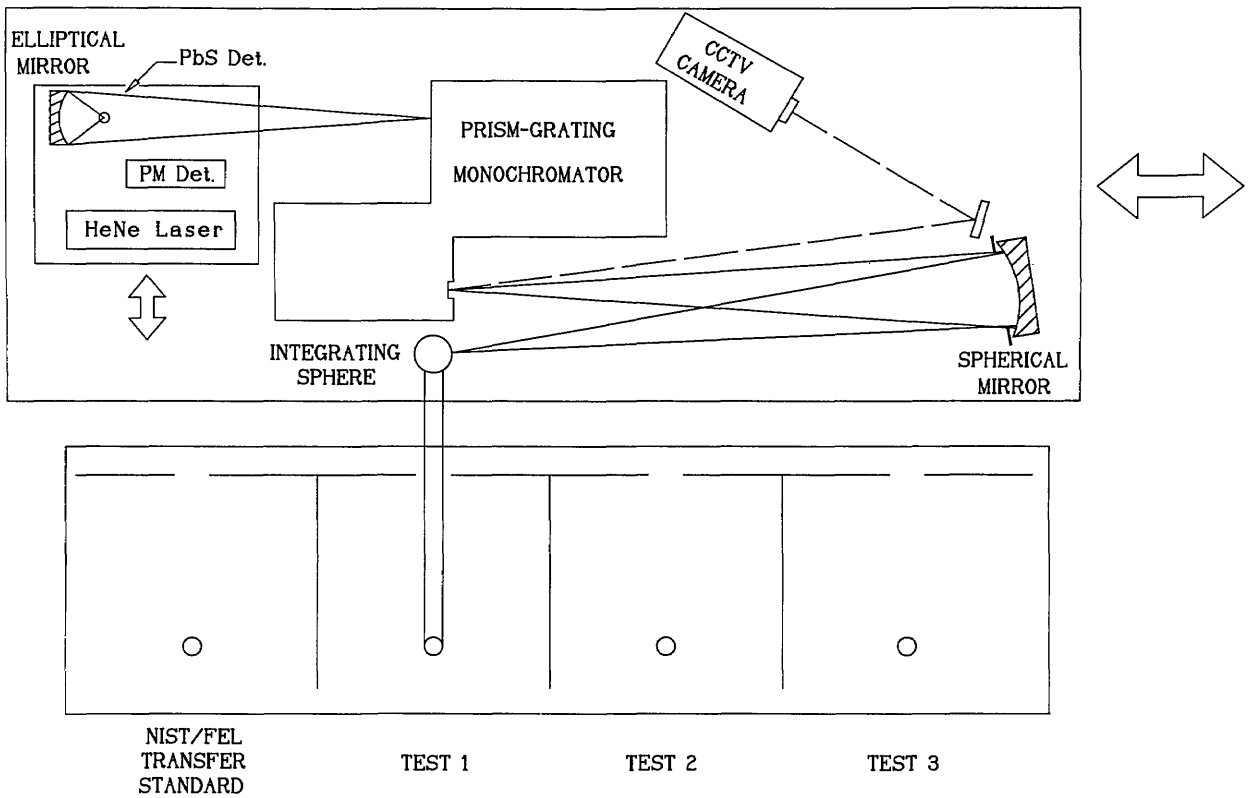

Figure 3. NIST spectral irradiance measurement equipment.

6. Data Analysis

After the completion of all measurements, the following data analysis was carried out by NIST staff.

(a) The percent differences from NIST defined by Eq. (1) were computed as a function of wavelength for both the round-one and round-two spectral irradiance values reported by the participating laboratories for each intercomparison lamp.

(b) The differences between these round-one and round-two differences from NIST were compared to the lamp voltage readings recorded for each lamp by the participants and by NIST. This comparison revealed a few cases in which unduly large discrepancies between the participants' round-one and round-two measurements appeared to be caused by bistable behavior of a lamp. Upon notification of these findings, five laboratories requested that the measurements of one of their lamps be excluded from the data analysis. The average absolute differences between the round-one and round-two data for the remaining lamps were small (ranging from 1.4% at 250 nm through 0.5% at 600 nm to 1% at 2400 nm) and were not included in the error analysis.

(c) The averages of the round-one and round-two percent differences from NIST were computed for each lamp, and the average of these differences of all the lamps measured by each participating laboratory was computed to serve as the "grand mean" for each laboratory. A sample of the data analysis for one laboratory is shown in Appendix B.

(d) As an independent measure for judging the statistical significance of the grand-mean differences, the quadrature combination of the one standard deviation uncertainties quoted by NIST and each laboratory was computed.

Appendix C contains a plot for each laboratory showing its grand mean percent difference from NIST and the combined Lab/NIST one standard deviation uncertainty.

7. Results and Discussion

Table 2 shows the grand-mean percent differences from NIST and the one standard deviation uncertainties of each laboratory's measurements. A plot of the grand-mean differences versus wavelength is shown in Fig. 4. Differences greater than ±6% are not shown on this plot, but can be found in Table 2.

As a visual aid in relating the results obtained for each laboratory to their estimated uncertainties, every grand-mean difference that exceeds 1.1 times[3] the combined laboratory/NIST uncertainty associated with it (as defined in Sec. 6(d), above) has been highlighted in Table 2. The number of measurements thus identified is:

ultraviolet region (250 to 350 nm)
16 of 75 measurements (21%)

visible region (400 to 800 nm)
15 of 80 measurements (19%)

infrared region (900 to 2400 nm)
48 of 102 measurements (47%)

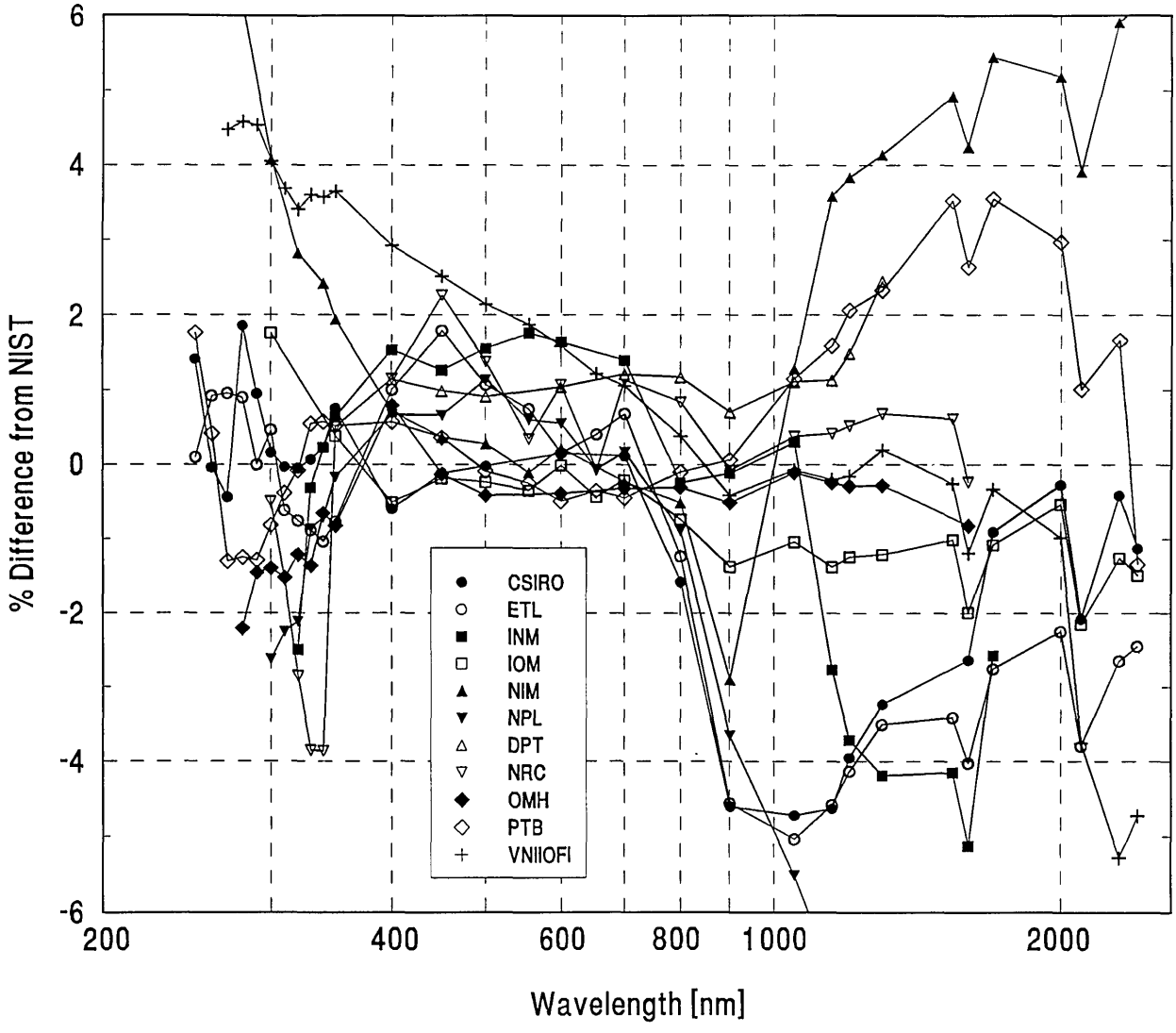

Figure 4. Grand-mean percent differences from NIST of all participants' spectral-irradiance measurements.

[3] The 1.1 factor was applied to avoid computer rejection of data that fell just barely outside the one standard deviation level.

This result should, however, be viewed with caution because it depends on the uncertainty estimates provided by the participating laboratories and because these estimates vary considerably among laboratories. We noted that the participants' uncertainty estimates for many of the highlighted measurements in Table 2 are quite low, and that there are several instances in which grand-mean differences of similar magnitude but larger estimated uncertainties survived the "highlighting" criterion used in Table 2. In this context it may be of interest to compare the uncertainties estimated by each laboratory to the average of the estimates provided by all laboratories. This average, excluding the uncertainty of measurements which deviate significantly from the world mean (NIM in the 250 to 280 nm region and NPL in the 900 to 2400 nm region) is shown in Table 3 as a function of wavelength, and hence it may be seen that the participants' uncertainty estimates are lower than average in the case of 54 of the 79 highlighted measurements in Table 2. This appears to indicate that the uncertainties assigned by some national laboratories may be too small, at least at the one standard deviation level.

As a measure of the world-wide consistency of spectral-irradiance measurements we calculated both the average and the standard deviation of the grand-mean differences from NIST, again excluding the measurements which deviate significantly from the world mean (NIM in the 250 to 280 nm region and NPL in the 900 to 2400 nm region). The results of this calculation are also given in Table 3 and show that the world-average difference from NIST is within the world-average uncertainty estimate for every intercomparison wavelength and exceeds its own standard deviation at one wavelength only (250 nm). However, the standard deviation of the world-average difference from NIST is within the world-average uncertainty estimate only in the visible region, but exceeds it for several ultraviolet wavelengths and for every infrared wavelength from 900 nm upwards. Using the standard deviation of the world average as a measure, we estimate the consistency of the national scales and the intercomparison measurements to be on the order of 1% in the visible region (400 to 800 nm) and on the order of 2 to 4% in the ultraviolet and infrared regions. The overall spread of results is, of course, greater and may be inferred from Table 2.

Table 3. World averages of one standard deviation uncertainty estimates, percent differences from NIST, and comparison with 1975 ETL intercomparison

	World average of the estimated uncertainties of all laboratories	World average and standard deviation of grand-mean differences from NIST		World average and standard deviation of differences from world average of 1975 ETL intercomparison	
WL (nm)	Av unc[a] (%)	Av[b] (%)	Std dev[b] (%)	Av (%)	Std dev (%)
250	2.82	1.10	0.88		
260	2.30	0.43	0.48		
270	1.75	0.92	2.54		
280	1.83	0.78	2.68		
290	1.69	0.55	2.44		
300	2.69	0.57	2.32	0.00	1.33
310	2.18	−0.38	1.95		
320	2.15	−0.37	2.22		
330	1.88	−0.38	2.09		
340	1.76	0.09	2.12		
350	1.66	0.66	1.32	0.00	1.14
400	1.31	0.85	0.95	0.00	1.42
450	1.26	0.89	0.96		
500	1.09	0.70	0.84	0.00	0.77
555	1.04	0.58	0.86		
600	1.05	0.50	0.74	0.00	0.54
654.6	1.07	0.12	0.61		
700	1.00	0.42	0.70	0.00	0.54
800	1.09	−0.29	0.84	0.00	2.42
900	1.31	−1.38	1.95		
1050	1.54	−0.78	2.44		
1150	1.54	−0.48	2.72		
1200	1.55	−0.21	2.63		
1300	1.59	0.17	2.57		
1540	1.44	0.73	3.05		
1600	1.57	−0.50	2.73		
1700	1.54	0.66	3.14		
2000	1.61	0.69	2.80		
2100	1.77	−1.14	3.03		
2300	1.87	−0.34	3.84		
2400	1.95	−0.83	3.66		

[a] Does not include the uncertainties of NIM from 250 to 280 nm or of NPL from 900–2400 nm.
[b] Does not include the grand-mean differences of NIM from 250 to 280 nm or of NPL from 900–2400 nm.

Figure 4 and Table 3 show that the spectral-irradiance measurements performed by NIST assigned slightly lower values than the world average throughout the visible region and at several ultraviolet wavelengths, and tend to be slightly higher in the infrared region. In particular, Fig. 4 shows that dips on the order of 1% appear in most participants' differences from NIST at 1600 and 2100 nm. These dips may be caused by variations in the NIST scale which are within NIST's uncertainty estimates.

We looked for systematic differences between spectral-irradiance scales based on different physical principles. As noted in Sec. 4(a), the NIST scale and a large number of the others are based on blackbodies. As may be seen in Fig. 5, the three scales based on absolute detector radiometry (IOM, DPT, and NRC above 700 nm) show no significant differences from NIST or from the world average and were therefore judged to be consistent with blackbody scales. However, the three detector based scales appear to have better agreement in the ir region than the non-detector based scales. The only other measurements not based on blackbody physics (the synchrotron-based NPL measurements below 370 nm) appear to have yielded somewhat lower values than NIST near 300 nm.

For comparison purposes, we have included on the right-hand side of Table 3 the standard deviations of the world averages obtained in the 1975 spectral-irradiance intercomparison conducted by ETL [3].[4] This shows that the results of the present intercomparison are not too different, except that more laboratories participated and that a greater spectral region was covered.

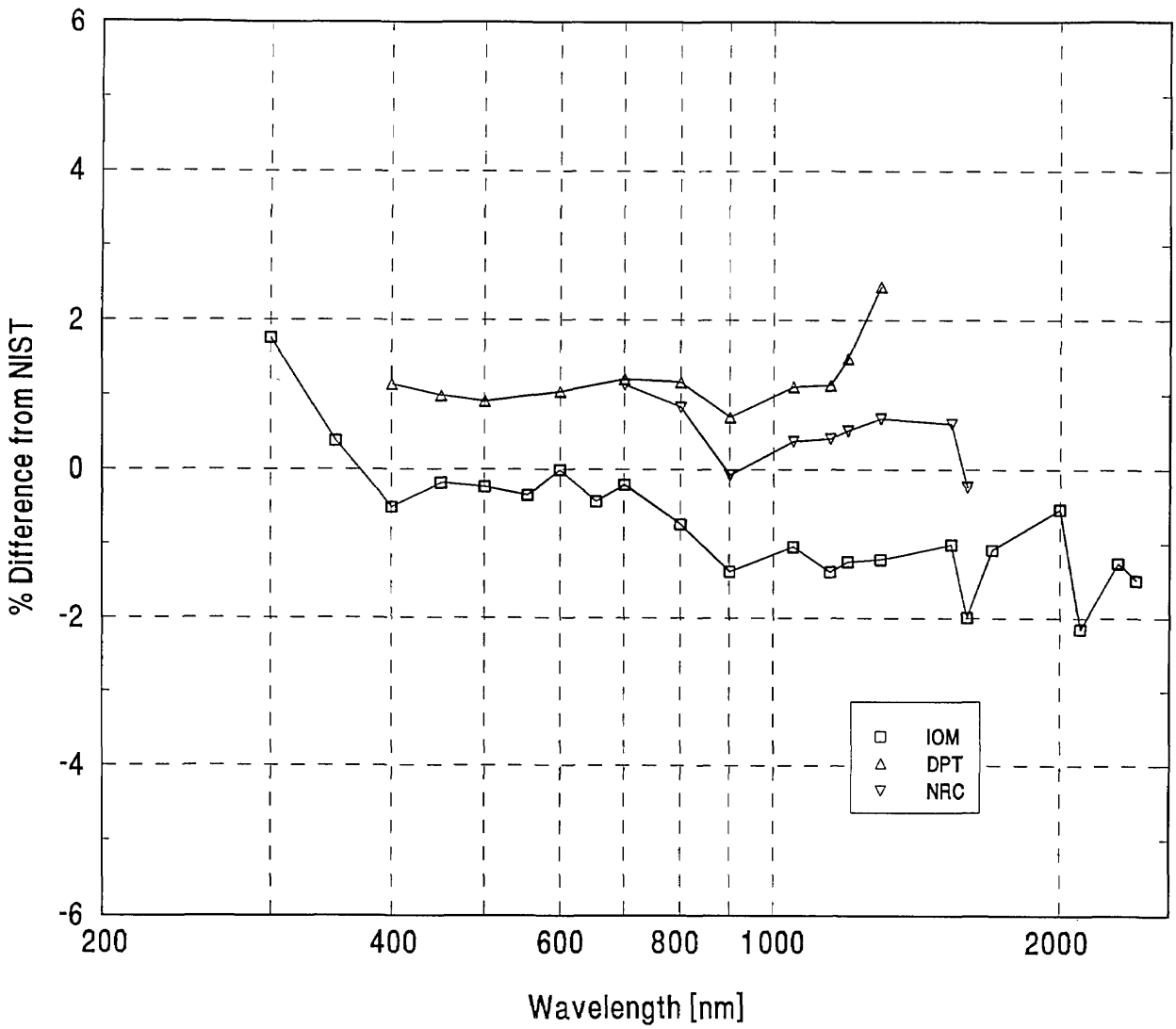

Figure 5. Grand-mean percent differences from NIST of participants with detector-based scales.

[4] The world average and the standard deviation of differences from world average were recalculated without using the ASMW data.

8. Appendix A. Descriptions of the Scale Derivations of the Participating Laboratories

Each laboratory was asked to give a one page or less description of the derivation of its spectral irradiance scale. These descriptions that were submitted are given here.

8.1 Derivation of the NIST (USA) Spectral Irradiance Scale

Realize Spectral Radiance Scale

1. A beam conjoiner is used to measure the responsivity (linearity) of the photomultiplier amplifier system of our spectroradiometer.
2. Lamp V25 (high stability Quinn-Lee type vacuum lamp) is calibrated against a gold point blackbody at 654.6 nm.
3. Lamp C706 (high stability GEC type vacuum lamp) is calibrated against V25 at 654.6 nm—C706 has approximately eight times the output of V25 at 654.6 nm.
4. Lamp C706 is used to determine the temperature of a variable temperature blackbody which operates over a range of 1050 to 2700 K.
5. The spectral radiance of a test source is compared to the spectral radiance of the blackbody at some test wavelength and Placnk's equation is used to determine the spectral radiance of the test source.

Realize Spectral Irradiance Scale on Primary Working Standards

1. Steps 4 and 5 from above are carried out to perform a spectral radiance calibration on the output of a small integrating sphere source (5.1 cm diameter sphere with a 1.8 cm diameter exit aperture) from 250 to 2400 nm.
2. Our spectroradiometer is then put in its spectral irradiance mode where it has a small averaging sphere (3.8 cm diameter sphere with a 1.2 cm entrance aperture) as the receiving optic.
3. At each wavelength the output of the primary working standards are compared to the output of the integrating sphere source.
4. The aperture sizes of the integrating sphere and the averaging sphere are accurately known and we accurately measure the distance between the two apertures. With this information we can calculate the spectral irradiance of the sphere source at the aperture of the averaging sphere.
5. After determining the ratio of a primary working standard output to the sphere source output, we can calculate the spectral irradiance of the primary working standard. This is done for each primary working standard.

Spectral Irradiance Scale Transfer

1. Four primary working standards are used to calibrate a group of 12 test lamps.
2. Each test lamp is measured four times—once in each of four test positions and against each of the four primary working standards.

8.2 Derivation of the CSIRO (Australia) Spectral Irradiance Scale

Relative Spectral Radiance Scale

The temperature of a tungsten-tube type cavity radiator (Osram lamp type Wi80) at about 2700 K was measured using broad-band filters, a non-selective thermal detector and application of Planck's law. Using Planck's law the relative spectral radiances were calculated for the limited wavelength range 350–800 nm.

Relative Spectral Irradiance Scale

1. A matched-pair of colour-corrected lenses, in conjugate positions with a magnification or demagnification of a factor of ten, was used to image the selected region of the cavity lamp or the whole filament of an irradiance standard lamp (Wotan type Wi41G) in turn, within the entrance aperture of an integrating sphere attached to a spectroradiometer. The transfer was also limited to the wavelength range 350–800 nm.
2. The scale of relative spectral irradiance was transferred from the Wotan lamp standards to working standard tungsten-halogen lamps (Ushio Electric 100 V 500 W) by irradiating in turn a barium sulphate plate which was imaged onto the spectroradiometer entrance slit.

Spectral Irradiance Scale—SI Units

The illuminance of each working standard tungsten-halogen lamp was measured at the defined position using an electrical substitution absolute radiometer fitted with a V(λ) correction filter with

accurately-measured spectral transmittances. The conversion factor 683 lm/W was used for the wavelength 555 nm, and correction was made for departure of the detector from V(λ). From the illuminance and the known relative spectral power distribution the spectral irradiances were calculated for the wavelength range 350–800 nm.

Spectral Irradiance Scale—uv and ir Spectral Regions

The CSIRO Spectral Irradiance Scale for the wavelength ranges 250–350 nm and 800–2400 nm was adopted in 1975 from the ETL (Japan) scale of 1973. We also observed at the time good agreement with the NPL (UK) scale over the range 290-760 nm. We have no knowledge of the dependence of this borrowed scale on IPTS scales.

As the CSIRO scale is not independently based for the wavelength ranges 250–340 nm and 850–2400 nm, we suggest that *only values from the CSIRO scale for the wavelength range 350–800 nm be used for the calculation of international mean values.*

8.3 Derivation of the ETL (Japan) Spectral Irradiance Scale

Realization of Spectral Radiance Scale on Shelf Standards—A

1. Three blackbodies, a gold-point, a nickel-tube, and a graphite-tube were constructed.
2. The temperature of the graphite-tube blackbody, which operated over a range of 2200 to 2500 K, was determined from the measured ratio of its spectral radiance to that of the gold-point black-body at 550, 600, and 650 nm.
3. The temperature of the nickel-tube blackbody, which operated within a range of 1520 to 1570 K, was determined by optical pyrometer calibrated against NRLM standard of radiance temperature.
4. Spectral radiances of six tungsten strip lamps (GE 30A/T24) were calibrated against those of the blackbodies from 250 to 2500 nm; all of the three blackbodies were referenced for the wavelengths longer than 1200 nm, whereas only the graphite-tube one was referenced for the shorter wavelengths.

Realization of Spectral Irradiance Scale on Shelf Standards—B

1. Spectral distributions of radiation from three quartz-bromine lamps (Ushio JPD-100-500-CS) were measured by comparing spectral irradiances alternately produced on a white diffusing surface by each of the lamps and by one of the strip lamps (our shelf standards of spectral radiance); two strip lamps were used.
2. The absolute value of spectral irradiance of each of the quartz-bromine lamps was measured at 580 and 600 nm by comparing spectral radiance of a smoked MgO surface irradiated by the lamp with that of one of the strip lamps; two strip lamps were used; the spectral radiance factor of the smoked MgO surface was determined from measured reflectance.
3. The absolute value of integrated irradiance from each of the quartz-bromine lamps was measured by a radiometer combined with a band-pass (300–2750 nm) filter; the radiometer was calibrated in terms of the ETL absolute radiometric scale. The absolute value of spectral irradiance was calculated from the measured integrated irradiance, spectral distribution determined in step 1, and the spectral transmittance of the filter.
4. The absolute value of spectral irradiance at 580 and 600 nm was determined by averaging the results of steps 2 and 3.
5. The spectral irradiance at the whole wavelength range of 250 to 2500 nm was determined by combining the results of steps 1 and 4.

Amendment of Spectral Irradiance Scale in the Shorter Wavelengths

1. Spectral distribution of the shelf standards was compared with that of synchrotron radiation over the wavelength range of 250 to 600 nm.
2. The spectral irradiance scale determined in step 5 of part B was amended in order that the spectral distribution would conform with the result of step 1 for the wavelengths shorter than 500 nm.

8.4 Derivation of the INM (France) Spectral Irradiance Scale

Realize Spectral Radiance Scale

1. A separate apparatus is used to measure the linearity of photomultiplier and photodiode of our spectroradiometer.
2. Two lamps 337C and 340C (20–24G GEC type gas filled lamps) are calibrated against radiance temperature standards of our pyrometry laboratory (high stability GEC type vacuum

lamp calibrated against gold point black body).
3. These lamps are used to determine the temperature of a variable temperature black body which operates over a range of 1500 to 1950 K.
4. The spectral radiance of test sources (339C and 367C) is compared to the spectral radiance of the black body and Planck's equation is used to determine the spectral radiance of the test source.

Realize Spectral Irradiance Scale on Intercomparison Lamps

1. At each wavelength our spectroradiometer is switched from radiance mode for response to radiance standard, to irradiance mode for response to irradiance source.
2. Relative irradiance values are calculated from ratio of these two responses. Irradiance is fixed to 1 for 550 nm.
3. Luminous intensity of intercomparison lamps is compared to luminous intensity standards. Luminous intensity scale is based on use of electrical substitution pyroelectric radiometer.
4. From relative irradiance values and luminous intensity we can calculate irradiance values.
5. Each intercomparison lamp is compared to two radiance standards lamps and four luminous intensity lamps.

8.5 Derivation of the IOM (Spain) Spectral Irradiance Scale

The spectral irradiance scale of the Institute of Optics is based on an electrically calibrated pyroelectric radiometer and maintained in FEL type lamps.

The derivation process is as follows:

a) Measurement of the spectral transmittance of interference filters.
b) Measurement of the irradiance produced by the lamps, filtered by the interference filters, at 50 cm away from the lamp by using the ECPR.
c) Corrections to the measurements in order to take into account filters thickness and bandwidth.
d) Interpolation of the lamp spectral irradiance values from the measurements points. The De Voss' approximation is used.

8.6 Derivation of the NIM (People's Republic of China) Spectral Irradiance Scale

Primary standard is a high temperature (about 2800 K, variable) black body radiator. A precise circular diaphragm is placed at the exit port of the radiator. The spectral irradiance was measured at the place which is departure from the precise diaphragm in a fixed distance (500 mm).

The secondary standard is a group of 10 tungsten-halogen lamps (1000 W).

The comparator is a high accuracy wide wavelength range spectral radiometer which was developed at NIM.

8.7 Derivation of the NPL (UK) Spectral Irradiance Scale

The NPL spectral irradiance scale is based, over the wavelength range 350–800 nm, on comparisons with a black body cavity radiator. The spectral radiance of a group of tungsten ribbon filament lamps was measured by a direct comparison with the radiance of the cavity radiator and a radiance/irradiance transfer was then carried out to establish a relative spectral irradiance scale. The irradiance scale is held by a group of secondary standard coiled tungsten filament lamps.

In order to maintain internal consistency between the various optical radiation scales maintained at NPL, the absolute level of the scale has been assigned by relating it to the national scale of luminous intensity which was established radiometrically and is based on the NPL cryogenic radiometer.

At wavelengths from 200–370 nm, the relative spectral power scale has been established based on synchrotron radiation, which was used to calibrate a group of low pressure deuterium lamps. Again, the first stage of the calibration involved the establishment of a scale of spectral radiance which was then used to provide a scale of relative spectral irradiance on the same deuterium lamps. The absolute level has been assigned by comparison at 350 nm with the black body based scale described above.

The accuracy of the scale has subsequently been checked and confirmed at a number of points in over the wavelength range 400–800 nm by the use of a series of filter radiometers, each consisting of a specially constructed narrow band interference

filter combined with a silicon call. The spectral responsivity curve for each of the radiometers was characterized using a tuneable dye laser and the absolute responsivity obtained by a direct comparison with the NPL spectral responsivity scale based on the cryogenic radiometer.

When the intercomparison started, work was in progress to extend the wavelength range covered by the NPL spectral irradiance scale into the infrared, but this work had not been completed. Rather than opt out completely in the infrared, NPL decided to measure the lamps and submit results based on a provisional calculation using published data for the emissivity of tungsten. It was hoped that these results could later be corrected to incorporate the new scale before the end of the intercomparison. Unfortunately, however, further unforseen problems were encountered which prevented NPL from completing the work on time.

8.8 Derivation of the DPT (South Africa) Spectral Irradiance Scale

Our spectral irradiance measurements were made over the wavelength region 400–1300 nm.

The method was based on an absolute radiometer and a series of interference filters which were used to determine the spectral irradiances of quartz halogen incandescent lamps at a number of discrete wavelengths. Values at intermediate wavelengths were obtained by interpolation.

The spectral transmittances of 11 interference filters together with a Schott K50 glass filter were measured with a Jobin Yvon Model HRD1 double monochromator, using a configuration which closely reproduces the actual geometry used in the spectral irradiance measurements. These measurements were verified on a Hitachi Model U-3400 spectrophotometer.

A pyroelectric detector, previously calibrated against an absolute radiometer, was then used in conjunction with the filter combinations mentioned above to measure the actual spectral irradiances around the different effective wavelengths.

Irradiance values at intermediate wavelengths were determined by a least square fitting to a polynomial function.

8.9 Derivation of the NRC (Canada) Spectral Irradiance Scale

UV-Visible (300–800 nm)

This scale is maintained on eight 500W quartz-halogen lamps similar to the lamps used in the last intercomparison [Suzuki and Ooba, Metrologia **12**, 123 (1976)]. The working distance is 50 cm. The lamps were calibrated originally by means of an NBS spectral irradiance standard. After the above intercomparison, the spectral irradiance values of the eight lamps were adjusted to be equal to the world mean of that intercomparison. These adjusted values have been used since, without applying ageing corrections.

Near-Infrared (700–1600 nm)

This is a new scale, realized at NRC in 1989-90. Electrical substitution absolute radiometers were used in conjunction with interference filters to measure directly the spectral irradiance of FEL and NPL/GEC tungsten-halogen lamps from 700 nm to 1600 nm, at 100 nm intervals. The working distance is 100 cm. Interpolation techniques are used to obtain values at intermediate wavelengths.

For This Intercomparison

The old scale (300–800 nm) was used to calibrate the lamps from 300 nm up to and including 654.6 nm. The lamps used in the intercomparison are some of the lamps used to realize the new scale in the near ir. The new scale spectral irradiance values were used from 700 to 1600 nm. A correction factor was applied to transfer from a working distance of 100 cm to a working distance of 50 cm. This correction factor was determined for each lamp by measuring the variation of irradiance with distance.

8.10 Derivation of the OMH (Hungary) Spectral Irradiance Scale

Realization of Spectral Irradiance Scale

1. Today our spectral irradiance scale is based on two FEL 8A/1000 W irradiance standard lamps calibrated by NIST.
2. We have developed a wide band filter-radiometer with eight bandfilters made of absorbing glasses and a precision aperture. The spectral response calibration of the device is based on our absolute spectral responsivity scale and high accuracy spectral transmittance measurements.
3. The integrated spectral responses were measured for the investigated irradiance standard lamps by means of the eight bandfilters.

4. The spectral irradiance of the standard lamps in the spectral range of 330–800 nm is being determined from the eight measurement results with the help of a least squares fitting deconvolution program. This program needs further development.
5. *The measurement results sent by OMH for the intercomparison are based on our calibrated lamps. We plan to send our bandfilter-radiometer based results too by May.*

Spectral Irradiance Scale Transfer

1. Our spectral irradiance transfer spectroradiometer consists of a small averaging sphere (10 cm diameter sphere with a 2.6 cm entrance aperture) as a receiving optic, a double grating monochromator, imaging optics, detectors (Si photodiode, PbS photoresistor, photomultiplier) and an ac current to voltage converter lock in system.
2. At each wavelength the output of our spectral irradiance standards were measured with our spectroradiometer.
3. At each wavelength the output of the test lamps were measured with our spectroradiometer.
4. Then the standard lamps were remeasured at each wavelength in order to take in consideration the long term instability of the measuring system.
5. After determining the ratio of the standard lamps output to the test lamps output, we can calculate the spectral irradiance of the test lamps.
6. Each lamp was measured four times.

8.11 Derivation of the PTB (Germany) Spectral Irradiance Scale

The spectral irradiance scale is based on a Planckian radiator with accurately known temperature and area realized by a variable-temperature blackbody with a large-area, water-cooled measuring aperture. The blackbody temperature of approximately 2800 K is measured with a linear pyrometer calibrated at PTB. The spectral irradiance at an accurately measured distance of 1 m to the aperture is derived from the spectral radiance of the Planckian radiator at the set temperature and the accurately measured area of the aperture with a diameter of approximately 10 mm. The transfer of the spectral irradiance scale of the blackbody to that of the standard lamp(s) is performed by comparing the radiance of a plane reflection standard (BaSO4) defining the measuring plane which is perpendicularly irradiated by both sources, blackbody and standard lamp(s), in succession. Each of our three CCPR test lamps is calibrated three times per round at a distance of 70 cm to the measuring plane against a group of four standard lamps where all lamps are placed on the same optical axis. In addition, an uncalibrated highly stabilized monitor or comparison lamp is always used to correct for residual instabilities of the electrical and optical setup during the measurement. The factors to correct the spectral irradiance of the test lamps for the required distance of 50 cm are measured separately, where it is verified that the factors are independent of wavelength.

An improved spectroradiometer is just being put into operation.

8.12 Derivation of the VNIIOFI (USSR) Spectral Irradiance Scale

Lamp Calibration Method

Calibrations of the lamps have been carried out against the Radiometric Standard of the USSR. Method of measurements is based on the use of a graphite blackbody model (BBM) of BBM-2500 type. Operating temperatures of the BBM can vary within the range of 1700 to 2600 K. The BBM temperature was maintained with the accuracy of ± 0.3 K. BBM-2500 was installed inside a vacuum chamber provided with a quartz output window which transmission spectrum was measured by the standard spectrophotometer.

BBM was mounted on a special support together with a test lamp, a set of screens, a rotatable integrating sphere and a mirror condenser used to focus the integrating sphere exit port onto the spectrometer entrance slit. The integrating sphere is made of "Halon" type material and has the following dimensions: the sphere diameter—40 mm, the entrance and exit port diameters—11 mm and 5 mm, respectively, with the angle between the ports being 90°. The sphere is fitted with a rotary mechanism to allow for turning the entrance port to face either the BBM or the test lamp. The condenser is built of two off-axis parabolic mirrors with a focus distance of 822 mm. The double monochromator HRD-1 ("Jobin Yvon," France) in combination with a set of photomultipliers and photoresistance cells was used as a spectrometer.

Calibration of the test lamps for spectral irradiance consisted of two stages.

1. During the first stage, the relative spectral irradiance distribution of the lamps was measured. Incidentally, the distance from the entrance port of the integrating sphere to the lamp was set at 1200 mm, while that to the BBM aperture diaphragm was 300 mm. The BBM aperture diaphragm was placed inside a vacuum chamber and had a diameter of 8 mm. this provided for ensuring an adequate level of signal from BBM throughout the entire spectrum range. Independence of the relative spectral distribution of irradiance against a distance to a lamp and the BBM aperture diaphragm was under control.
2. During the second stage, the lamp and the BBM aperture diaphragm were positioned at a distance of 500 ± 0.1 mm from the entrance port of the integrating sphere (besides, BBM aperture diaphragm was located outside the vacuum chamber and its diameter was 3 ± 0.001 mm) and the absolute spectrum of the lamp was found at several wavelengths in the visible region of the spectrum.

9. Appendix B. Plots Showing the Data Analysis for One of the Laboratories

Section 6 of the main paper describes the data analysis. A sample of the data analysis is given here. The data analysis for PTB is shown graphically in Figs. 6 to 10.

10. Appendix C. Plots of the Grand-Mean Percent Difference from NIST and the Combined Lab/NIST Uncertainty

Figures 11 to 21 show the grand-mean percent difference from NIST and the combined Lab/NIST uncertainty for each laboratory. The combined Lab/NIST uncertainty is the quadrature sum of the one standard deviation uncertainty reported by the laboratory and the one standard deviation uncertainty reported by NIST (given in Table 2).

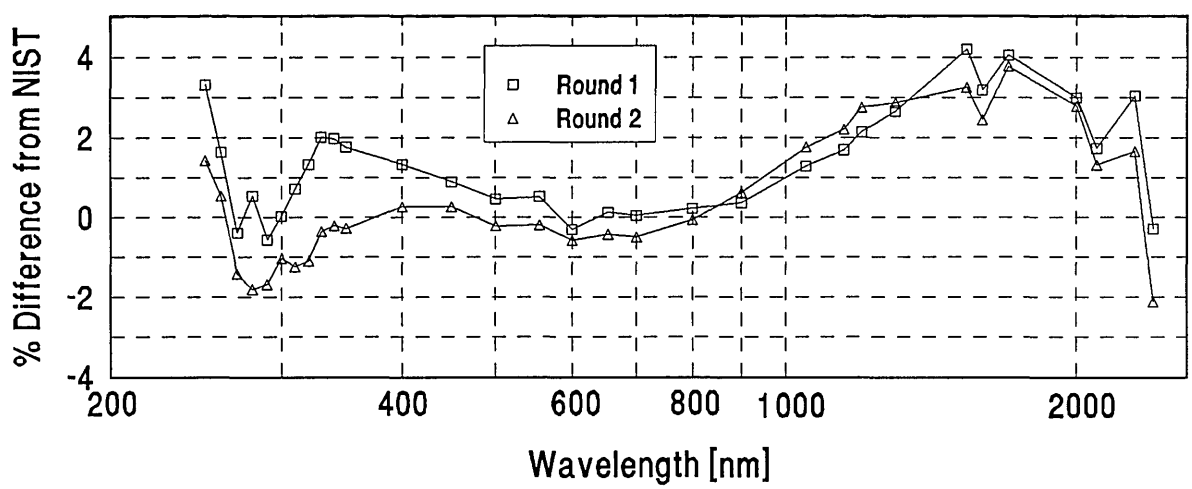

Figure 6. PTB Lamp E9 percent difference from NIST.

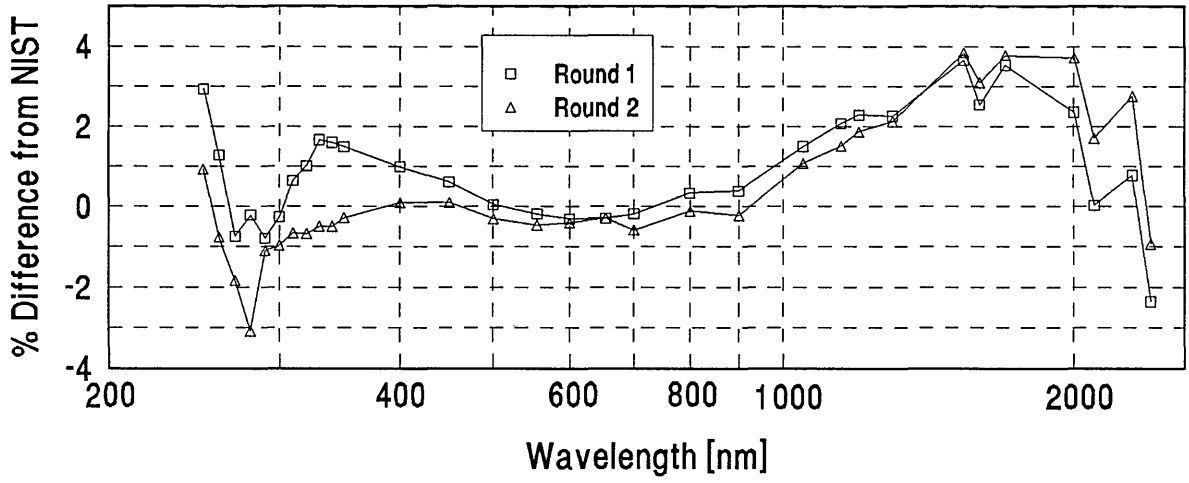

Figure 7. PTB lamp E10 percent difference from NIST.

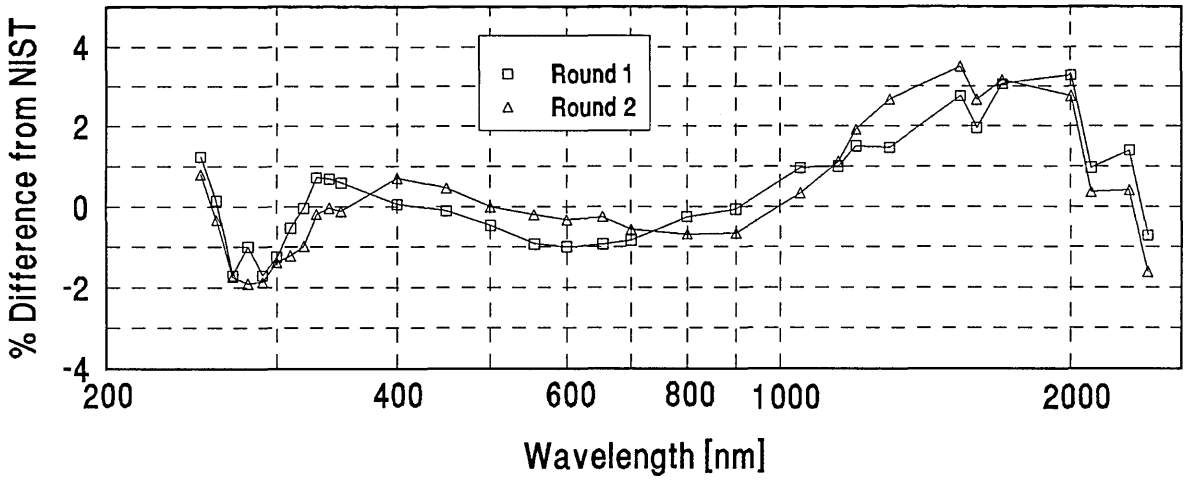

Figure 8. PTB lamp F28 percent difference from NIST.

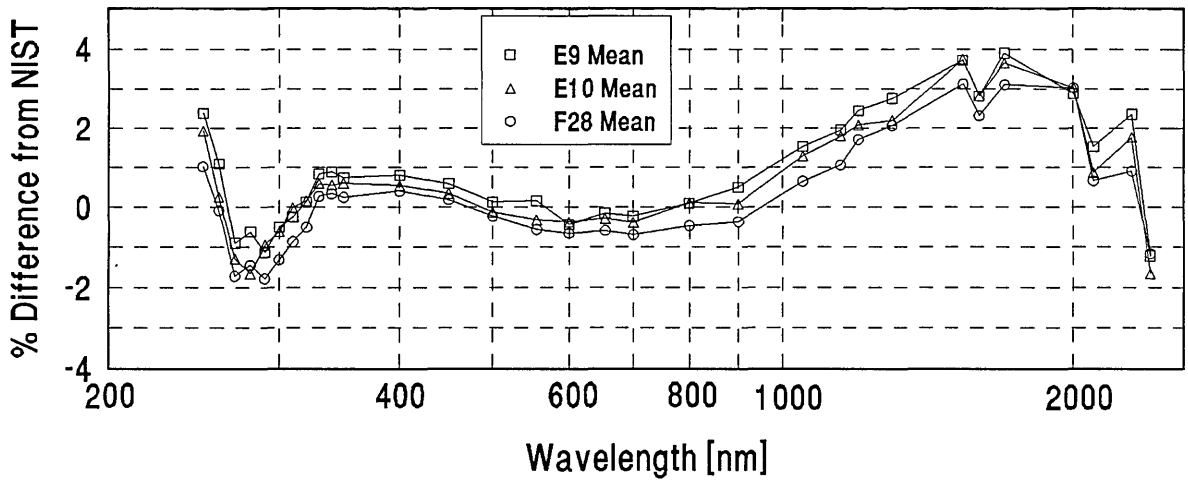

Figure 9. PTB percent difference from NIST.

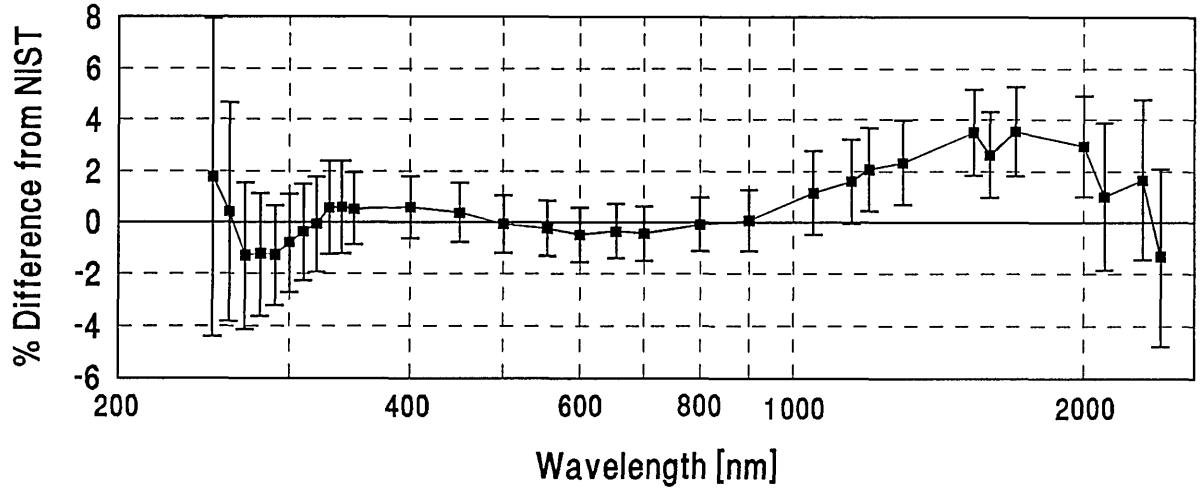

Figure 10. PTB grand-mean percent difference from NIST and combined PTB/NIST uncertainty.

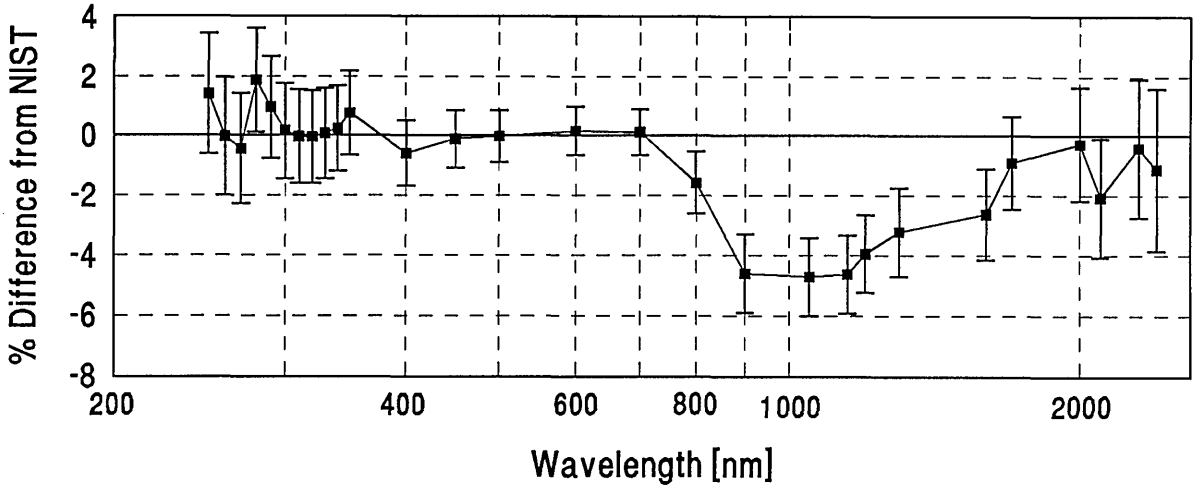

Figure 11. CSIRO grand-mean percent difference from NIST and combined CSIRO/NIST uncertainty.

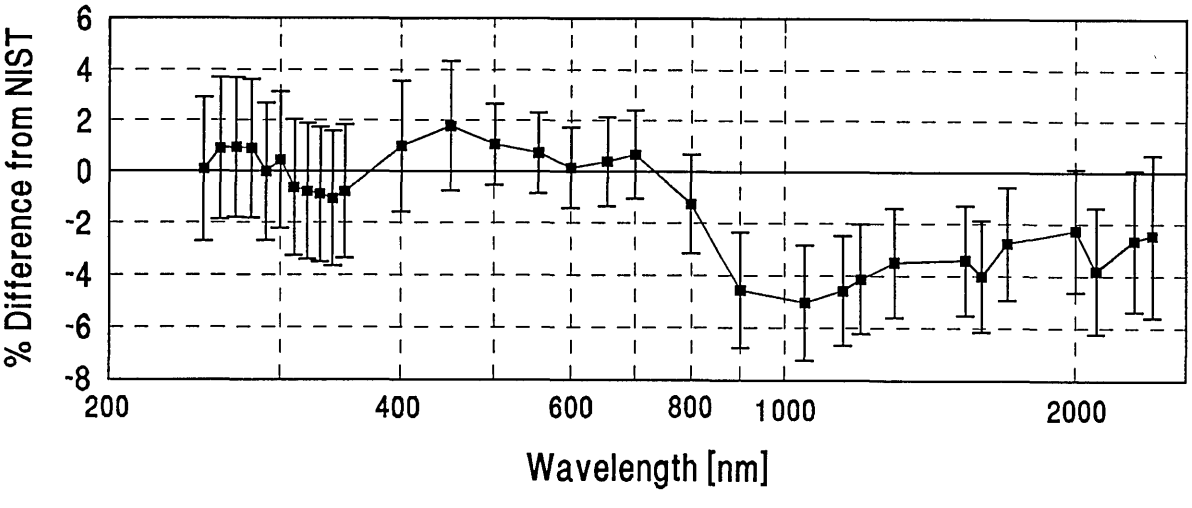

Figure 12. ETL grand-mean percent difference from NIST and combined ETL/NIST uncertainty.

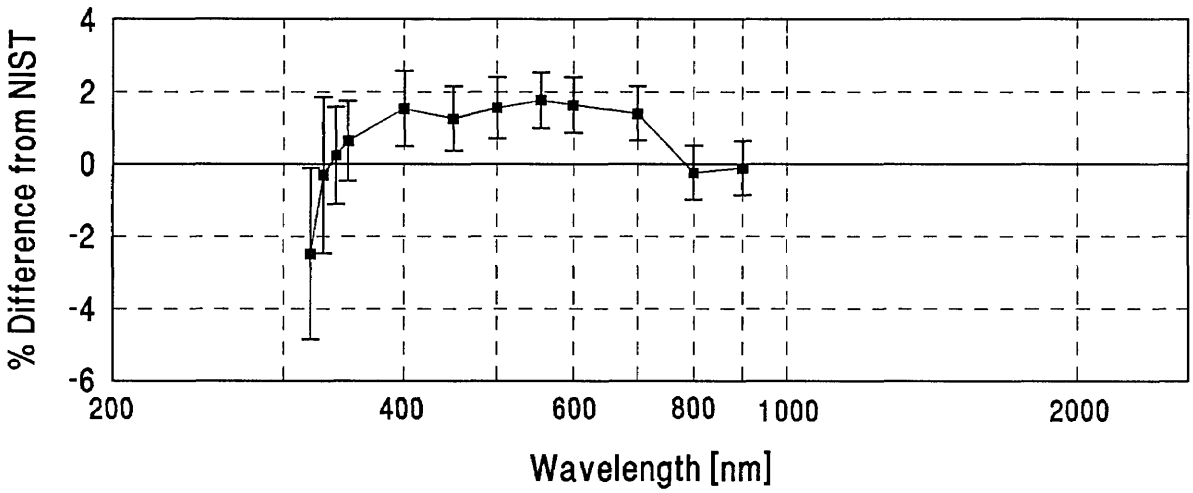

Figure 13. INM grand-mean percent difference from NIST and combined INM/NIST uncertainty.

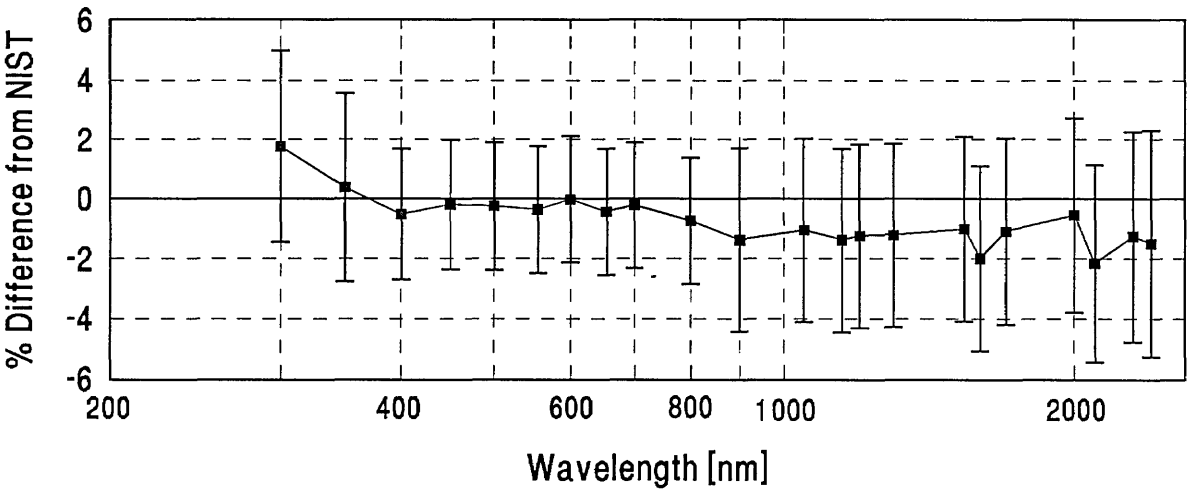

Figure 14. IOM grand-mean percent difference from NIST and combined IOM/NIST uncertainty.

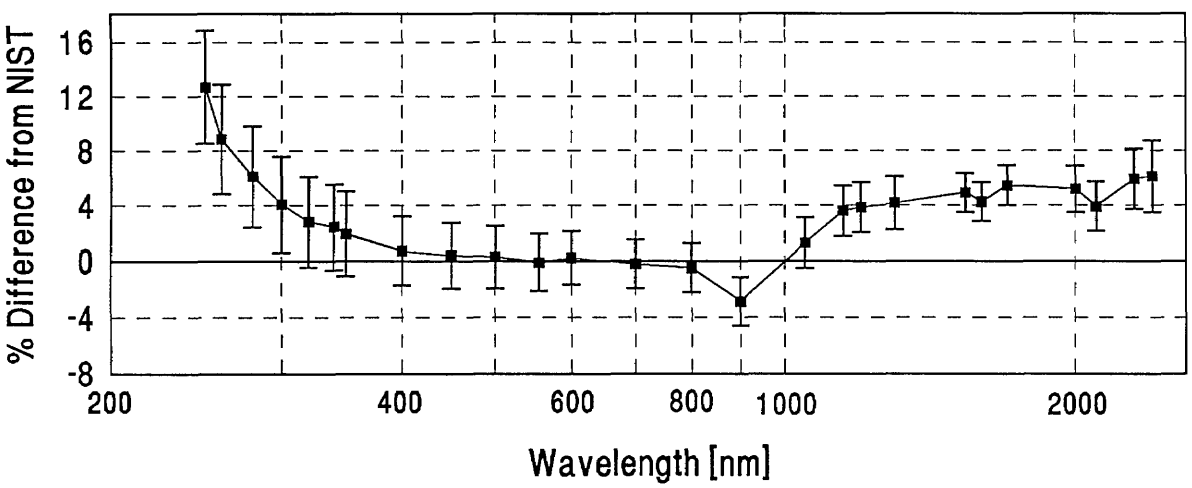

Figure 15. NIM grand-mean percent difference from NIST and combined NIM/NIST uncertainty.

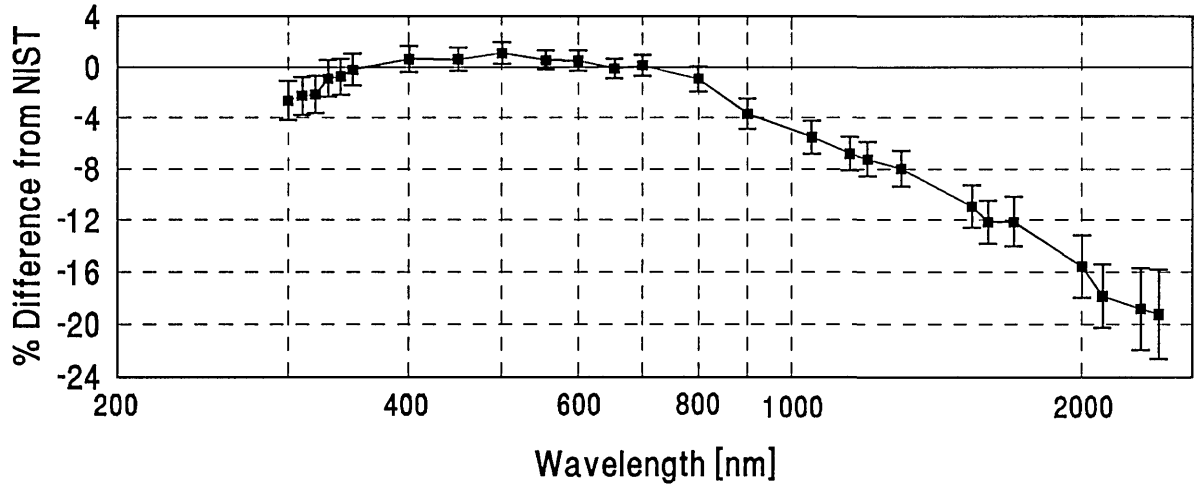

Figure 16. NPL grand-mean percent difference from NIST and combined NPL/NIST uncertainty.

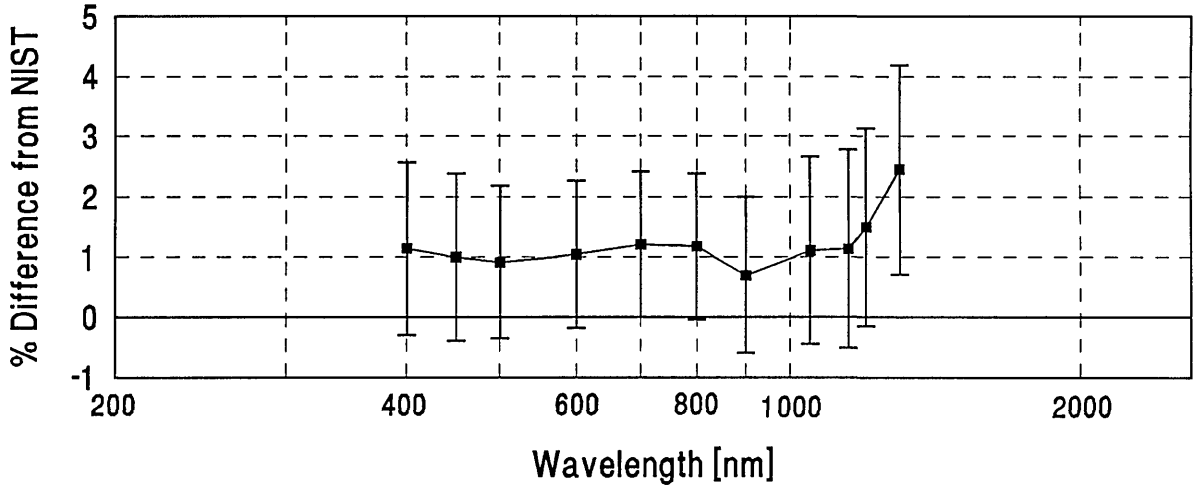

Figure 17. DPT grand-mean percent difference from NIST and combined DPT/NIST uncertainty.

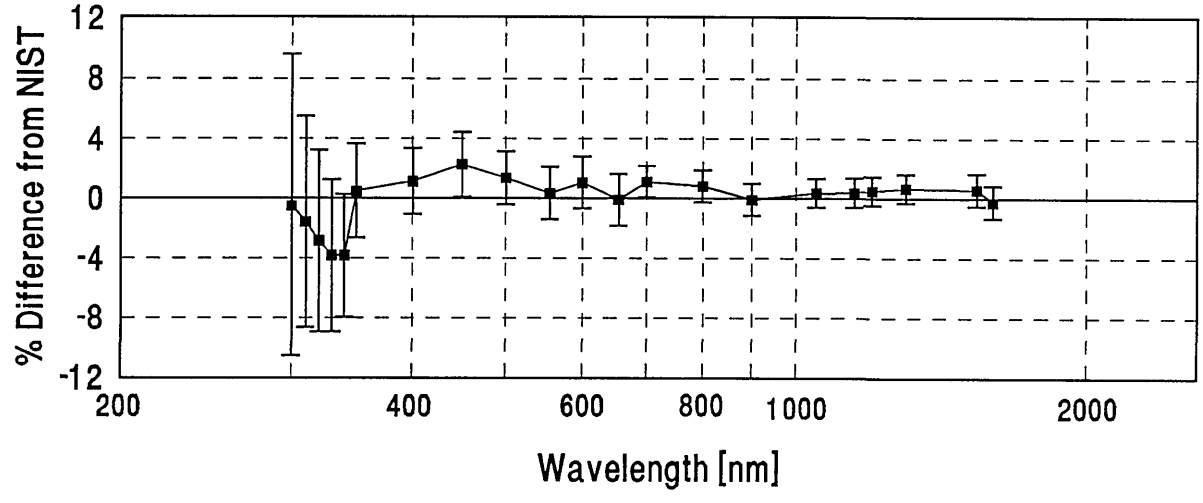

Figure 18. NRC grand-mean percent difference from NIST and combined NRC/NIST uncertainty.

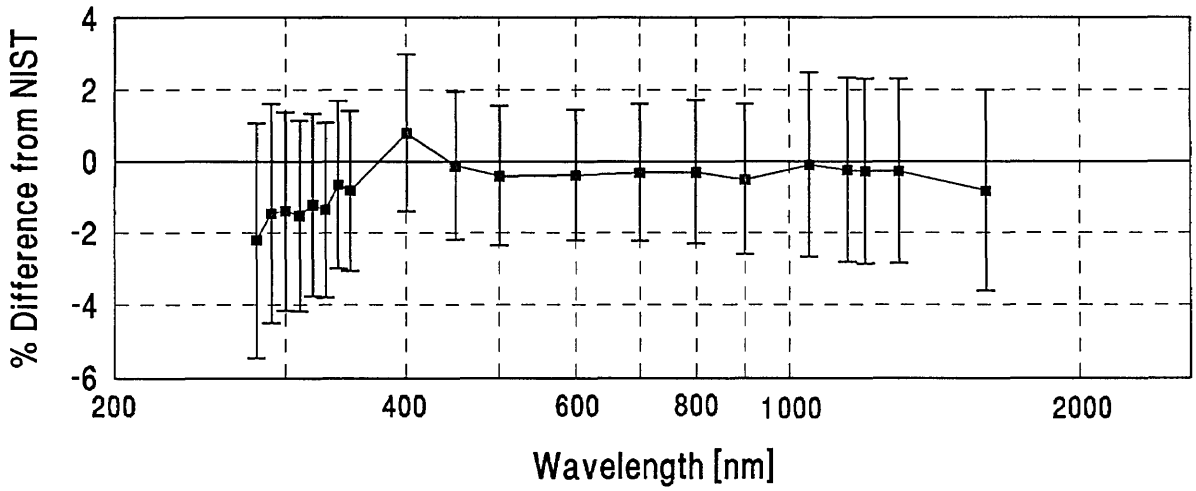

Figure 19. OMH grand-mean percent difference from NIST and combined OMH/NIST uncertainty.

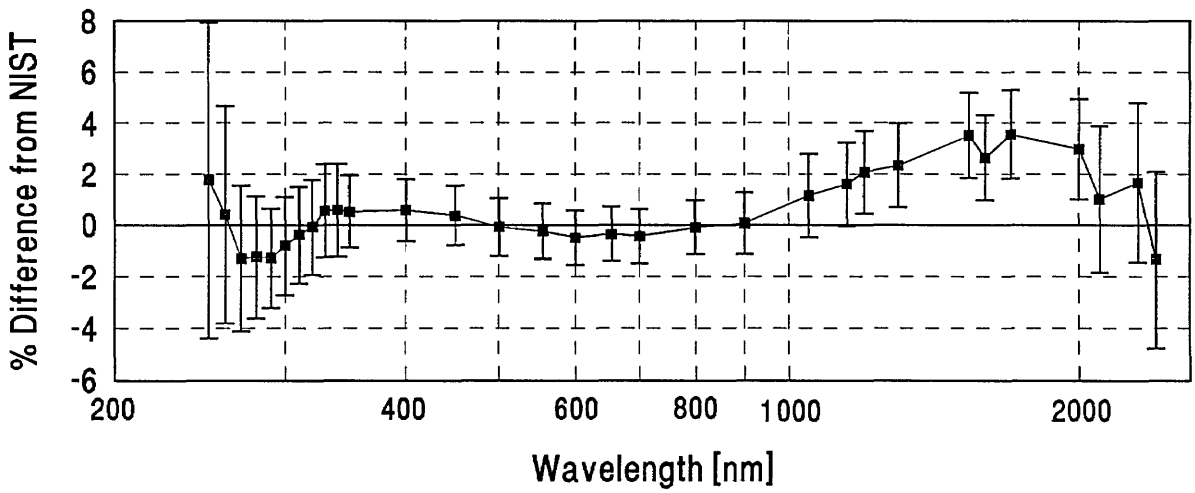

Figure 20. PTB grand-mean percent difference from NIST and combined PTB/NIST uncertainty.

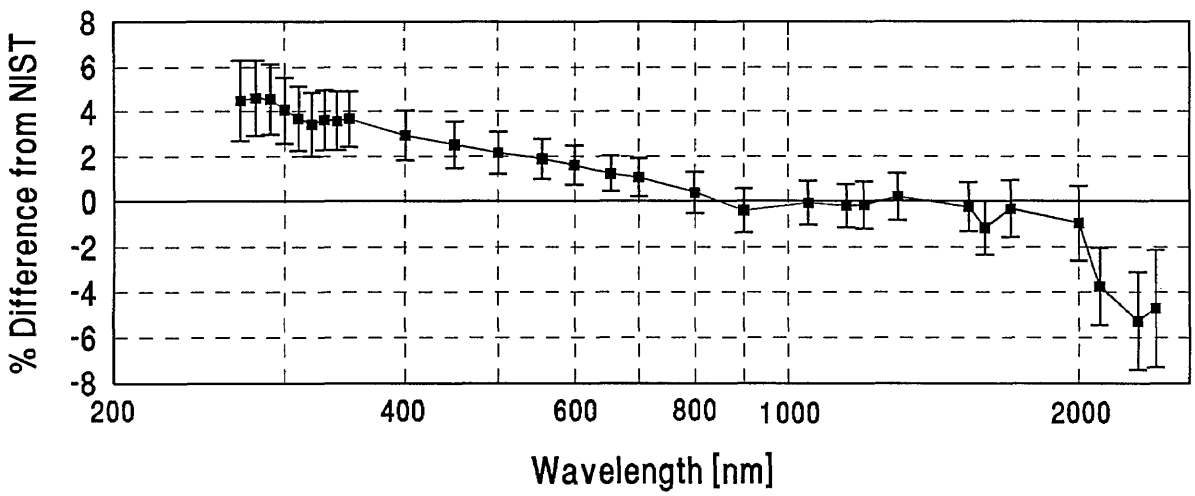

Figure 21. VNIIOFI grand-mean percent difference from NIST and combined VNIIOFI/NIST uncertainty.

11. References

[1] Comité Consultatif de Photometrie et Radiometrie, Report of 11th Session. BIPM, Sevres Cedex, France (1986).
[2] Comité Consultatif de Photometrie et Radiometrie, Report of 12th Session. BIPM, Sevres Cedex, France (1990).
[3] M. Suzuki and N. Ooba, Metrologia **12**, 123 (1976).
[4] T. M. Goodman and J. R. Moore, Report on the Development of a Tungsten-Halogen Lamp for Use as a Secondary Standard. BCR Contract #760/1/000/059/82/2-BCR-UK(30). NPL, Teddington, U.K. (1987).
[5] J. H. Walker, R. D. Saunders, J. K. Jackson, and D. A. McSparron, Spectral Irradiance Calibrations. NBS Special Publication 250-20. U.S. Government Printing Office, Washington, DC (1987).
[6] H. Preston-Thomas, Metrologia **27**, 3 (1990).
[7] K. D. Mielenz, R. D. Saunders, A. C. Parr, and J. J. Hsia, J. Res. Natl. Inst. Stand. Technol. **95**, 621 (1990).

About the authors: *James Walker is an optical physicist in the Radiometric Physics Division at NIST. Robert Saunders, an optical physicist, is presently the group leader of the Thermal Radiometry Group of the Radiometric Physics Division. John Jackson is responsible for making measurements in the Facility for Automated Spectroradiometric Calibrations (FASCAL) in the Radiometric Physics Division. Klaus Mielenz, a physicist, is the retired Chief of the Radiometric Physics Division.*

Volume 96, Number 6, November–December 1991
Journal of Research of the National Institute of Standards and Technology

[J. Res. Natl. Inst. Stand. Technol. 96, 669 (1991)]

Certification of SRM 1960: Nominal 10 μm Diameter Polystyrene Spheres ("Space Beads")

Volume 96 Number 6 November–December 1991

Thomas R. Lettieri, Arie W. Hartman, Gary G. Hembree[1], and Egon Marx

National Institute of Standards and Technology,
Gaithersburg, MD 20899

Experimental, theoretical, and calculational details are presented for the three independent micrometrology techniques used to certify the mean diameter of Standard Reference Material 1960, nominal 10 μm diameter polystyrene spheres ("space beads"). The mean diameters determined by the three techniques agreed remarkably well, with all measurements within 0.1% of each other, an unprecedented achievement in the dimensional metrology of microspheres. Center distance finding (CDF), a method based on optical microscopy, gave a value of 9.89 ± 0.04 μm, which was chosen to be the certified mean diameter. The supporting measurements were done using metrology electron microscopy (MEM) and resonance light scattering (RLS). The MEM technique, based on scanning electron microscopy, yielded 9.89 ± 0.06 μm for the mean diameter of the microspheres in vacuum, while the RLS value was 9.90 ± 0.03 μm for the microspheres in liquid suspension. The main peak of the diameter distribution for SRM 1960 is nearly Gaussian with a certified standard deviation of 0.09 μm, as determined by CDF. Off the main peak, there are about 1% oversized particles and a negligible amount of undersized particles. The report gives a detailed description of the apparatus, the experimental methods, the data-reduction techniques, and an error analysis for each of the micrometrology techniques. A distinctive characteristic of this SRM is that it was manufactured in microgravity aboard the NASA space shuttle Challenger and is the first commercial product to be made in space.

Key words: electron microscopy; length; light scattering; metrology; microgravity; micrometrology; microscopy; microspheres; particles; particle sizing; polystyrene spheres; reference materials; sizing; standards.

Accepted: October 1, 1991

1. Introduction

The National Institute of Standards and Technology (NIST), in a cooperative effort with ASTM, has completed the certification of a series of monodisperse particle-sizing Standard Reference Materials (SRMs) for use in instrument calibration and as benchmark standards for microdimensional metrology [1,2]. Six SRMs are now available: SRM 1691 (nominal 0.3 μm spheres); SRM 1690 (nominal 1 μm spheres); SRM 1962 (nominal 3 μm spheres); SRM 1960 (nominal 10 μm spheres); SRM 1961 (nominal 30 μm spheres); and SRM 1965 (a microscope slide containing the nominal 10 μm spheres).

The present report describes the certification process for SRM 1960, nominal 10 μm diameter spheres (Figs. 1, 2, and 3). Three micrometrology techniques were used to get an accurate mean di-

[1] Present address: Department of Physics, Arizona State University, Tempe, AZ 85287.

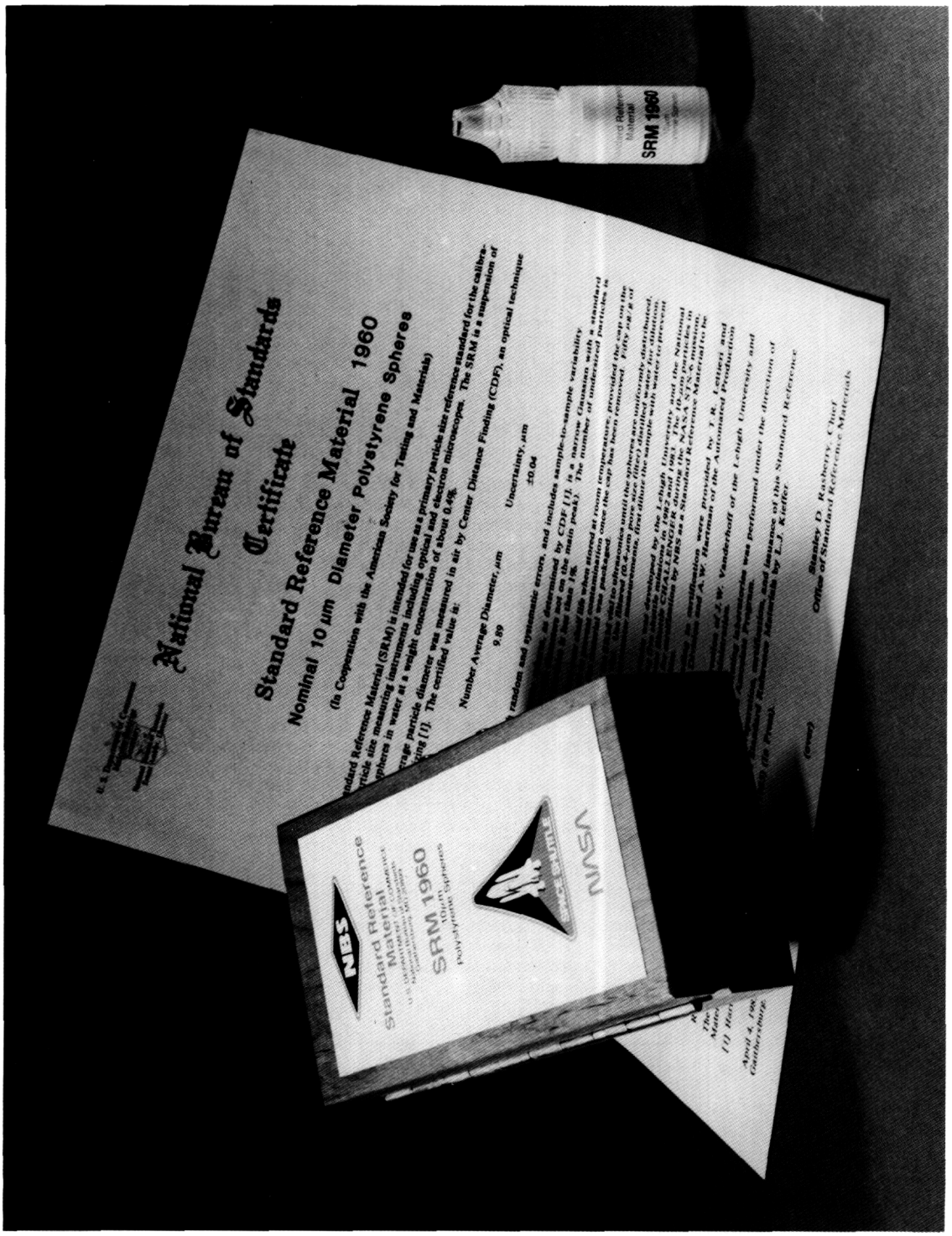

Fig. 1. Photo of NIST Standard Reference Material 1960 showing a vial of the SRM, the certificate, and the package.

ameter for these polystyrene microspheres [3]: center distance finding (CDF), metrology electron microscopy (MEM), and resonance light scattering (RLS). The results from each technique agreed to well within the stated uncertainties, with the CDF value of 9.89 ± 0.04 μm assigned as the certified mean diameter. In addition, CDF was used to get a certified value of 0.09 μm for the standard deviation of the main peak of the size distribution.

SRM 1960 is packaged in 5 ml plastic vials at a weight concentration of particles of 0.4% (Fig. 1); there are thus about 40 million particles in each vial. To prevent the growth of biological organisms, 50 ppm of sodium azide were added as a biocide before the material was packaged. The material is also available on a microscope slide (SRM 1965) for calibrating optical microscopes, among other uses in micrometrology [4]. The SRM 1960 spheres were grown in a microgravity environment aboard the NASA space shuttle Challenger during its STS-6 mission in April 1983, making this SRM the first product to be made in space for commercial use [5]. Details of the polymerization processes used to grow the microspheres are given elsewhere [6].

In this report, the experimental, theoretical, and calculational procedures for each technique, and their sources of uncertainty, are discussed in detail. The center distance finding technique is described first, followed by descriptions of metrology electron microscopy and resonance light scattering.

2. Center Distance Finding

The certified diameter for SRM 1960 was determined using center distance finding (CDF). This micromeasurement technique uses a conventional optical microscope and has the advantages of high resolution (0.03 μm, comparable to that of electron microscopy), high accuracy (the image magnification of an optical microscope is a stable, well known number), and a non-harsh environment (no vacuum, no electron beam irradiation). For these reasons, and because of the high accuracy of the technique, the CDF values for the mean diameter and the size distribution width were the ones chosen to be the certified values for the SRM.

2.1 Experimental Approach

In the CDF technique, the microspheres are arranged on a microscope slide as two-dimensional contacting structures, which are then illuminated with parallel light (Fig. 4). In this configuration, each transparent microsphere acts like a positive lens and refracts the transmitted light into a small, circular focal spot (Fig. 4). These spots mark the locations of the microsphere centers, and the center distances (CDs) between contacting spheres contain the diameter information that is desired. The dot patterns are then photographed and the CDs measured from the photographic film and converted into distances in the object plane, using accurately known values for the optical image magnification on-axis and elsewhere in the field of view (FOV). This procedure is much more precise than the microsphere edge detection used in conventional array sizing [7].

If, as is often the case with monosize microsphere materials, the particles have a Gaussian size distribution, then the CDs will also be normally distributed with a standard deviation that is $\sqrt{2}$ times smaller (because each CD averages over the diameters of two spheres [8]). Conversely, when the measured microsphere material exhibits a Gaussian CD distribution, both the mean diameter and the diameter distribution can be deduced. This can be done with an uncertainty much smaller than the wavelength of the light used in the microscope.

In the CDF measurements of SRM 1960, the microsphere structures were not the usual hexagonal arrays, but instead were disordered assemblies (Fig. 5). These are used in order to avoid measurement errors caused by air gaps between spheres [9]; such air gaps are natural to hexagonal arrays and will lead to errors in the CDF measurements (see "CDF Error Analysis" section).

Since the CDF technique relies on accurate measurements of sphere centers in photomicrographs, the film scale must be well known everywhere in the FOV used, and the dimensional stability of the photographic film must be sufficient to support these measurements. Thus, a precision calibration of the microscope for image magnification everywhere in the utilized FOV is an essential part of the microsphere diameter-distribution measurement by CDF. The procedure used to calibrate the microscope for image magnification is described in the Appendix. Figure 6 shows the magnification values vs. off-axis distances determined using this calibration procedure [8]. The area on the film that was used in the measurements had a diameter of about 80% of the short dimension of the 100×125 mm film (i.e., about 80 mm in diameter).

Volume 96, Number 6, November–December 1991
Journal of Research of the National Institute of Standards and Technology

National Institute of Standards & Technology

Certificate

Standard Reference Material 1960

Nominal 10 μm Diameter Polystyrene Spheres

(In Cooperation with the American Society for Testing and Materials)

This Standard Reference Material (SRM) is intended for use as a primary particle size reference standard for the calibration of particle size measuring instruments including optical and electron microscopes. The SRM is a suspension of polystyrene spheres in water at a weight concentration of about 0.4%.

The number average particle diameter was measured in air by center distance finding (CDF), an optical technique related to array sizing [1]. The certified value is:

Number Average Diameter, μm	Uncertainty, μm
9.89	±0.04

The uncertainty consists of both random and systematic errors, and includes sample-to-sample variability.

The size distribution of the polystyrene spheres, as determined by CDF [1], is a narrow Gaussian with a standard deviation of 0.9% (excluding particles with diameters not on the main peak). The number of undersized particles is negligible and the number of oversized particles is less than 1%. Supporting measurements were made using resonance light scattering and metrology electron microscopy. The results from these techniques for the diameter were: resonance light scattering (9.90 ± 0.03 μm) and metrology electron microscopy (9.89 ± 0.06 μm).

The material is expected to have at least a four-year shelf life when stored at room temperature, provided the cap on the vial is not removed. Care should be exercised to prevent contamination once the cap has been removed. Fifty μg/g of sodium azide was added as a biocide before the material was packaged.

Before sampling, manually shake and/or expose the SRM vial to ultrasonics until the spheres are uniformly distributed, then take a sample by squeezing a drop from the vial. Use filtered (0.4-μm pore size filter) distilled water for dilution. When electrolytes are used for electrical sensing zone counter measurements, first dilute the sample with water to prevent agglomeration.

The technology necessary to produce these polystyrene particles was developed by the Lehigh University and the National Aeronautics and Space Administration (NASA) during five shuttle missions in 1982 and 1983. The 10-μm particles in SRM 1960 were manufactured in space aboard the Space Shuttle CHALLENGER during the NASA STS-6 mission, 4-9 April 1983. The particles were provided by NASA for certification by NIST as a SRM to be made available to the scientific and technical communities.

The technical direction and physical measurements leading to certification were provided by T.R. Lettieri, A.W. Hartman, and G.G. Hembree of the Precision Engineering Division.

Gaithersburg, MD 20899
October 18, 1991
(Revision of Certificate dated 4-4-85)

William P. Reed, Chief
Standard Reference Materials Program

(over)

Fig. 2. The certificate which comes with SRM 1960.

Manufacture of the particles was carried out under the direction of J.W. Vanderhoff of the Lehigh University and D.M. Kornfeld of the National Aeronautics and Space Administration.

The overall coordination of the measurements by the cooperating laboratories was performed under the direction of R.C. Obbink, Research Associate, ASTM/NIST Research Associate Program.

The technical and support aspects involved in the revision, update, and issuance of this Standard Reference Material were coordinated through the Standard Reference Materials Program by N.M. Trahey. The original coordination of certification efforts was performed by L.J. Kieffer.

[1] Hartman, A.W., Powder Technology 46 pp. 109-120 (1986).

Cooperative determinations were performed in the following laboratories:

Climet Corporation, Redlands, California, L.D. Carver.
Duke Scientific Corp., Palo Alto, California, S.D. Duke.
Eastman Kodak Co., Rochester, New York, B.C. Wood.
Food & Drug Administration, Minneapolis, Minnesota, G.S. Oxborrow.
General Electric Co., Worthington, Ohio, E.J. Connors.
Lehigh University, Bethlehem, Pennsylvania, J.W. Vanderhoff.
National Aeronautics & Space Administration, Huntsville, Alabama, D.M. Kornfeld.
Pacific Scientific, Menlo Park, California, L.D. Carver.
Particle Data Laboratories, Ltd., Elmhurst, Illinois, R. Karuhn.

The following results are given for information only:

Method	Laboratory	Number Average Diameter (μm)	Standard Deviation of Distribution (μm)
Optical Microscopy	Duke	9.90	0.05
	FDA	10.215	0.176
	Kodak	9.93	---
Electron Microscopy	Lehigh	9.96	0.115
	Kodak	9.90	0.05
Sensing Zone	Duke	9.89	0.08
	G.E.	10.02	---
	Climet	10.08	---
	NASA	9.93	0.12
	Pacific Scientific	10.1	---
	Particle Data	9.94	---

Fig. 2. The certificate which comes with SRM 1960 (reverse).

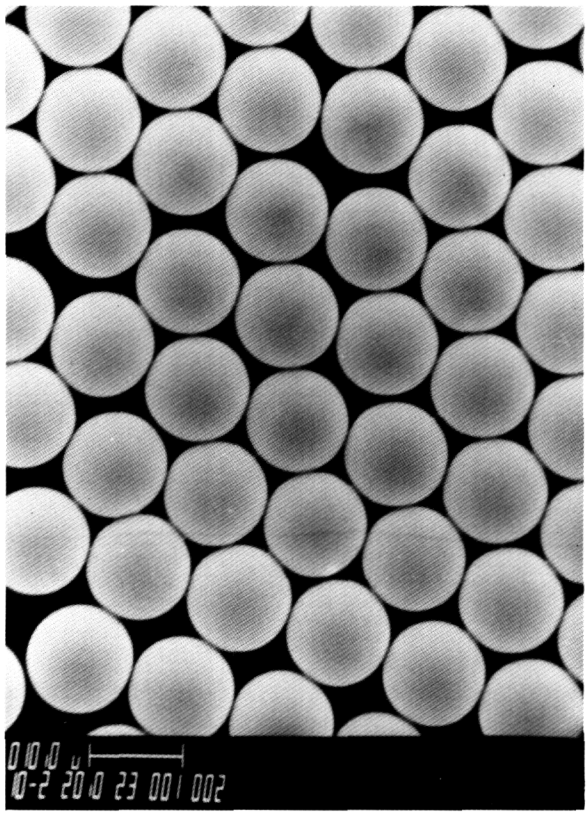

Fig. 3. Scanning electron microscope photomicrograph of the SRM 1960 microspheres.

2.2 Experimental Method

Six samples of microspheres (C1-C6) were taken from four different vials of SRM 1960 and then diluted from 0.4% weight concentration to about 0.1% weight concentration using ultra-pure, 25 MΩ cm water. For each sample, a drop of the diluted suspension was placed on a microscope slide, spread out, and then allowed to dry. Sparse and disordered structures (much like strands of beads) formed, in which most spheres had only one or two contacting neighbors. In such structures, air gaps, which would cause measurement errors, are unlikely to develop [7].

The microscope slide was then illuminated by parallel, quasi-monochromatic light approximated by stopping the microscope condenser all the way down and putting a green filter into the beam. The parallel light was focussed by the individual microspheres to a common back focal plane. Photomicrographs taken of the focal plane showed focal-spot patterns which corresponded to the microsphere structures (Fig. 5). The focal spots were small and circular, about 0.5-1.0 μm in diameter in the object plane, the smallest spots (0.5 μm diameter) being obtained by a judicious choice of film material and exposure time.

The film scale was chosen to be large enough that the distances between focal spots could be measured with a resolution of about 1 part in 300 to 1 part in 500, but not so large that excessive numbers of photographs had to be taken to cover a measured sample of about 2000 spheres, in total. Such a large sample size was needed to get an accurate value for the standard deviation. If only the mean diameter were desired, then about 200 spheres would have been enough. A useful film scale is 500×, giving 5 mm CDs in the photomicrographs.

For reasons of speed and convenience, Polaroid[2] Type 57 (3000 ASA) positive film was used. This material has low graininess, and the dimensional stability is adequate for the CDF measurements [8]. Focal-spot spacings on the film were measured automatically in a coordinate measuring machine (CMM) using a low-power (30×) microscope as the probe. To make a CD measurement, the CMM microscope cross hairs were centered on a focal spot, and the x-y coordinates of the spot were automatically entered into computer memory at the push of a button. To decrease the effect of film graininess, the microscope was slightly defocused, enabling an experienced observer to visually pinpoint the center of each spot, which typically had a diameter of about 0.3 mm, to a precision of 0.01 mm (or 0.02 μm in the object plane). A computer program then calculated the CD spacings. In this manner, sphere CDs were found with a precision of about ±0.03 μm.

2.3 CDF Results

The data taken from the photographic film were distances, c, between sphere centers. Using the above CDF procedures, c-values were measured, and the c-distribution was plotted and verified for normality. Then, the mean diameter (d_m) and the standard deviation (σ_d) of the microspheres were determined using $d_m = c_m$ and $\sigma_d = \sqrt{2} \times \sigma_{cd}$, where σ_{cd} is the standard deviation of the center distance measurements. The results of the CDF measurements on SRM 1960 are given in Table 1, and the diameter distribution is shown in Fig. 7.

[2] Certain commercial equipment, instruments, or materials are identified in this paper to specify adequately the experimental procedure. Such identification does not imply recommendation or endorsement by the National Institute of Standards and Technology, nor does it imply that the materials or equipment identified are necessarily the best available for the purpose.

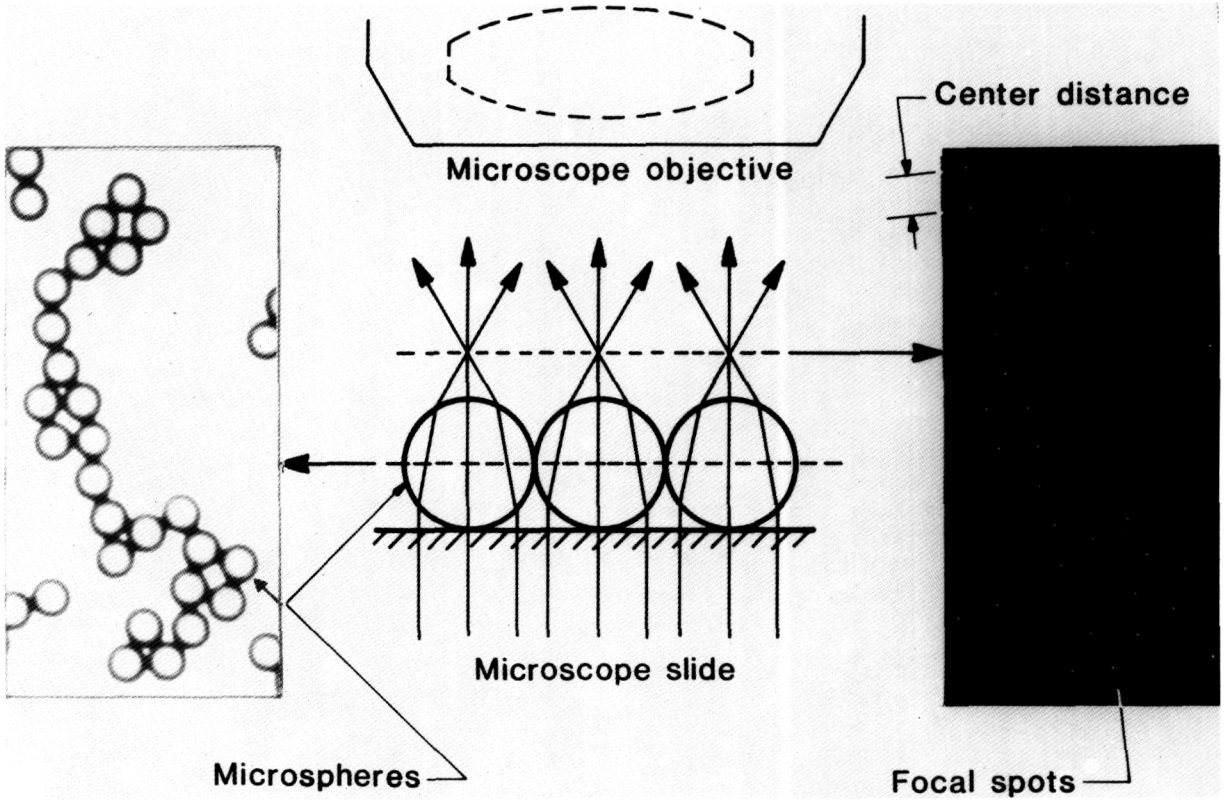

Fig. 4. The center distance finding (CDF) technique.

A useful consequence of the CDF technique is that the sphericity of the individual particles can be determined by looking at the shape of the photographed focal spots. In general, the focal spots were visually of circular shape, with occasional (<1%) shapes that were elongated by 5–10% or more. Considering that the elongation of the focal spot is the same as that of the sphere, it can be concluded that the vast majority of SRM 1960 microspheres has an asphericity amounting to less than 0.5% (as measured perpendicular to the line of sight). In short, these particles are very close to being perfect spheres.

2.4 CDF Error Analysis

As with all measurements, both random and systematic errors occurred in the CDF measurements described above. The major random errors were center-finding uncertainty, film instability, magnification scatter, and small sample size (sampling error). The primary sources of systematic error were image magnification error, image distortion error, and sphere flattening. Uncertainties due to air gaps and foreign material between microspheres were determined to be negligible.

Note that in all of the error analyses below (for CDF, MEM, and RLS), the random errors are given as 3σ (99% confidence level). In addition, all of the random uncertainties contain a component due to vial-to-vial variability, if present, since particles from several vials were measured by each technique.

2.4.1 CDF Random Errors An estimate of the random error in the CDF measurements can be obtained by finding the 3σ of the five valid diameter measurements in Table 1. For these measurements the 3σ random uncertainty, R, is calculated to be ± 0.0047 μm; this is the value of the random error used later to calculate the total uncertainty [Eq. (3)]. In addition, it is useful to determine the sources of the various CDF random errors and calculate estimates for their individual contributions. These error sources are discussed below.

Center-Finding Uncertainty and Film Instability. These two errors limit the ability to reproducibly locate the center of a given focal spot on the photograph. The cross hair in the probe microscope of the CMM was placed over the center of a photographed focal spot, guided by the eye of a trained observer. As noted earlier, the probe microscope

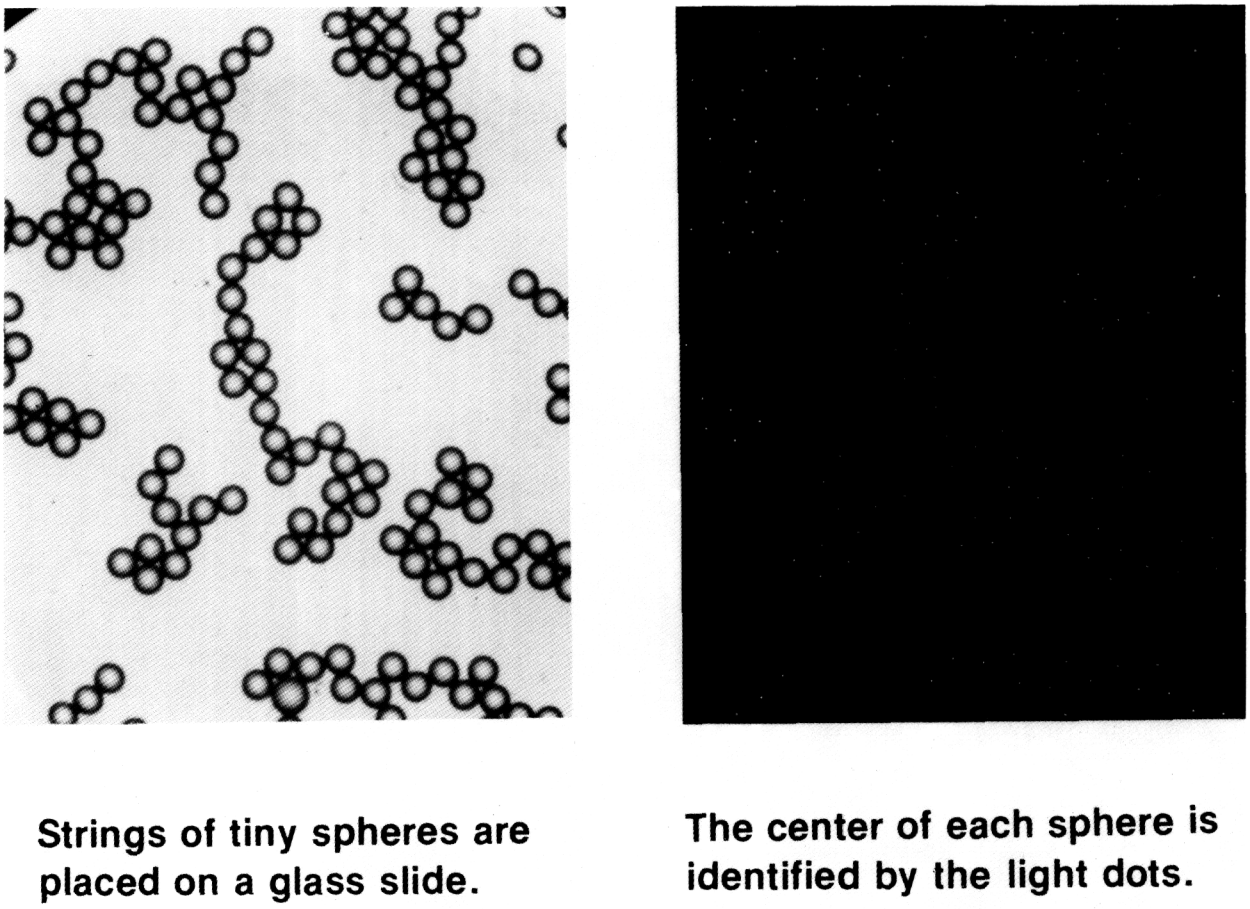

Fig. 5. CDF disordered assemblies.

was slightly defocused in order to reduce the effect of film graininess. This centering process is limited by the acuity of the eye and its sensitivity to rotational symmetry. It is also affected by the dimensional stability of the film: photographic emulsions are known to shift laterally after exposure due to film developing, fixing, and drying. The combined effect of these two sources is a scatter in the measured X-Y coordinates of a focal spot when photographed and measured under identical circumstances. This (combined) error contribution to single measurements of CDs is a random one and was measured as follows. A row containing 16 microspheres was centered in the FOV, and its corresponding row of focal spots was photographed five times; all CDs between adjacent spheres in the row were measured in each photograph. The data obtained were scaled such that all sets of five CDs had the same average value. This removed the effects of unequal sphere size and of any spurious changes in magnification associated with the process of taking repeated photographs. The result was a pooled set of 75 CDs. When analyzed, the data showed a 3σ scatter of 38 μm in a single measurement of a 5 mm CD (0.075 μm in the object plane). As measured earlier [8], the dimensional stability of the Polaroid film is known to be about 10 μm across the entire film.

Assuming these two sources of error combine in quadrature, the CD uncertainty contribution from the focal-spot-pinpointing process is slightly less than 40 μm. This corresponds to a ±0.08 μm random error per CD measurement in the object plane.

Magnification Scatter. When the microscope is refocused between exposures, the object distance changes somewhat: the final image shifts along the optical axis, its distance to the photo eyepiece changes, and the magnification varies accordingly. However, if the film plane is held fixed, the image scale in the film remains constant (to first approximation), although the image loses sharpness.

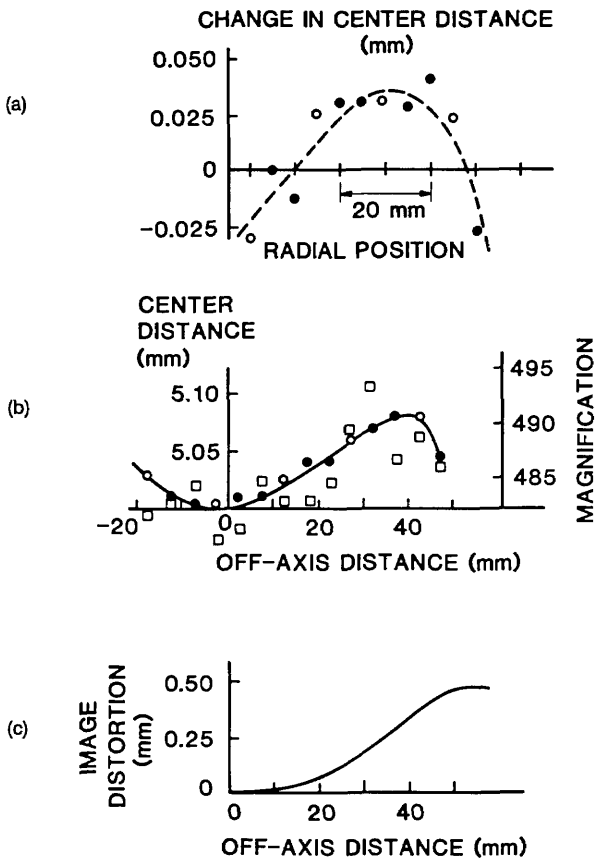

Fig. 6. Microscope calibration curves for image magnification and distortion.

The situation changes when fresh film is inserted into the cassette. The flexible film sheet is held by its edges, no vacuum platen is used, and the film plane can change in axial position by some 0.1 to 0.2 mm. The distance to the photo eyepiece is typically 150 mm, hence spurious changes in film scale can be expected at the 0.1% level. These changes were measured as follows.

Using the five photographs mentioned earlier, the lengths of row sections containing 1, 2, 3, 4, etc., CDs were measured, up to the full FOV. For each set of five nominally equal lengths, the length scatter was found and plotted against the length itself. The plot shown in Fig. 8 approaches, for large lengths, a straight line passing through the origin. The slope of this line shows that part of the total length scatter is proportional to length and, thus, is caused by fluctuations in magnification. These amounted to a 0.2%, or ± 0.02 μm, random error when measuring 10 μm lengths.

Sampling Error. The sampling error, due to the finite sample chosen from a large population of microspheres, is given by:

$$r = t_m(0.005)\sigma_d/\sqrt{n} \qquad (1)$$

in which σ_d is the standard deviation of the diameter distribution, t_m is the Student t-value for m degrees of freedom at the 99% confidence level and $n \approx 2000$ is the number of microspheres sized by CDF (the value of m is one less than this). Substituting into Eq. (1) gives a value of 0.27 μm sampling error for a single measurement of d_m, or ± 0.006 μm for all 2000 measurements.

Total Random Error. Summing the above contributions in quadrature gives a total random uncertainty of ± 0.006 μm, in good agreement with the 3σ random uncertainty (± 0.0047 μm) calculated from the five CDF measurements.

2.4.2 CDF Systematic Errors *Image Magnification and Distortion Errors*. The section of the stage micrometer that was imaged had a length of 160 μm and had been calibrated at NIST with ± 0.04 μm accuracy using a photoelectric image

Table 1. Results from center distance finding

Vial No.	Sample No.	Photos taken	Spheres measured	Outliers Over	Outliers Under	Diameter (μm) Mean	Diameter (μm) Median
1	C1	20	1074	11	0	9.891	9.892
1	C2	2	132	1	0	9.912[a]	9.905[a]
1	C3	2	107	2	0	9.890	9.888
2	C4	4	265	0	0	9.889	9.888
3	C5	6	239	3	0	9.892	9.878
4	C6	4	224	2	0	9.893	9.884
Combined		38	2041	19	0	9.891[b]	9.886[b]
						$3\sigma_{n-1} = 0.0047$[b]	0.016[b]

[a] Statistical outliers.
[b] These values do not include the statistical outliers.

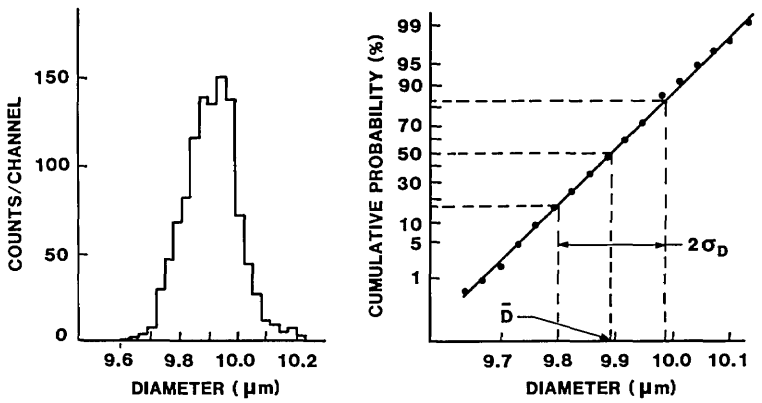

Fig. 7. Diameter distribution of the SRM 1960 spheres, as determined using CDF.

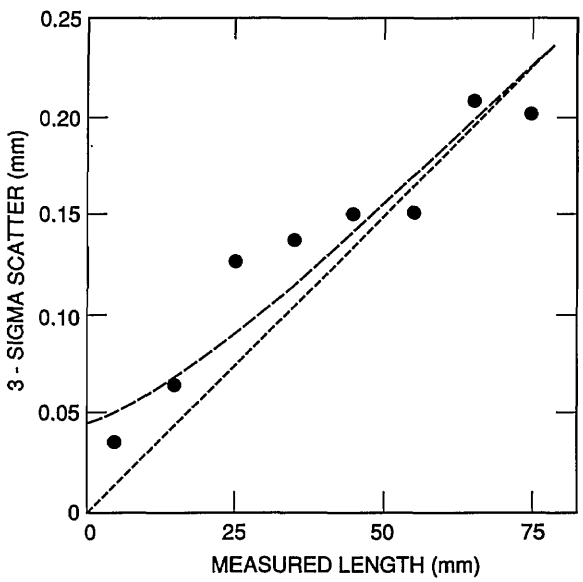

Fig. 8. Scatter in the microscope magnification.

scanner and traveling stage with interferometric readout. This amounts to a systematic error of ±0.003 μm when measuring 10 μm distances. The microscope image of the stage micrometer was 90 mm long, measured with an uncertainty of 0.05 mm, resulting in a systematic error contribution of ±0.006 μm.

To account for image distortion, the uncertainty in the length correction of the micrometer image was 0.05 mm, giving a ±0.006 μm systematic error on the mean diameter. The micrometer image length was found by taking 5 repeated exposures, thus reducing the magnification scatter to 0.09% (compared to 0.2% for a single exposure) giving a ±0.009 μm systematic error in the microsphere diameter measurement.

The scale distortion in Fig. 6b is found with an uncertainty of 0.01 mm, or 0.2%. The image magnification as a function of off-axis distance is thus known to about 0.3%. The scale-distortion relationship could have been entered into the computer-automated, CD-measuring algorithm as a lookup table. Here, however, the distortion data was used to make a transparent overlay that was placed over each measured piece of film. The overlay consisted of a series of concentric zones marked with appropriate corrections for measured CDs. The use of an overlay adds an estimated ±0.01 μm systematic error and a ±0.02 μm random error, when measuring 10 μm lengths anywhere across the FOV.

Sphere Flattening. The primary forces which adhere small particles (diameter < 50 μm) to dry surfaces are van der Waals forces. During drying, strong capillary forces act on the microspheres, bringing them into intimate contact [9]. Since the polystyrene spheres of SRM 1960 have optically smooth surfaces, the van der Waals attraction at the initial area of contact will pull adjacent areas into contact. This phenomenon is resisted by elastic sphere deformation.

Muller et al. [10] have analyzed the balance between these two processes. They give expressions for the flattening of spheres in contact with a flat substrate and show the sphere deformation at and around the contact area, indicating that the active, non-contacting zone is relatively small when no external forces are present. In that case, the flattening of a sphere contacting an equal-size sphere will be essentially equal to that of a sphere contacting a plane, and the Muller expression can be doubled to find the decrease in sphere CD due to the van der Waals attraction. The diameter correction for sphere flattening will then be:

$$\Delta d_f = +\frac{1}{4}\left(\frac{3(1-\nu^2)^2 r A^2}{2E^2\epsilon^4}\right)^{1/3}, \quad (2)$$

in which ν = the Poisson constant = 0.3 for polystyrene; r = sphere radius = 5 μm; A = Hamaker constant = 1×10^{-12} erg for polystyrene surfaces; E = Young's modulus = 3×10^{10} dyn/cm^2 for polystyrene; and ϵ = closest distance of approach = 0.3 nm. Substituting these values into Eq. (2) gives a systematic diameter correction due to van der Waals attraction amounting to +0.002 μm.

Air Gaps. Air gaps between spheres, if present, would result in an overestimate of the mean diameter [7]. Gaps wider than about 0.2 μm can be found by visual inspection of the microsphere images. Narrower gaps can be detected in selected, sparse structures that are arranged as chains or strands and which contain a triangular sphere arrangement at two or more locations (Fig. 5). Measuring one triangle yields three radii. Sphere diameters farther along the chain are found from CD measurements between known and unknown spheres, until the whole group is measured. The process is then repeated, starting from another triangle. The result is two sets of sphere diameters and, if these are equal within experimental limits (i.e., if there is closure), the air gaps can be assumed absent in that structure. The measured chain should preferably be short, to reduce measurement error accumulation. Spot checks like this in the microsphere preparation confirmed the likely absence of air gaps in the CDF measurements reported here.

Another indication of the absence of air gaps could be found by observing the sphere-grouping process during drying of the deposited microspheres. Just before final drying, spheres which had already attached themselves to the substrate were seen to be pulled toward each other in a "snap-like" fashion, giving the impression that they were torn loose from the substrate by a water film acting like a stretched elastic membrane. This mechanism is unlikely to result in air gaps.

Thus, for purposes of the present calibration process, air gaps were assumed to be absent in the measured microsphere structures.

Foreign Material. Since the bottled SRM 1960 suspension contains 50 ppm of a biocide (sodium azide), it is possible that a surface coating of this foreign material can cause an overestimate of the mean diameter. In the CDF measurements, the microspheres covered about 5% of the glass slide area. Given the 0.4% weight concentration of particles in the bottled SRM, if all of the fungicide stays behind after drying as a hard, uniform layer coating both the spheres and the slide, this coating will add, at most, $0.0001\times d_m$ to the measured diameter of the spheres. Such a small correction can be safely neglected.

In addition, dilution by one and two orders of magnitude did not change the measured mean diameter, suggesting that any coating between the spheres is punctured in the last moments of drying. This is also indicated by the behavior of the drying spheres, which snap together into intimate contact. For the purpose of the SRM 1960 certification by CDF, it is therefore assumed that no foreign material is present between the dried spheres.

2.4.3 Total Diameter Uncertainty from CDF

All of the contributions to the CDF measurement uncertainty are summarized in the error budget in Table 2. The total error is given by [11]

$$U_T = R + U_S$$
$$= R + |\delta_m| + |\delta_d| \quad (3)$$

in which R is the total random error = 0.0047 μm, U_S is the total systematic error, δ_m is the systematic image-magnification error and δ_d is the systematic image-distortion error. Substituting the various error values into Eq. (3) gives a total uncertainty of ±0.04 μm for the CDF measurements.

2.5 Final Results of the CDF Measurements

The final results for the CDF calibration are: $d_m = 9.89 \pm 0.04$ μm and $\sigma_d = 0.09 \pm 0.01$ μm. The diameter uniformity within vial and between vials is ±0.1%. The microsphere diameter distribution was found to be normal (Gaussian) from 1% to 99%. The number of outliers found by visual inspection (i.e., finding spheres with diameters clearly outside the main peak, by $0.05\times d_m$ or more) is approximately 1% for oversized particles and negligible for undersized particles.

3. Metrology Electron Microscopy

A supporting technique used in the measurement of the SRM 1960 microspheres was metrology electron microscopy (MEM). The value of the MEM technique is that it ties the dimensional measurements of the microspheres to the wavelength of a stabilized helium-neon laser, a widely

Table 2. CDF error budget[a]

Measurement	Error source	Random error (μm)	Systematic error (μm)
CD measurement	Film stability and readout	0.08	
	Magnification scatter	0.02	
	Sphere flattening at contact		0.002
Sampling ($n \approx 2000$)		0.27	
Off-Axis magnification	Measuring off-axis magnification (make overlay)		0.01
	(use overlay)	0.02	
On-Axis magnification	Stage micrometer (SM) calibration		0.003
	SM image-length readout		0.006
	SM image-length correction		0.006
	Magnification scatter		0.009
Total error per measurement		0.28	0.036
Total error on d_m		0.006	0.036

[a] The errors are for a single center-distance measurement.

used secondary length standard. In addition, the technique provides a check for possible systematic errors in the other techniques which may be due to environmental factors: for CDF, the particles are measured dry in air, while for RLS they are measured in a liquid environment. In contrast, the MEM measurements are made on the microspheres in an ultra-high vacuum, providing a test for possible dimensional instability and/or outgassing of the polystyrene particles.

3.1 Experimental Apparatus

The MEM system is based on a commercial ultra-high vacuum scanning electron microscope (SEM) with a field-emission electron gun [12]. In the MEM, the electron beam is fixed in position, so that it acts as a reference point or cross hair. The microsphere is then translated through the e-beam using an electro-mechanically scanned stage (Fig. 9). Displacement of the stage is monitored by a commercial heterodyne interferometer system which uses a stabilized helium-neon laser to set the metric [12]. In this way, the MEM measurement of the microsphere diameter is directly tied to the wavelength of the helium-neon laser ($\approx$632.8 nm).

The MEM stage uses a piezoflex driving element whose displacement is magnified by two sets of flexure-pivot lever arms [13]. The stage is fabricated from a single piece of 304 stainless steel and has a maximum displacement of 170 μm. Roll, pitch, and yaw are all less than 2 arcsec with 3 kV applied voltage on the piezo-electric transducer (PZT). With the piezoflex stage, the displacement of the microspheres across the electron beam is as smooth as the applied voltage down to the sub-nanometer level [13].

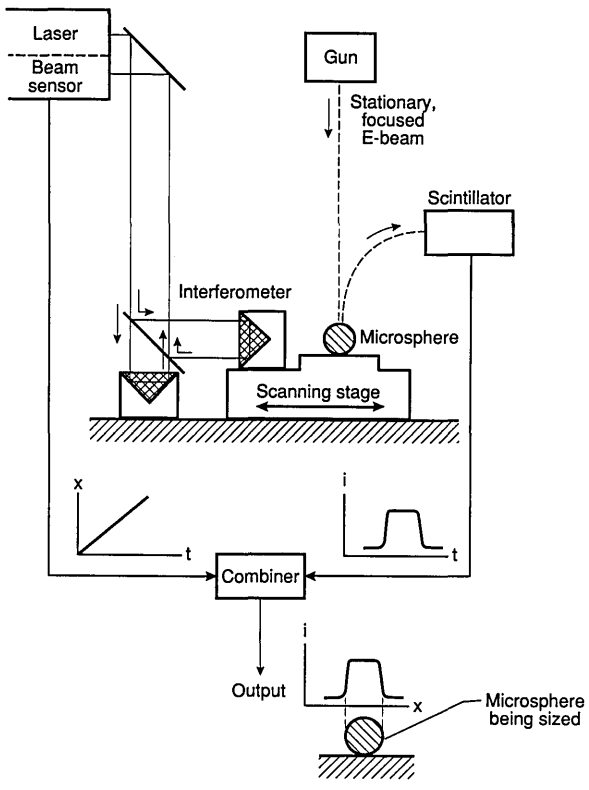

Fig 9. Schematic diagram of the metrology electron microscope (MEM) system.

As the particle is scanned through the e-beam, the position of the stage is monitored by a heterodyne fringe-counting interferometer; for the SRM 1960 microspheres, the scan time across a particle was about 10 s. The interferometer is a single-pass Michelson type with a polarizing beamsplitter and glass retroreflectors [14]. The measurement retroreflector is removable to allow alignment of the stage interferometer before installation in the microscope. To minimize dead-path errors, the reference and measurement optical paths are made equal in the interferometer arrangement. In operation, the laser beam enters and exits the beamsplitter through a window on top of the vacuum chamber of the SEM (Fig. 9).

A bright-field transmission detector was employed to collect the intensity profile while a particle was being scanned. As shown in Fig. 10, this detector consists of a small aperture placed in front of a scintillation detector. When the angular size (β) of the aperture, as measured from the specimen, is equal to or smaller than the angular size (α) of the electron beam, the detector will only produce a significant signal if the beam does not scatter from the specimen [12]. In the present case, the aperture was about 1.5 mm in diameter, which corresponds

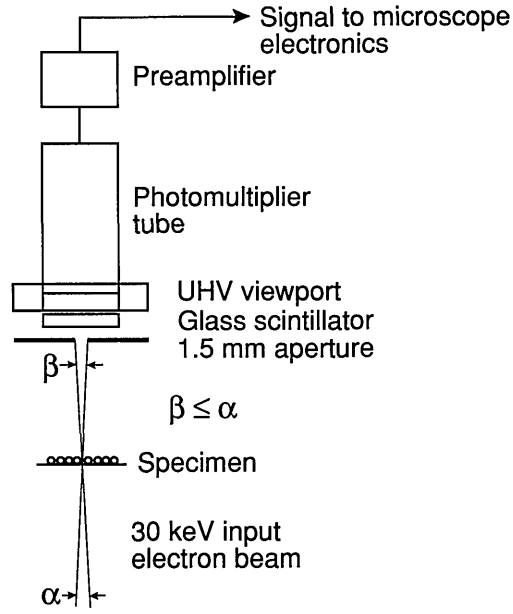

Fig. 10. Schematic diagram of the bright-field imaging mode in the MEM.

to an angular size of 3.5 mrad. At 30 keV beam energy and a working distance of 25 mm, this size matches that of a 10 nm electron probe. Beam current in the measurements was about 0.5 nA.

After a particle was scanned, a computer analysis of the electron-intensity profile gave its measured diameter. Since the edge resolution under the above noted e-beam conditions was less than the interferometer resolution of 16 nm, the edge-detection algorithm in the computer code could easily locate the transition point from the particle to the background. The algorithm determined the edges of a particle by calculating a separate threshold for each edge based on 10% of the total rise or fall from the background level (Fig. 11).

3.2 Experimental Method

The SRM 1960 samples were prepared for the MEM by diluting one drop from a vial into 50 ml of 18 MΩ cm deionized water and then ultrasonicating, settling, and decanting 80% of the supernatant liquid. This washing cycle was repeated three times for each sample to remove as much of the water-soluble additives as possible. A small drop of the washed suspension was dried down onto a thin carbon foil supported by a 200-mesh copper TEM grid and then overcoated with about 20 nm of amorphous carbon in a vacuum evaporator to minimize charging in the electron beam. After overcoating, the grids were loaded into the MEM chamber, which was pumped down to a 10^{-8} Torr vacuum.

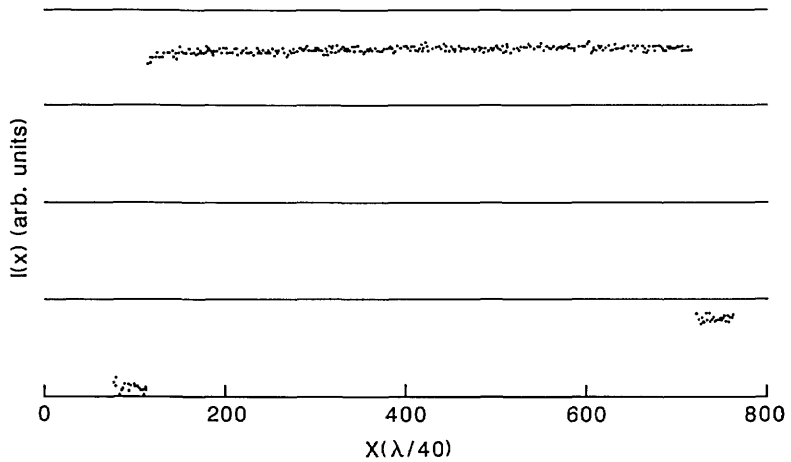

Fig. 11. MEM intensity profile of an SRM 1960 microsphere.

Three different vials of SRM 1960 were sampled, and one grid was prepared from each sample (these are labelled M1, M2, and M3). About 30 individual microspheres were measured on each grid to give good statistics on the mean-diameter determination; this was not enough particles, however, to get an accurate measure of the standard deviation. Visibly obvious outliers were not included in the measurements.

The computer-based data acquisition system was programmed to set up a scan and then pause between each diameter measurement to allow the operator to locate, manually position, and then focus on each particle to be measured. After the operator switched the MEM to spot mode and restarted the measurement computer program, the program controlled the stage scan, collected the data on intensity vs. stage position, calculated the particle diameter, and reported the measured diameter value. After all of the particles in one sample were measured, the computer program calculated the mean diameter.

For the first sample (M1), all of the microspheres were scanned three times to determine the amount of particle shrinkage due to e-beam irradiation; typically, about 3% shrinkage was measured after the three scans (see Table 3). To avoid this problem, only the first particle scan was used for all of the MEM measurements.

3.3 MEM Results

A typical trace of the inverted bright-field intensity profile for a single SRM 1960 microsphere is shown in Fig. 11. The intensity was sampled at 500 points, equally spaced in time, and the stage position was recorded simultaneously. The total scan length was approximately 10.6 μm; therefore, each sampled point corresponds to about 20 nm in stage displacement. As the profile in Fig. 11 indicates, the transition at the edges is sharp to within one sampled point, making the edge-detection algorithm relatively straightforward, as noted.

A summary of the results for the three samples, labelled M1, M2, and M3, are presented in Table 4. Several measurements in each sample were discarded as being outliers, either over- or undersized, as determined by a discordancy test based on the sample kurtosis [15]. In each case, the outlier was more than 3σ away from the mean, either lower or higher in diameter. The final reported number-average mean diameter, d_m, is taken to be the mean value of the three independent measurements, 9.886 μm.

Table 3. Repeat MEM measurements from five microspheres in sample M1[a,b]

Particle #	d_1	d_2	d_3	d_1–d_3	σ_{n-1}
1	9.890	9.875	9.859	0.031	0.016
2	9.859	9.811	9.796	0.063	0.033
3	9.875	9.827	9.827	0.048	0.028
4	9.875	9.859	9.811	0.064	0.033
5	9.811	9.764	9.764	0.047	0.027
Mean	9.862	9.827	9.811	0.051	

[a] All measurements are in μm.
[b] The σ_{n-1} are the standard deviations of the three measurements.

Table 4. Results from metrology electron microscopy

Sample	N	d (μm)	s_m[a] (μm)
M1	28	9.884	0.013
M2	28	9.881	0.014
M3	25	9.894	0.020
Combined	81	9.886 $3\sigma_{n-1}=0.018$ μm	0.016

[a] s_m is the standard error on the mean of the N measurements in each sample.

3.4 MEM Error Analysis

Random errors are the major source of uncertainty in the MEM measurements, the primary ones being sampling error, spatial resolution and (random) e-beam wander, and cosine error. The systematic uncertainties include least-count in the interferometer, digitization of stage travel, and e-beam erosion of the microspheres. Potential error sources that were determined to be negligible in the MEM measurements were due to particle outgassing in a vacuum, carbon coating on the particles, and interferometer error.

3.4.1 Random MEM Errors An estimate of the random error in the MEM results was obtained by finding the 3σ of the data in Table 4. This value, ±0.018 μm, was used in the calculation of the total MEM error,

$$U_T = R + U_S$$

$$= R + |\delta_{ic}| + |\delta_d| + |\delta_e|. \quad (4)$$

Possible sources of this random error are summarized below.

Sampling. As with the CDF measurements, the sampling error arises from the limited number of microspheres measured, as taken from a population with a finite size distribution having a standard deviation, σ_d, of 0.9% of the mean diameter. Using Eq. (1) with $n=81$, a value of ±0.03 μm is obtained for the MEM sampling error.

Spatial Resolution and e-Beam Wander. The point-to-point resolution of the scanning electron microscope used in the MEM measurements, essentially due to finite spot size and random beam wander, was measured to be ±0.02 μm. Since two microsphere edges have to be detected, the random uncertainty is $\sqrt{2}$ times this or 0.028 μm per measurement. The random error for 81 measurements is thus $0.028/\sqrt{81}=0.003$ μm.

Cosine Error. Cosine error occurs in the MEM if the microsphere is not measured along the diameter but, rather, along a chord of the projected sphere image. This error is expected to be small, since it is easy to visually determine the diameter of a circle to better than 1 part in 30. Using the expression for cosine error,

$$\delta_c \approx d_m(1-\cos\alpha) \approx d_m(\alpha^2/2) \quad (5)$$

in which d_m is the mean diameter of the microspheres and α is the scan-angle error, this uncertainty was determined to be at most 0.014 μm per measurement, assuming $\alpha \leq 3°$. Since this is a one-sided error, the random error for all 81 measurements is approximately $0.014/4=0.003$ μm.

Total Random Error. Combining the above three components in quadrature gives a total random error of ±0.03 μm, somewhat higher than the $R=0.018$ μm determined from the three MEM measurements of the mean diameter.

3.4.2 Systematic MEM Errors *Least Count in Interferometer*. The least-count systematic uncertainty in MEM is due to the inability to determine the intensity-transition point in the microsphere scans to better than the least count of the interferometer, which is $\lambda/40=16$ nm (Fig. 11). Since two transitions must be determined (one on either side of the particle), this error is equal to twice the halfwidth of the sampled point, or ±0.016 μm.

Digitization of Stage Travel. The MEM stage travel of 10.6 μm was sampled at 500 equidistant points, resulting in a $10.6/500$ μm $=0.02$ μm systematic error on the measurement of stage displacement.

E-Beam Erosion of the Microspheres. This error arises from erosion of the SRM 1960 microspheres as they pass through the e-beam. To minimize this effect, only the first MEM scan of a particle was used to determine the mean diameter. Nevertheless, there will still be some residual particle shrinkage for one scan. The magnitude of the shrinkage was determined by repeatedly scanning across the same line on a microsphere; this was done for ≈60 microspheres in sample M1. Typical results for three scans of 5 microspheres measured

sequentially from this sample are given in Table 3. From all of the measurements, the decrease in particle diameter due to electron irradiation was determined to be about 0.1% per scan, or about a ± 0.01 μm systematic error in the mean diameter.

3.4.3 Total Diameter Uncertainty from MEM

All of the MEM errors are summarized in Table 5. As specified by Eq. (3), these errors are combined as Eq. (4), which gives the total uncertainty on the MEM measurement as ± 0.06 μm. In Eq. (4), δ_{lc} is the least-count error, δ_d is the stage digitization error, and δ_e is the e-beam erosion error.

Table 5. MEM error budget[a]

	Error source	Random (μm)	Syst. (μm)
Random	Sampling	0.03	
	Spatial resolution	0.003	
	Cosine error	0.003	
Systematic	Interferometer least count		0.016
	Stage travel digitization		0.02
	E-Beam erosion		0.01
Total error		0.03	0.046

[a] The errors are for all 81 MEM measurements.

3.5 Final Results of the MEM Measurements

The mean diameter of SRM 1960 determined from metrology electron microscopy is 9.89 ± 0.06 μm.

4. Resonance Light Scattering

The third technique used in the certification of SRM 1960 was resonance light scattering (RLS). This method uses the sharp resonances which occur in the Mie light scattering cross-sections of dielectric microspheres as a function of incident light frequency [16]. Resonance light scattering spectra can be used to accurately determine the diameter of a single microsphere by quantitatively comparing the experimental resonance wavelengths with those calculated from a Mie scattering model [17]. In principle, a sufficient number of SRM 1960 particles could have been individually measured in this manner to build up the size distribution. However, in the RLS experiments described in the present report, a simpler method was used whereby a single RLS spectrum is measured from a large number of microspheres in liquid suspension [18]. The peaks in this collective spectrum are broader than those in single-particle spectra, but are still sharp enough to yield high-resolution diameter information.

4.1 Experimental Apparatus

The experimental RLS apparatus is diagramed in Fig. 12 [18]. The ring dye laser was pumped by an argon-ion laser, and its intensity was stabilized by an electro-optical feedback system. The beam was vertically incident into a glass sample cell filled with SRM 1960 microspheres in water suspension: the cell was 55 mm high × 45 mm wide × 20 mm thick. Input laser power to the sample was typically 60 to 80 mW at 620 nm and 90 to 120 mW at 570 nm with the Rhodamine 590 dye used. Wavelength scanning was accomplished with a piezoelectric inchworm micrometer which rotated a birefringent plate inside the dye-laser cavity. A complete spectrum was collected in about 20 min so that particle settling was not a problem.

The light scattered at 90° was detected with a silicon photodiode and a lock-in amplifier with output connected to a strip-chart recorder. Either the light intensity polarized parallel to the scattering plane ($I_\parallel$) or that polarized perpendicular to the scattering plane ($I_\perp$) could be detected by proper orientation of the collection arm and the polarizer (Fig. 12).

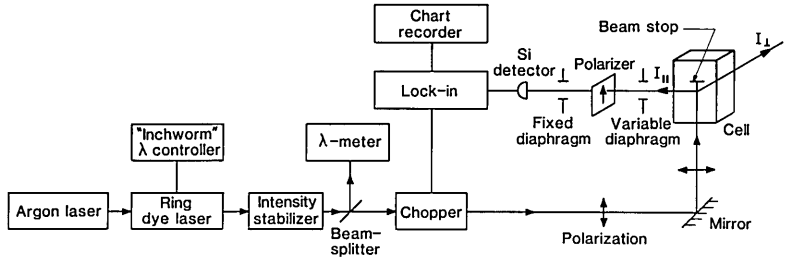

Fig. 12. Schematic of the resonance light scattering (RLS) apparatus.

Since accurate alignment of the optics is critical to obtaining valid RLS spectra, a low-power He-Ne laser and a right-angle prism were used to carefully align the optical cell with both the incident dye laser beam and the collection arm. (Errors introduced by improper cell alignment are discussed in a later section.) Several additional considerations for obtaining valid RLS spectra from a microsphere suspension are discussed in Ref. [18].

4.2 Experimental Technique

Before loading the glass cell with particles, it was thoroughly washed using acetone and deionized water filtered through a 0.2 μm pore-size filter. The cell was then filled with filtered water, five drops of SRM 1960 were added, and the cell was ultrasonically vibrated to mix the particles and remove air bubbles.

To minimize multiple scattering, particle volume concentration was kept to about 15 ppm [19]. With a measured acceptance angle, Γ, of 0.8° the volume of particles sampled was about 27 mm^3, so that with a 15 ppm concentration of particles, there were on average about 800 microspheres within the sampled volume. Although this is a relatively large number of sampled microspheres, a long (3 s) time constant was used on the lock-in amplifier to minimize the statistical fluctuation noise and to reduce Brownian motion noise. The Brownian motion of the particles was calculated to occur on a time scale of about 30 ms.

Five samples of SRM 1960, labeled R1, R2, R3-1, R3-2, and R3-3, were used in the RLS measurements. Samples R1 and R2 came from different vials of SRM 1960, while samples R3-1, R3-2, and R3-3 were all taken from a third vial. At least six RLS spectra, three $I_\parallel$ and three $I_\perp$, were taken for each of the five samples. After a spectrum was taken, peak wavelengths were measured from tic marks made at 10 nm intervals on the chart paper. Four peaks were measured in the $I_\parallel$ spectra and three were measured in the $I_\perp$ spectra.

4.3 Computer Analysis

The calculated RLS spectra in Fig. 13 were generated on a CYBER 205 computer using a vectorized program based on Wiscombe's Mie-scattering code [20]. The Mie intensities for a single dielectric sphere are [21]

$$I_\perp(\theta,x)=\frac{I_0}{k^2R^2}\left|\sum_{n=1}^{\infty}\frac{2n+1}{n(n+1)}\left[a_n\frac{P_n^1(\cos\theta)}{\sin\theta}+b_n\frac{dP_n^1(\cos\theta)}{d\theta}\right]\right|^2, \quad (6)$$

$$I_\parallel(\theta,x)=\frac{I_0}{k^2R^2}\left|\sum_{n=1}^{\infty}\frac{2n+1}{n(n+1)}\left[a_n\frac{dP_n^1(\cos\theta)}{d\theta}+b_n\frac{P_n^1(\cos\theta)}{\sin\theta}\right]\right|^2, \quad (7)$$

where θ is the scattering angle, $x=\pi d/\lambda$ is the size parameter of the particle, d is the microsphere diameter, λ is the incident light wavelength in water, I_0 is the intensity of the incoming beam, R is the distance from the particle to the detector, P_n^1 is an associated Legendre function, $k=2\pi/\lambda$ is the wavenumber, and a_n and b_n are the Mie scattering coefficients which are functions of x [21].

The wavelength dispersions of the refractive indices of polystyrene and water were taken into account using linear interpolation formulas from published data [22] over the wavelengths of interest (570 to 620 nm). (For the broad, collective resonance peaks of the present experiment, linear

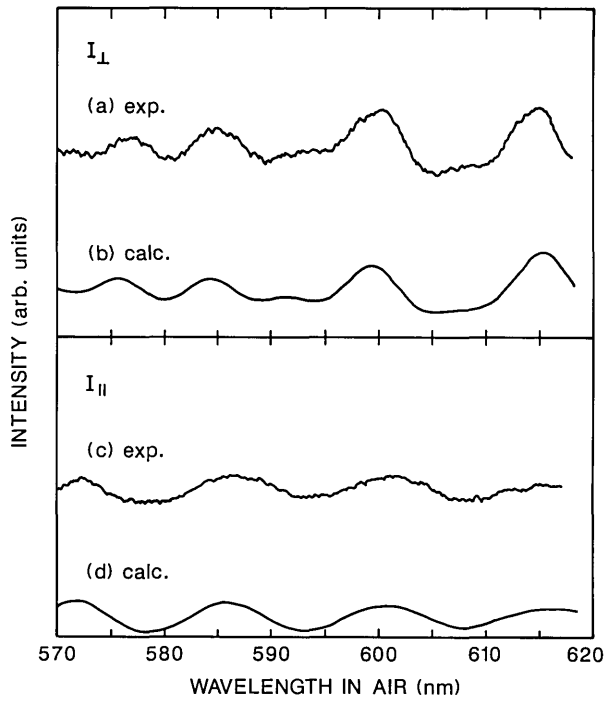

Fig. 13. RLS spectra of SRM 1960 microspheres in liquid suspension ($I_\parallel$ and $I_\perp$).

approximations were more than satisfactory, although they would not be for the sharp resonances of the individual microspheres.) If λ is in nanometers, then

$$n_w \approx 1.353 - 3.33 \times 10^{-5}\lambda \quad (8)$$

and

$$n_p \approx 1.638 - 4.06 \times 10^{-5}\lambda \quad (9)$$

are the refractive indices of water and polystyrene, respectively.

To account for the size distribution of the SRM 1960 microspheres, it was assumed that the diameters have a Gaussian distribution and that the suspended particles scatter independently. This allows integration over diameter and computation of an average light-scattering intensity:

$$\bar{I}_{\perp,\parallel}(\lambda,\theta) \approx \int_{d_m-\delta}^{d_m+\delta} d\xi \exp[-(\xi - d_m)^2/(2\sigma_d^2)] \, I_{\perp,\parallel}(\theta, \pi\xi/\lambda), \quad (10)$$

where d_m is the mean diameter and σ_d is the standard deviation of the size distribution. (Note that this expression ignores the small variation in scattered intensity with diameter; this will not affect the mean-diameter measurement.) The integration, which extends over $2\delta = 6\sigma_d$, was carried out by computing the scattered intensity for an extended range of the size parameter (10,000 values) and then summing the appropriate values multiplied by the Gaussian factor. Typically, about 1/5 of the 10,000 values were included in each sum.

4.4 RLS Results

Representative RLS spectra for $I_\parallel$ and $I_\perp$ are shown in Fig. 13. Figure 13 shows a calculated spectrum for a collective sample of dielectric microspheres and an experimentally measured spectrum for a water suspension of SRM 1960 microspheres. From each of the experimental RLS spectra, the peak wavelengths were measured as noted earlier. Table 6 gives the measured wavelengths for each of the five samples (R1, R2, R3-1, R3-2, and R3-3); these values are the means from at least three RLS spectra.

A mean diameter for the SRM 1960 microspheres can be determined by RLS since the peak wavelengths in a collective spectrum vary almost linearly with particle diameter [18]. This is due to the fact that the frequency of a peak in a single-particle spectrum is a function of d/λ only, neglecting the (small) wavelength dispersion of the refractive indices. This near-linearity of d vs. λ for a collective spectrum permits an analytical best-fit diameter if the estimated diameter is close to the minimum of the square deviation, $Q(d)$:

$$Q(d) = \sum_{i=1}^{8} [\lambda_i^m - \lambda_i^{th}(d)]^2, \quad (11)$$

where λ_i^m represent the seven measured peak wavelengths and λ_i^{th} represent the corresponding calculated peak wavelengths (four $I_\parallel$ peaks and three $I_\perp$ peaks). Using the calculated peak wavelengths (λ_i^0) for a diameter (d_{mo}) near a minimum of Eq. (11) and invoking the (near) proportionality between λ and d, the diameter d_{min} which corresponds to the minimum Q can be computed by taking the derivative of Eq. (11) and setting it equal to

Table 6. Peak wavelengths and diameters from RLS[a]

	Sample					
	R1	R2	R3-1	R3-2	R3-3	
$I_\parallel$	576.8 nm	575.7 nm	576.2 nm	576.5 nm	576.6 nm	
	584.1	583.3	584.2	584.3	584.6	
	599.3	599.4	599.9	599.6	599.5	
	615.2	614.7	614.2	614.3	614.0	
$I_\perp$	572.0	571.9	572.4	572.1	572.1	
	586.0	586.1	586.1	586.3	586.4	
	601.5	601.2	601.1	600.7	600.9	
d_{min}, μm	9.901	9.894	9.899	9.898	9.898	$3\sigma_{n-1} = 0.0076$ μm
Q, nm^2	3.8	8.0	5.8	5.8	29.9	

[a] All wavelengths are the means of data from at least three RLS spectra.

zero. The resulting expression for the best-fit diameter is:

$$d_{\min} = \frac{\Sigma \lambda_i^m \lambda_i^0}{\Sigma (\lambda_i^0)^2} d_{mo}. \quad (12)$$

It should be noted that the Q vs. d curve has a series of near-periodic local minima [18], so that the above procedure yields, in general, a series of "best-fit" diameters, one at each local minimum. This would make it difficult to match the peaks in the RLS spectra of single microspheres, in which there are many peaks of different polarization and order [16]. However, peak assignment is much simpler for the collective RLS spectra of the present experiment since there are far fewer, and much broader, peaks. Thus, a unique best-fit diameter can be easily obtained. Starting from the CDF result of 9.89 μm as the value for d_{mo}, a least-square diameter was determined for each of the five samples of SRM 1960; the results are summarized in Table 6. The within-vial agreement for samples C1, C2, and C3 was better than 0.001 μm, or 0.01% of the mean diameter. The other results, for samples A and B, differed from this value by a detectable amount. This may be evidence for a small amount of vial-to-vial variability in mean diameter of SRM 1960, although this possibility was not pursued.

The RLS-determined diameter of the SRM 1960 microspheres is taken to be the mean of the five values or 9.898 μm.

4.5 RLS Error Analysis

There are several sources of random and systematic error in the RLS technique. The most significant random errors are in the measurements of peak wavelength and scattering angle. The biggest contributions to the systematic uncertainties are in refractive index, peak wavelength, scattering angle, acceptance angle, and intensity variation of the laser beam. Possible error sources that were assumed to be small and were therefore neglected are: multiple scattering, sampling, polarization misalignment, backscattering, agglomeration, particle inhomogeneities, particle asphericity, and temperature effects.

4.5.1 Random RLS Errors The 3σ random error, R, determined from the five diameter measurements in Table 6 is ±0.0076 μm, and this value is used in Eq. (13) to calculate the total uncertainty of the RLS measurements. Various potential sources of this random error are discussed below.

Wavelength. Random errors in the measurement of the peak wavelengths are the irreproducible variations in locating the peak of a broad resonance. This, in turn, is due to the width of the resonance, to noise on the experimental RLS spectra, and to random nonlinearities in the wavelength scanning. The specified accuracy of the wavelength meter is better than 1 part in 10^5, so that random and systematic errors in the wavelength meter can be safely ignored.

The random wavelength error was determined by calculating the standard deviation of the peak wavelengths from the three repeat RLS spectra taken on each sample. This was done for all peaks in all the spectra, and a mean taken of these numbers; the result was $3\sigma_\lambda = 0.45$ nm. Since the measured wavelengths are all approximately 600 nm, this gives a random diameter uncertainty of ±0.008 μm per measurement, or ±0.004 μm for all five RLS measurements.

Scattering Angle. The random component of the scattering angle error is due to slight, irreproducible misalignments of the optical cell when it is repositioned between spectra. To determine the effect on diameter measurement due to this error, RLS spectra were calculated for $\theta = 89°$ to 91° in 0.1° intervals, and a best-fit diameter was determined at each of these angles. The variation in diameter was only about 0.01 μm for the 1° change in scattering angle. Thus, using an estimated maximum random angle error of ±1°, the error due to random misalignment of the optical cell is calculated to be about ±0.01 μm per measurement, or ±0.005 μm for all five measurements.

Total Random Error. Summing the above two contributions in quadrature gives a total random uncertainty of ±0.0064 μm, in good agreement with the 3σ random uncertainty (±0.0076 μm) calculated from the five RLS measurements.

4.5.2 Systematic RLS Errors *Refractive Index*. Uncertainty in the refractive index of polystyrene is the largest source of error in the RLS measurements. As discussed in Refs. [23] and [24], the values for n_p for individual 1 μm diameter polystyrene spheres ranged from 1.577 to 1.595 (at $\lambda = 632.8$ nm) when measured by different researchers. Several possible explanations have been proposed for this spread in values including: experimental uncertainties when measuring single particles; surface coatings on dried particles; and real differences in

optical properties from particle to particle. In the present study, the bulk value for n_p was used because the RLS spectra average over many particles, eliminating possible differences between particles, and because the SRM 1960 microspheres are much larger than the 1 μm spheres mentioned above, minimizing possible size effects. The bulk index was taken to be 1.588 (at $\lambda = 632.8$ nm), with an uncertainty of ±0.001 and a V-number dispersion of 30.8, as measured by Matheson and Saunderson [25].

In addition to n_p error, there are also small errors resulting from the use of linear dispersion relations for n_p and n_w and from uncertainties in the bulk value of n_w. These are estimated to give, at most, another 0.0005 systematic error in the refractive index. Thus, the total refractive index error is 0.0015, which results in a systematic diameter uncertainty of ±0.01 μm.

Wavelength. As noted earlier, the systematic error in the wavelength meter is negligible. However, this assumes static conditions, i.e., that the laser wavelength is not changing. Because the wavelength is, in fact, continuously changing during an RLS spectrum measurement, a systematic offset results from the 2 s time constant of the wavelength meter and the 3 s time constant of the lock-in amplifier. Since the wavelength scan rate in the RLS measurements was 0.05 nm/s, the combined time constant of 5 s results in a maximum systematic offset error of 0.±25 nm in wavelength or ±0.004 μm in diameter.

Scattering Angle. Since the scattering angle, θ, was experimentally set by autocollimating the incident laser beam from two (nominally) orthogonal sides of the optical cell, systematic scattering-angle errors may arise from two different sources: (i) inaccuracies in the optical cell angles and (ii) systematic misalignment of the optical cell.

To measure this component of error, the alignment helium-neon laser beam was autocollimated off all four sides of the cell and the maximum beam offset determined. The angle error measured in this manner was about ±0.5°. There are other indications that the systematic angle errors were less than 1°; these come from inspection of Fig. 13, viz., the good agreement between the experimental RLS spectra and the spectra calculated for exactly 90°. Note that although the peak wavelengths do not change much with angle, the peak amplitudes do change dramatically as a function of angle (Fig. 14). The excellent match in peak amplitudes between calculation and experiment is a good indication that θ was very close to 90°. In addition, for θ's other than 90°, the peaks that were suppressed at 90° make significant contributions to the spectra (Fig. 14). No such extraneous peaks were seen, further evidence for a scattering angle very close to 90°.

Taking the systematic angle error to be at most ±0.5° results in an upper limit of ±0.005 μm on the diameter uncertainty.

Acceptance Angle. In addition to the scattering-angle uncertainty, there is an error component due to the finite acceptance angle, Γ, of the collection optics [18]. This angle was measured to be ±0.8° at the half-transmission points. Using this value as input, calculations were performed in which 1/2 of the intensities at 90.4° and 89.6° were added to the intensity at 90°. The resultant shift in the peak wavelengths was less than ±0.06 nm, giving a systematic diameter uncertainty of ±0.001 μm.

Laser Intensity Variation. Because of the wavelength-dependent properties of the laser intensity stabilizer, the intensity that was incident upon the microsphere suspension was not constant, but instead increased by about 50% as the dye laser scanned from 620 to 570 nm. Typical laser powers were 60 to 90 mW at 620 nm, and 90 to 120 mW at

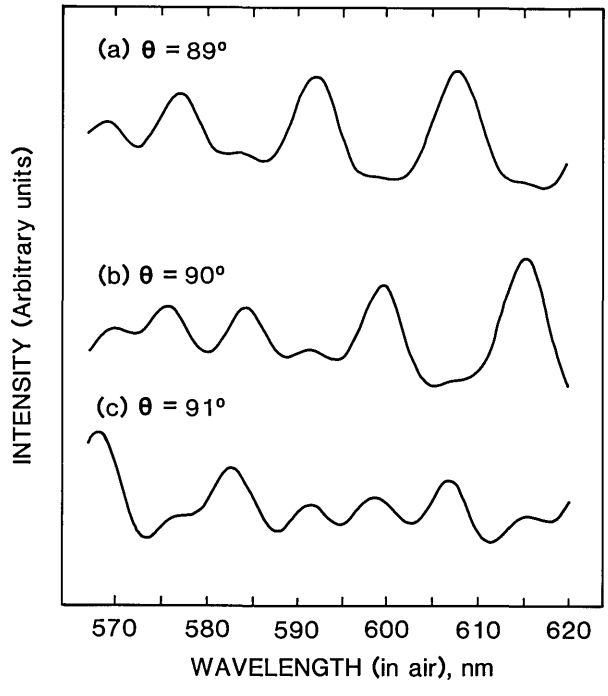

Fig. 14. Calculated RLS spectra for 89°, 90°, and 91°.

570 nm. The effect of this input power rise was simulated in computer calculations by including a linear intensity factor in Eq. (10). The resulting shift in peak wavelengths was less than ±0.1 nm, for a maximum diameter uncertainty of ±0.002 μm.

4.5.3 Total Diameter Uncertainty from RLS

The above errors in the RLS measurement are summarized in Table 7. They can be combined to get the total error by using the expression

$$U_T = R + U_S$$

$$= R + |\delta_n| + |\delta_\lambda| + |\delta_\theta| + |\delta_\Gamma| + |\delta_I|, \qquad (13)$$

in which R and U_S are the total random and total systematic components, respectively, of the measurement error. The systematic errors in diameter measurement are: δ_n, refractive index uncertainty; δ_λ, peak wavelength uncertainty; δ_θ, scattering-angle uncertainty; δ_Γ, finite-acceptance-angle error; and δ_I, an error due to a linear rise in the laser intensity as the wavelength was varied.

Substituting the various error values into Eq. (13) gives a total uncertainty of ±0.03 μm at the 99% confidence level (3σ), for the RLS-determined mean diameter of SRM 1960.

Table 7. RLS error budget[a]

	Error source	Random (μm)	Syst. (μm)
Random	Wavelength	0.004	
	Scattering angle	0.005	
Systematic	Refractive index		0.01
	Wavelength		0.004
	Scattering angle		0.005
	Acceptance angle		0.001
	Intensity		0.002
Total error		0.006	0.022

[a] The errors are for all five RLS measurements.

4.6 Final Results of the RLS Measurements

The mean diameter of SRM 1960 determined from resonance light scattering is 9.90 ± 0.03 μm.

5. Summary and Conclusions

The results for the mean diameter of the SRM 1960 microspheres, as determined by all three micrometrology techniques, are summarized in Table 8. The agreement between the measurements is excellent, well within the stated uncertainties of the techniques: this study is probably the most accurate intercomparison of its type ever made in the dimensional metrology of microspheres.

Table 8. Summary of results for mean diameter of SRM 1960

Technique	d_m, μm	Unc., μm
CDF	9.89	±0.04
MEM	9.89	±0.06
RLS	9.90	±0.03

It is significant that all of the measurements of SRM 1960 were made on the particles in different physical environments, under different measurement conditions, and using different physical principles to determine the mean particle size. With center distance finding, the microspheres were measured dry, in air. By comparison, with metrology electron microscopy they were measured dry and in an ultrahigh vacuum and, moreover, were irradiated with relatively high-energy electrons (30 keV). Finally, with resonance light scattering, the SRM 1960 microspheres were suspended in water at room temperature and pressure. Despite these environmental differences, the excellent agreement between all three measurements is evidence that the physical principles of the measurements are understood and that major systematic errors were accounted for. The mutual agreement is also an indication that the polystyrene microspheres of SRM 1960 are not significantly affected by their environment, at least for those used here. In particular, there was no evidence for particle outgassing in an ultra-high vacuum.

In summary, SRM 1960 is an accurately calibrated standard artifact for micrometrology applications that is highly uniform in size and shape and is dimensionally stable under reasonable changes in environment. It should find many uses in industry, technology, and basic research.

6. Appendix A. Microscope Calibration for Image Magnification and Distortion

In this Appendix, a description is given of the microscope calibration process. The commercial microscope calibrated in this manner had a 20×, 0.50 N.A. objective, a 2.0× relay lens, and a 12.5× photo eyepiece.

First, one row of a hexagonal array of 10 μm SRM 1960 microspheres is positioned so as to cross the center of the microscope field of view (FOV), and its focal spots are photographed. Next, the microscope slide is shifted in-line by three sphere diameters and photographed again. The distances between adjacent sphere centers are measured in both photographs, and changes in them are plotted (Fig. 6a). If image distortion is present, these systematic length changes, which are proportional to the object shift, will also depend on the initial position of each sphere pair.

The data points in Fig. 6a are then used to find the accumulated length changes when a line segment of length d (= one sphere center distance) is shifted in-line from one side of the FOV to the other, moving in steps $3d$ long and starting at the far left position (indicated by circles). The process is repeated starting at the second left position, then again at the third. The result is three groups of data points which are shifted vertically as a group relative to each other until they fall into a best fit on a common curve (Fig. 6b). This curve represents, in relative terms, the change in film scale when moving along a FOV diameter. In other words, the curve represents the image magnification in terms of its on-axis value (the scale distortion). A graphic integration of Fig. 6b shows how much a point image will be displaced from its nominal position due to the variation of magnification across the FOV (this is the image distortion).

Next, a section of a calibrated stage micrometer is positioned so as to almost fill the FOV (to maximize data resolution), and then it is photographed. The image length is measured and corrected for image distortion using Fig. 6c. The corrected length now yields the on-axis value of the image magnification. Combined with the data in Fig. 6b, one now has the complete magnification curve for the combination of microscope objective, relay lens (if any), and projection eyepiece that was used.

The justification for the above calibration procedure can be found by considering that the image distortion of well centered, high quality microscope optics is not a function of orientation in the FOV, but only of the off-axis distance. Its derivative with respect to radius represents the scale distortion (Fig. 6b), and its second derivative shows by how much a line segment will change if it is radially shifted from a selected off-axis point (Fig. 6a). Adopting a $3d$ shift rather than a $1d$ shift results in better data resolution in Fig. 6b. However, this did not result in an averaging over three center distances, only over one.

Acknowledgments

The authors thank John Vanderhoff, Russell Obbink, Dale Kornfeld, Joseph Fu, and Theodore Doiron for valuable input to this project.

7. References

[1] T. R. Lettieri, in Optical Particle Sizing: Theory and Practice, G. Gouesbet and G. Grehan, eds., Plenum, New York (1988).
[2] NIST Standard Reference Materials Catalog 1990-1991, R. L. McKenzie, ed., Natl Inst. Stand. Technol., Gaithersburg, MD (1990).
[3] T. R. Lettieri, A. W. Hartman, G. G. Hembree, and E. Marx, J. Coll. Int. Sci. **131**, 550 (1989).
[4] A. W. Hartman and R. L. McKenzie, Description of the SRM 1965 Microsphere Slide, NIST SP260-107, Natl. Inst. Stand. Technol., Gaithersburg, MD (1988).
[5] G. Mulholland, G. Hembree, and A. W. Hartman, Sizing of Polystyrene Spheres Produced in Microgravity, NBSIR 84-2914, Natl. Bur. Stand. (U.S.), Gaithersburg, MD (1985).
[6] D. Kornfeld, Monodisperse Latex Reactor (MLR), NASA TM-86487, NASA, Washington, DC (1985).
[7] H. E. Kubitschek, Nature **192**, 48 (1960).
[8] A. W. Hartman, Powder Technol. **46**, 109 (1986).
[9] R. A. Bowling, Solid-State Sci. Technol., 2208 (Sept. 1985); G. Brown, J. Polymer Sci. **22**, 723 (1956).
[10] V. M. Muller, V. S. Yuschenko, and B. V. Derjaguin, J. Coll. Int. Sci. **77**, 91 (1980).
[11] M. G. Natrella, Experimental Statistics, NBS Handbook 91, Natl. Bur. Stand. (U.S.), Gaithersburg, MD (1963).
[12] G. G. Hembree, in Proceedings of the 44th Annual Meeting of the Electron Microscopy Society of America, G. W. Bailey, ed., San Francisco Press, San Francisco (1986); S. Jensen, G. Hembree, J. Marchiando, and D. Swyt, in Semiconductor Microlithography VI, Proceedings of SPIE, Vol. 275, J. Day, ed., SPIE, Bellingham, Wash. (1981).
[13] F. E. Scire and E. C. Teague, Rev. Sci. Instrum. **49**, 1735 (1978).
[14] Instruction Manual for Hewlett-Packard Model 5526A Laser Measurement System (1972).
[15] V. Barnett and T. Lewis, Outliers in Statistical Data, Wiley, New York (1978).
[16] A. Ashkin and J. M. Dziedzic, Appl. Opt. **20**, 1803 (1981); P. Chylek, J. T. Kiehl, and M. K. W. Ko, Phys. Rev. A **18**, 2229 (1978).
[17] T. R. Lettieri, W. D. Jenkins, and D. A. Swyt, Appl. Opt. **20**, 2799 (1981); C. C. Hill, C. K. Rushforth, R. E. Benner, and P. R. Conwell, Appl. Opt. **24**, 2380 (1985); P. Chylek, V. Ramaswamy, A. Ashkin, and J. M. Dziedzic, Appl. Opt. **22**, 2302 (1983).
[18] T. R. Lettieri and E. Marx, Appl. Opt. **25**, 4325–4331 (1986).
[19] H. Napper and R. H. Ottewill, J. Coll. Int. Sci. **19**, 72 (1964).
[20] W. J. Wiscombe, Appl. Opt. **19**, 1505 (1980).
[21] M. Kerker, The Scattering of Light and Other Electromagnetic Radiation, Academic Press, New York (1969).
[22] G. W. C. Kaye and T. H. Laby, eds., Tables of Physical and Chemical Constants, Longman, London (1973).

[23] G. W. Mulholland, A. W. Hartman, G. G. Hembree, E. Marx, and T. R. Lettieri, Development of a One-Micrometer-Diameter Particle Size Standard, SRM 1690, NBS SP260-95, Natl. Bur. Stand. (U.S.), Gaithersburg, MD (1985).
[24] G. W. Mulholland, A. W. Hartman, G. G. Hembree, E. Marx, and T. R. Lettieri, J. Res. Natl. Bur. Stand. (U.S.) **90**, 3 (1985).
[25] L. A. Matheson and J. L. Saunderson, Optical and Electrical Properties of Polystyrene, in Styrene: Its Polymers, Copolymers, and Derivatives, R. H. Boundy and R. F. Boyer, eds., Reinhold Publ., New York (1952).

About the authors: *Thomas R. Lettieri, Arie W. Hartman, and Egon Marx are physicists with the Precision Engineering Division of the Manufacturing Engineering Laboratory, where they have certified a number of particle sizing Standard Reference Materials using various optical techniques. When this work was being done, Gary G. Hembree was also a physicist at NIST. He is now with Arizona State University.*

Volume 96, Number 6, November–December 1991
Journal of Research of the National Institute of Standards and Technology

[J. Res. Natl. Inst. Stand. Technol. 96, 693 (1991)]

Construction and Calibration of the NIST Large-Area-Source X-Ray Counting System

Volume 96 | Number 6 | November–December 1991

J. M. R. Hutchinson, M. P. Unterweger, and P. A. Hodge

National Institute of Standards and Technology,
Gaithersburg, MD 20899

This paper describes the construction and calibration of the NIST large area x-ray counting system. ^{238}Pu sources 8 in (20.32 cm) by 5 in (12.70 cm) thick, emitting L x rays in the range of 12–20 keV are calibrated for total emission rate and also for rate through a centrally located 3 in (7.63 cm) diameter aperture. Alpha particle emission rates are obtained using the known x-ray to alpha particle abundances. The sources will be used to calibrate alpha-particle surface monitors.

Key words: calibration; efficiency curve; large area source; plutonium-238; proportional counting; x ray.

Accepted: October 30, 1991

1. Introduction

Recently the National Institute of Standards and Technology (NIST) has developed a calibrated system for measuring the L x-ray-counting rate of large area sources of plutonium. The system was requested by the United States Air Force (USAF) primary calibration laboratory in order to calibrate large area standards for its secondary and tertiary laboratories. The objective was to tie the USAF calibrations to NIST standards and thereby take the first step towards "traceability" of USAF surface monitoring equipment.

The program required the construction of a jig which holds a NaI(Tl) detector at a precise distance from a vertically moveable platform on which the large area source may be positioned. Distances from the source-to-detector can be adjusted and held accurately. The second part of the program was to determine the ^{238}Pu L x-ray counting efficiencies as a function of source-to-detector distance for both a rectangular source and circular sources of various diameters. A number of published calculations and tables exist of photon efficiencies at various distances from NaI(Tl) detectors for these geometries [1]. Generally, though, the accuracies given in these reports are in the range of 5–10 percent for the dimensions of the present arrangement, especially for close-in geometries for which the source dimensions exceed those of the detector by a wide margin. The aim of the program is to provide efficiency values with accuracies of 5 percent or less.

The calibration procedure was first to check the system calibration with a calibrated point source which can give the efficiencies for all distances from an analytical expression of the solid angle subtended by the "black" detector from the source. Values of the count rates for rectangular and circular large area sources at various distances were fitted to a mathematical expression which reduced to the point source values for zero source size. The calibration of one of the sources was then compared with the x-ray results by alpha-particle counting.

The utility of photon measurements for field monitoring is described by the NARP manual [2] which recommends low-energy gamma instruments for field surveys of plutonium contamination. Alpha measurements should be used "primarily for personnel monitoring and when field use is necessary, on smooth surfaces only, e.g., pavement and building surfaces."

2. Large Area X-Ray Counting System

The large-area-defined-solid angle NaI(Tl) x-ray counting system is shown schematically in Fig. 1 and in a photograph in Fig. 2. It consists of a 1/32 in (0.079 cm)[1] thick, 31/32 in (2.46 cm) diameter NaI(Tl) detector. The detector is thick enough to ensure that all impinging U L x rays (following the alpha decay of ^{238}Pu) are absorbed except those which are lost in the 0.005 in (0.013 cm) Be window and the Al reflector. The detector is mounted on an XP1010 phototube which has a noise level equivalent to one keV photon energy. The platform is vertically moveable over approximately 14 in (35.56 cm) by means of a precision spindle which is moved manually with a wheel which can reproduce the vertical position to 0.001 in (0.003 cm). The source platform is large enough to be able to mount any size source that could be useful for the calibration of surface monitoring systems. Tests were made on the NIST coordinate measuring machine. The true distance of the platform for selected positions is given in Table 1.

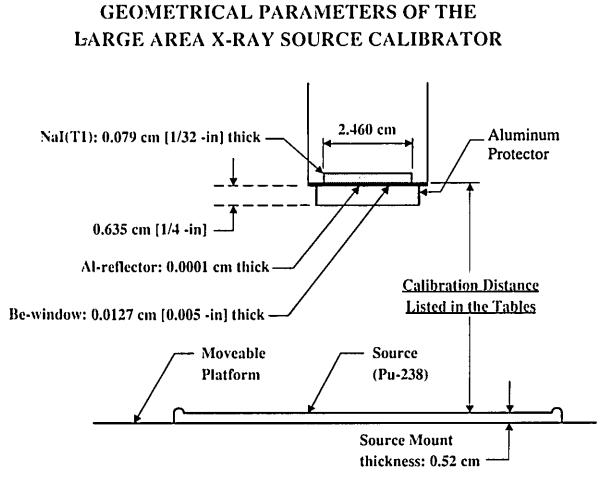

Fig. 1. Schematic diagram of the x-ray system.

Table 1. Coordinate measurement data showing setting accuracies of the platform movement with the spindle

Dial wheel setting (in)	(cm)	Distance measurement from 0.000 setting
.000	(0.0)	0.000
1.000	(2.54)	0.9990
2.000	(5.08)	2.0000
3.000	(7.62)	2.9990
4.000	(10.16)	4.0000
5.000	(12.70)	4.9995
6.000	(15.24)	6.0010
7.000	(17.78)	6.9995
8.000	(20.32)	8.0005
9.000	(22.86)	9.0010
10.000	(25.40)	10.0010
11.000	(27.94)	11.0020
12.000	(30.48)	12.0020
13.000	(33.02)	13.0010
14.000	(35.56)	14.0000

The vertical variability from horizontal is approximately 0.014 in (0.036 cm) maximum over the face of the platform. Deviation of the center from the labeled value is 0.002 in (0.006 cm).

A schematic diagram of the electronics is shown in Fig. 3. The pulses are fed from the amplifier with microsecond resolving time into the pulse height analyzer whose output is recorded on a PC. A typical NaI(Tl) spectrum of the U L x rays in the decay of ^{238}Pu is shown in Fig. 4.

3. Sources and Baffles

A NIST "point" source was used to check for the correct functioning of the system and to determine the efficiency of the detector for x rays at large distances. It consists of ^{238}Pu electroplated onto a thin platinum foil 6 mm in diameter and mounted onto a 1 in (2.54 cm) diameter polished stainless steel disc. The photon emission spectrum with a Ge detector from this source is shown in Fig. 5. The U L x-ray peaks occur between 11 and 20 keV. Contributions from activation of the platinum occur at 8 and 11 keV and are 7±2 percent of the intensity

[1] The dimensions are given in U.S. customary units with their SI equivalents in parentheses because the instrument is designed and calibrated in inches and fractions thereof.

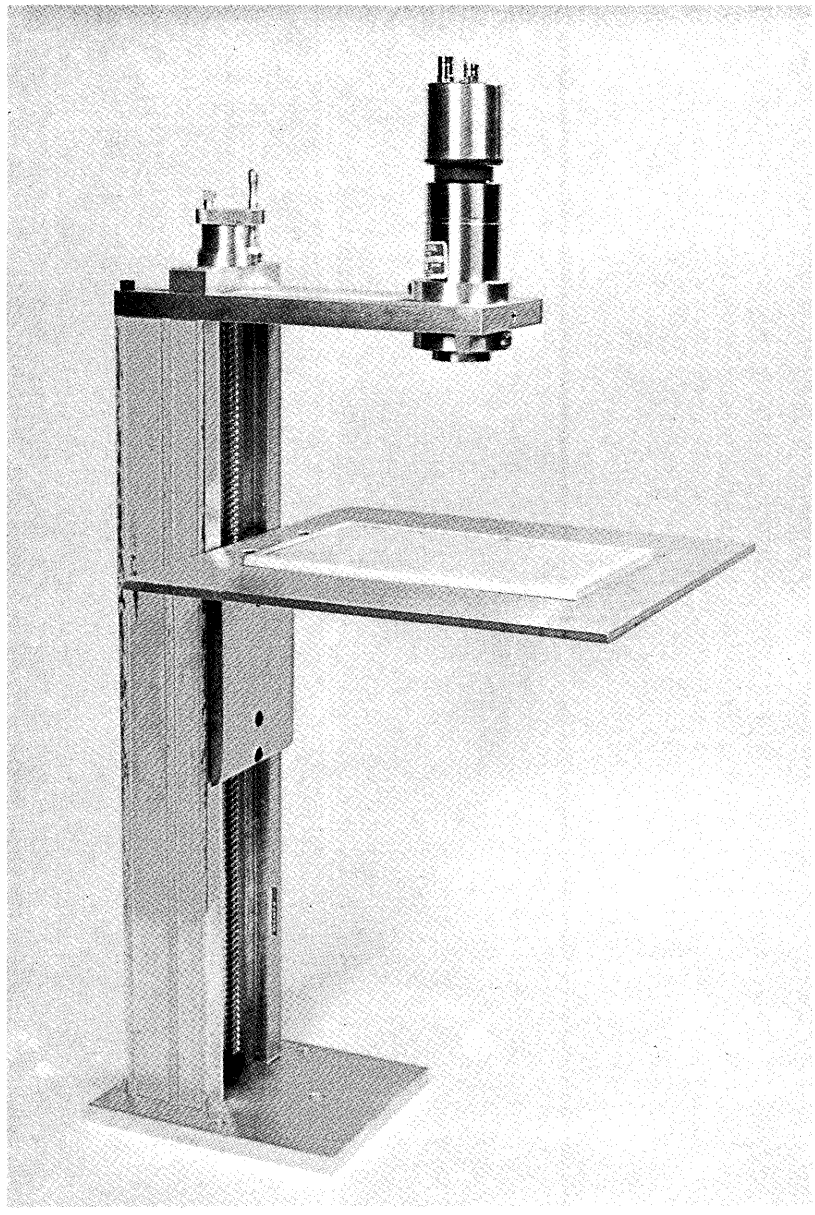

Fig. 2. Photograph of the x-ray system.

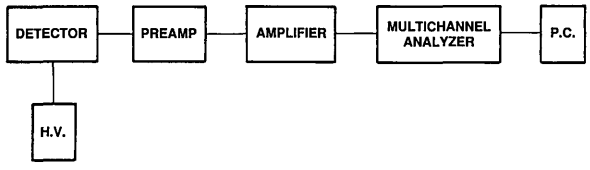

Fig. 3. Schematic diagram of the electronics of the x-ray system.

of the U L x rays. In addition, the possibility exists for self activation of the source, i.e., high energy L x rays stimulating lower energy x rays in the plutonium or being lost entirely from the photon spectrum. Because the solid angle from source to detector can be calculated exactly (within the accuracies of the measured dimensions of the source-to-detector distance and diameter of the detector) and the source activity is known, the correct functioning of the system was checked with measurements with this source.

A large area source is shown in Fig. 6. The photon emission spectrum with a Ge detector from this source is shown in Fig. 7. The dimensions are 8 in (20.32 cm) by 5 in (12.70 cm). Disc sources were produced by covering it and other similar sources with baffles of 1 in (2.54 cm), 2 in (5.08 cm), and

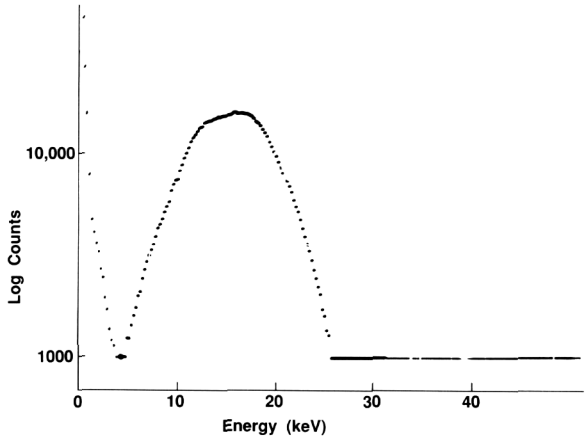

Fig. 4. Spectrum of a NaI(Tl) source.

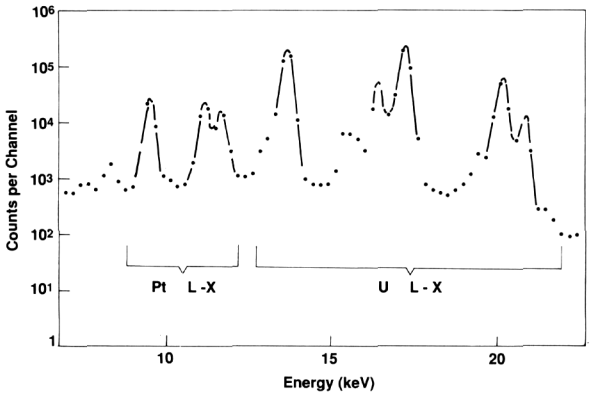

Fig. 5. Ge spectrum of a ^{241}Am point source electroplated on a platinum substrate.

3 in (7.62 cm) diameter holes cut in either stainless steel or aluminum (6061) plates. The plutonium is anodized onto the aluminum foil which is attached to a solid aluminum baseplate. A radiogram is shown of one of the "hotter" sources showing an array of radioactive sites, 4 mm distance center-to-center (Fig. 8). The weaker sources were also anodized but, in these, the radioactivity is continuously distributed. The observed homogeneity of these sources has been discussed elsewhere [3] and was found to be in the range of ±5 percent for a 3 in (7.62 cm) diameter area.

4. X-Ray Efficiency Curve

4.1 Point Source

Measurements were taken of the point source with the NaI(Tl) detector at distances from 1 in (2.54 cm) to 7 in (17.78 cm) from the source to the face of the detector.

The expression for the solid angle from a point source at a distance h to a circular aperture with radius, r, is:

$$\epsilon = 0.5 - h/2R \qquad (1)$$

where ϵ is the solid angle, or in this case, the efficiency, and $R^2 = r^2 + h^2$. A correction was made for the scattering by the intervening air, and absorption by the Be window and the Al reflector.

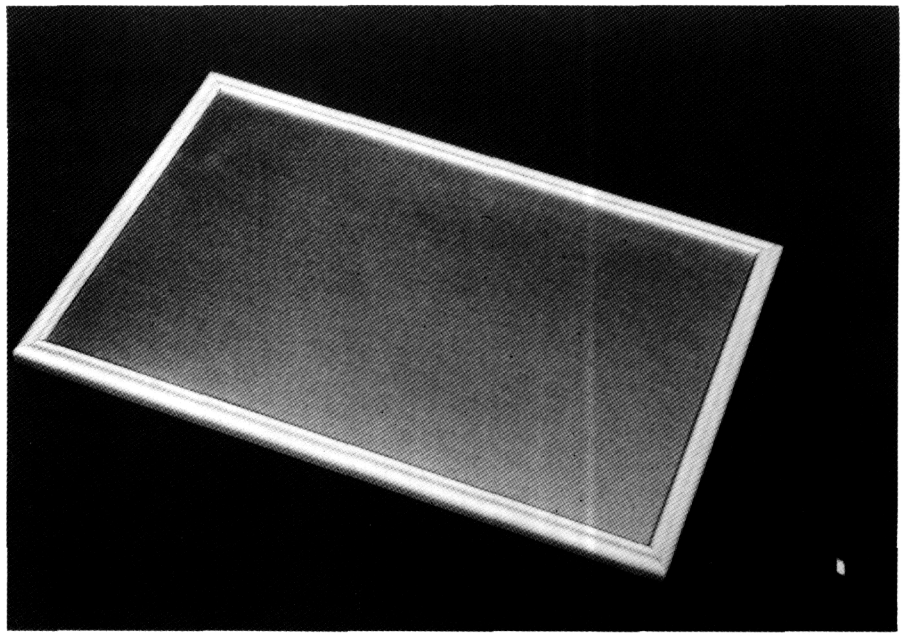

Fig. 6. Large area ^{238}Pu source.

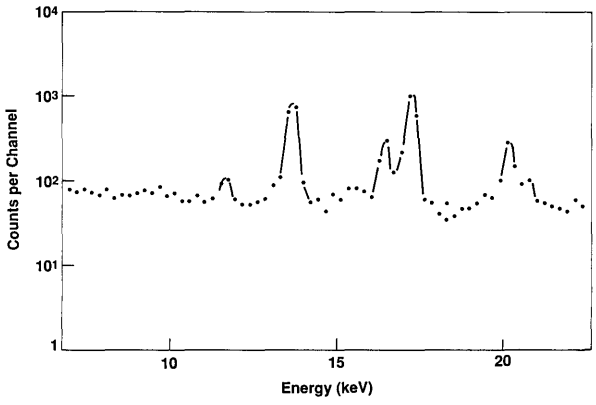

Fig. 7. Ge spectrum of the large area ^{238}Pu source.

The experimental value appears to be 5 percent greater than the calculated value. However 7 ± 2 percent of the NaI(Tl) peak has been determined to be stimulated x rays from the platinum substrate. Subtracting this value leaves the experimental value in good agreement with the prediction in Eq. (1).

4.2 Large Area Sources

The value for the activity of source AA372, the most active of the sources, was determined two ways:

(i) By taking the count rate at 14 in (35.56 cm) with a 3 in (7.62 cm) disc baffle and assuming that it was essentially a point source at that distance and computing the efficiency according to Eq. (1) (adjusting for air and Be and Al reflector absorption). The result was multiplied by the ratio of the total rectangular area to the area of the 3 in disc to obtain the total activity, and

(ii) By alpha-particle counting AA370 [3], a relatively low activity source that would not overload the internal gas counting system, and comparing AA370 and AA372 by x-ray counting and external alpha counting, and from these data determining the activity of AA372. A source self-absorption correction of 5.8 percent was determined as follows. (It should be remembered that the source is anodized so that the active material is embedded in aluminum oxide and significant absorption is to be expected.)

A Si surface barrier spectrum as shown in Fig. 9 was taken. The distribution, except for a small amount of tailing, starts at 80 percent of the range. This is because the activity at its deepest is impregnated to a depth corresponding to 20 percent of the

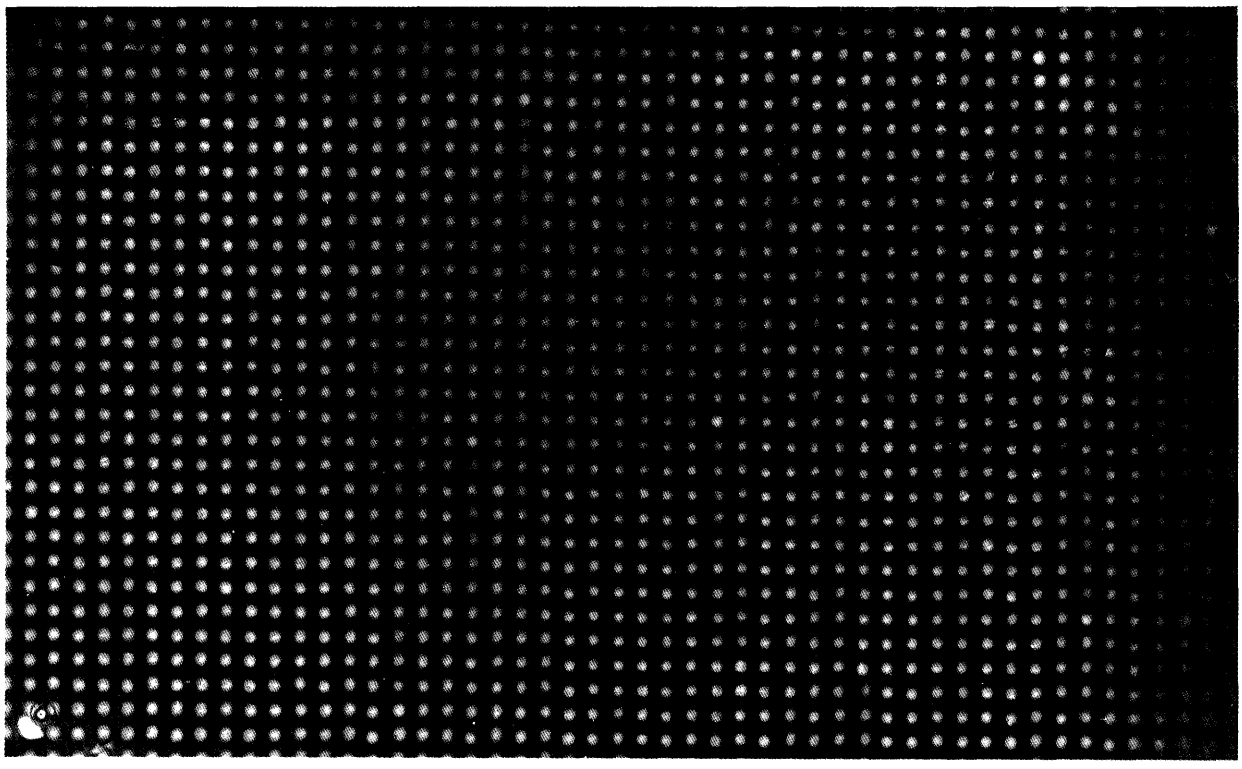

Fig. 8. Radiograph of the large area source showing an array of radioactive sites.

range. The $C_{2\pi}/N_0$ value for this situation has been calculated by Lucas et al. [4]. However, the spectrum peaks at 100 percent of the range and tails off at lower energies corresponding to a depth profile for the activity of maximum near the surface and tailing off to a maximum depth of 20 percent of the range.

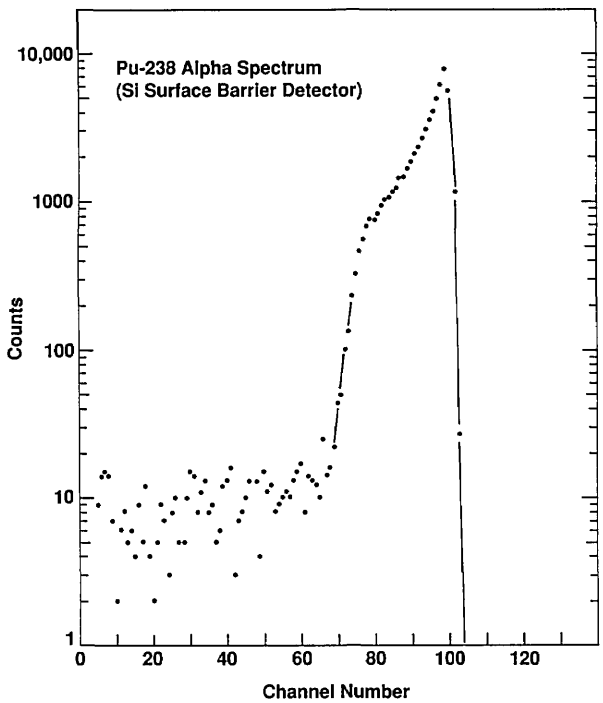

Fig. 9. Si surface barrier spectrum of a large area ^{238}Pu source.

To determine the overall $C_{2\pi}/N_0$ value, values of $C_{2\pi}/N_0$ at 80, 85, 90, 95, and 100 percent of the range were calculated. Counts in a rectangular area corresponding to 80–100 percent of the range were calculated from the pulse height spectrum and assigned a corresponding $C_{2\pi}/N_0$ value. This fraction of the spectrum was subtracted, and the 85 percent fraction was then calculated, etc. The overall $C_{2\pi}/N_0$ was taken as the weighted average. The weighted sets of $C_{2\pi}/N_0$ were added together with the result that the average value of $C_{2\pi}/N_0$ for the large area source was 0.473, or a correction to the activity of 5.8 percent which agreed with the manufacturer's value of 5.5 percent. The overall results are shown below.

Activity of AA372 ^{238}Pu Source by Two Methods

X-Ray Counting

$$DPS = N f (1/\epsilon)\ (R/0.1155)$$
$$= (4.3141\ (1/0.299\times10^{-3})\ (5.70/0.1155)$$
$$= 7.12\times10^{5}\ (5/4/91)$$

where N = cps at 14 in (35.56 cm)
f = x-ray absorption in air, Be, Al
ϵ = geometrical point source efficiency at 14 in (35.56 cm) (Lx/dps) = 0.1155

Alpha Particle Counting

$$DPS = C\times2\times S\times(372/370)\times D$$
$$= 2459\times2\times1.058\times148\times0.963$$
$$= 7.41\times10^{5}$$

where $C = 2\pi\alpha$ count rate of 370 (7/31/86) 2 to convert to 4π
S = scattering correction
(372/370) = measured ratio by x-ray counting
D = decay to 5/4/91

The alpha results differ from the x-ray results by 4 percent, a value not outside the range of possible uncertainties as discussed in the next section.

U x-ray efficiency curves were then generated for the rectangular and disc shaped sources by first taking data at 1 in (2.54 cm) through 14 in (35.56 cm) for these geometries. The data corrected for air, Be, and Al absorption were fitted using a χ^2 minimization technique which generated the following equations for the efficiency for the 3 in (7.62 cm) disc and the rectangular sources.

Circular source:

$$\epsilon_{cir} = \epsilon_{pt} + (0.5-\epsilon_{pt})(-0.23095)\cdot\left(\frac{R}{r}\right)^2\cdot\frac{r^4}{(h^2+r^2)^2}$$
$$+(0.5-\epsilon_{pt})(0.04236)\cdot\left(\frac{R}{r}\right)^4\cdot\frac{h^2\cdot r^6}{(h^2+r^2)^4} \quad (2)$$

where R = radius of source in cm (3.795 cm).

Rectangular source:

$$\epsilon_{rec} = \epsilon_{pt} + (0.5-\epsilon_{pt})(-0.17197)\cdot\frac{(a^2+b^2)}{(2r)^2}\cdot\frac{r^4}{(h^2+r^2)^2}$$
$$+(0.5-\epsilon_{pt})(0.03370)\cdot\frac{(a^4+(10/9)\cdot(a^2\cdot b^2)+b^4)}{(2r)^4}$$
$$\cdot\frac{h^2\cdot r^6}{(h^2+r^2)^4} \quad (3)$$

where a and b are the length and width of the rectangular source in cm (a = 20.3 cm, b = 12.725 cm) and where

$$\epsilon_{pt} = \frac{(0.5-h)}{(2\cdot(h^2+r^2)^{1/2}\cdot1.07} \quad (4)$$

where h = distance from detector to source in cm
r = radius of detector in cm (1.230312).

The total efficiency curves,

$$(\epsilon_{cir})_{total} = \epsilon_{cir} f$$

and

$$(\epsilon_{rec})_{total} = \epsilon_{rec} f$$

where f = x-ray absorption in air, Be, and Al are shown in Figs. 10a and 10b and the total efficiency values for the measured distances are listed numerically in Tables 2 and 3.

5. Uncertainty Listing

The uncertainties in the value for the efficiencies in curves are as follows:

	Percent
Activity of point source	1.0
Estimate of percentage of Pt x rays	2.0
X-ray abundance	1.5
Air, Be, Al absorption estimates	1.5
Uncertainties in fitted parameters	1.5
Counting uncertainties	0.2
Source positioning	0.1
Total 1 s.d. (uncertainties taken in quadrature)	3.4

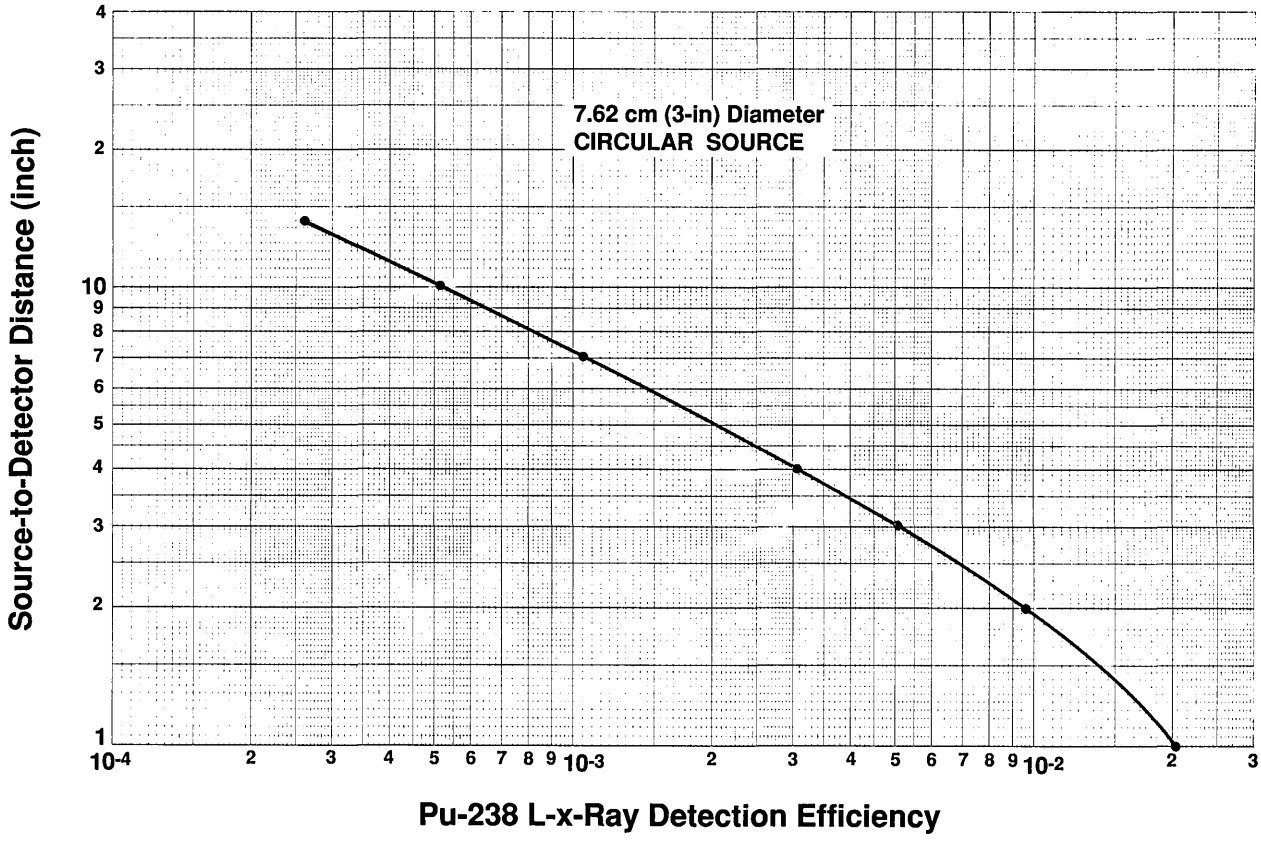

Fig. 10a. X-ray efficiency curve for the 3 in (7.62 cm) disc source as a function of distance from the front face of the NaI(Tl) detector.

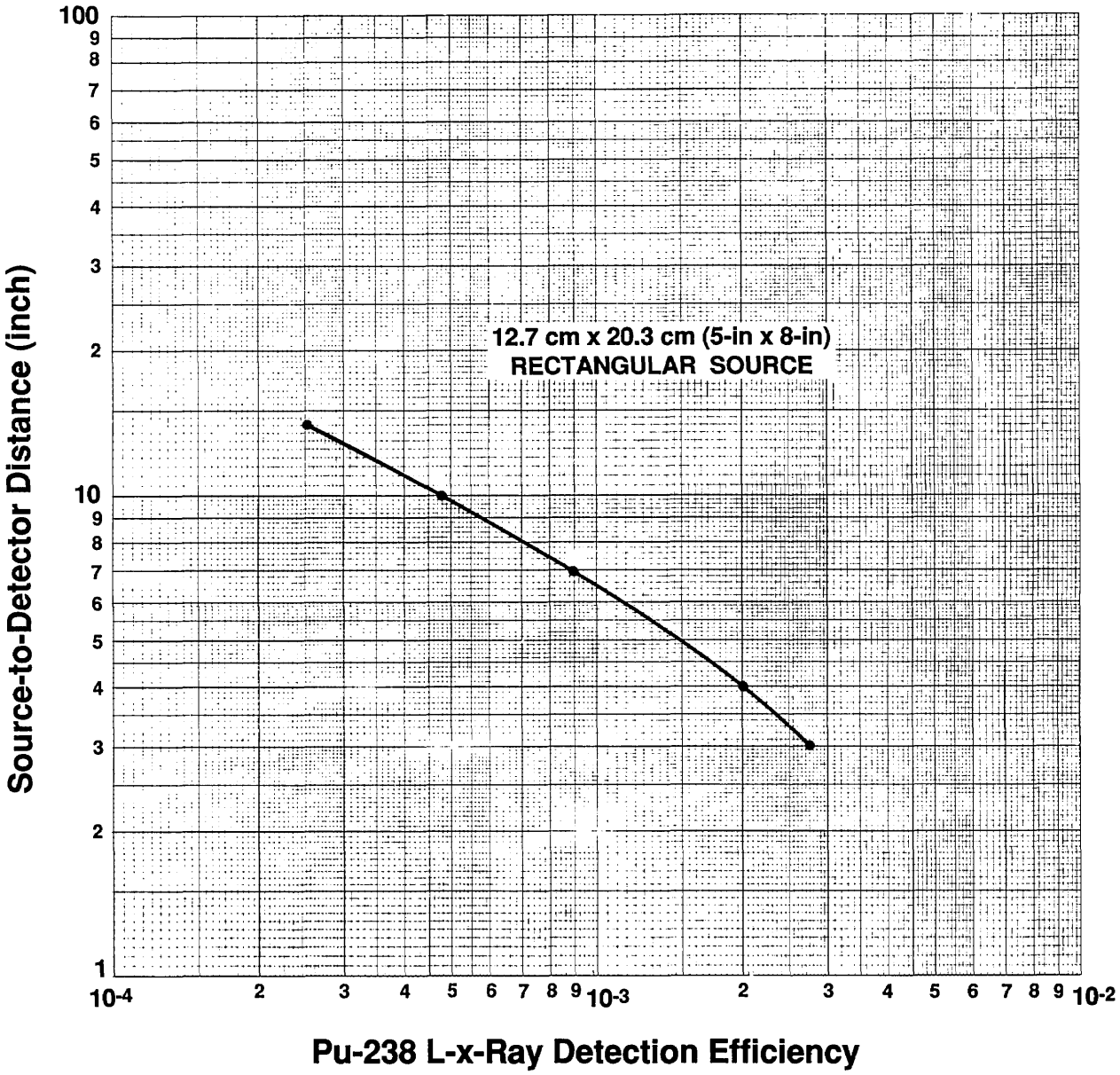

Fig 10b. X-ray efficiency curve for the 8 in (20.32 cm) × 5 in (12.70 cm) rectangular source as a function of distance from the front face of the NaI(Tl) detector.

Table 2. Numerical listing of the calculated and measured efficiencies for the 3 in diameter baffled source

Source to detector distance in in	Calculated efficiency	Measured efficiency
1.00 (2.54 cm)	2.359×10^{-2}	2.360×10^{-2}
1.25 (3.18 cm)	1.951×10^{-2}	
1.50 (3.81 cm)	1.602×10^{-2}	
1.75 (4.45 cm)	1.317×10^{-2}	
2.00 (5.08 cm)	1.089×10^{-2}	1.081×10^{-2}
2.25 (5.72 cm)	9.086×10^{-3}	
2.50 (6.35 cm)	7.660×10^{-3}	
2.75 (6.99 cm)	6.522×10^{-3}	
3.00 (7.62 cm)	5.607×10^{-3}	5.634×10^{-3}
3.25 (8.26 cm)	4.863×10^{-3}	
3.50 (8.89 cm)	4.252×10^{-3}	
3.75 (9.53 cm)	3.746×10^{-3}	
4.00 (10.16 cm)	3.322×10^{-3}	3.360×10^{-3}
4.25 (10.80 cm)	2.965×10^{-3}	
4.50 (11.43 cm)	2.661×10^{-3}	
4.75 (12.07 cm)	2.400×10^{-3}	
5.00 (12.70 cm)	2.175×10^{-3}	
5.25 (13.34 cm)	1.979×10^{-3}	
5.50 (13.97 cm)	1.809×10^{-3}	
5.75 (14.61 cm)	1.659×10^{-3}	
6.00 (15.24 cm)	1.526×10^{-3}	
6.25 (15.88 cm)	1.409×10^{-3}	
6.50 (16.51 cm)	1.304×10^{-3}	
6.75 (17.15 cm)	1.211×10^{-3}	
7.00 (17.78 cm)	1.127×10^{-3}	1.141×10^{-3}
7.25 (18.42 cm)	1.051×10^{-3}	
7.50 (19.05 cm)	9.829×10^{-4}	
7.75 (19.69 cm)	9.208×10^{-4}	
8.00 (20.32 cm)	8.644×10^{-4}	
8.25 (20.96 cm)	8.129×10^{-4}	
8.50 (21.59 cm)	7.658×10^{-4}	
8.75 (22.23 cm)	7.227×10^{-4}	
9.00 (22.86 cm)	6.830×10^{-4}	
9.25 (23.50 cm)	6.465×10^{-4}	
9.50 (24.13 cm)	6.127×10^{-4}	
9.75 (24.77 cm)	5.816×10^{-4}	
10.00 (25.40 cm)	5.527×10^{-4}	5.563×10^{-4}
10.25 (26.04 cm)	5.258×10^{-4}	
10.50 (26.67 cm)	5.009×10^{-4}	
10.75 (27.31 cm)	4.776×10^{-4}	
11.00 (27.94 cm)	4.559×10^{-4}	
11.25 (28.58 cm)	4.357×10^{-4}	
11.50 (29.21 cm)	4.167×10^{-4}	
11.75 (29.85 cm)	3.989×10^{-4}	
12.00 (30.48 cm)	3.822×10^{-4}	
12.25 (31.12 cm)	3.666×10^{-4}	
12.50 (31.75 cm)	3.518×10^{-4}	
12.75 (32.39 cm)	3.379×10^{-4}	
13.00 (33.02 cm)	3.248×10^{-4}	
13.25 (33.66 cm)	3.125×10^{-4}	
13.50 (34.29 cm)	3.008×10^{-4}	
13.75 (34.93 cm)	2.897×10^{-4}	
14.00 (35.56 cm)	2.793×10^{-4}	2.810×10^{-4}

Table 3. Numerical listing of the calculated and measured efficiencies for the 8×5 in source

Source to detector distance in in	Calculated efficiency	Measured efficiency
3.00 (7.62 cm)	3.094×10^{-3}	3.904×10^{-3}
3.25 (8.26 cm)	2.827×10^{-3}	
3.50 (8.89 cm)	2.611×10^{-3}	
3.75 (9.53 cm)	2.421×10^{-3}	
4.00 (10.16 cm)	2.247×10^{-3}	2.250×10^{-3}
4.25 (10.80 cm)	2.088×10^{-3}	
4.50 (11.43 cm)	1.940×10^{-3}	
4.75 (12.07 cm)	1.804×10^{-3}	
5.00 (12.70 cm)	1.679×10^{-3}	
5.25 (13.34 cm)	1.564×10^{-3}	
5.50 (13.97 cm)	1.458×10^{-3}	
5.75 (14.61 cm)	1.361×10^{-3}	
6.00 (15.24 cm)	1.273×10^{-3}	
6.25 (15.88 cm)	1.191×10^{-3}	
6.50 (16.51 cm)	1.117×10^{-3}	
6.75 (17.15 cm)	1.048×10^{-3}	
7.00 (17.78 cm)	9.854×10^{-4}	9.800×10^{-4}
7.25 (18.42 cm)	9.276×10^{-4}	
7.50 (19.05 cm)	8.743×10^{-4}	
7.75 (19.69 cm)	8.252×10^{-4}	
8.00 (20.32 cm)	7.798×10^{-4}	
8.25 (20.96 cm)	7.379×10^{-4}	
8.50 (21.59 cm)	6.990×10^{-4}	
8.75 (22.23 cm)	6.630×10^{-4}	
9.00 (22.86 cm)	6.296×10^{-4}	
9.25 (23.50 cm)	5.985×10^{-4}	
9.50 (24.13 cm)	5.695×10^{-4}	
9.75 (24.77 cm)	5.425×10^{-4}	
10.00 (25.40 cm)	5.173×10^{-4}	5.188×10^{-4}
10.25 (26.04 cm)	4.938×10^{-4}	
10.50 (26.67 cm)	4.717×10^{-4}	
10.75 (27.31 cm)	4.511×10^{-4}	
11.00 (27.94 cm)	4.317×10^{-4}	
11.25 (28.58 cm)	4.135×10^{-4}	
11.50 (29.21 cm)	3.964×10^{-4}	
11.75 (29.85 cm)	3.803×10^{-4}	
12.00 (30.48 cm)	3.651×10^{-4}	
12.25 (31.12 cm)	3.508×10^{-4}	
12.50 (31.75 cm)	3.372×10^{-4}	
12.75 (32.39 cm)	3.245×10^{-4}	
13.00 (33.02 cm)	3.124×10^{-4}	
13.25 (33.66 cm)	3.009×10^{-4}	
13.50 (34.29 cm)	2.901×10^{-4}	
13.75 (34.93 cm)	2.798×10^{-4}	
14.00 (35.56 cm)	2.700×10^{-4}	2.733×10^{-4}

Acknowledgment

The authors are grateful to S. J. Bright for performing many of the early measurements which provided a basis for organizing the final sets of measurements, and to F. J. Schima for the data in Figs. 5 and 7. This work was partially supported by grants from the United States Air Force, Newark Air Force Base, Newark, OH (U.S. Air Force Contract No. 2803 ABG/ACFS) and the Department of the Navy, NAV/Sea Systems Command, Alexandria, VA.

6. References

[1] C. C. Grosjean and W. Bossaert, Table of Absolute Detection Efficiencies of Cylindrical Scintillation Gamma-Ray Detectors, Computing Laboratory of the University of Ghent, Jozef Plateaustraat 22, Ghent, Belgium (1965).

[2] Nuclear Weapon Accident Response Procedures (NARP) Manual, developed by the Defense Nuclear Agency, Washington, D.C. 20305 (January 24, 1984).

[3] J. M. R. Hutchinson and S. J. Bright, The NBS Large Area Alpha-Particle Counting Systems, J. Res. Natl. Bur. Stand. **92**, 311 (1987).

[4] L. L. Lucas and J. M. R. Hutchinson, Study of the Scattering Correction for Thick Uranium-Oxide and Other Alpha-Particle Sources (Part 1: Theoretical), Int. J. Appl. Rad. Isotopes **27**, 35 (1976).

About the authors: J. M. R. Hutchinson, M. P. Unterweger, and P. A. Hodge are members of the Radioactivity Group of the Ionizing Radiation Division at NIST's Physics Laboratory.

Volume 96, Number 6, November–December 1991
Journal of Research of the National Institute of Standards and Technology

[J. Res. Natl. Inst. Stand. Technol. 96, 703 (1991)]

Simulators of Superconductor Critical Current: Design, Characteristics, and Applications

Volume 96 Number 6 November–December 1991

L. F. Goodrich, A. N. Srivastava, and T. C. Stauffer

National Institute of Standards and Technology,
Boulder, CO 80303

The superconductor simulator is an electronic circuit that emulates the extremely nonlinear voltage-current characteristic (the basis of a critical-current measurement) of a superconductor along with its other major electrical properties. Three different types of simulators have been constructed: the passive, active, and hybrid simulator. The passive simulator has the fewest circuit components and offers the least amount of versatility, while the active and hybrid simulators offer more versatility and consequently have more components. Design, characteristics, and applications of the superconductor simulator along with a summary of features are presented. These simulators are high precision instruments, and are thus useful for establishing the integrity of part of a superconductor measurement system. They are potentially useful for testing the measurement method and data acquisition and analysis routines. The 50 A simulator provides critical-current precision of 0.1% at a 1 μV signal. This is significantly higher than the precision of a superconducting standard reference material. The superconductor simulator could significantly benefit superconductor measurement applications that require high-precision quality assurance.

Key words: critical current; data acquisition; data analysis; electronic circuit; high-T_c; low-T_c; measurement method; standard; superconductor; superconductor simulator; voltage-current characteristic.

Accepted: September 30, 1991

1. Introduction

The superconductor simulator emulates the extremely nonlinear voltage-current characteristics of a superconductor. By measuring this characteristic, a "critical current" of the simulator can be obtained. Thus, the simulator can aid in determining the integrity of part of a critical-current measurement system.

A superconductor's critical current (I_c) is a measure of its current carrying capacity, and is defined as that current at which a specified electric-field criterion (E_c), or resistivity criterion (ρ_c) is achieved in the specimen.

The voltage-current (V-I) characteristic of the superconductor can often be modeled by the empirical equation:

$$V = V_o(I/I_o)^n \tag{1}$$

where I_o is the observed current at a voltage V_o, and n reflects the abruptness of the transition from the superconducting to the normal state. Typical values of n range from 10 to 100. For a more complete discussion of the definition of critical current and the V-I characteristic, consult Refs. [1,2]. The

superconductor simulator's critical current is determined in the same manner as for a superconductor.

The process of measuring the critical current of a superconductor is challenging, since it requires measuring low voltages under high current conditions. The critical-current standard-test-method of the American Society for Testing and Materials has an uncertainty of ±5%. The superconductor simulator's precision is on the order of 0.1% with a 1 μV signal level. This level of precision exceeds the recommendations of the ASTM for present superconductor measurements.

The simulator provides a simple, expedient, and repeatable test of a complex measurement system. Another test method using a I_c standard reference material, SRM 1457 (low-T_c, Cu/Nb-Ti wire) exists. However, it has enormous startup costs if the experimenter does not already have a high current and high magnetic field capability. This single-use device also requires the ability to operate at liquid helium temperatures. High-T_c reference materials do not exist yet, and could be subject to degradation and other instabilities. The simulator operates at room temperature and is a multiple-use device, since its characteristics are stable with time and use. It can also be used with both high-T_c and low-T_c measurement systems.

Three different types of simulators have been designed: the passive, hybrid, and the active simulator. The passive simulator consists of non-active, low-reactance components. Thus, its electrical characteristics should not significantly depend on frequency in the region of interest. This device is useful in comparing measurement methods with different frequency characteristics, such as the dc and ac methods or the dc and pulse methods. For a complete discussion of these measurement methods, see Refs. [3,4].

The passive simulator can be considered to be a sample substitution box; the experimenter connects the simulator to the measurement system as though it were a superconductor. Since the simulator operates at room temperature, its temperature dependence was extensively studied. Thus, voltage and current measurements and data analysis routines can be thoroughly tested. After a successful test is performed on the simulator, the integrity of part of the measurement system can be established.

The hybrid simulator has the same electrical components as the passive simulator, but it also contains an insulated oven with an electronic temperature controller. The temperature controller keeps the diode, a key component of the circuit, at a constant temperature. Thus, the response of the simulator will be less a function of room temperature.

The active simulator has operational amplifiers, a temperature controller for the diode, and other active components in its circuitry. These components may have some frequency dependence, since wire wound resistors were used and the gain of the op-amps may depend on frequency. Thus, this simulator could yield different critical currents depending upon which measurement method is used. It is therefore only intended to be used with the dc measurement method. The active components allow the user to select the values of n and I_c.

Although the active simulator's critical current may vary with measurement method, given a measurement technique, it can test the ability of a data acquisition and analysis routine to handle widely varying values of n and I_c. Since data acquisition and analysis to determine I_c with a large variability in n can be difficult, the active simulator was designed to have a wide range of n values. The range of n for the active simulator is from 25 to 150. Values of n much greater than 150 are possible, but they are not relevant for superconductor characterization at this time.

The active simulator, unlike a passive or hybrid simulator, is not a sample substitution box. Instead of being connected to the measurement system as an actual sample, this simulator takes its input from the current supply's current shunt, not the output current of the supply. Thus the I_c of one active simulator could be 10 mA to 10 kA depending on the resistive value of the current supply's current shunt.

2. Simulator Operation and Design Considerations

The simulators described here rely on a diode (Zener diode #1N5252B) to generate a nonlinear voltage-current characteristic. It is important to realize that in a superconductor, the voltage increases from zero abruptly near a certain current. In a diode, however, the current increases from zero abruptly near a certain voltage. Thus, to emulate a superconductor, the diode characteristic must be "inverted" so that near a specified current the measured voltage increases.

Passive and hybrid simulators have a single, preset n characteristic and can have many different values of I_c. The value of n varies slightly with voltage; the quiescent value of n is mainly determined by the diode, and is selectable by using

diodes with different voltage-current characteristics. These simulators have an n-value of approximately 25, whereas the active simulator has a variable n-value feature. Passive and hybrid simulators are best suited for applications under 100 A, whereas the active simulator is suited for use over 100 A.

2.1 Passive and Hybrid Simulator Operation

Figure 1 shows the circuit diagram for the passive simulator. The passive simulator consists of four resistors: R1, R2, R3, and R4, and a Zener diode Z1. The resistors are made from manganin resistance wire which has a low temperature dependence. A regular diode could be used in place of the Zener, although the values of n are generally lower for regular diodes. The resistor R1 is the main current branch; it carries most of the current from the power supply. The current branch connected in parallel with R1, called the parallel current branch, generates the desired voltage-current response.

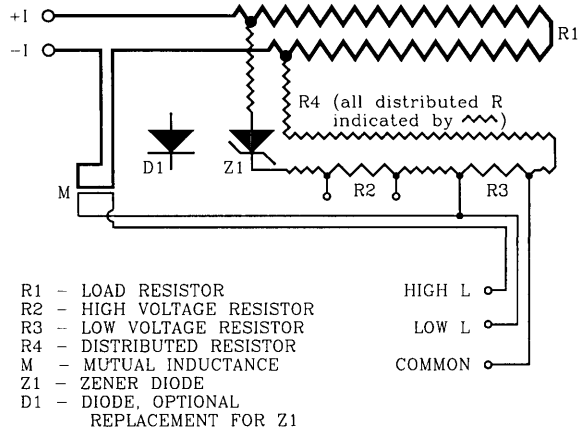

Figure 1. Circuit diagram for the passive simulator. The voltage signal across R2 is denoted as V2, and the signal across R3 is denoted as V3. The hybrid simulator has the same circuit, except the diode Z1 is enclosed in a temperature controller.

The parallel current branch abruptly starts conducting current when the voltage drop across R1 is near the threshold voltage of the forward-biased Zener diode (approximately 0.7 V). The current through the parallel branch increases rapidly until the voltage across the current limiting resistors, R2 and R4 (R4 is a distributed resistance), becomes significant compared to 0.7 V. At this point, this resistance protects the diode from conducting too much current, which could lead to irreversible shifts in the V-I characteristic. The voltage drop across the series resistor R3 is the simulated sample voltage, and is denoted by V3. Since the value of resistor R2 is approximately 100 times greater than that of R3, the voltage signal on R2, V2, can be used to accurately infer the "actual" lower voltage signal V3. The voltage at R2 could be normalized by the measured ratio of resistances R3 and R2.

Examples of V-I data from the 50 A passive simulator are given on Figs. 2 and 3. These curves were taken by measuring V3 on the simulator. An analog nanovoltmeter was used to obtain the voltage data on Fig. 2. The measured voltage at currents below 25 A was typically zero within ±2 nV, which is at the noise level of the analog voltmeter. Measurements of V2 indicated that the actual voltage V3 was zero in this region to within ±0.1 nV. These results were typical for all simulators including the active simulator. Most of the characterization of the simulators was done at higher sample voltages with digital nanovoltmeters as shown on Fig. 3. The dynamic range of the digital voltmeters allows for characterization over a wide range of voltages. The range of interest is typically from 0.1 to 10 μV.

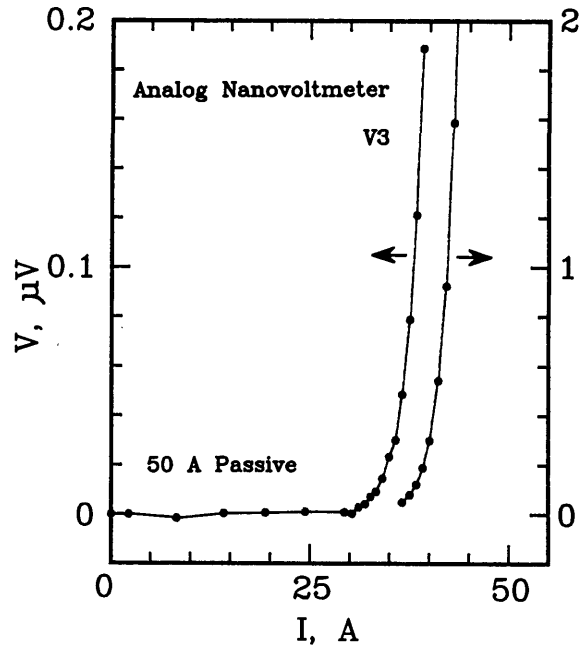

Figure 2. Linear plot of voltage versus current in the low voltage region of the 50 A passive simulator; the voltage across R3 (V3) was measured with an analog nanovoltmeter. The right-most curve is a continuation of the data on an expanded scale, shown on the right-hand axis.

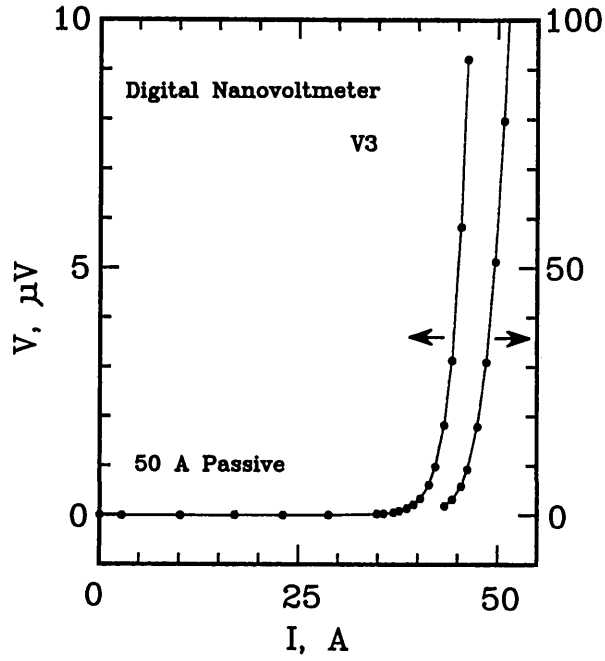

Figure 3. Linear plot of voltage versus current in the high voltage region of the 50 A passive simulator; voltage across R3 (V3) was measured with a digital nanovoltmeter. The right-most curve is a continuation of the data on an expanded scale, shown on the right-hand axis.

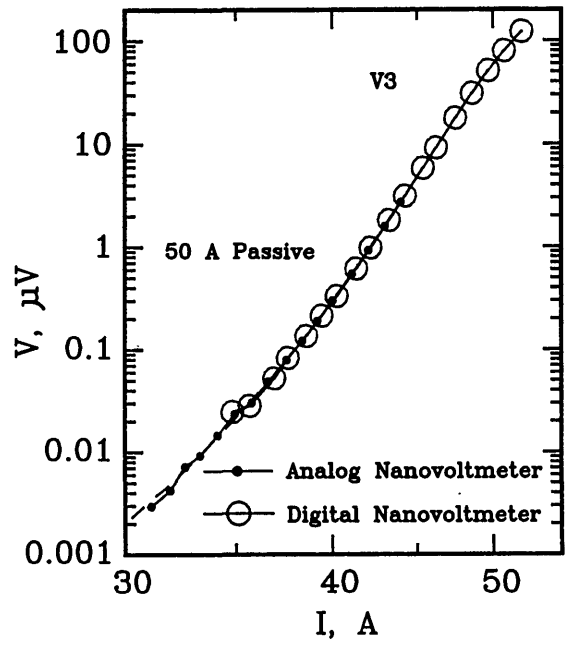

Figure 4. Full logarithmic plot of voltage versus current in the high- and low-voltage region of the 50 A passive simulator.

To illustrate that the *V-I* characteristic of the simulator can be approximated by Eq. (1), a full logarithmic plot of the *V-I* characteristic is given on Fig. 4. This plot is linear, in accordance with the empirical equation:

$$\log V = \log V_0 + n \cdot \log(I/I_0), \qquad (2)$$

where n is the slope of this curve. The data on Fig. 4 are the same as those on Figs. 2 and 3. The dashed line in the low voltage region is the curve obtained by measuring the voltage across R2. The agreement is within a few nV on the low voltage region.

To obtain higher critical currents, the connections of the parallel branch can be moved to a smaller portion of the resistance wire R1. In effect, a voltage divider is created along R1, and a higher current will be needed to generate the 0.7 V diode threshold voltage. In this manner, the critical current is effectively increased. Likewise, moving the taps to a larger section of R1 decreases I_c. Instead of physically moving the connections along R1, a low-thermal, low-resistance switch can be installed in the simulator to achieve the same effect.

The hybrid simulator is identical to the passive simulator except that it has a temperature-control circuit to maintain the diode Z1 at a nearly constant temperature. Thus, the temperature dependence of the hybrid simulator is significantly reduced.

2.2 Passive and Hybrid Simulator Design Considerations

When designing the passive simulator, care was taken to reduce unwanted effects of high self-inductance and power dissipation. The resistor R1 in Fig. 1 is made of manganin resistance wire (or a strip, for high current applications) and dissipates most of the power drawn from the current supply. It is therefore kept outside the simulator box, and away from the other circuit components to reduce thermoelectric voltages. In addition to physically separating R1 from the rest of the circuit, the parallel current branch was connected using manganin wire soldered to R1. These contacts also aided in reducing thermoelectric voltages. Regions of the circuit that are not subject to wide temperature variations use copper wire.

To further reduce thermoelectric effects, lead-shot bags (cloth bags containing lead-shot) were placed upon the R2-R3-Z1 circuitry, thus keeping each of these elements at nearly the same (but not necessarily constant) temperature. Thus, temperature gradients due to the heat from resistor R1 or

the environment were reduced within the circuit. The voltage taps were constructed with continuous twisted 14 AWG copper wire to reduce thermoelectric effects. Also, as standard practice, the connections to the voltmeter inputs were thermally shielded using lead-shot bags.

Table 1 shows the resistance specifications for the active, hybrid, and passive simulators. The active simulator's resistances will be discussed in Sec. 2.4. Resistors R1, R2, and R3 are defined as the resistance between their respective voltage taps. Resistor R4 is defined as the total distributed resistance in the parallel circuit branch. The 6th column of Table 1 is the ratio of R2 to R3, the significance of which will be discussed in detail later.

The values of R2, R3, and R4 were chosen to result in an n versus V characteristic that peaks in the region of 1 to 10 μV, which is the region of interest in superconductor characterization. The n-value is typically 25 for the passive and hybrid simulators. The small value of R3 was chosen to better approximate the impedance of a superconducting sample. However, an extremely small value of R3 would result in diode self-heating, since a larger current would be required to achieve the same signal level. The voltage tap separation on R2 was chosen such that the included resistance was about 100 times the resistance between the taps on R3, as indicated on Table 1.

To reduce the simulator's temperature dependence, resistors R1, R2, R3, and R4 were made of manganin wire, whose resistance has a low temperature dependence. The parallel branch connection wires were also made of manganin (part of the distributed resistance R4). Thus, most of the temperature variation of the simulator could be attributed only to the diode. This dependence was on the order of 0.3% change in I_c per °C.

The resistor R1 is bifilar, meaning that it is wound back onto itself so that most magnetic flux lines cancel each other, thus reducing self inductance. High self inductances could lead to frequency dependent simulator characteristics. In this case, the simulator's critical current would vary with measurement method.

In superconductors, a mutual inductance exists between the specimen and the specimen voltage taps due to the area enclosed between the specimen and the voltage tap leads. Although this inductance is unavoidable, it can be reduced by minimizing the area subtended by the voltage taps and the conductor. To emulate this mutual inductance, the main current branch and the voltage taps from the parallel current branch are brought into close proximity of one another. This inductive coupling cannot be achieved through the side of a conductive box; they must be in close proximity within the simulator's box or coupled through an insulating side of the box. This coupling is shown on Fig. 1 indicated by M. To model both high and low mutual inductance scenarios, two different voltage tap connections were made: one connection contained the coupling to the main current branch, while the other did not.

The mutual inductance becomes very noticeable when using the pulse current measurement method. The magnitude of this mutual inductance was chosen to approximate typical values observed in superconductor measurements. The low-inductance lead was included in the simulator design to provide a more "ideal" test device to be used to separate possible inductive effects in the measurement system or method.

Since one function of the passive simulator is to compare the I_c results obtained from two different measurement methods, it is important to distinguish between variations in I_c due to either the intrinsic properties of the simulator or the measurement apparatus. In some situations, variations in n and I_c are due to the measurement apparatus. This was investigated by measuring the voltages across R2 and R3, and determining critical cur-

Table 1. Resistance values for the simulators

Simulator	Input R, mΩ	R1, Ω	R2, Ω	R3, mΩ	R2/R3	R4, Ω
Passive, 2 A	N/A	0.349	3.12	31.3	99.36	2.53
Passive, 25 A	N/A	0.304	3.25	32.4	100.29	2.27
Passive, 50 A	N/A	0.160	3.25	32.4	100.29	2.27
Hybrid, 2 A	N/A	0.347	3.49	34.6	100.84	2.09
Active, 0.5 A	100.	N/A	100.2	1004	99.75	N/A
Active, 50 A	1.00	N/A	100.2	1004	99.75	N/A
Active, 500 A	0.100	N/A	100.2	1004	99.75	N/A
Active, 3000 A	0.0167	N/A	100.2	1004	99.75	N/A

rents for each measurement. Since the two resistors differ by a factor of about 100, the signal magnitude was about 100 times greater at R2. Uncertainties in the correct I_c at low criteria using R3 were virtually eliminated by using the signal on R2. Thus, a lack of precision in I_c at low criteria could be attributed to the inability of the apparatus to measure low voltages accurately, not an intrinsic instability of the simulator at these signal levels.

In order to make direct comparisons between critical currents at various electric field criteria, artificial "lengths" were attributed to resistors R2 and R3. The signal strength at R2 is about 100 times greater than R3, so appropriate lengths had to be chosen to normalize the electric fields at these resistors. Since typical voltage tap separations are on the order of 1 to 100 cm on superconducting samples, the voltage taps on R2 have a length of about 100 cm associated with them, while the taps on R3 have a length of 1 cm. Thus, the "electric fields" at these voltage taps are equivalent at a given current.

An experimenter may want to use the passive simulator as a test device instead of a reference device. In this case, the simulator could be designed to have several different critical currents depending on a switch setting. Since this may lead to additional variability in I_c, a reference device will most likely have only one value of I_c, as well as a fuse to protect it from over-current damage.

2.3 Active Simulator Operation

The active simulator is not driven directly by the output of the current supply. Instead, its input is taken from the current supply's shunt resistor. The shunt resistor serves the same function as R1 in the passive simulator. Thus, the critical current of the simulator is simply the current at which the shunt resistor reaches some target voltage. For example, if a current supply has a 50 mV shunt, then one critical current would be that current required to generate 50 mV across the shunt. Therefore, if the current required to generate 50 mV is 100 A, the critical current is 100 A. This design feature makes the active simulator a versatile component of a measurement system.

2.4 Active Simulator Design Considerations

The active simulator does not emulate the subtle effects of a superconductor; it is meant for use as a circuit that generates various values of n and I_c. The circuit diagram for the active simulator is shown in Fig. 5. The active simulator circuit consists of 3 stages: two cascaded operational amplifiers (op-amps), and an output stage consisting of a Zener diode and resistors that simulate the sample voltage.

The first stage of the circuit is a differential amplifier that amplifies the input signal coming from the current supply's current-shunt resistor. To obtain different values of I_c with a given shunt resistor, the amplification of this stage is changed with a two-pole switch. Therefore, it is possible to obtain a lower (or higher) critical current for a given shunt resistor. Typical input signal values are: 20, 30, and 50 mV. The higher the amplification, the smaller the critical current.

The second stage of the circuit is a non-inverting amplifier that, in conjunction with the diode, generates different values of n for a given I_c. The two-pole n-switch changes two resistance values to allow the n-value to be changed without significantly affecting I_c. As the switch decreases the feedback resistance, the gain is decreased and thus the n-value is decreased.

In order to maintain nearly the same critical current with a different value of n, the reference voltage of the non-inverting amplifier must be changed (the second pole of this switch). Through an iterative process, values of n and appropriately adjusted reference voltages were determined so that the critical currents at a given sample voltage were approximately the same. A target sample voltage of approximately 120 μV across R3 was selected. Figure 6 is a full logarithmic plot of V versus I for the active simulator for one I_c setting and 8 different n values. Notice that the curves intersect near the target voltage of 120 V. The eight curves in Fig. 6 correspond to the eight n-value adjustment switch settings on Fig. 5. The highest n-value (about 140) corresponds to the open switch setting.

The third stage consists of the Zener diode, and the current-limiting resistor R2, and the sample voltage resistor R3. These provide the same function as the passive simulator. Unlike the passive simulator, however, there is no provision for high mutual inductance on these voltage taps.

Table 1 indicates typical shunt resistances for the 0.5, 50, 500, and 3000 A active simulators. These resistances were calculated on the basis of a 50 mV input signal. The input terminals of the active simulator are connected across the shunt resistor. The values of R4 are not applicable here, since discrete resistors were used instead of distributed wire resistors.

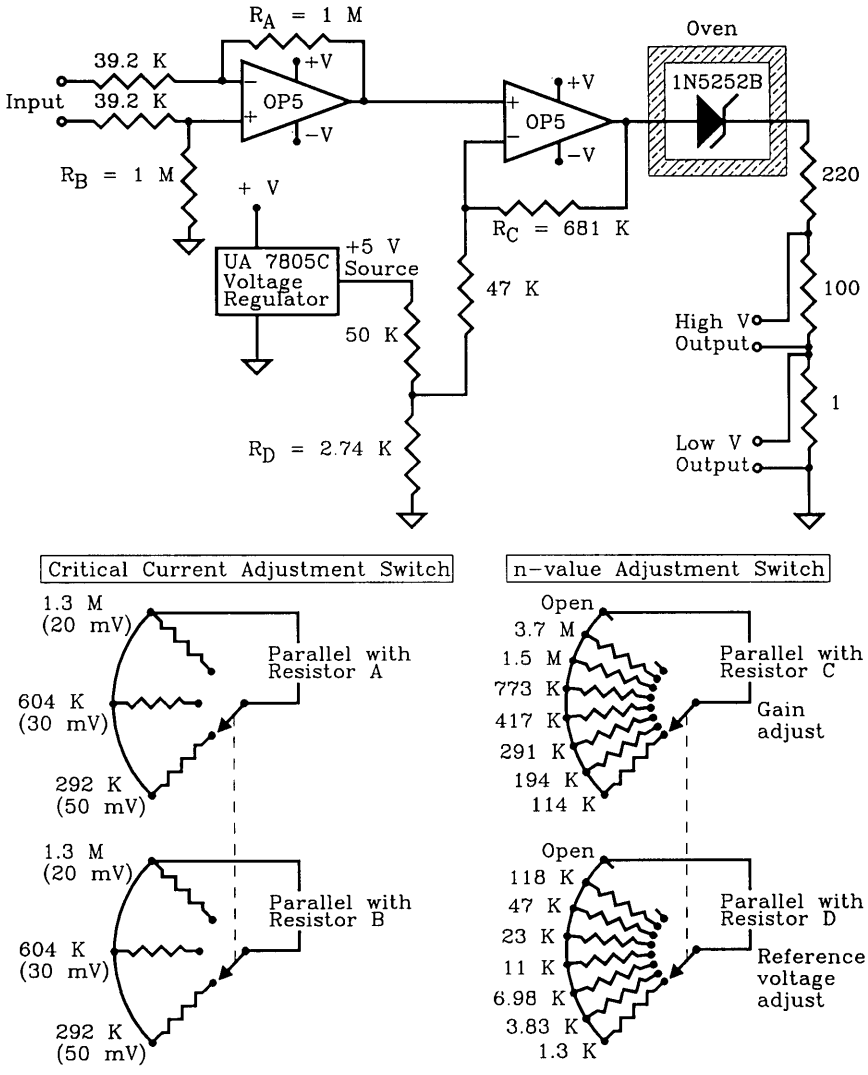

Figure 5. Circuit diagram of the active simulator along with diagrams of the critical-current adjustment switch and the *n*-value adjustment switch.

3. Data Acquisition and Analysis

The superconductor simulators described here can be used to establish the integrity of a superconductor data acquisition system. This section gives a brief overview of the acquisition system that was used in conjunction with these simulators. This information is given to specify the way that these simulators were characterized. It is by no means the only system that can be used with the simulators. For a full discussion of various superconductor measurement systems, consult Refs. [3,5].

Measurement systems can vary in complexity from a simple analog recorder that monitors the voltage-current characteristic, to a sophisticated computerized data-acquisition system that monitors several additional experimental parameters. The choice of measurement system depends on considerations such as the number of samples to be measured, accuracy and precision requirements, and the number of experimental parameters that need to be monitored.

3.1 Data Acquisition System

One motivation for designing the simulators was to determine the integrity of the data-acquisition system described here, and to study the effects of current ripple on superconductor measurements [6]. This system is computer controlled and relies

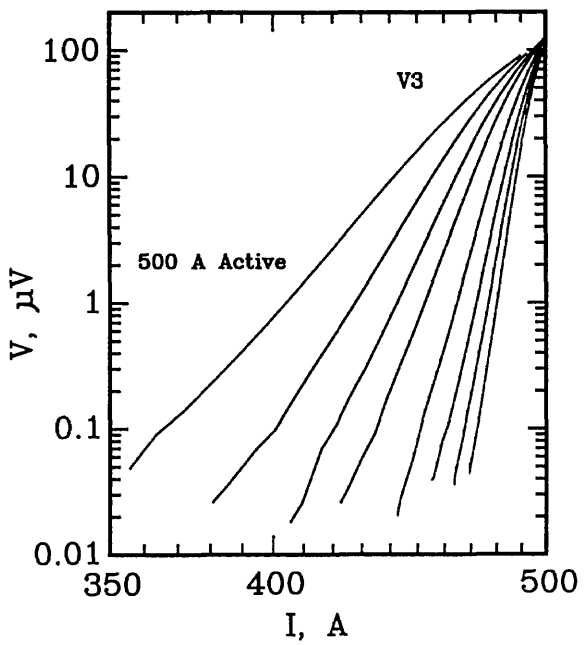

Figure 6. Full logarithmic plot of voltage versus current for the 500 A active simulator. Each curve corresponds to a different setting of the n-value switch in Fig. 3. The n-values range from about 25 to 144. These curves converge near 120 μV.

on analog or digital voltmeters[1] to make voltage and current measurements. The system is capable of monitoring magnetic field, sample temperature, and other important experimental parameters.

The step-and-hold-current method was used to determine the critical current of the superconductor simulator. As the name suggests, the sample current is abruptly increased to a preset level, and held at that level while the sample voltage and current are measured. From that level, the sample current is again abruptly increased to another preset level and held. This cycle is repeated until a preset current limit or voltage limit is reached.

The preset current levels, or current setpoints, are determined to maximize the characterization of the entire V-I curve. The curve is divided into two regions: a low-current/low-voltage region, and a high-current/high-voltage region. In the low-current region, the setpoints are chosen to be equally spaced on a linear scale. In the high-current regions, the current setpoints are chosen to correspond to voltages that are equally spaced on a logarithmic scale. The current setpoint that divides the low-current region from the high-current region corresponds to a sample voltage that is just below the voltage noise level.

Table 2 contains current setpoints for n-values of 25, 58, and 122. These setpoints are listed as percentages of I_{24}, which is the current at the 24th setpoint. This current corresponds to a guessed value of the maximum current.

Table 2. Target voltages and current setpoint patterns for three n-values

Setpoint #		V_{tar} (μV)	% of I_{24} $n=25$	% of I_{24} $n=58$	% of I_{24} $n=122$
1			0.0	0.0	0.0
2			11.7	14.3	15.5
3	Equal		23.5	28.7	31.0
4	ΔI		35.2	43.0	46.5
5			47.0	57.3	62.1
6			58.7	71.7	77.6
7	Transition	0.004	70.5	86.0	93.1
8	region	0.008	73.1	87.4	93.8
9		0.018	75.9	88.8	94.5
10		0.032	77.3	89.5	94.9
11		0.056	78.7	90.2	95.2
12		0.100	80.2	90.9	95.6
13		0.180	81.7	91.6	95.9
14		0.320	83.2	92.4	96.3
15		0.560	84.8	93.1	96.7
16	Equal	1.000	86.3	93.8	97.0
17	$\Delta\log(V)$	1.800	87.9	94.6	97.4
18		3.200	89.5	95.3	97.8
19		5.600	91.2	96.1	98.1
20		10.00	92.9	96.9	98.5
21		18.00	94.6	97.6	98.9
22		32.00	96.4	98.4	99.3
23		56.00	98.2	99.2	99.6
24		100.0	100.0	100.0	100.0
25	Zero check		0.0	0.0	0.0

Setpoints 1 through 6 in Table 2 correspond to the low-current region of the V-I characteristic, and are equally spaced on a linear scale. Setpoints 7 and 8 correspond to the transition region from low currents to high currents. Setpoints 9 through 24 correspond to equally spaced voltages on a logarithmic scale. Setpoint 25 is for a zero current measurement of voltage for thermal corrections. This pattern is illustrated on Figs. 2, 3, and 4. The symbols along the curves indicate the individual setpoints. The lowest non-zero current point deviates from this pattern because of the turn-on characteristics of the current supply. Otherwise, the points illustrate this pattern. The 24th point is off the scale of Figs. 2 and 3.

[1] Certain commercial equipment, instruments, or materials mentioned in this paper might be indirectly identified by their particular properties. Such identification does not imply recommendation or endorsement by the National Institute of Standards and Technology, nor does it imply that the materials or equipment identified are necessarily the best available for the purpose.

To determine the critical current after a *V-I* curve is obtained, an electric field criterion is applied to the characteristic. For a complete discussion of critical current measurement methodology, consult Refs. [1,3].

3.2 Role of the Simulator in Data Acquisition Systems

In general, the more sophisticated the acquisition system, the more testing it must undergo to establish its integrity. Thus, the computer-controlled system discussed above must be exhaustively tested.

The simulator is an idealization of a superconductor's electrical characteristics: the *V-I* curve, thermoelectric voltages, and mutual inductances. It can therefore be used to test a measurement system's integrity under various experimental conditions. For example, to determine the integrity of the measurement system under conditions of high mutual inductance, an experimenter would use the high inductance terminals of the simulator; for high thermoelectric noise conditions, a lead-shot bag could be removed from the voltage-tap terminals. Similar tests can be performed for low-inductance conditions and other experimental phenomena.

The idealization of the superconductor simulator enables the experimenter to understand the limitations of a particular measurement system and method. With a standard reference material, these limitations may be misinterpreted as properties of the superconductor instead of the measurement system.

Although the simulator provides an expedient test for the measurement system, it does not test the magnet, cryostat, temperature controller, or other similar devices. A standard reference material is best suited for testing these components. There are events such as sample motion, contact heating, early quenches, and irregular or unstable *V-I* characteristics that are not emulated by these simulators. Such phenomena may be emulated in future designs.

3.3 Systematic Errors in Data Analysis

The empirical model of a superconductor's *V-I* characteristic given in Eq. (1) is a simple approximation to the actual characteristic. Systematic errors arise from this approximation, and could be avoided by using a more sophisticated model. For example, a least-squares power-series representation of the *V-I* characteristic could be used as long as there are not too many adjustable parameters.

Perhaps the least realistic aspect of the empirical model is the constancy of n in Eq. (1). In general, n changes along the *V-I* curve of a real superconductor, so a more sophisticated model would take this into account. The approach used in this analysis routine to allow for variations in n is to divide the non-zero portion of the *V-I* curve into overlapping intervals, fitting the *V-I* points in each interval, and calculating a value of n for each interval. Thus, to determine I_c at various criteria, one would use the fit parameters that corresponds to that criterion.

The intervals that were used with these simulators are given in Table 3. The first column of Table 3 contains the electric field criterion that would be used to determine a critical current. The following two columns contain the upper and lower limits of the electric field window. The initial and terminal points of each interval are somewhat arbitrary in this model. These values are not necessarily optimal, but are included here for completeness. They were selected based on the noise level of the system and on a compromise between accuracy and precision. The last column indicates the ratio of the upper limit to the lower limit. This ratio monotonically decreases with increasing electric field criterion, in order to include more data points in electric field intervals where the signal-to-noise ratio is small.

Table 3. Electric field windows used in computer aided data analysis

E_c criteria (μV/cm)	E_c top (μV/cm)	E_c bottom (μV/cm)	Ratio = top/bottom
0.1	1.5	0.06	25
0.2	2.4	0.12	20
0.5	3.6	0.20	18
1.0	5.0	0.30	17
2.0	8.0	0.60	13
5.0	15.0	1.50	10
10.0	21.0	3.00	7
20.0	50.0	10.0	5
50.0	100.0	20.0	5
100.0	140.0	28.0	5

The critical current at a specified electric field is determined by interpolating the current to that criterion using the appropriate value of n and the constant $V_o/(I_o)^n$. Systematic errors were found to be on the order of 0.1% at a criterion of 0.1 μV/cm when using this method. At criteria of 1 μV/cm and

above, these errors were almost undetectable. In order to increase precision in I_c determinations, more points along the *V-I* curve could be used, but that would increase the systematic error since then a larger portion of the curve would be used in the calculation. This tradeoff must be taken into consideration when developing data analysis software.

Another technique to more accurately characterize the *V-I* curve is to perform a polynomial fit in n. An expression of this form would characterize the *V-I* curve, but it may not be applicable for a range of materials, temperatures, or magnetic fields.

4. Superconductor Simulator Performance

A systematic study of various electrical characteristics of the passive, active, and hybrid simulators was performed, and the results are shown below. These studies included a characterization of I_c versus temperature, I_c versus time, n versus V, effects of inductance on I_c, and effects of current magnitude and current ripple on simulator characteristics.

4.1 Temperature Dependence of I_c

The critical current of a superconductor is a strong function of temperature. For example, for the standard reference material SRM 1457 (Cu/Nb-Ti), a 21.2% change in I_c per K is observed at an applied field of 2 T. At higher fields, this temperature dependence is amplified. For example, at 8 T, the temperature coefficient is approximately 62% per K. This level of temperature dependence makes testing the measurement system with the SRM a challenging task. The superconductor simulator, however, has a temperature coefficient on the order of 0.3% per K. Figure 7 shows the percent difference of the measured critical current on R3 from a linear fit of critical currents over a temperature interval of 10 °C near room temperature. As this figure indicates, most of the 0.1 μV/cm data lies within ±0.4% of the fit line and within ±0.1% for 1.0 μV/cm. Higher electric field criteria have even less variability. If the critical currents were measured on R2, the uncertainty reduces to less than ±0.1% of the fit line for all electric field criteria, indicated on Fig. 8. Thus, the simulator is superior to the SRM for testing the system for repeatability in I_c measurements, even after taking the variability in room temperatures and liquid helium temperatures into account.

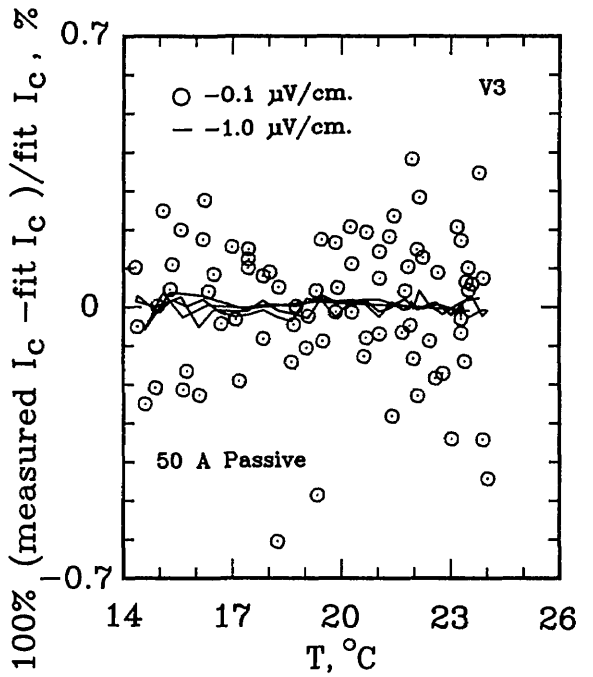

Figure 7. Difference from linear temperature fit for the 50 A ($n \approx 25$) passive simulator. Data obtained using R3, 80 points used in the fit.

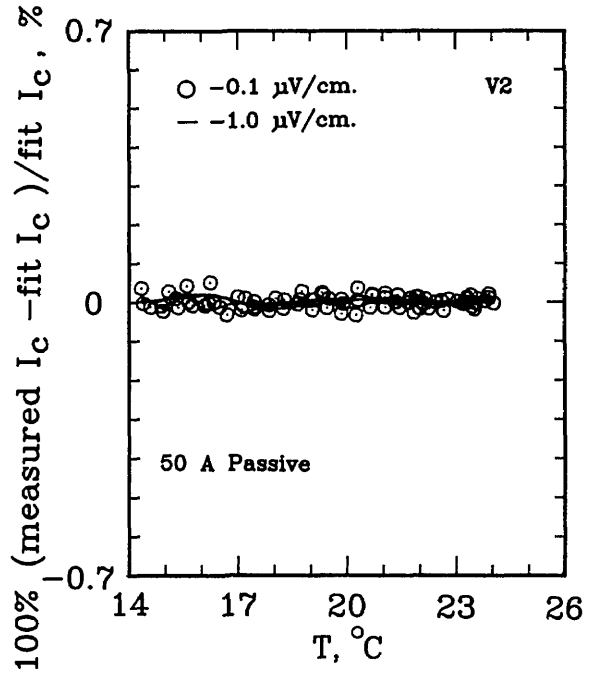

Figure 8. Difference from linear temperature fit for the 50 A ($n \approx 25$) passive simulator. Data obtained using R2, 80 points used in the fit.

Tables 4 and 5 show critical-current temperature coefficients for the active, passive, and hybrid simulators at various electric field criteria as characterized by:

$$I_c = b + m \cdot T \qquad (3)$$

where I_c and b are in A, m is in A/°C, and T is in °C. Table 4 contains data for the active simulator, while Table 5 contains data for the passive and hybrid simulator. Each linear fit used between 40 and 120 points. Each data set contained points taken with both increasing and decreasing temperature. There was no significant hysteresis with direction of temperature sweep for temperature rates-of-change as large as 3 °C/h. The temperature range of each set was not identical, but they were all near room temperature. Because the temperature range did not include 0 °C, comparisons of I_c were not made 0 °C (using just b), but at a temperature of 23 to 26 °C. The first and second columns identify the simulator and typical electric field criteria, while the following two columns give values of b and m at those criteria. The 5th and 6th columns show the standard deviation from the fitted line for R2 and R3, respectively.

Table 4. Coefficients of temperature variation for active simulators at various electric field criteria using V2, along with coefficients of variation for the critical currents determined using V2 and V3, and % difference in critical currents determined using V2 and V3

Simulator	Criteria (μV/cm)	b (A)	m (A/°C)	dev I_c (V2) (%)	dev I_c (V3) (%)	ΔI_c (%)
Active, 0.5 A	0.1	0.3680	-1.06×10^{-5}	0.007	0.185	−0.080
50 mV, $n=25$	1.0	0.4047	-1.08×10^{-5}	0.006	0.020	−0.001
40 points	10.0	0.4423	-1.19×10^{-5}	0.005	0.006	0.000
23.6–27.9 °C	100.0	0.4944	-1.01×10^{-5}	0.006	0.006	0.001
Active, 0.5 A	0.1	0.4354	-1.74×10^{-5}	0.005	0.083	−0.052
50 mV, $n=58$	1.0	0.4535	-2.03×10^{-5}	0.005	0.010	−0.004
40 points	10.0	0.4718	-1.99×10^{-5}	0.005	0.005	−0.001
24.2–27.9 °C	100.0	0.4970	-2.47×10^{-5}	0.008	0.008	0.000
Active, 0.5 A	0.1	0.4688	-3.35×10^{-5}	0.005	0.040	−0.026
50 mV, $n=122$	1.0	0.4776	-2.68×10^{-5}	0.003	0.005	−0.001
40 points	10.0	0.4869	-3.42×10^{-5}	0.004	0.004	0.000
25.4–27.4 °C	100.0	0.4995	-3.41×10^{-5}	0.007	0.007	0.000
Active, 50 A	0.1	43.582	-3.53×10^{-3}	0.012	0.079	−0.009
50 mV, $n=58$	1.0	45.371	-3.42×10^{-3}	0.005	0.010	0.002
120 points	10.0	47.203	-3.56×10^{-3}	0.005	0.005	0.001
20.9–27.4 °C	100.0	49.726	-3.76×10^{-3}	0.019	0.019	0.001
Active, 500 A	0.1	435.96	-4.57×10^{-2}	0.008	0.085	−0.037
50 mV, $n=58$	1.0	453.76	-4.12×10^{-2}	0.005	0.011	−0.002
40 points	10.0	472.01	-3.98×10^{-2}	0.005	0.005	0.000
19.5–25.9 °C	100.0	496.99	-3.24×10^{-2}	0.006	0.006	0.000
Active, 3000 A	0.1	2597.1	$+9.12\times10^{-2}$	0.031	0.081	−0.017
50 mV, $n=58$	1.0	2706.4	$+5.77\times10^{-2}$	0.023	0.025	0.000
40 points	10.0	2821.7	-8.98×10^{-2}	0.017	0.017	0.000
20.2–26.1 °C	100.0	2978.9	-1.55×10^{-1}	0.012	0.012	0.000
Active, 0.2 A	0.1	0.1749	$+4.38\times10^{-6}$	0.011	0.075	−0.030
20 mV, $n=58$	1.0	0.1822	$+7.70\times10^{-7}$	0.009	0.013	−0.005
40 points	10.0	0.1895	$+7.25\times10^{-7}$	0.011	0.010	−0.003
24.7–26.6 °C	100.0	0.1996	$+4.10\times10^{-6}$	0.016	0.016	−0.002
Active, 0.3 A	0.1	0.2612	$+9.93\times10^{-6}$	0.011	0.069	−0.013
30 mV, $n=58$	1.0	0.2721	$+6.51\times10^{-6}$	0.009	0.012	−0.004
40 points	10.0	0.2831	$+1.66\times10^{-6}$	0.008	0.008	−0.001
24.4–28.8 °C	100.0	0.2988	-1.91×10^{-5}	0.012	0.013	0.000

Table 5. Coefficients of temperature variation for the hybrid and passive simulators at various electric field criteria using V2, along with coefficients of variation for the critical currents determined using V2 and V3, and % difference in critical currents determined using V2 and V3

Simulator	Criteria (μV/cm)	b (A)	m (A/°C)	dev I_c (V2) (%)	dev I_c (V3) (%)	ΔI_c (%)
Hybrid, 2 A	0.1	1.6200	$+1.30\times10^{-5}$	0.008	0.162	0.225
120 points	1.0	1.8006	$+1.12\times10^{-5}$	0.007	0.020	0.027
19.6–26 °C	10.0	1.9864	$+1.10\times10^{-5}$	0.005	0.006	0.003
	100.0	2.2150	$+2.39\times10^{-5}$	0.012	0.012	0.000
Passive, 2 A	0.1	1.8476	-6.18×10^{-3}	0.024	0.262	−0.076
120 points	1.0	2.0047	-5.56×10^{-3}	0.013	0.030	−0.011
14.2–29.0 °C	10.0	2.1680	-4.96×10^{-3}	0.009	0.010	−0.005
	100.0	2.3804	-4.46×10^{-3}	0.013	0.013	−0.004
Passive, 25 A	0.1	20.982	-6.67×10^{-2}	0.013	0.182	−0.097
80 points	1.0	23.042	-6.38×10^{-2}	0.012	0.021	−0.008
13.8–24.2 °C	10.0	25.017	-5.74×10^{-2}	0.008	0.008	−0.001
	100.0	27.473	-5.14×10^{-2}	0.009	0.009	−0.002
Passive, 50 A	0.1	41.098	-1.31×10^{-1}	0.017	0.186	−0.110
80 points	1.0	45.135	-1.26×10^{-1}	0.011	0.020	−0.007
14.3–24 °C	10.0	48.997	-1.13×10^{-1}	0.007	0.007	−0.002
	100.0	53.805	-1.01×10^{-1}	0.014	0.014	−0.003

Table 4 also contains data showing the active simulator's performance with different critical current ranges. For an n-value of 58, critical currents of 0.2, 0.3, 0.5, 50, 500, and 3000 A were obtained, along with the temperature fit parameters b and m for each electric field criterion. The active simulator has an almost negligible temperature dependence, on the order of 0.007% ΔI_c/°C at 1 μV/cm. For a given power supply, different critical currents can be obtained by changing the gain of the first stage of the active simulator circuit.

Although the current characteristic of a diode is exponentially related to temperature, a linear approximation is appropriate since small temperature swings are being considered about a quiescent temperature of 23 °C. No significant departure from linearity was observed for temperature ranges of approximately 10 °C.

For a given diode, the temperature fit parameters b and m are linearly related to the rated critical current. In Table 5, for example, the 50 A passive simulator and the 2 A passive simulator have a ratio of m-values (and b-values) of approximately 25, which is the ratio of the rated critical currents. Since the critical currents are inversely related to the input resistor R1, this ratio scales inversely with R1.

Table 5 also shows that the temperature dependence of the passive simulator is small. For example, for the 2 A passive simulator at a signal level of 1 μV/cm, the temperature dependence is on the order of 0.27% ΔI_c/°C. For the hybrid simulator, this dependence is less than 0.001% ΔI_c/°C. The hybrid simulator has a lower temperature dependence than that of the active simulator because the active simulator has more components (operational amplifiers, resistors) outside the temperature controlled oven.

The last column shows a percentage difference in critical current between the voltages at R3 and R2, normalized with respect to the voltage at R2. At higher electric field criteria, this difference is significantly reduced. For the passive and hybrid simulators, the difference in I_c at 1 μV/cm between V3 and V2 was about 0.01%. These values were generally less than the standard deviation of the temperature dependence of V3 about the fit line. For the active simulator, these differences were typically 0.005%. This smaller value is due, in part, to the higher value of n for the active simulator.

Figures 9 and 10 show the percent difference of the measured critical current on R3 from a linear fit of critical currents over a temperature interval of 6–7 °C for the 50 A active simulator and the 2 A hybrid simulator. The data scatter on Fig. 9 is slightly less than that in Fig. 10 because of the higher n-value of the active simulator: the active simulator is set at $n=58$ for Fig. 9, whereas the hybrid simulator has an n of 25 in Fig. 10. This lower scatter is due to the fact that the same voltage error results in a smaller change in I_c for a curve with a higher n-value.

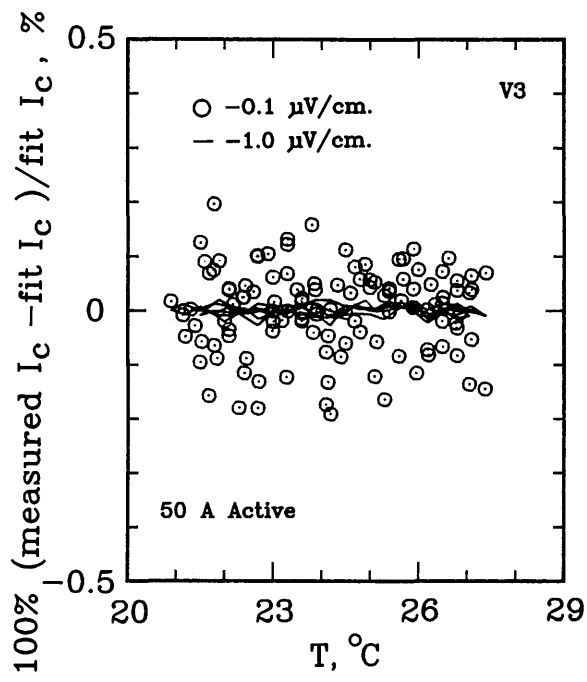

Figure 9. Difference from linear temperature fit for the 50 A ($n \approx 58$) active simulator. Data obtained using R3, 120 points used in the fit.

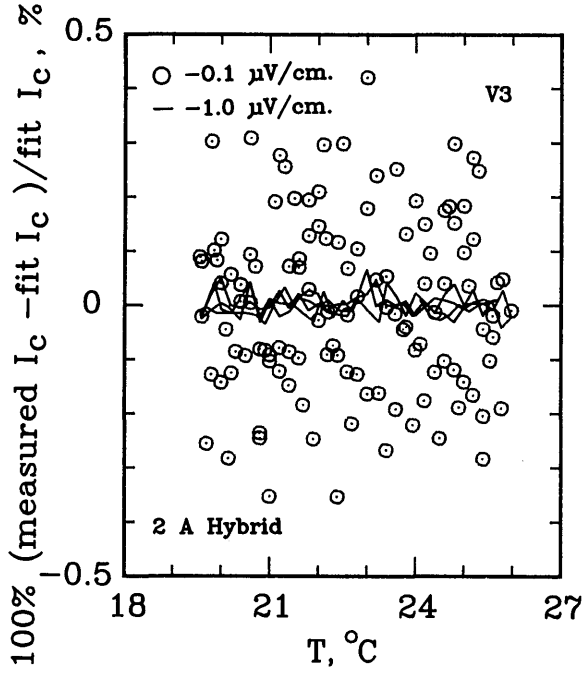

Figure 10. Difference from linear temperature fit for the 2 A ($n \approx 25$) hybrid simulator. Data obtained using R3, 120 points used in the fit.

This is further illustrated in the active simulator data shown in Table 4. The first three sets in Table 4 have the same I_c but three different n-values: 25, 58, and 122, respectively. The coefficients of variation reduce with increasing n. Thus, the higher the n-value, the greater the precision possible in critical-current measurements.

4.2 Low-Voltage Data

An experiment was performed to establish the precision and accuracy of the simulator at lower electric field criteria. A comparison of the performance of analog and digital voltmeters was also made.

The dual-voltage-tap feature implemented in these simulators has a broad range of applications. For example, these taps could be used to compare the measurement precision of analog and digital voltmeters. In this experiment, the analog meter could be connected to the low voltage taps R3 (voltage signal V3), and the digital meter to the high voltage taps. Because of the relative signal size, a less sensitive device can be used on R2 (voltage signal V2). This experiment was conducted, and the resultant data is shown in Table 6. The analog voltmeter was able to accurately measure small voltages with an uncertainty of 2 nV (standard deviation about 3 nV). The digital voltmeter uncertainty is on the order of 10 nV (standard deviation about 27 nV).

Tables 6 and 7 show the temperature coefficients for the 50 A passive simulator at low electric field criteria. Table 6 contains data which were taken using a digital nanovoltmeter on R2 (the high voltage tap, V2), and an analog nanovoltmeter on R3 (low voltage tap, V3). The data on Table 7 were taken using digital nanovoltmeters on both taps. Comparing the data taken on R3 for the digital voltmeter and the analog voltmeter shows that the coefficients of variation differ by a factor of 3. This is not as large as the ratio of the noise levels of the two meters because the method of curve fitting reduces the effects of noise. The accuracies indicated by the ΔI_c in the last column are about the same for the two systems. This indicates that higher noise levels do not severely compromise accuracy. With signals of 1 μV or more, the digital meter and the analog meter have similar responses.

4.3 Stability of I_c over Time

The stability of the simulators' characteristics is crucial for their use as reference devices. Thus,

Table 6. 50 A passive simulator temperature coefficients at low electric field criteria using V2, along with coefficients of variation for the critical currents determined using V2 and V3, and % difference in critical currents determined using V2 (digital nanovoltmeter) and V3 (analog nanovoltmeter)

Simulator	Criteria (μV/cm)	b (A)	m (A/°C)	dev I_c (V2) (%)	dev I_c (V3) (%)	ΔI_c (%)
Passive, 50 A	0.01	36.775	-1.41×10^{-1}	0.051	0.749	0.099
40 points	0.10	41.154	-1.36×10^{-1}	0.019	0.089	0.010
18.9–28.3 °C	1.00	45.146	-1.25×10^{-1}	0.009	0.010	−0.001

Table 7. 50 A passive simulator temperature coefficients at low electric field criteria using V2, along with coefficients of variation for the critical currents determined using V2 and V3, and % difference in critical currents determined using V2 (digital nanovoltmeter) and V3 (digital nanovoltmeter)

Simulator	Criteria (μV/cm)	b (A)	m (A/°C)	dev I_c (V2) (%)	dev I_c (V3) (%)	ΔI_c (%)
Passive, 50 A	0.01	36.819	-1.43×10^{-1}	0.051	1.99	−0.082
120 points	0.10	41.150	-1.36×10^{-1}	0.023	0.288	−0.128
16.2–26.2 °C	1.00	45.141	-1.25×10^{-1}	0.010	0.024	−0.004

experiments were performed in order to quantify any differences in critical current over time. Table 8 shows the results of these experiments. The blank spaces in this table indicate data that were unavailable. The change in critical current over a period of 56 d was less than 0.02% for the 2 A hybrid simulator at an electric field criterion of 1 μV/cm. The change in critical current over a period of 106 d was about 0.01% for the 2 A passive simulator at an electric field criterion of 1 μV/cm. Only the critical current of the active simulator seemed to have a finite drift with time at a rate of about 0.016%/month.

The stability of thermoelectric offset voltages with time was characterized, since this can affect the I_c. The passive simulator typically developed an offset voltage of less than 10 nV during the time (~2 min) of a dc measurement of I_c. This is typical of the thermoelectric voltages observed during superconductor testing.

4.4 Effect of Power Supply on Critical Current

The active simulator was designed for use with any dc power supply. Table 9 compares critical currents and their associated shunt voltages for the 50 mV active simulator. All data were taken on R2, with an electric field criterion of 10 μV/cm. The equivalent shunt voltage in this table refers to the voltage across the power supply's input resistor at the rated critical current. Thus, regardless of the actual critical current, the shunt voltage (and hence the input signal to the active simulator) stays within 0.06% of 47.124 mV except for the measurements using the high-current power supply. Most of this 0.06% is a result of the small drift in I_c with time mentioned above.

The larger capacity power supplies exhibited a greater percent difference from the 10 A supply. This is due to the effects of current ripple in these supplies, and is reduced with the introduction of current-ripple filtering, as is shown on the last row of Table 9.

The introduction of current ripple changes the determined critical current. Due to the voltage-current relationship described by Eq. (1), the greater the n-value for a given modulation, the greater the reduction in the determined critical current. The reduction in critical current at a given electric field criterion is a function of the *peak* value of the current ripple, as opposed to the rms value. These effects have been extensively studied, and are discussed in Ref. [6].

Since current ripple is more prevalent in higher-current power supplies, an active current filter was designed and installed in a 3000 A power supply. Current filtering is performed by inverting the ripple component of the signal and adding the inverted component back to the power supply's original signal. In this manner, the current ripple can be reduced by a factor of 8. Typically, the 3000 A power supply's ripple has a peak of 37 A without active filtering. With the active filter, the peak value of ripple is reduced to approximately 4.5 A. A detailed discussion of the 3000 A active current filter of the power supply is given in Ref. [7]. The effect of current ripple in this simulator is quantitatively similar to the effect on a superconductor.

Table 8. Stability of critical currents determined using R2 over time for the hybrid, passive, and active simulators. ΔI_c calculated by 100% $[I_c(\text{day } \#x) - I_c(\text{day } \#1)]/I_c(\text{day } \#1)$

Simulator	Criteria (μV/cm)	$\Delta I_c = 100\%\ [I_c(\text{day } \#x) - I_c(\text{day } \#1)]/I_c(\text{day } \#1)$ (# in parentheses indicates day #x)		
Hybrid	0.1	0.048 (7)	−0.042 (8)	−0.002 (56)
2 A	1.0	0.010 (7)	−0.019 (8)	−0.007 (56)
	10.0			−0.007 (56)
	100.0			−0.008 (56)
Passive	0.1	−0.001 (2)	0.025 (8)	0.042 (106)
2 A	1.0	0.011 (2)	0.009 (8)	0.012 (106)
	10.0	0.000 (2)	0.000 (8)	0.000 (106)
	100.0	−0.002 (2)	0.002 (8)	−0.034 (106)
Passive	0.1	−0.027 (8)	−0.036 (9)	−0.029 (139)
50 A	1.0	0.006 (8)	0.000 (9)	0.002 (139)
	10.0			0.001 (139)
	100.0			−0.035 (139)
Active	0.1	0.000 (6)	−0.062 (69)	−0.042 (104)
0.5 A	1.0	−0.010 (6)	−0.043 (69)	−0.055 (104)
	10.0	−0.016 (6)	−0.041 (69)	−0.055 (104)
	100.0	−0.008 (6)	−0.028 (69)	−0.043 (104)

Table 9. Comparison of the equivalent shunt voltage for an active simulator at a temperature of 26 °C and $n = 58$ using different power supplies. $E_c = 10$ μV/cm, data taken on R2, 50 mV shunt resistor rating

Day #	Power supply rating, A	Input R (mΩ)	I_c ($T = 26$ °C) (A)	Shunt V (mV)	% difference w.r.t #135
135	10 A	100.	0.4712	47.124	0.000
140	10 A	100.	0.4712	47.116	−0.017
178	1000 A	1.	47.111	47.111	−0.027
195	1000 A	0.1000	470.97	47.097	−0.057
196	3000 A	0.0167	2819.3	46.989	−0.286
198	3000 A with filtering	0.0167	2823.3	47.055	−0.146
203	10 A	100.	0.4710	47.105	−0.040
238	10 A	100.	0.4710	47.098	−0.055

According to the models in [6], a peak ripple of 37 A on a direct current of 2819 A in a superconductor with an n-value of 58 would reduce I_c by about 0.3%. These results were in close agreement. The effect of 4.5 A peak ripple should have been about 0.04%, but was slightly larger, at 0.10%. This takes into account the drift of I_c with time. This extra effect may be due to the small spikes from the SCR (silicon-controlled rectifier) that are still present on the supply. The 10 A and the 1 kA current supplies have extremely low current ripple and no SCR spikes. Circuit details for these two supplies are given in Refs. [8,9], respectively.

4.5 Comparison of n-Value between the Simulator and Superconductors

The characteristics of the simulator are comparable to those of both low-T_c and high-T_c superconductors. Typically, "n" in Eq. (1) is used as a quality index for the superconductor. The higher the n, the greater the superconductor filament homogeneity. The active simulator can generate V-I characteristics with a wide variety of n's. For a complete discussion of the quality index n for superconductors and the shape of the V-I curve, consult Refs. [10,11,12].

Three types of superconductors were tested: YBCO thin film, Nb_3Sn, and Nb-Ti. The YBCO is

a high-T_c sample, and the latter two are low-T_c samples. Figures 11 and 12 show the n versus log voltage plots for a YBCO sample at 76 and 4 K, respectively. Figures 13 and 14 are n versus voltage plots for Nb_3Sn and Nb-Ti superconductors. The Nb-Ti sample is the standard reference material SRM 1457. Figure 15 plots n versus voltage for the 500 A active simulator. These eight curves correspond to the eight n-value adjustment switch settings on Fig. 5. At voltages below 0.1 μV, the variation in n is due to limitations in voltage measurements.

Figure 11 plots n-versus voltage for YBCO at 76 K and fields of 0 and 1 T. All measurements were made using the dc method. These values of n lie between approximately 10 and 30. Figure 12 plots n versus voltage for a YBCO sample at liquid helium temperatures and at four magnetic fields, 0, 2, 4, and 10 T. These values of n can be as high as 100.

Figures 13 and 14 show n values between 30–50 for Nb_3Sn (6 and 12 T), and 40–90 for Nb-Ti (4, 6, 8, 9 T), respectively. The increase in value of n at high voltages on Figs. 12 and 14 is due to slight sample heating.

Figure 15 plots n versus voltage for the active simulator using measurements on R3. In this plot,

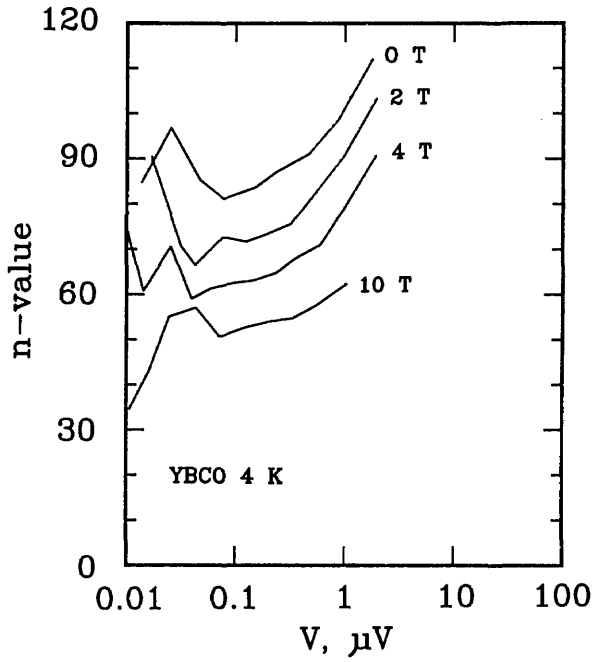

Figure 12. Plot of n-value versus voltage for a YBCO superconductor at 4 K at magnetic fields of 0, 2, 4, and 10 T. The increase in n-value above 1 μV is due to sample heating. The critical currents ranged from 5 to 4 A, the voltage tap separation was 0.3 cm, and the area of the superconductor was 3×10^{-7} cm^2.

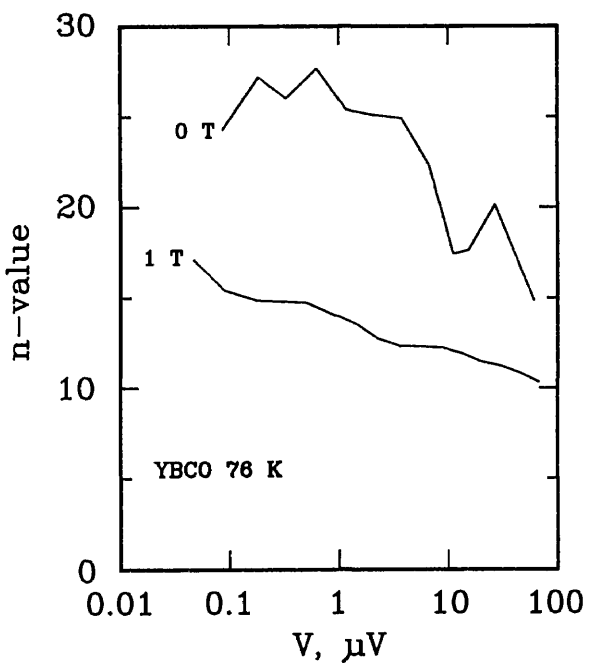

Figure 11. Plot of n-value versus log voltage for a YBCO superconductor at 76 K at magnetic fields of 0 and 1 T. The critical currents ranged from 2 to 0.2 A, the voltage tap separation was 0.5 cm, and the area of the superconductor was 1.5×10^{-6} cm^2.

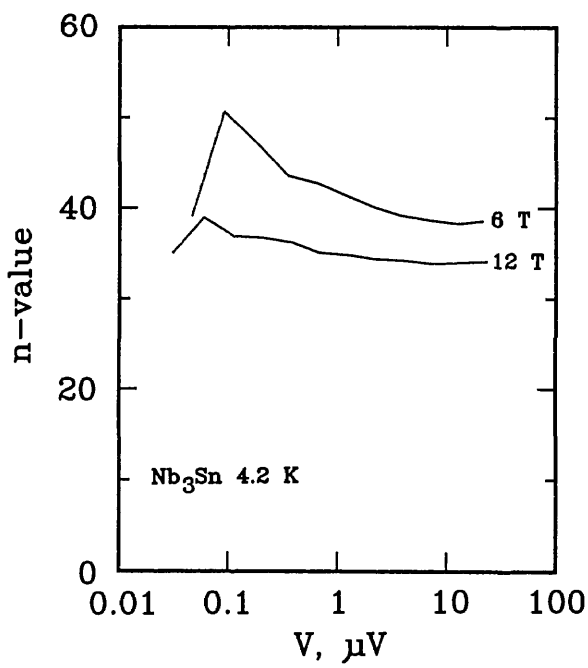

Figure 13. Plot of n-value versus voltage for a Nb_3Sn superconductor at magnetic fields of 6 and 12 T. The critical currents ranged from 500 to 185 A, the voltage tap separation was 16 cm, and the area of the non-copper was 2.9×10^{-3} cm^2.

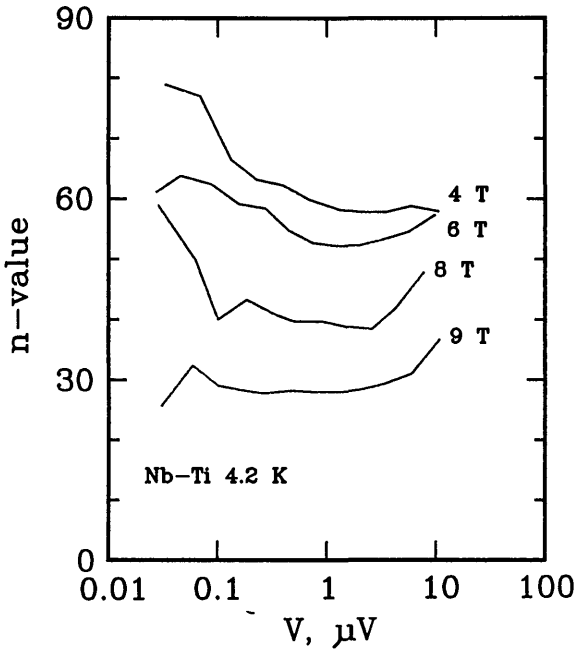

Figure 14. Plot of n-value versus voltage for a Nb-Ti superconductor at magnetic fields of 4, 6, 8, and 9 T. These data were taken on the standard reference material SRM 1457. The critical currents ranged from 200 to 45 A, the voltage tap separation was 15 cm, and the area of the superconductor was 8.3×10^{-4} cm^2.

n was varied using the switch between values of 25 and 150. In the region between 0.1 and 10 μV, the values of n remained relatively constant, as in the case of superconductors. Thus, with this simulator, an experimenter can emulate a substantial range of values of n that are observed in superconductors. In Fig. 15, the highest n-value corresponds to an open circuit setting on the n-value switch on Fig. 5.

Figure 16 plots n versus voltage for the active simulator using voltage measurements on R2 (higher voltage signal). Values of n were inferred from these measurements and were plotted against the corresponding voltage, V3. This was done to illustrate that the actual n of the simulators at low voltages is still a well-behaved function of voltage. The plots of n versus voltage after this were also inferred from R2.

Figures 17 and 18 plots the n versus voltage for the 50 A passive simulator and the 2 A hybrid simulators. Each curve has a peak n-value of approximately 24. The shapes of these curves are representative of those taken on a superconductor if sample heating is not a problem.

4.6 Discussion of Inductance

The mutual inductance between the superconductor and the voltage taps was emulated in the

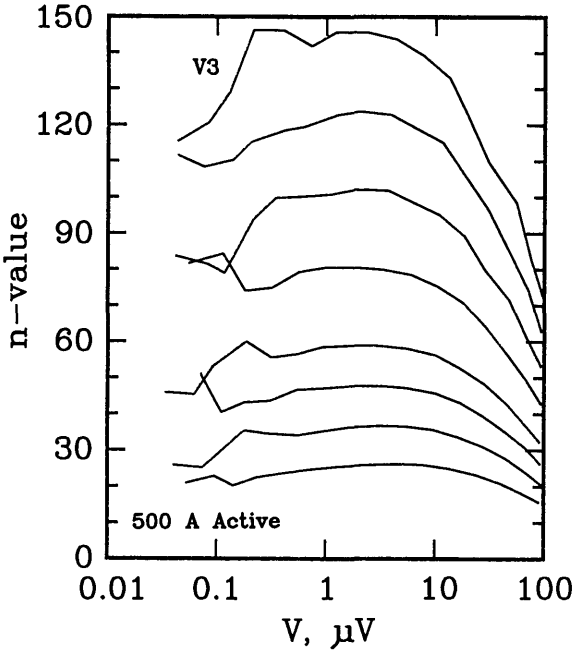

Figure 15. Plot of n-value versus voltage signal V3 for the 500 A active simulator.

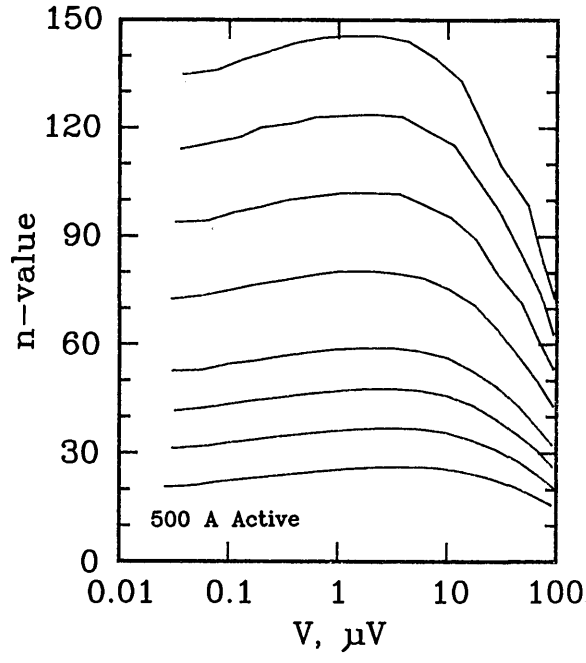

Figure 16. Plot of n-value versus voltage signal V3 for the 500 A active simulator using measurements on R2 (higher voltage signal, V2).

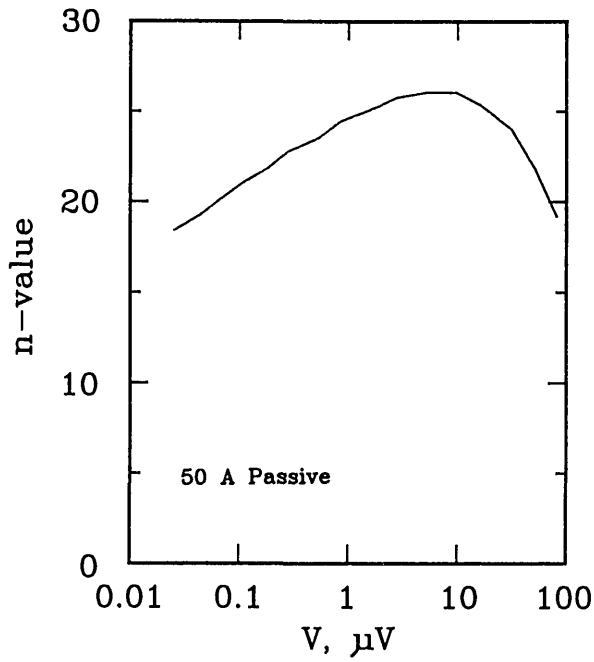

Figure 17. Plot of n-value versus voltage for the 50 A passive simulator.

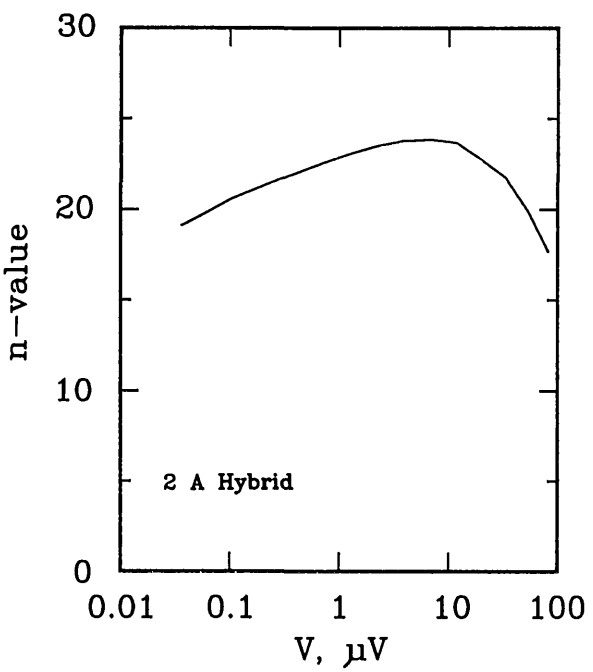

Figure 18. Plot of n-value versus voltage for the 2 A hybrid simulator.

passive and hybrid simulators. In both a superconductor and the simulator, the mutual inductance is approximately 2 nH for voltage taps separated by a few cm. Although this inductance may seem negligible, at ramp rates of 200,000 A/s it translates to a voltage of approximately 400 μV. Ramp rates of this magnitude are typical when using the pulse current technique to measure critical current.

Figures 19 and 20 are plots of the voltage waveform resulting from delivering a current pulse to the passive simulator. Figure 20 is an enlargement of the leading edge of the current and voltage pulses. The voltage spikes at the leading and trailing edges of the voltage waveform on Fig. 19 are due to the mutual inductance of the simulator. The voltage spikes peak near the peak dI/dt. The polarity of the induced voltage with positive dI/dt is the same as the polarity of the resistive transition of the superconductor. This polarity was chosen to test the acquisition and analysis system. The amount by which the measured voltage was different from zero in the low-current portion of the V-I characteristic (where the actual voltage is zero), would indicate the existence of a problem with the induced, ground-loop, or common-mode voltages.

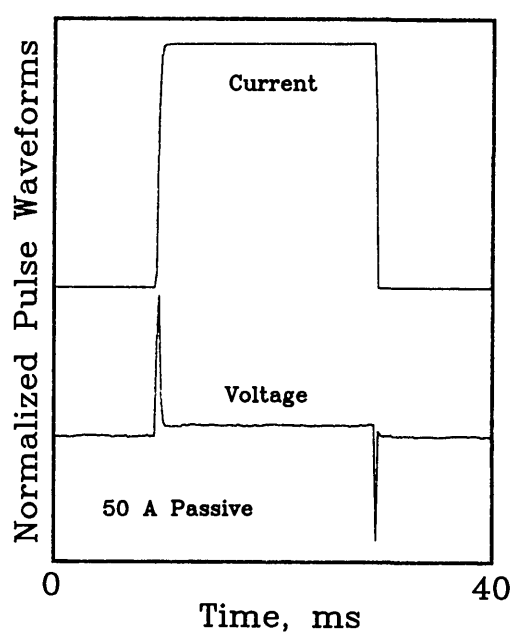

Figure 19. Current and resultant voltage pulses delivered to the 50 A passive simulator. Maximum current = 48.1 A, peak voltage = 180 μV, steady state voltage drop = 20 μV, frequency band pass = dc to 10 kHz. Positive and negative voltage spikes correspond to positive and negative dI/dt.

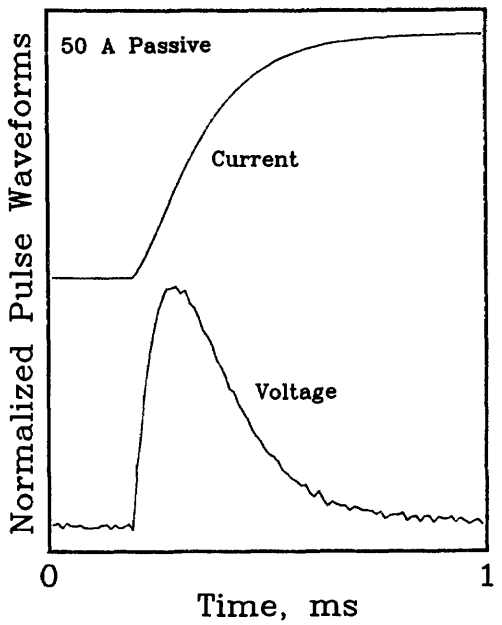

Figure 20. Enlargement of the leading edge of a current and resultant voltage pulse. Maximum current = 45.6 A, maximum dI/dt = 188,000 A/s, peak voltage = 400 μV, frequency band pass = dc to 100 kHz.

5. Discussion

The superconductor simulators discussed here represent an important step in diagnostic test equipment for superconductor measurement systems. These devices can aid the experimenter in determining sources of systematic errors in data analysis routines, data acquisition systems, and other problems in the measurement system. Currently, the simulators emulate the major electrical characteristics of superconductors. In the future, however, the simulators could have additional features added to make them more comprehensive test devices.

Some additional features that could be added to the simulators include a button to increase electrical noise at the voltage taps, current-transfer emulation, simulation of a sample quench, and shifting V-I characteristics.

Electrical noise could be incorporated in the active simulator by introducing a noise generator at the voltage taps. When the appropriate button is pressed, the noise generator signal could be combined with the output voltage. For a passive simulator, instead of a noise generator, an antenna could be used to increase the signal noise level.

The addition of the noise generator signal to the output signal could be done at two locations in the circuit: at the input junction (before the nonlinear circuit elements), or at the output stage (after the nonlinear elements). Inserting the noise component before the nonlinear elements would result in a nonlinear amplification of the noise at the output stage, whereas implementing the noise at the output stage would result in an increase in the quiescent noise level. Current ripple from the current supply in a superconductor can be best emulated by adding the noise signal at the input stage. Either of these implementations may be appropriate depending upon what test is being performed.

To simulate current transfer in the simulator, a large resistor (approximately 25 kΩ) should be added in parallel with the diode. With this addition, the current transfer corrections in the data analysis routines could also be tested.

Sample quenches could be implemented in the simulator by installing a quench detector (a device that interrupts current flow in the event that the sample voltage exceeds a preset voltage-trip point) across resistor R1, and setting the voltage-trip point near or below 0.7 V. Thus, as the current is increased through the simulator, it will be interrupted before the diode starts conducting current, and a null voltage-current characteristic would be obtained.

A "shifting" voltage-current characteristic could be obtained by temporarily short-circuiting resistors R2 and/or R3 or the diode. In this manner, the sample voltage would seem to shift with a steady current ramp.

The overall quality of the active simulator could be improved by exchanging the operational amplifiers in the circuit with instrument-quality amplifiers. Although this would increase the cost of the simulator, the stability, linearity, frequency response, and input impedance of the simulator would probably be favorably affected.

5.1 Uses of the Simulators

The applications for the superconductor simulator range from use as a training aid to a device used in the development of new test methods, to a standard test device used to characterize and identify sources of error within a measurement system. For example, simulators are useful for training experimenters who lack experience in making superconductor measurements. Instead of using expensive superconductor samples, and expending cryogens,

the simulators can be used many times at room temperatures. Thus, inexperienced experimenters can practice measuring the critical current of the simulator and can familiarize themselves with the test apparatus.

Experimenters already familiar with superconductor measurements can use the simulators to develop new measurement systems and methods without consuming actual samples and their associated high costs. The stability of the simulator's *V-I* characteristic over time allows the experimenter to determine sources of variation between the new measurement scheme and standard schemes. The superconductor simulator could be used as a standard test device for interlaboratory comparison of measurement systems and methods. The active and the passive simulators can be used as test devices for the measurement apparatus and measurement method. The simulators can aid in identifying common-mode voltages and ground loops in the pulse method of critical current determination since the lower currents should have no voltage drop.

The accuracy of the simulator is limited by the accuracy of the current-sensing resistors, voltmeters used for current and voltage measurements, and the accuracy of the measurement of room temperature or diode temperature. One distinct advantage of the hybrid and active simulators is that the accuracy of the temperature measurement is not as significant as it is for the passive device. It should also be noted that the calibration of the current-sensing resistor is not tested by the active simulator because of the way in which it gets its input signal. For these reasons, the hybrid simulator may be the best candidate for use as a reference device to compare measurements. The total uncertainty of the hybrid simulator is estimated to be about $\pm 0.2\%$ at 1 μV/cm with the uncertainty of the current sensing resistor being the major source of uncertainty.

6. Summary

The superconductor simulator's electrical characteristics have been extensively investigated. The salient points of these studies are given below:

General Features:

- The simulators can test the integrity of a complex measurement system.
- These simulators exhibit a small temperature dependence, and a small drift with time (less than 0.06% ΔI_c in a 3 month period).
- The variability of these simulators is typically less than 0.1% at a voltage of 1 μV. Large values of n or greater signal levels reduce this variability.
- Each simulator is equipped with two sample voltage taps: R2 passively generates a voltage that is approximately 100 times greater than the signal at R3. The simulators are well behaved at voltages below 0.01 μV.
- Each simulator's response to current ripple is comparable to that of a superconductor.

Passive Simulator:

- Can be used as a superconductor sample substitution box.
- Small number of passive, low-reactance components.
- Critical currents: 2, 25, 50 A.
- n-value: 25.
- Temperature dependence: less than a superconductor, typically about 0.3% ΔI_c/°C at a voltage level of 1 μV.

Hybrid Simulator:

- Can be used as a standard reference device.
- Circuit identical to that of the passive circuit, except the Zener diode is enclosed in a temperature controller.
- Critical current: 2 A.
- n-value: 25.
- Temperature dependence: typically about 0.001% ΔI_c/°C at a voltage level of 1 μV.

Active Simulator:

- Best suited for generating *V-I* characteristics with a wide range of n-values and critical currents.

- Circuitry contains active components such as operational amplifiers.
- Critical currents: 0.5 to 3000 A.
- n-value: 25 to 150.
- Temperature dependence: typically about 0.007% ΔI_c/°C at a voltage level of 1 μV.

7. Conclusions

The superconductor simulator represents a simple answer to the problem of testing a complex measurement system. The simulator does not test effects of sample mounting, magnetic field, temperature control, or other similar experimental factors. However, it isolates effects solely due to the measurement system from all of the effects that can lead to variability in critical current measurements. The exploitation of its capabilities can make a dramatic difference in characterizing the current carrying capacity of low-T_c and high-T_c materials. It allows the experimenter to understand the limitations of a measurement system and the factors that can create errors in the measurement. In many modern computer controlled data acquisition systems, it is imperative that the system and analysis routines be thoroughly tested. The simulators discussed here provide such a test facility.

The passive simulator is the simplest to construct and has the fewest components, and is adequate for some applications. The hybrid simulator has the same circuitry as the passive simulator, with the addition of a temperature control oven for the diode. The hybrid simulator is best suited for use as a reference device. The active simulator is a complicated circuit with a large number of components. It is not a sample substitution box, but it is the most versatile simulator.

The simulators are a superior technology for testing the integrity of superconductor measurement systems, since they offer significantly higher precision and accuracy. The temperature coefficient for the simulators is less than 0.3% ΔI_c/°C for the passive simulator and about 0.007% ΔI_c/°C for the active simulator and about 0.001% ΔI_c/°C for the hybrid simulator at a 1 μV signal level. The standard reference material SRM 1457, on the other hand, has a temperature coefficient of 21% ΔI_c/K at a magnetic field of 2 T, and does not offer the features of stability or multiple use feature that the simulators do. The temperature coefficient of the simulators is significantly less than that of the SRM, even after considering the relative variability of liquid helium and room temperatures. The total uncertainty of the hybrid simulator is estimated to be about ±0.2%, with the uncertainty of the current sensing resistor as the major source of this total uncertainty. This is significantly less than the uncertainty of the present superconducting reference material, which is ±1.71 to ±2.57%, depending on the magnetic field.

Acknowledgments

The passive simulator circuit is based on an idea by J. W. Ekin and J. Brauch of NIST. The authors extend their thanks to W. P. Dubé for discussions on the simulator. The work described in this paper was funded by NIST. Work on the passive and active simulators in 1984–1986 was supported by the Department of Energy—Fusion and High Energy Physics. This early work focused on the effects of ripple on the critical current and its measurement. The early active simulator used a different circuit, but it had similar characteristics. These characteristics were suitable for the ripple experiment. The present simulators have better defined characteristics and offer much greater utility.

8. References

[1] L. F. Goodrich and S. L. Bray, Cryogenics **30**, 667 (1990).
[2] American Society for Testing and Materials, Standard Test Method for D-C Critical Current of Composite Superconductors- B714, Annual Book of ASTM Standards, Vol. 02.03, Philadelphia (1990).
[3] L. F. Goodrich, Cryogenics **31**, 720 (1991).
[4] L. F. Goodrich and A. N. Srivastava, Comparison of Transport Critical Current Measurement Methods, to be published in Adv. Cryo. Eng. Mat. **38**.
[5] J. Moreland, Y. K. Li, L. F. Goodrich, A. Roshko, and R. H. Ono, Science and Technology of Thin-Film Superconductors 2, Plenum Press, NY (1990) p. 429.
[6] L. F. Goodrich and S. L. Bray, Cryogenics **28**, 737 (1988).
[7] S. L. Bray and L. F. Goodrich, ed. L. F. Goodrich, NBSIR 88-3308 (1988) p. 44.
[8] S. L. Bray and L. F. Goodrich, Meas. Sci. Technol. **1**, 491 (1990).
[9] S. L. Bray, L. F. Goodrich, and W. P. Dubé, Rev. Sci. Instrum. **60**, 261 (1989).
[10] W. H. Warens, J. Appl. Phys. **63**, 1651 (1988).
[11] D. ter Avest, G. Schoenmaker, H. G. Knoopers, and L. J. M. van de Klundert, Measurements of the resistive transition in very long sample superconductors, to be published in Adv. Cryo. Eng. Mat. **38**.
[12] D. ter Avest, E. M. J. Niessen, and L. J. M. van de Klundert, The effect of a non-uniform critical current density on the resistive transition in composite superconductors, to be published in Adv. Cryo. Eng. Mat. **38**.

About the authors: *Dr. Loren F. Goodrich is a Senior Staff Physicist, Ashok N. Srivastava is an Electrical Engineering graduate student at the University of Colorado at Boulder and works part time at NIST-Boulder, and Theodore C. Stauffer is an Electronics Technician. All of the authors work in the Superconductor and Magnetic Measurements Group of the Electromagnetic Technology Division at NIST, Boulder.*

Volume 96, Number 6, November-December 1991
Journal of Research of the National Institute of Standards and Technology

[J. Res. Natl. Inst. Stand. Technol. 96, 725 (1991)]

Molar Heat Capacity (C_v) for Saturated and Compressed Liquid and Vapor Nitrogen from 65 to 300 K at Pressures to 35 MPa

Volume 96 Number 6 November-December 1991

J. W. Magee

National Institute of Standards and Technology,
Boulder, CO 80303

Molar heat capacities at constant volume (C_v) for nitrogen have been measured with an automated adiabatic calorimeter. The temperatures ranged from 65 to 300 K, while pressures were as high as 35 MPa. Calorimetric data were obtained for a total of 276 state conditions on 14 isochores. Extensive results which were obtained in the saturated liquid region ($C_v^{(2)}$ and C_σ) demonstrate the internal consistency of the C_v (ρ,T) data and also show satisfactory agreement with published heat capacity data. The overall uncertainty of the C_v values ranges from 2% in the vapor to 0.5% in the liquid.

Key words: calorimeter; heat capacity; high pressure; isochoric; liquid; measurement; nitrogen; saturation; vapor.

Accepted: August 30, 1991

Glossary

a,b,c,d,e	Coefficients for Eq. (7)
C_v	Molar heat capacity at constant volume
C_v^0	Molar heat capacity in the ideal gas state
$C_v^{(2)}$	Molar heat capacity of a two-phase sample
C_σ	Molar heat capacity of a saturated liquid sample
V_{bomb}	Volume of the calorimeter containing sample
V_m	Molar volume, $dm^3 \cdot mol^{-1}$
P	Pressure, MPa
P_σ	Vapor pressure
ΔP	Pressure rise during a heating interval
T	Temperature, K
T_c	Critical-point temperature
T_1, T_2	Temperature at start and end of heating interval
ΔT	Temperature rise during a heating interval
Q	Calorimetric heat energy input to bomb and sample
Q_0	Calorimetric heat energy input to empty bomb
N	Moles of substance in the calorimeter
ρ	Fluid density, $mol \cdot dm^{-3}$
ρ_σ	Saturated liquid density
μ	Chemical potential

1. Introduction

Accurate measurements of thermodynamic properties, including heat capacity, are needed to establish behavior of higher order temperature derivatives of an equation of state $P(\rho, T)$. In particular, the heat capacity at constant volume (C_v) is related to $P(\rho,T)$ by:

$$C_v - C_v^0 = -T\int_0^\rho (\partial^2 P/\partial T^2)_\rho \, d\rho/\rho^2 \qquad (1)$$

where C_v^0 is the ideal gas heat capacity. Consequently, C_v measurements which cover a wide range of (P, ρ, T) states are beneficial to the development of an accurate equation of state for the substance.

The amount of experimental data on the calorimetric properties of nitrogen is very limited. Measurements of C_v are mostly confined to atmospheric pressure. Only two published works concern C_v measurements at elevated pressure. First, Voronel et al. [1] obtained 69 experimental values of C_v at temperatures from 106 to 167 K at densities close to the critical density, with an emphasis on the temperature variation of C_v near the critical point (126.2 K). However, these authors give neither the pressures nor the densities at which the measurements were performed. Thus, comparisons with the C_v data of Voronel et al. are difficult at best. In the only other experimental study at elevated pressures, Weber [2] performed measurements at temperatures from 91 to 242 K using the same calorimeter as used in this work. The combined works of Voronel et al. and Weber

leave gaps in the C_v surface between the triple point (63.15 K) and 91 K, and for temperatures above 242 K.

Published experimental results for the heat capacity of the saturated liquid (C_σ) are more available than those for C_v at elevated pressures. When combined, the data of Weber [2], Giauque and Clayton [3], and Wiebe and Brevoort [4] range from 65 to 125 K. However, none of these works spans the entire temperature domain for saturated liquid nitrogen. Thus, we cannot be certain how the various data will intercompare. In this work, the goals include extending the published data for C_v to temperatures as low as the triple point, and also to near ambient temperature. A second goal is to measure C_σ over temperatures from the vicinity of the triple point to that of the critical point, and to compare these measurements with published data and with predictions from published equations of state.

2. Experimental

The apparatus in Fig. 1 has a long history dating to its original construction for liquid hydrogen calorimetry. Its mechanical details remain essentially unchanged since they were described by Goodwin [5]. Instrumentation, however, has been changed extensively. The older instruments were replaced with electronic versions, each equipped with an IEEE-488 standard interface for two-way communication with a microcomputer. The arrangement of the new instruments is shown in Fig. 2.

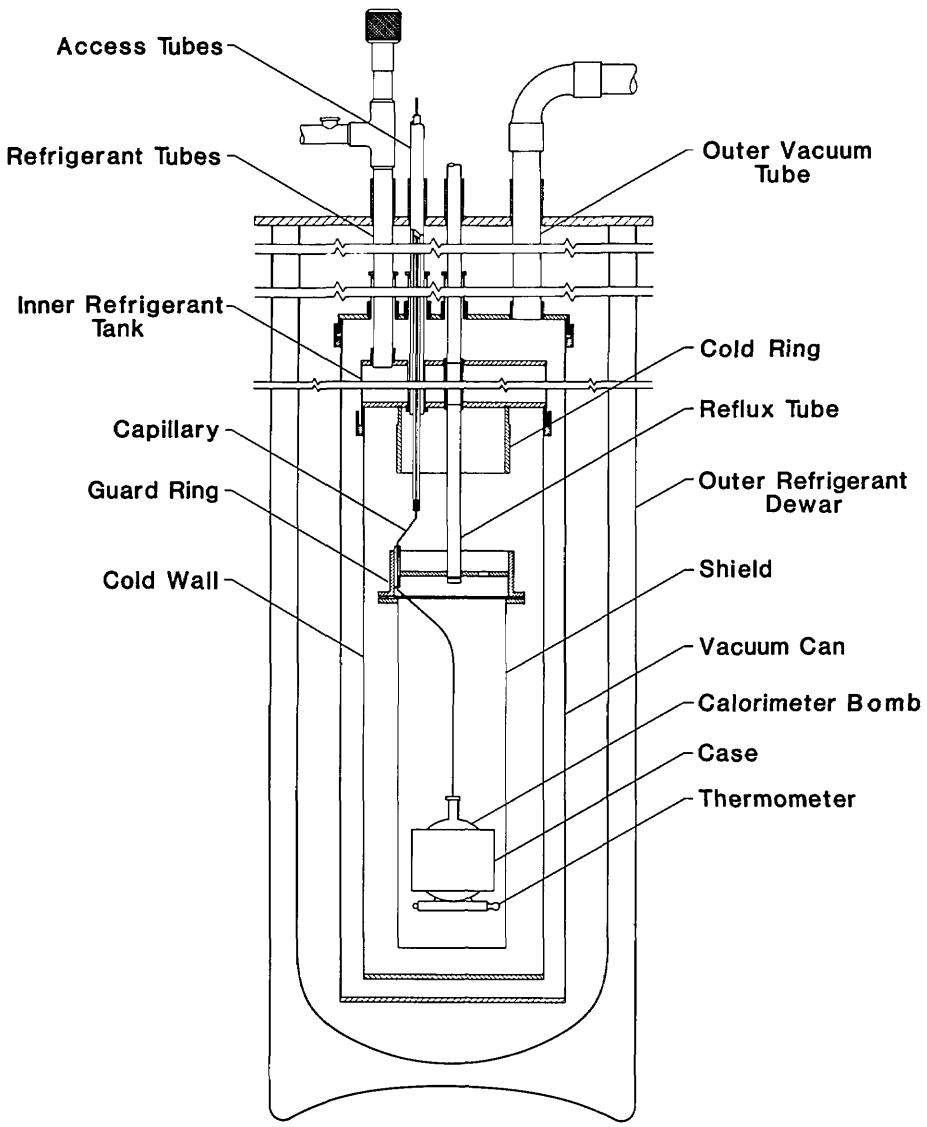

Figure 1. Details of the adiabatic calorimeter.

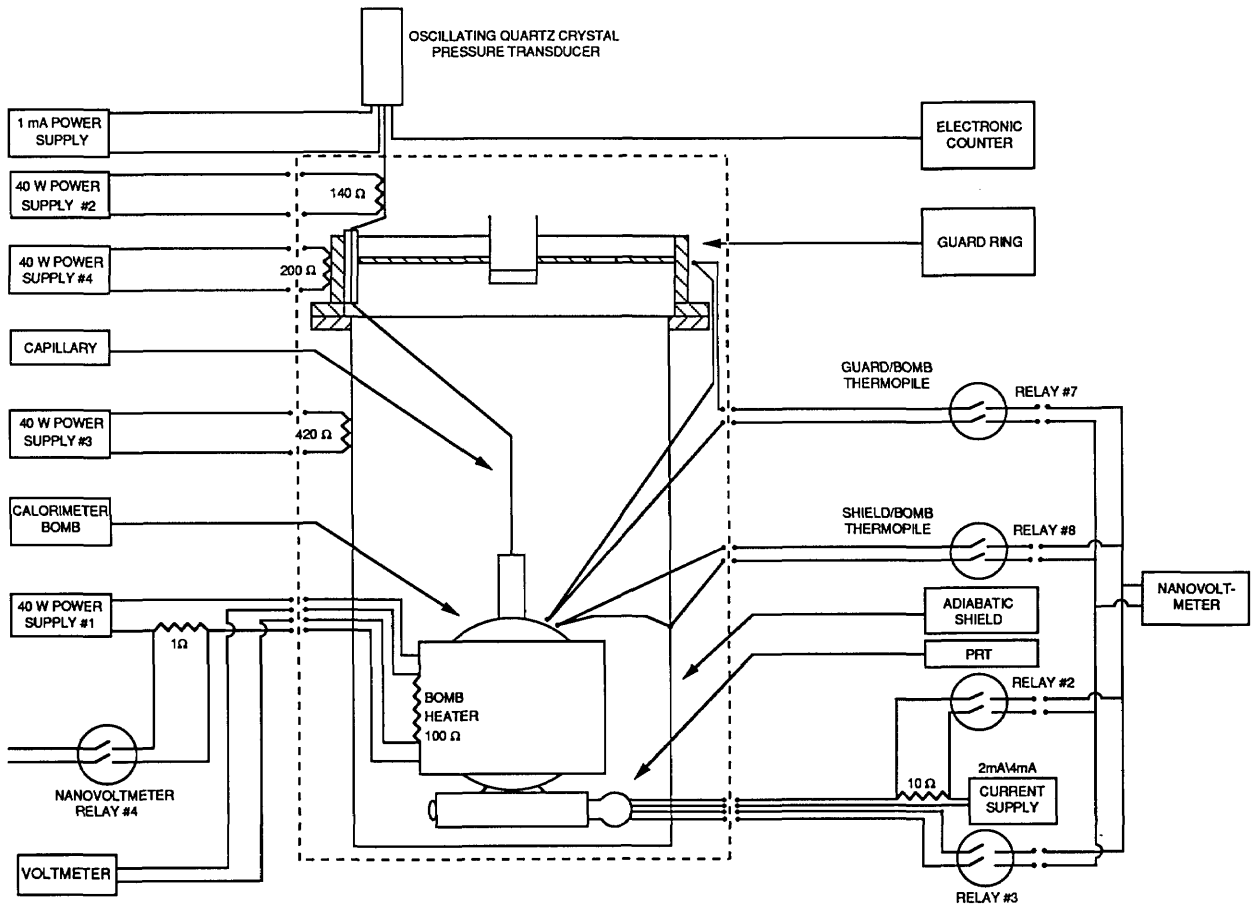

Figure 2. Instrumentation of the adiabatic calorimeter.

An experimental heat capacity is the applied heat (Q) corrected for the heat applied to the empty calorimeter (Q_0) per unit temperature rise (ΔT) per mole (N) of substance. In terms of the observed measurements, the heat capacity is given by,

$$C_v = (Q - Q_0)/(N\Delta T). \quad (2)$$

The applied heat is the product of the time-averaged power and the elapsed time of heating. Measured power is the product of instantaneous current and potential applied to the 100 Ω heater wound on the surface of the calorimeter bomb. During a heat measurement a series of five power measurements with an accuracy of 0.01% were made at 100 s intervals. Time was determined with a microcomputer clock to a resolution of 10^{-4} s. Elapsed time was computed with an accuracy of 0.001%. The heat (Q_0) applied to the empty calorimeter has been determined by several series of calorimetric experiments on a thoroughly cleaned and evacuated sphere. These results include those of Roder [6] from 86 to 322 K and of Mayrath [7] from 91 to 340 K in addition to new data from 29 to 99 K, as presented in Table 1. The combined Q_0 data sets were fitted to the expression,

$$Q_0(T) = \sum_{i=1}^{12} C_i\,(T_2^i - T_1^i) \quad (3)$$

by applying a chord-fitting method to ΔT values ranging from 0.5 to 20 K. Details will follow in a later section.

Temperatures were measured with an automated circuit consisting of a 25 Ω encapsulated platinum resistance thermometer calibrated on the IPTS-68 by the NIST Temperature and Pressure Division, a 10 Ω standard resistor calibrated by the NIST Electricity Division, a stable (±2 ppm) electronic current source, and a bank of ultralow thermal emf ($<1\times10^{-10}$ V/K) relays multiplexing a precise nanovoltmeter. Potential measurements were made with the thermometer current flowing in both forward and reverse directions. An average thermometer resistance was calculated in order to avoid errors from spurious emfs. It is thought that

the absolute temperatures derived this way are accurate within 0.03 K and precise to ±0.002 K. During this work we reproduced the generally accepted triple point temperature of N_2 to less than 0.002 K as a further check on the validity of this claim. Temperature rises (ΔT) were established within 0.004 K by linear extrapolation of the preheating and the post-heating temperature drift data to the midpoint time of the heat cycle.

Pressure was measured with an oscillating quartz crystal pressure transducer whose signal was fed to a precise timer/counter. This instrument had a range of 70 MPa and was calibrated with a piston gauge. The experimental uncertainty of the measured pressure is estimated to be ±0.01% of full scale at pressures above 3 MPa, or ±(0.03−0.05)% of the pressure at lower pressures. Finally, the number (N) of moles of substance in the calorimeter is the product of the calorimeter volume (V_{bomb}) and the molar density (ρ) derived from the equation of state [8] which has an uncertainty of ±0.1%. The calorimeter volume was obtained from a previous calibration [9] as a function of temperature and pressure, and is accurate to ±0.1%. The value of N derived in this way is believed to have an uncertainty of ±0.2%. If a weighing method was used to evaluate N, the error would drop to ±0.01%. Other details will follow in a later section.

The spherical bomb depicted in Fig. 1 is constructed of Type 316 stainless steel with a wall thickness of 0.15 cm and an internal volume of 72.739 cm^3 at 100 K. To prepare for an isochoric experiment, N_2 was charged at a pressure of 10 MPa and at a suitable bomb temperature until the target density was obtained. Then the sample was cooled to near 63 K with liquid Ne refrigerant, or to near 80 K when liquid N_2 was used. Each run commenced in the vapor+liquid region. The heater power was set to obtain about a 4 K temperature rise during each experiment. Apparatus control was then turned over to the microcomputer. A Fortran program was responsible for control of the cell heater. The guard and shield heaters followed the rise of the cell temperature using a specially tuned proportional-integral-derivative algorithm [10]. The program recorded, at periodic intervals, the bomb temperature, the cell pressure, and the voltage and current applied to the cell heater. Another Fortran program calculated heat capacity using the raw data as input. The raw data were not processed when the initial (T_1) and final (T_2)

Table 1. Experimental heat values of the empty calorimeter

T K	ΔT K	Q_0 J	$Q_{0,calc}$ J	Diff.[b] %	dQ_0/dT[c] $J \cdot K^{-1}$	$C_{0,calc}$[d] $J \cdot K^{-1}$	Diff.[e] %
33.2131	12.0335	90.26328	90.49135	−0.3	7.501	−1.564	120.85
42.7043	6.9579	90.66839	90.76538	−0.1	13.031	8.785	32.58
48.8077	5.2636	90.47602	90.51839	−0.05	17.189	14.768	14.09
53.6257	4.3835	90.42722	90.35803	0.08	20.629	19.149	7.18
57.7245	3.8312	90.32820	90.20241	0.1	23.577	22.652	3.92
29.4295	4.0968	22.95437	22.89193	0.2	5.603	−6.072	208.37
33.0460	3.1274	22.88944	22.66654	1.0	7.319	−1.758	124.02
35.9052	2.5777	22.83842	22.59133	1.0	8.860	1.508	82.98
38.3089	2.2236	22.81414	22.57683	1.0	10.260	4.157	59.48
42.8741	6.9005	90.65877	90.78388	−0.1	13.138	8.958	31.81
48.9372	5.2363	90.48850	90.52425	−0.04	17.281	14.890	13.84
53.7321	4.3646	90.36904	90.30011	0.08	20.705	19.242	7.07
57.8148	3.8176	90.26715	90.12809	0.2	23.645	22.727	3.88
61.4343	3.4396	90.19663	90.04630	0.2	26.223	25.655	2.17
64.7215	3.1554	90.04881	89.86412	0.2	28.538	28.189	1.22
67.7579	2.9392	89.98361	89.83021	0.2	30.615	30.427	0.61
70.5975	2.7668	89.96804	89.83038	0.2	32.517	32.436	0.25
73.2786	2.6229	89.88941	89.75887	0.1	34.271	34.260	0.03
75.8258	2.5022	89.86651	89.69035	0.2	35.915	35.930	−0.04
78.2613	2.3990	89.73939	89.61554	0.1	37.407	37.471	−0.17
80.5992	2.3119	89.73409	89.62376	0.1	38.814	38.901	−0.22
82.8526	2.2316	89.62329	89.46169	0.2	40.161	40.235	−0.18
85.0322	2.1666	89.61274	89.55121	0.07	41.361	41.485	−0.30
87.1452	2.1046	89.55704	89.45610	0.1	42.553	42.661	−0.25
89.1993	2.0501	89.55862	89.41201	0.2	43.685	43.770	−0.19
91.2015	1.9998	89.49705	89.31963	0.2	44.753	44.820	−0.15
93.1555	1.9544	89.42748	89.24169	0.2	45.757	45.817	−0.13

Table 1. Experimental heat values of the empty calorimeter—Continued

T K	ΔT K	Q_0 J	$Q_{0,calc}$ J	Diff.[b] %	dQ_0/dT[c] J·K^{-1}	$C_{0,calc}$[d] J·K^{-1}	Diff.[e] %
95.0632	1.9143	89.39781	89.22528	0.2	46.700	46.763	−0.14
96.9314	1.8760	89.35200	89.13514	0.2	47.629	47.666	−0.08
98.7621	1.8412	89.29452	89.06914	0.3	48.498	48.527	−0.06
62.3556	10.2210	274.4339	274.6478	−0.08	26.850	26.377	1.76
71.5780	8.2580	273.7197	273.9020	−0.07	33.146	33.111	0.11
79.2821	7.1899	273.2521	273.5237	−0.1	38.005	38.101	−0.25
86.1019	6.5020	272.9280	273.1325	−0.08	41.976	42.085	−0.26
92.3337	6.0173	272.6679	272.7770	−0.04	45.314	45.401	−0.19
29.1443	4.1877	22.95278	22.91044	0.2	5.481	−6.421	217.15
32.8341	3.1736	22.88800	22.66570	1.0	7.212	−2.005	127.80
35.7294	2.6077	22.85388	22.59940	1.0	8.764	1.311	85.05
38.1597	2.2428	22.80479	22.57232	1.0	10.168	3.996	60.70
42.7520	6.9371	90.60546	90.71014	−0.1	13.061	8.834	32.36
48.8448	5.2576	90.48330	90.55201	−0.08	17.210	14.803	13.99
53.6546	4.3758	90.36902	90.28945	0.09	20.652	19.174	7.16
57.7485	3.8264	90.26860	90.15482	0.1	23.591	22.672	3.90
61.3737	3.4432	90.16708	89.99313	0.2	26.187	25.607	2.21
64.6661	3.1618	90.09233	89.92512	0.2	28.494	28.147	1.22

[a] Equation (3).
[b] $100\ (Q_0 - Q_{0,calc})/Q_0$.
[c] Derived from Eq. (3).
[d] Reference [11].
[e] $100\ (dQ_0/dT - C_{0,calc}/dQ_0/dT$.

temperatures obtained during a heat capacity measurement straddled the saturation temperature. Each isochoric run was continued until the upper limit of either the temperature (300 K) or pressure (35 MPa) was obtained.

3. Results

A significant adjustment must be applied to the raw heat capacity data for the energy required to heat the empty calorimeter from the initial (T_1) to the final temperature (T_2). For this work, Q_0/Q ranged from 0.89 to 0.27. Since the published Q_0 data had a lower limit of 86 K, experiments were conducted to extend the data to temperatures as low as 29 K. The results are shown in Table 1. An examination of the empty calorimeter's heat capacity (C_0) revealed that it is s-shaped when plotted against temperature. Further, C_0 has a sharp curvature below 100 K. Combined, these properties make a high quality fit to raw C_0 data difficult. In the face of these difficulties, efforts to define a $C_0(T)$ function were made by previous workers [6,9]. For this work, however, I fitted the data to the integral heat (Q_0) function, Eq. (3), which is monotonic with no inflection. Values of C_0 can then be recovered from the derivative with temperature, $C_0 = dQ_0/dT$. Table 1 presents the raw data (Q_0, T, ΔT), Q_0 values calculated from the best fit to Eq. (3), and C_0 from an earlier study [11]. The coefficients of Eq. (3) are presented in Table 2. Calculated C_0 values establish that the new experimental measurements of C_0 are both smooth and consistent with previous measurements to less than 0.19% at temperatures from 90 to 100 K, the region of overlap. This is depicted graphically in Fig. 3, which also shows that an extrapolation of our earlier calibration [11] would have led to serious errors at temperatures below 80 K.

Table 2. Coefficients of the function $Q_0(T)$, Eq. (3), of the empty calorimeter

i	C_i
1	$1.070179528057 \cdot 10^{1}$
2	$-4.721695058560 \cdot 10^{-1}$
3	$9.985458119236 \cdot 10^{-3}$
4	$3.443201289415 \cdot 10^{-6}$
5	$-1.486069268038 \cdot 10^{-6}$
6	$1.901352098615 \cdot 10^{-8}$
7	$-1.300438485128 \cdot 10^{-10}$
8	$5.607423959480 \cdot 10^{-13}$
9	$-1.572000054992 \cdot 10^{-15}$
10	$2.789945522377 \cdot 10^{-18}$
11	$-2.854347532609 \cdot 10^{-21}$
12	$1.284323931260 \cdot 10^{-24}$

The nitrogen sample used for this study is of very high purity. An analysis was furnished by the

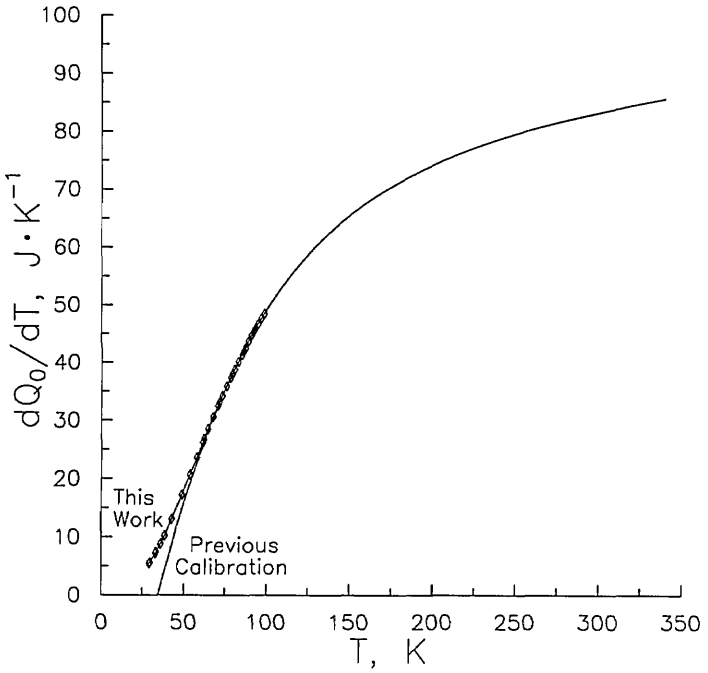

Figure 3. Heat capacity $C_0 = dQ_0/dT$ of the empty calorimeter: previous calibration [11]; this work (◇).

vendor. The impurities present in the research grade sample are 0.2 ppm CO_2, 0.2 ppm total hydrocarbons, 1 ppm O_2, and 1 ppm H_2O. In addition, we performed our own analysis using gas chromatography-mass spectroscopy and confirmed these results.

The raw and reduced data for each run are presented in Table 3 for two-phase states, and in Table 4 for single-phase vapor and liquid states. Sufficient raw data are presented in Tables 3 and 4 to allow rechecking these computations or to reprocess the raw data using other equations for any adjustments to the experimental data. Data for the number of moles (N) in the calorimeter are provided in both Tables 3 and 4. These data identify and tie together the two-phase and single-phase portions of each isochoric run. Table 3 presents values of the two-phase heat capacity at constant volume ($C_v^{(2)}$) and the saturated liquid heat capacity (C_σ) at the midpoint temperature (T) of each heating interval. Values of the saturated liquid heat capacity C_σ are obtained by adjusting $C_v^{(2)}$ measurements with the thermodynamic relation,

$$C_\sigma = C_v^{(2)} - T\rho_\sigma^{-2}(d\rho_\sigma/dT)(dP_\sigma/dT) + T[\rho_\sigma^{-1} - \rho^{-1}]\, d^2P_\sigma/dT^2 \qquad (4)$$

where ρ_σ and P_σ are the density and pressure of the saturated liquid and ρ is the bulk density of the sample residing in the bomb. The derivative quantities were calculated using the formulation of Jacobsen et al. [8].

Corrections to the experimental heat capacity calculated using Eq. (2) for vaporization of sample are given by

$$C_{\Delta H} = \delta N_c\, \Delta H_v\, N^{-1}\, \Delta T^{-1} \qquad (5)$$

where δN_c is the number of moles vaporized during a heating interval and ΔH_v is the molar heat of vaporization calculated using the equation of state [8]. Thus, Eq. (5) corrects for the heat which drives a portion of the sample into the capillary by evaporation during a heat capacity experiment in the two-phase region. It is at most equal to 0.06% of $C_v^{(2)}$. In Table 3 the column labeled difference refers to calculations for C_σ made with the equation of state in Ref. [8]. This equation of state correctly predicts the values within ±2%. Corrections for PV work on the bomb are given by

$$C_{PV} = k\,[T_2(\partial P/\partial T)_{\rho 2} - \Delta P/2]\, \Delta V_m/\Delta T \qquad (6)$$

where $k = 1000$ J·MPa^{-1}·dm^{-3}, the pressure rise is $\Delta P = P_2 - P_1$, and the volume change per mole is $\Delta V_m = \rho_2^{-1} - \rho_1^{-1}$. The derivative has been calculated with the equation of state [8]. The PV work correction is important only for single-phase samples and varies between 0.26 and 3.8% of the value of C_v. The largest such corrections occur for the highest density isochores.

Table 3. Experimental two-phase heat capacities

T K	ρ_σ mol·dm^{-3}	P_σ MPa	N mol	V_{bomb} cm^3	ΔT K	$Q/\Delta T$ J·K^{-1}	C_0[a] J·K^{-1}	Adj.[b] J·mol^{-1}·K^{-1}	Adj.[c]	C_σ J·mol^{-1}·K^{-1}	$C_{\sigma,calc}$[d]	Diff.[e] %	$C_v^{(2)}$ J·mol^{-1}·K^{-1}
67.634	30.358	0.027	2.1485	72.682	2.084	150.852	30.338	−0.001	0.013	55.99	56.68	−1.23	55.98
69.703	30.057	0.037	2.1485	72.685	2.060	152.557	31.811	−0.001	0.038	56.16	57.08	−1.64	56.12
64.800	30.755	0.017	2.1485	72.678	2.120	148.342	28.248	−0.001	−0.007	55.71	55.66	0.09	55.72
66.904	30.462	0.024	2.1485	72.681	2.091	150.277	29.807	−0.001	0.007	55.95	56.48	−0.95	55.94
68.981	30.163	0.033	2.1485	72.683	2.067	152.020	31.302	−0.001	0.028	56.13	56.96	−1.49	56.10
65.223	30.697	0.018	2.0461	72.678	2.199	142.980	28.565	−0.001	−0.052	55.69	55.86	−0.30	55.75
71.685	29.760	0.050	2.0461	72.687	2.115	148.491	33.184	−0.001	−0.017	56.29	57.31	−1.81	56.30
73.785	29.436	0.066	2.0461	72.691	2.088	150.148	34.596	−0.002	0.016	56.46	57.45	−1.75	56.44
75.859	29.106	0.085	2.0461	72.694	2.066	151.757	35.951	−0.002	0.064	56.65	57.55	−1.59	56.58
77.912	28.772	0.109	2.0461	72.698	2.043	153.329	37.253	−0.002	0.129	56.86	57.64	−1.38	56.73
66.191	30.562	0.022	1.9346	72.680	2.281	137.823	29.284	−0.001	−0.114	55.83	56.25	−0.75	55.95
70.686	29.911	0.043	1.9346	72.686	2.216	141.662	32.497	−0.001	−0.127	56.23	57.21	−1.73	56.36
72.887	29.575	0.058	1.9346	72.689	2.189	143.357	33.998	−0.002	−0.119	56.37	57.40	−1.83	56.49
75.060	29.234	0.077	1.9346	72.693	2.161	145.116	35.434	−0.002	−0.099	56.57	57.51	−1.66	56.67
77.206	28.888	0.100	1.9346	72.696	2.136	146.775	36.809	−0.002	−0.063	.77	57.61	−1.48	56.83
79.325	28.537	0.128	1.9346	72.700	2.111	148.482	38.127	−0.003	−0.008	57.03	57.72	−1.20	57.04
81.420	28.182	0.161	1.9346	72.704	2.086	150.150	39.392	−0.004	0.070	57.33	57.86	−0.94	57.2
83.492	27.822	0.199	1.9346	72.708	2.064	151.701	40.605	−0.004	0.175	57.61	58.06	−0.79	57.43
85.538	27.457	0.243	1.9346	72.712	2.040	153.400	41.770	−0.005	0.309	58.02	58.32	−0.52	57.71
87.564	27.087	0.293	1.9346	72.716	2.018	154.969	42.889	−0.006	0.479	58.42	58.65	−0.40	57.94
81.404	28.185	0.160	1.7683	72.704	2.210	141.220	39.382	−0.004	−0.314	57.28	57.86	−1.01	57.59
83.601	27.802	0.201	1.7683	72.708	2.181	143.094	40.669	−0.005	−0.257	57.67	58.07	−0.70	57.93
85.772	27.415	0.248	1.7683	72.712	2.152	144.875	41.901	−0.005	−0.169	58.07	58.36	−0.49	58.24
87.915	27.022	0.302	1.7683	72.717	2.126	146.576	43.080	−0.006	−0.043	58.49	58.72	−0.39	58.53
90.032	26.624	0.363	1.7683	72.721	2.101	148.271	44.210	−0.007	0.126	58.98	59.16	−0.31	58.85
92.122	26.220	0.433	1.7683	72.726	2.076	150.010	45.293	−0.008	0.345	59.56	59.69	−0.22	59.22
94.187	25.810	0.510	1.7683	72.731	2.048	151.854	46.332	−0.010	0.623	60.29	60.31	−0.03	59.67
96.227	25.392	0.595	1.7683	72.736	2.025	153.632	47.328	−0.011	0.970	61.08	61.03	0.08	60.11
98.246	24.965	0.690	1.7683	72.741	2.002	155.294	48.286	−0.012	1.396	61.90	61.84	0.09	60.50
100.239	24.530	0.793	1.7683	72.746	1.981	156.885	49.205	−0.013	1.915	62.79	62.77	0.04	60.88
82.384	28.015	0.178	1.6152	72.706	2.645	134.159	39.961	−0.005	−0.742	57.59	57.95	−0.63	58.33
85.012	27.552	0.231	1.6152	72.711	2.604	136.253	41.474	−0.006	−0.728	57.96	58.25	−0.50	58.69
87.597	27.081	0.294	1.6152	72.716	2.560	138.526	42.908	−0.007	−0.668	58.54	58.66	−0.20	59.21
90.143	26.603	0.367	1.6152	72.722	2.522	140.545	44.269	−0.008	−0.551	59.06	59.19	−0.21	59.61
92.648	26.117	0.451	1.6152	72.727	2.480	142.835	45.561	−0.010	−0.364	59.86	59.84	0.03	60.22
95.116	25.621	0.548	1.6152	72.733	2.444	144.930	46.789	−0.011	−0.093	60.66	60.62	0.06	60.75
97.546	25.115	0.656	1.6152	72.739	2.407	147.066	47.957	−0.013	0.280	61.63	61.55	0.14	61.35
99.939	24.597	0.777	1.6152	72.745	2.371	149.220	49.069	−0.014	0.776	62.77	62.62	0.23	61.99
102.299	24.064	0.912	1.6152	72.751	2.336	151.445	50.128	−0.016	1.421	64.13	63.87	0.41	62.71
104.623	23.516	1.059	1.6151	72.758	2.300	153.724	51.137	−0.018	2.251	65.74	65.32	0.64	63.49
106.913	22.949	1.221	1.6151	72.764	2.267	155.933	52.099	−0.020	3.314	67.57	67.04	0.79	64.26
80.773	28.292	0.150	1.4726	72.703	2.828	125.246	39.005	−0.004	−1.186	57.38	57.81	−0.75	58.57
83.582	27.806	0.201	1.4725	72.708	2.776	127.586	40.658	−0.006	−1.281	57.76	58.07	−0.54	59.04
86.336	27.312	0.262	1.4725	72.714	2.722	129.958	42.215	−0.007	−1.336	58.26	58.44	−0.31	59.60
89.038	26.812	0.334	1.4725	72.719	2.674	132.254	43.684	−0.008	−1.337	58.82	58.94	−0.21	60.15
91.691	26.304	0.418	1.4725	72.725	2.624	134.661	45.073	−0.010	−1.272	59.57	59.57	−0.01	60.84
94.297	25.787	0.514	1.4725	72.731	2.579	136.915	46.386	−0.012	−1.126	60.35	60.35	0.00	61.47
96.859	25.260	0.624	1.4725	72.737	2.537	139.315	47.631	−0.013	−0.878	61.37	61.27	0.17	62.25
99.379	24.720	0.747	1.4725	72.744	2.494	141.680	48.812	−0.015	−0.507	62.54	62.35	0.31	63.05
101.858	24.165	0.885	1.4725	72.750	2.454	144.025	49.933	−0.017	0.015	63.89	63.62	0.43	63.88
104.296	23.595	1.038	1.4725	72.757	2.415	146.316	50.997	−0.020	0.728	65.43	65.10	0.51	64.71
106.695	23.004	1.205	1.4725	72.763	2.375	148.691	52.009	−0.022	1.683	67.31	66.86	0.67	65.63
109.051	22.391	1.388	1.4725	72.770	2.334	151.228	52.970	−0.024	2.952	69.65	68.98	0.96	66.70
111.367	21.749	1.585	1.4725	72.777	2.292	153.974	53.884	−0.027	4.646	72.58	71.61	1.35	67.94
113.643	21.069	1.799	1.4725	72.785	2.252	156.554	54.754	−0.029	6.947	76.04	74.98	1.40	69.10
81.647	28.143	0.165	1.3285	72.704	3.388	118.221	39.527	−0.005	−1.809	57.44	57.88	−0.78	59.25

Table 3. Experimental two-phase heat capacities—Continued

T K	ρ_σ mol·dm^{-3}	P_σ MPa	N mol	V_{bomb} cm^3	ΔT K	$Q/\Delta T$ J·K^{-1}	C_0[a] J·K^{-1}	Adj.[b] J·mol^{-1}·K^{-1}	Adj.[c] J·mol^{-1}·K^{-1}	C_σ J·mol^{-1}·K^{-1}	$C_{\sigma,calc}$[d] J·mol^{-1}·K^{-1}	Diff.[e] %	$C_v^{(2)}$ J·mol^{-1}·K^{-1}
84.998	27.554	0.230	1.3285	72.711	3.303	121.151	41.466	−0.007	−2.035	57.96	58.25	−0.49	59.99
88.268	26.957	0.312	1.3285	72.718	3.224	124.090	43.271	−0.009	−2.202	58.64	58.78	−0.24	60.84
91.461	26.349	0.410	1.3285	72.725	3.151	126.869	44.954	−0.011	−2.287	59.38	59.51	−0.23	61.66
94.579	25.730	0.525	1.3285	72.732	3.080	129.751	46.526	−0.013	−2.264	60.38	60.44	−0.10	62.64
97.629	25.097	0.660	1.3284	72.739	3.011	132.621	47.996	−0.015	−2.100	61.59	61.58	0.01	63.69
100.613	24.447	0.814	1.3284	72.747	2.945	135.501	49.375	−0.018	−1.757	63.05	62.95	0.16	64.81
103.532	23.776	0.988	1.3284	72.755	2.883	138.375	50.668	−0.021	−1.182	64.81	64.61	0.32	66.00
106.388	23.082	1.183	1.3284	72.763	2.819	141.416	51.882	−0.024	−0.300	67.07	66.62	0.67	67.37
109.182	22.356	1.398	1.3284	72.771	2.757	144.536	53.023	−0.027	1.001	69.85	69.11	1.06	68.85
111.918	21.589	1.635	1.3284	72.779	2.698	147.622	54.097	−0.030	2.900	73.26	72.34	1.27	70.36
114.590	20.769	1.894	1.3284	72.788	2.638	150.947	55.107	−0.034	5.719	77.82	76.71	1.43	72.10
117.198	19.872	2.174	1.3284	72.796	2.571	154.802	56.057	−0.037	10.092	84.38	83.09	1.54	74.29
83.765	27.773	0.204	1.1744	72.709	3.572	111.790	40.763	−0.007	−2.856	57.64	58.09	−0.79	60.49
90.722	26.492	0.385	1.1744	72.723	3.377	118.236	44.571	−0.012	−3.576	59.15	59.32	−0.29	62.73
97.307	25.165	0.645	1.1744	72.738	3.203	124.537	47.844	−0.017	−3.872	61.42	61.45	−0.05	65.29
100.473	24.478	0.806	1.1744	72.746	3.121	127.671	49.312	−0.020	−3.762	62.94	62.88	0.09	66.70
103.560	23.770	0.990	1.1744	72.755	3.045	130.854	50.680	−0.024	−3.405	64.83	64.62	0.32	68.24
106.571	23.036	1.196	1.1744	72.763	2.970	134.054	51.958	−0.027	−2.718	67.15	66.76	0.58	69.87
109.508	22.268	1.425	1.1744	72.772	2.897	137.424	53.153	−0.031	−1.569	70.15	69.45	1.00	71.72
112.372	21.456	1.677	1.1743	72.781	2.825	140.822	54.271	−0.035	0.256	73.91	72.98	1.27	73.65
115.163	20.582	1.953	1.1743	72.790	2.750	144.606	55.319	−0.039	3.157	79.14	77.88	1.59	75.98
117.873	19.619	2.251	1.1743	72.799	2.669	148.891	56.297	−0.043	7.971	86.77	85.29	1.70	78.80
120.500	18.507	2.572	1.1743	72.808	2.578	154.045	57.211	−0.047	16.851	99.26	98.10	1.17	82.41
81.860	28.106	0.168	1.0520	72.705	3.858	103.795	39.652	−0.007	−3.431	57.55	57.90	−0.60	60.99
85.660	27.435	0.245	1.0520	72.712	3.732	107.241	41.838	−0.009	−4.080	58.11	58.34	−0.40	62.19
89.337	26.756	0.342	1.0520	72.720	3.612	110.744	43.843	−0.012	−4.675	58.93	59.00	−0.13	63.60
92.902	26.066	0.461	1.0520	72.728	3.502	114.073	45.689	−0.015	−5.180	59.82	59.91	−0.15	65.00
96.354	25.365	0.601	1.0520	72.736	3.395	117.635	47.389	−0.018	−5.550	61.21	61.07	0.23	66.76
99.718	24.645	0.765	1.0520	72.744	3.303	121.054	48.967	−0.022	−5.741	62.76	62.51	0.40	68.50
102.980	23.906	0.953	1.0520	72.753	3.209	124.327	50.427	−0.026	−5.686	64.53	64.27	0.41	70.22
106.154	23.140	1.166	1.0519	72.762	3.122	127.718	51.784	−0.030	−5.298	66.85	66.43	0.62	72.14
109.240	22.340	1.403	1.0519	72.771	3.036	131.229	53.046	−0.034	−4.440	69.84	69.17	0.95	74.28
112.240	21.495	1.665	1.0519	72.780	2.951	134.957	54.221	−0.039	−2.888	73.81	72.79	1.39	76.70
115.155	20.584	1.952	1.0519	72.789	2.865	138.905	55.316	−0.043	−0.211	79.20	77.87	1.68	79.41
117.981	19.577	2.263	1.0519	72.799	2.778	143.249	56.335	−0.048	4.516	87.08	85.68	1.62	82.57
120.707	18.408	2.598	1.0519	72.809	2.672	148.849	57.281	−0.052	13.769	100.76	99.56	1.19	86.99
80.375	28.360	0.144	0.8789	72.702	4.307	93.168	38.766	−0.007	−4.560	57.35	57.78	−0.76	61.91
84.593	27.626	0.222	0.8789	72.710	4.121	97.154	41.237	−0.010	−5.688	57.95	58.19	−0.42	63.64
88.638	26.887	0.322	0.8789	72.718	3.954	101.081	43.470	−0.013	−6.791	58.77	58.86	−0.15	65.56
92.528	26.140	0.447	0.8789	72.727	3.813	104.844	45.500	−0.017	−7.818	59.70	59.80	−0.17	67.52
96.277	25.381	0.598	0.8789	72.736	3.674	108.706	47.352	−0.022	−8.715	61.08	61.04	0.06	69.79
99.896	24.606	0.775	0.8789	72.745	3.550	112.394	49.049	−0.026	−9.422	62.62	62.60	0.04	72.04
103.393	23.809	0.979	0.8789	72.754	3.430	116.261	50.607	−0.031	−9.860	64.80	64.52	0.43	74.66
106.778	22.983	1.211	0.8789	72.764	3.319	120.056	52.043	−0.037	−9.921	67.42	66.93	0.72	77.34
110.053	22.119	1.471	0.8789	72.773	3.214	123.926	53.369	−0.042	−9.432	70.79	70.04	1.07	80.22
113.221	21.200	1.758	0.8788	72.783	3.108	128.099	54.594	−0.048	−8.089	75.49	74.27	1.60	83.57

[a] Derived from Eq. (3). $C_0 = dQ_0/dT$.
[b] Equations (5) and (6).
[c] Equation (4).
[d] Reference [8].
[e] 100 $(C_\sigma - C_{\sigma,calc})/C_\sigma$.

Table 4. Experimental single-phase heat capacities

T K	ρ mol·dm^{-3}	P MPa	N mol	V_{bomb} cm^3	ΔT K	$Q/\Delta T$ J·K^{-1}	C_0[a] J·K^{-1}	Adj.[b]	C_v J·mol^{-1}·K^{-1}	$C_{v,calc}$[c]	Diff.[d] %
66.1756	30.9599	8.5838	2.2520	72.739	2.9305	107.357	29.273	1.28	33.26	31.76	4.526
9.0867	30.8819	14.4587	2.2477	72.785	2.8898	108.710	31.377	1.24	33.09	31.98	3.33
71.9548	30.8328	20.2568	2.2456	72.832	2.8506	110.186	33.368	1.22	32.95	32.13	2.49
74.7849	30.8035	25.9553	2.2449	72.879	2.8157	111.573	35.254	1.21	32.76	32.18	1.76
77.5788	30.7869	31.5376	2.2452	72.927	2.7814	112.954	37.044	1.22	32.58	32.17	1.25
69.2774	30.8813	14.9188	2.2478	72.789	3.4450	108.863	31.512	1.23	33.11	32.00	3.34
72.6946	30.8246	21.7709	2.2454	72.844	3.3915	110.553	33.868	1.21	32.91	32.15	2.30
76.0585	30.7943	28.4964	2.2449	72.901	3.3428	112.208	36.079	1.21	32.69	32.19	1.53
72.6097	30.3311	11.8026	2.2073	72.773	2.9139	107.734	33.811	1.16	32.29	31.30	3.06
75.5013	30.2825	17.2998	2.2051	72.818	2.8762	109.104	35.720	1.16	32.11	31.41	2.17
78.3559	30.2515	22.6862	2.2042	72.864	2.8386	110.564	37.530	1.16	31.97	31.46	1.61
81.1743	30.2318	27.9586	2.2042	72.910	2.8076	111.831	39.245	1.18	31.76	31.45	0.99
83.9583	30.2188	33.1070	2.2046	72.956	2.7718	113.210	40.874	1.20	31.62	31.39	0.73
72.0307	30.3444	10.7150	2.2080	72.764	2.9234	107.377	33.419	1.17	32.29	31.27	3.14
74.9320	30.2907	16.2231	2.2054	72.809	2.8824	108.874	35.350	1.16	32.16	31.40	2.38
77.7934	30.2568	21.6323	2.2044	72.855	2.8466	110.217	37.179	1.16	31.97	31.45	1.62
80.6178	30.2352	26.9234	2.2042	72.901	2.8122	111.579	38.912	1.17	31.80	31.45	1.10
83.4075	30.2209	32.0913	2.2045	72.947	2.7793	112.913	40.557	1.19	31.64	31.41	0.73
77.0893	29.5526	8.6948	2.1502	72.759	2.9544	106.205	36.736	1.06	31.24	30.51	2.34
80.0185	29.5055	13.7919	2.1481	72.802	2.9149	107.584	38.550	1.07	31.08	30.57	1.62
82.9065	29.4743	18.7781	2.1471	72.846	2.8759	108.936	40.266	1.08	30.91	30.60	1.02
85.7558	29.4528	23.6465	2.1468	72.889	2.8404	110.320	41.892	1.10	30.79	30.58	0.67
88.5715	29.4368	28.3997	2.1469	72.933	2.8069	111.676	43.434	1.12	30.68	30.53	0.46
85.2388	28.1342	6.0948	2.0469	72.756	2.9975	104.445	41.602	0.89	29.82	29.39	1.46
88.2096	28.0972	10.4732	2.0453	72.795	2.9579	105.825	43.239	0.91	29.70	29.37	1.12
91.1399	28.0717	14.7565	2.0446	72.835	2.9212	107.095	44.788	0.93	29.56	29.35	0.70
94.0353	28.0522	18.9399	2.0443	72.874	2.8869	108.360	46.257	0.95	29.44	29.31	0.41
96.8947	28.0364	23.0260	2.0442	72.914	2.8548	109.573	47.648	0.97	29.32	29.26	0.20
99.7227	28.0232	27.0294	2.0444	72.953	2.8259	110.653	48.970	1.00	29.18	29.20	−0.07
102.5197	28.0104	30.9381	2.0446	72.993	2.7951	111.823	50.225	1.02	29.10	29.12	−0.05
92.3233	26.5920	3.1853	1.9345	72.748	3.0508	102.476	45.396	0.73	28.79	28.46	1.13
95.3475	26.5632	6.9012	1.9334	72.783	3.0172	103.613	46.902	0.75	28.59	28.35	0.86
98.3344	26.5439	10.5495	1.9329	72.819	2.9797	104.856	48.328	0.77	28.48	28.28	0.70
101.2850	26.5288	14.1182	1.9327	72.855	2.9451	106.022	49.677	0.79	28.36	28.23	0.48
104.2006	26.5166	17.6147	1.9328	72.890	2.9134	107.127	50.956	0.81	28.25	28.17	0.27
107.0820	26.5049	21.0309	1.9329	72.926	2.8842	108.191	52.169	0.83	28.14	28.11	0.13
109.9340	26.4947	24.3895	1.9331	72.961	2.8541	109.272	53.322	0.86	28.08	28.04	0.14
112.7578	26.4840	27.6783	1.9333	72.997	2.8304	110.181	54.419	0.88	27.96	27.97	−0.04
105.7600	24.2453	4.8752	1.7648	72.791	3.0766	100.935	51.619	0.55	27.39	27.28	0.40
108.8264	24.2371	7.7000	1.7650	72.822	3.0460	101.875	52.880	0.57	27.18	27.11	0.26
111.8576	24.2317	10.4814	1.7653	72.852	3.0164	102.853	54.074	0.59	27.03	27.00	0.11
114.8599	24.2259	13.2159	1.7657	72.883	2.9831	103.887	55.207	0.61	26.95	26.92	0.12
117.8323	24.2205	15.9078	1.7660	72.913	2.9560	104.861	56.283	0.63	26.87	26.85	0.08
120.7784	24.2140	18.5546	1.7663	72.944	2.9311	105.701	57.306	0.65	26.74	26.78	−0.13
123.6977	24.2071	21.1602	1.7665	72.975	2.9064	106.567	58.279	0.67	26.66	26.71	−0.18
126.5950	24.1991	23.7239	1.7667	73.005	2.8807	107.485	59.206	0.69	26.64	26.64	−0.03
129.4678	24.1907	26.2495	1.7668	73.036	2.8633	108.096	60.090	0.70	26.47	26.58	−0.43
132.3201	24.1817	28.7374	1.7669	73.067	2.8364	109.073	60.934	0.72	26.52	26.51	0.04
135.1429	24.1724	31.1832	1.7669	73.098	2.8135	109.817	61.738	0.74	26.47	26.45	0.09
137.9433	24.1626	33.5919	1.7670	73.128	2.7945	110.542	62.506	0.75	26.43	26.39	0.17
112.3409	22.1595	3.1882	1.6131	72.793	3.5832	98.547	54.260	0.41	27.04	27.02	0.07
115.9124	22.1468	5.6836	1.6128	72.823	3.5489	99.454	55.593	0.43	26.76	26.59	0.64
119.4468	22.1408	8.1621	1.6130	72.852	3.5135	100.436	56.849	0.45	26.57	26.35	0.85
122.9472	22.1381	10.6204	1.6135	72.883	3.4780	101.363	58.032	0.46	26.39	26.19	0.76
126.4129	22.1302	13.0294	1.6136	72.913	3.4438	102.298	59.149	0.48	26.25	26.07	0.71
129.8462	22.1242	15.4143	1.6138	72.943	3.4128	103.165	60.204	0.50	26.12	25.97	0.57
133.2459	22.1177	17.7654	1.6140	72.974	3.3829	104.003	61.201	0.52	26.00	25.88	0.46
136.6150	22.1102	20.0821	1.6141	73.004	3.3532	104.893	62.145	0.54	25.95	25.80	0.58
119.3182	20.2246	3.7560	1.4727	72.815	3.6281	97.117	56.804	0.31	27.06	27.03	0.08
122.9365	20.2050	5.7012	1.4717	72.841	3.6044	97.697	58.029	0.33	26.62	26.41	0.80

Table 4. Experimental single-phase heat capacities—Continued

T K	ρ mol·dm^{-3}	P MPa	N mol	V_{bomb} cm^3	ΔT K	$Q/\Delta T$ J·K^{-1}	C_0[a] J·K^{-1}	Adj.[b]	C_v J·mol^{-1}·K^{-1}	$C_{v,calc}$[c]	Diff.[d] %
126.5253	20.1948	7.6456	1.4715	72.867	3.5761	98.407	59.185	0.35	26.30	26.04	1.01
130.0849	20.1876	9.5802	1.4715	72.893	3.5480	99.139	60.276	0.36	26.05	25.80	0.94
133.6139	20.1808	11.4985	1.4716	72.920	3.5169	99.966	61.307	0.38	25.89	25.63	1.01
137.1129	20.1750	13.4013	1.4717	72.947	3.4894	100.687	62.281	0.39	25.70	25.50	0.81
140.5803	20.1679	15.2807	1.4717	72.974	3.4628	101.401	63.203	0.41	25.55	25.38	0.65
147.4210	20.1529	18.9728	1.4717	73.028	3.4039	102.823	64.903	0.44	25.33	25.19	0.57
150.8021	20.1443	20.7859	1.4716	73.055	3.3782	103.547	65.689	0.45	25.28	25.10	0.69
127.3163	18.2448	5.2548	1.3291	72.848	4.1564	95.609	59.432	0.25	26.97	26.86	0.41
131.4649	18.2238	6.9785	1.3280	72.874	4.1314	96.084	60.685	0.27	26.39	26.15	0.90
135.5815	18.2155	8.7087	1.3279	72.901	4.1031	96.688	61.860	0.28	25.95	25.73	0.84
139.6662	18.2082	10.4320	1.3279	72.928	4.0666	97.462	62.964	0.30	25.69	25.45	0.93
126.4530	16.2966	3.8154	1.1869	72.834	4.2098	94.283	59.162	0.17	29.41	29.79	−1.26
130.6765	16.0985	5.0768	1.1729	72.856	4.2449	93.387	60.452	0.19	27.89	27.83	0.21
134.9085	16.0823	6.4036	1.1721	72.879	4.2317	93.468	61.672	0.20	26.93	26.67	0.96
139.1213	16.0846	7.7470	1.1726	72.902	4.2110	93.845	62.820	0.22	26.25	25.99	0.99
143.3060	16.0869	9.0928	1.1732	72.926	4.1806	94.410	63.898	0.23	25.78	25.55	0.92
147.4574	16.0876	10.4346	1.1736	72.951	4.1517	95.028	64.911	0.24	25.43	25.24	0.74
130.2059	14.1938	4.4025	1.0340	72.849	4.3099	92.049	60.312	0.15	30.54	30.34	0.67
134.5362	14.2878	5.4914	1.0412	72.870	4.3446	91.257	61.568	0.16	28.36	27.98	1.33
138.8786	14.3485	6.6081	1.0459	72.892	4.3393	91.358	62.756	0.17	27.18	26.72	1.70
143.2083	14.3826	7.7332	1.0487	72.914	4.3162	91.743	63.874	0.18	26.40	25.98	1.59
147.5123	14.4028	8.8591	1.0505	72.936	4.2922	92.214	64.924	0.19	25.79	25.49	1.14
132.0747	11.7620	4.4567	0.8569	72.854	4.4820	88.512	60.863	0.12	32.14	31.55	1.86
136.5879	11.9194	5.3117	0.8686	72.874	4.5294	87.555	62.138	0.13	29.13	28.63	1.75
141.1204	11.9827	6.1771	0.8735	72.894	4.5279	87.530	63.343	0.14	27.56	27.08	1.74
145.6394	12.0146	7.0439	0.8760	72.915	4.5080	87.872	64.474	0.15	26.57	26.17	1.49
150.1322	12.0316	7.9074	0.8775	72.935	4.4773	88.395	65.535	0.15	25.90	25.58	1.24
132.5996	10.2076	4.3573	0.7437	72.855	4.7041	84.345	61.015	0.11	31.27	31.44	−0.55
137.3223	10.1724	5.0568	0.7413	72.874	4.7362	83.715	62.338	0.11	28.73	28.59	0.47
142.0505	10.1587	5.7565	0.7405	72.893	4.7206	83.850	63.581	0.12	27.26	27.05	0.79
146.7525	10.1507	6.4513	0.7401	72.912	4.6912	84.319	64.743	0.12	26.33	26.12	0.82
151.4228	10.1446	7.1397	0.7399	72.932	4.6574	84.904	65.829	0.13	25.66	25.50	0.63
156.0526	10.1406	7.8212	0.7398	72.952	4.6183	85.575	66.844	0.13	25.19	25.04	0.57
160.6436	10.1369	8.4954	0.7397	72.972	4.5785	86.222	67.795	0.14	24.77	24.69	0.34
165.1919	10.1336	9.1617	0.7397	72.992	4.5417	86.855	68.686	0.14	24.42	24.40	0.08
169.6996	10.1302	9.8204	0.7396	73.012	4.5066	87.610	69.523	0.15	24.30	24.15	0.61
174.1710	10.1264	10.4716	0.7395	73.032	4.4733	88.099	70.311	0.15	23.89	23.94	−0.21
178.6041	10.1225	11.1153	0.7395	73.052	4.4369	88.735	71.055	0.16	23.75	23.76	−0.05
183.0001	10.1189	11.7521	0.7394	73.072	4.4042	89.342	71.757	0.16	23.61	23.60	0.08
187.3635	10.1153	12.3825	0.7393	73.092	4.3729	89.907	72.423	0.17	23.48	23.45	0.10
191.6890	10.1125	13.0069	0.7393	73.112	4.3382	90.510	73.054	0.17	23.43	23.33	0.47
195.9802	10.1105	13.6259	0.7394	73.132	4.3119	91.024	73.653	0.18	23.31	23.21	0.44
200.2466	10.1079	14.2391	0.7394	73.152	4.2886	91.478	74.225	0.18	23.15	23.11	0.18
204.4752	10.1060	14.8466	0.7395	73.172	4.2636	91.925	74.769	0.19	23.01	23.02	−0.02
210.0585	10.1008	15.6420	0.7394	73.198	8.4399	92.646	75.456	0.20	23.06	22.91	0.65
218.3924	10.0959	16.8298	0.7394	73.239	8.3530	93.507	76.421	0.20	22.90	22.77	0.58
226.6318	10.0911	17.9990	0.7395	73.279	8.2747	94.275	77.311	0.21	22.72	22.65	0.29
234.7910	10.0834	19.1453	0.7393	73.319	8.1942	95.062	78.136	0.22	22.66	22.55	0.47
242.8663	10.0801	20.2847	0.7395	73.359	8.1251	95.797	78.902	0.23	22.60	22.47	0.60
250.8702	10.0748	21.4044	0.7395	73.399	8.0608	96.445	79.617	0.24	22.51	22.40	0.53
258.8035	10.0694	22.5096	0.7395	73.439	7.9993	97.065	80.285	0.25	22.46	22.33	0.56
266.6768	10.0636	23.6003	0.7395	73.479	7.9311	97.777	80.912	0.26	22.60	22.28	1.40
274.4971	10.0578	24.6790	0.7394	73.519	7.8800	98.376	81.500	0.27	22.63	22.24	1.74
282.2634	10.0524	25.7471	0.7394	73.558	7.8414	98.751	82.054	0.27	22.40	22.20	0.91
289.9925	10.0466	26.8042	0.7394	73.598	7.7978	99.164	82.577	0.28	22.25	22.16	0.39
297.6971	10.0405	27.8527	0.7394	73.638	7.7563	99.611	83.075	0.29	22.16	22.13	0.12
305.4009	10.0343	28.8964	0.7393	73.679	7.7187	100.111	83.551	0.30	22.15	22.11	0.21
130.8320	8.3415	3.9188	0.6076	72.846	5.0045	79.223	60.498	0.09	30.73	31.55	−2.69
135.8440	8.2185	4.4754	0.5988	72.864	5.0201	79.040	61.933	0.09	28.48	28.47	0.04
140.8426	8.1615	5.0222	0.5948	72.883	4.9925	79.288	63.271	0.10	26.84	26.86	−0.08

Table 4. Experimental single-phase heat capacities—Continued

T K	ρ mol·dm^{-3}	P MPa	N mol	V_{bomb} cm^3	ΔT K	$Q/\Delta T$ J·K^{-1}	C_0[a] J·K^{-1}	Adj.[b]	C_v J·mol^{-1}·K^{-1}	$C_{v,calc}$[c]	Diff.[d] %
145.7985	8.1292	5.5589	0.5926	72.902	4.9437	79.989	64.513	0.10	26.02	25.90	0.46
150.7101	8.1089	6.0866	0.5913	72.920	4.8982	80.696	65.668	0.11	25.32	25.26	0.23
155.5657	8.0962	6.6057	0.5905	72.939	4.8486	81.440	66.740	0.11	24.79	24.79	−0.01
160.3678	8.0871	7.1162	0.5900	72.958	4.7965	82.299	67.739	0.11	24.56	24.42	0.57
165.1232	8.0808	7.6198	0.5897	72.977	4.7509	82.975	68.673	0.12	24.13	24.12	0.04
169.8250	8.0756	8.1153	0.5895	72.996	4.7024	83.729	69.546	0.12	23.93	23.87	0.26
174.4834	8.0714	8.6044	0.5893	73.015	4.6666	84.377	70.365	0.13	23.64	23.66	−0.05
179.1053	8.0673	9.0873	0.5892	73.034	4.6259	85.022	71.136	0.13	23.43	23.47	−0.16
183.6860	8.0631	9.5638	0.5890	73.053	4.5857	85.724	71.864	0.14	23.39	23.31	0.36
190.3080	8.0587	10.2509	0.5889	73.080	9.0408	86.587	72.855	0.14	23.18	23.11	0.32
199.2457	8.0544	11.1748	0.5889	73.118	8.9245	87.626	74.093	0.15	22.84	22.88	−0.19
208.0556	8.0502	12.0803	0.5889	73.156	8.8087	88.670	75.214	0.16	22.70	22.70	−0.01
216.7534	8.0455	12.9687	0.5889	73.193	8.6985	89.692	76.237	0.16	22.68	22.55	0.58
225.3505	8.0409	13.8425	0.5888	73.231	8.6044	90.566	77.177	0.17	22.55	22.43	0.56
233.8541	8.0362	14.7024	0.5888	73.269	8.5230	91.372	78.044	0.18	22.44	22.32	0.51
242.2773	8.0314	15.5501	0.5888	73.306	8.4479	92.085	78.848	0.19	22.28	22.24	0.18
250.6135	8.0268	16.3857	0.5887	73.344	8.3741	92.764	79.595	0.19	22.17	22.17	0.03
258.8895	8.0217	17.2106	0.5886	73.381	8.3097	93.448	80.292	0.20	22.17	22.10	0.31
267.1020	8.0167	18.0258	0.5886	73.419	8.2442	94.122	80.944	0.21	22.24	22.05	0.86
275.2560	8.0116	18.8314	0.5885	73.456	8.1783	94.784	81.556	0.22	22.36	22.00	1.59
283.3544	8.0065	19.6284	0.5884	73.493	8.1280	95.267	82.129	0.22	22.22	21.96	1.18
291.4014	8.0018	20.4184	0.5884	73.531	8.0823	95.733	82.670	0.23	22.09	21.93	0.75
299.4287	7.9968	21.2024	0.5883	73.568	8.0399	96.127	83.183	0.24	21.86	21.90	−0.16
307.4412	7.9916	21.9817	0.5882	73.606	7.9875	96.620	83.674	0.24	21.82	21.87	−0.25
127.3144	6.0901	3.2938	0.4435	72.831	5.4232	73.354	59.431	0.08	31.31	30.48	2.66
132.7254	6.1679	3.7382	0.4493	72.850	5.3865	73.729	61.052	0.08	28.14	27.70	1.56
138.0861	6.1711	4.1600	0.4497	72.868	5.3243	74.524	62.544	0.08	26.57	26.21	1.37
143.3730	6.1676	4.5679	0.4495	72.886	5.2530	75.465	63.915	0.08	25.62	25.32	1.18
148.5902	6.1628	4.9645	0.4493	72.904	5.1815	76.438	65.178	0.09	24.98	24.73	1.02
153.7331	6.1594	5.3516	0.4492	72.922	5.1152	77.392	66.343	0.09	24.51	24.29	0.90
158.8084	6.1569	5.7305	0.4491	72.941	5.0505	78.312	67.421	0.10	24.16	23.95	0.84
163.8194	6.1554	6.1022	0.4491	72.959	4.9947	79.120	68.422	0.10	23.72	23.68	0.19
168.7682	6.1542	6.4671	0.4491	72.977	4.9387	79.975	69.354	0.10	23.54	23.45	0.41
173.6621	6.1533	6.8261	0.4492	72.995	4.8845	80.791	70.223	0.11	23.42	23.25	0.71
178.5030	6.1525	7.1796	0.4492	73.013	4.8418	81.426	71.038	0.11	23.01	23.08	−0.31
183.2876	6.1519	7.5277	0.4493	73.031	4.7966	82.111	71.802	0.11	22.83	22.93	−0.46
188.0301	6.1506	7.8706	0.4493	73.050	4.7514	82.818	72.522	0.12	22.80	22.81	−0.03
192.7222	6.1498	8.2091	0.4494	73.068	4.7141	83.461	73.200	0.12	22.71	22.69	0.10
197.3785	6.1487	8.5435	0.4494	73.086	4.6762	84.077	73.843	0.12	22.65	22.59	0.27
201.9963	6.1476	8.8742	0.4494	73.104	4.6439	84.619	74.453	0.13	22.50	22.50	−0.02
206.5742	6.1467	9.2013	0.4495	73.122	4.6119	85.171	75.032	0.13	22.43	22.42	0.04
211.1170	6.1455	9.5246	0.4495	73.140	4.5784	85.692	75.583	0.13	22.35	22.35	0.03
215.6256	6.1443	9.8447	0.4495	73.157	4.5517	86.159	76.109	0.14	22.22	22.28	−0.29
225.9475	6.1421	10.5756	0.4496	73.199	8.9395	87.304	77.239	0.14	22.23	22.15	0.34
234.7724	6.1397	11.1968	0.4496	73.235	8.8400	88.190	78.134	0.15	22.19	22.06	0.60
243.4888	6.1378	11.8087	0.4497	73.270	8.7463	88.958	78.959	0.16	22.06	21.98	0.34
252.1201	6.1352	12.4110	0.4497	73.306	8.6624	89.740	79.725	0.16	22.11	21.92	0.87
260.6670	6.1324	13.0049	0.4498	73.341	8.5795	90.456	80.437	0.17	22.15	21.86	1.32
269.1402	6.1297	13.5919	0.4498	73.377	8.5140	91.088	81.100	0.18	22.12	21.81	1.41
277.5386	6.1271	14.1718	0.4498	73.412	8.4513	91.647	81.720	0.18	22.02	21.77	1.16
285.8948	6.1237	14.7451	0.4498	73.447	8.3925	92.204	82.303	0.19	21.99	21.73	1.16
294.1859	6.1206	15.3127	0.4498	73.483	8.3413	92.662	82.851	0.19	21.77	21.70	0.32
302.4355	6.1171	15.8745	0.4497	73.518	8.2861	93.249	83.370	0.20	21.88	21.68	0.92

[a] Derived from Eq. (3). $C_0 = dQ_0/dT$.
[b] Equation (6).
[c] Reference [8].
[d] 100 $(C_v - C_{v,calc})/C_v$.

While we have observed that $C_v^{(2)}$ values are a function of both T and ρ, C_σ values are a function of T only. Hence, C_σ data provide us with a valuable check of the accuracy of our measurements by direct comparison with published data. Figure 4 shows the behavior of C_σ from near the N_2 triple point to near the critical point temperature where it rises sharply. Also shown in Fig. 4 are results of Weber [2] and Giauque and Clayton [3], whose data have uncertainties of ±0.5% and ±1%, respectively. In order to intercompare the data sets, our data were fitted to the expression,

$$C_\sigma = a + bT + cT^2 + dT^3 + eT/\sqrt{T - T_c} \ . \qquad (7)$$

The coefficients of Eq. (7) are given in Table 5. Deviations of the C_σ data of Refs. [2] and [3] from this expression were calculated also. The data of Refs. [2] and [3] were the most accurate available. This work overlaps the temperature range of both previous studies. The deviations of all the C_σ measurements from Eq. (7) are shown in Fig. 5. We may conclude from Fig. 5 that the data of Refs. [2] and [3] are consistent with this work within ±1% with 95% of these data within ±0.2%.

It is also important to examine the internal consistency of our data. Perhaps the most interesting test of the internal consistency of the data derives from the relation

$$C_v^{(2)}/T = -\mathrm{d}^2\mu/\mathrm{d}T^2 + V_m\, \mathrm{d}^2P_\sigma/\mathrm{d}T^2 \qquad (8)$$

due to Yang and Yang [12], where μ is the chemical potential and V_m is the molar volume. This thermodynamic relation implies that when plotted on isotherms, $C_v^{(2)}/T$ should be linear versus molar volume. To simplify this test, the measured $C_v^{(2)}$ data in Table 3 were fitted to the expression,

$$C_v^{(2)} = a + bT + cT^2 + dT/(T - T_c)^{0.1} \qquad (9)$$

and new values were computed at integral temperatures from 65 to 125 K. Selected $C_v^{(2)}$ isotherms are shown in Fig. 6. We have observed that $C_v^{(2)}$ varies linearly with V_m within the experimental precision (±0.15%) of the data.

Table 5. Coefficients of the function $C_\sigma(T)$, Eq. (7)[a,b]

Coefficient	Value
a	0.469355×10^{2}
b	0.211629×10^{0}
c	-0.490463×10^{-4}
d	0.184354×10^{-4}
e	0.129524×10^{1}

[a] Units are $J \cdot mol^{-1} \cdot K^{-1}$ and K.
[b] Temperature range is 64 to 118 K.

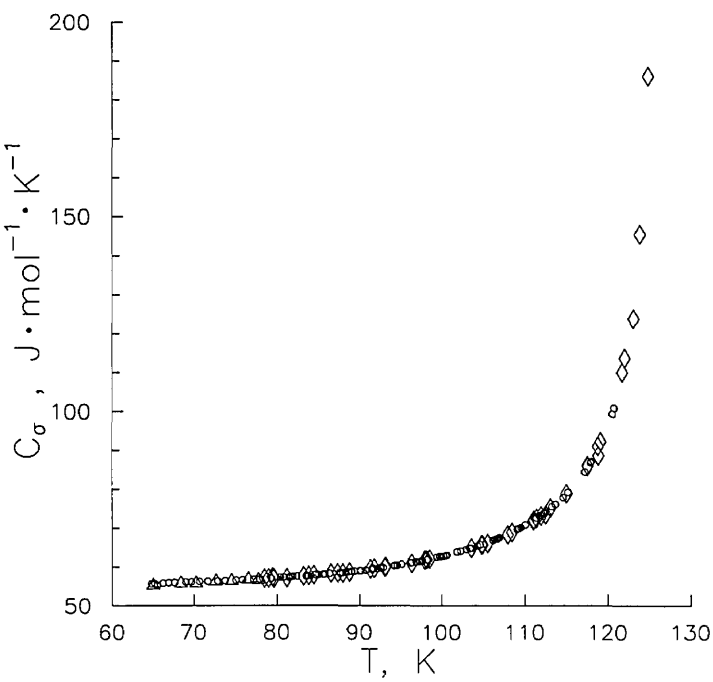

Figure 4. Saturated liquid heat capacity: Weber [2] (◇); Giauque and Clayton [3] (Δ); this work (○).

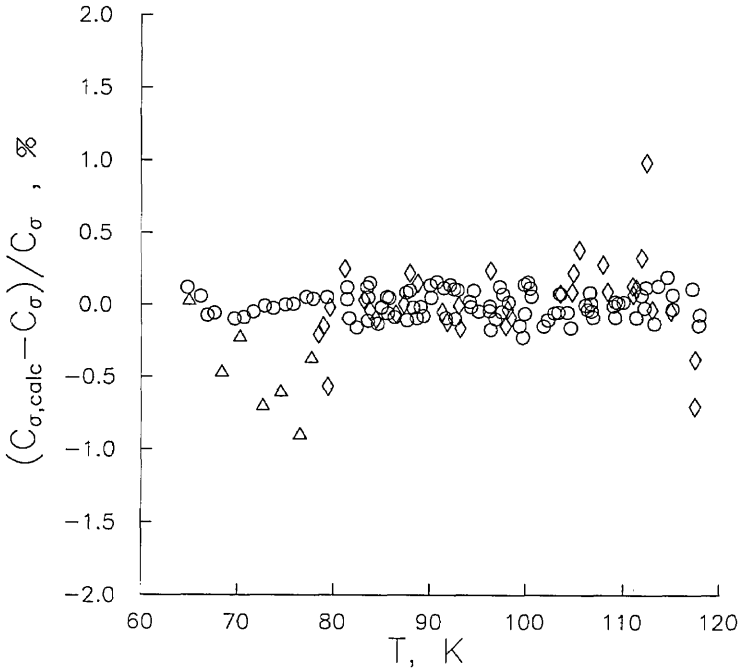

Figure 5. Deviations of saturated liquid heat capacity from Eq. (7): Weber [2] (◇); Giauque and Clayton [3] (Δ); this work (○) used in fit.

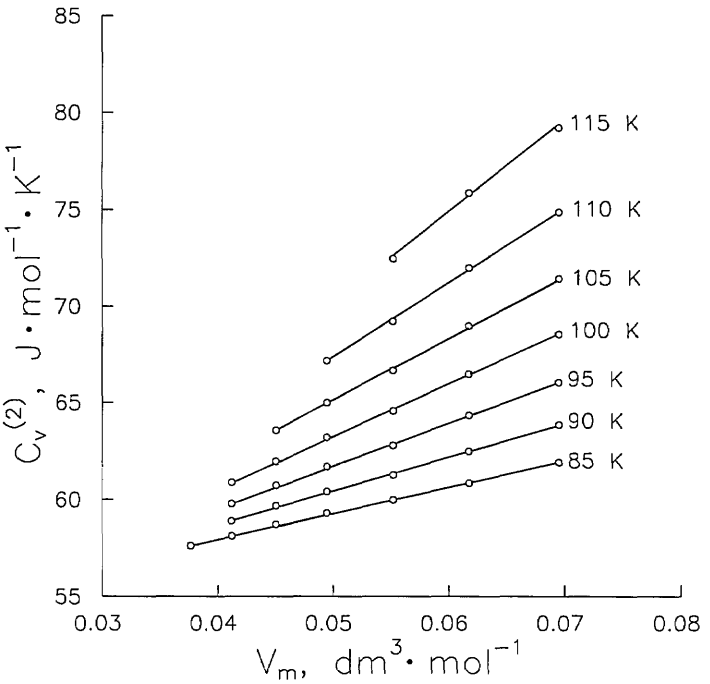

Figure 6. Two-phase heat capacity $C_v^{(2)}$ interpolated to integral temperatures.

Further, we have obtained values of d^2P_σ/dT^2 at integral temperatures, given in Table 6. Also shown in Table 6 are experimental values from Weber [2] and calculated values of this derivative which are from published vapor pressure equations [8,13]. The agreement of this work with published values is better than $\pm 3 \times 10^{-5}$ MPa · K^{-2}.

Table 6. Comparison of the vapor pressure second derivatives d^2P/dT^2 from heat capacity measurements with published experimental values and with values from vapor pressures

	$(d^2P/dT^2) \times 10^5$ MPa · K^{-2}			
	Experimental		Calculated	
T, K	This work	Weber [2]	Jacobsen et al. [8]	Goodwin [13]
85	157		158	158
90	192	195	194	194
95	232		231	232
100	270	270	270	271
105	308		310	312
110	353	355	354	355
115	409		407	403

Values of the molar heat capacity at constant volume are depicted in Fig. 7. Shown in this plot are single-phase C_v isochores at each of the 14 different filling densities of this work. As expected, C_v increases with density up to the critical density (approx. 11.21 mol · dm^{-3}), where it has a maximum value. Then at densities between the critical and twice the critical, C_v decreases to a local minimum value. These data are found in Table 4. Also given in Table 4 is a column labeled "diff." which gives the percent difference of this work from the equation of state in Ref. [8]. The authors of the equation of state estimate an accuracy of ±2% for their calculated heat capacities. With only a few exceptions, these calculations are in fact within ±2% of the data. Most significantly, however, in the temperature range from 66 to 78 K, the values calculated with their equation fall 1 to 5% below the results of this study. Undoubtedly, accuracies would be improved by a new fit of the equation of state which includes this data.

At highly compressed liquid densities greater than twice critical, C_v shows a rising trend which is indicative of hindered rotation of N_2 molecules. A broad generalization can be made for low molecular mass gases with regard to the existence of a minimum liquid C_v at 2.0 ρ_c. If we examine a plot of reduced residual heat capacity $(C_v - C_v^0)/R$ at saturated liquid states versus reduced density ρ/ρ_c, shown in Fig. 8, we find identical behavior for Ar [14], O_2 [14], and N_2. A single parabola represents data for these three gases within experimental error. As shown by Fig. 8, the vertex of this parabola is found at 2.0 ρ_c. I have not found a satisfactory

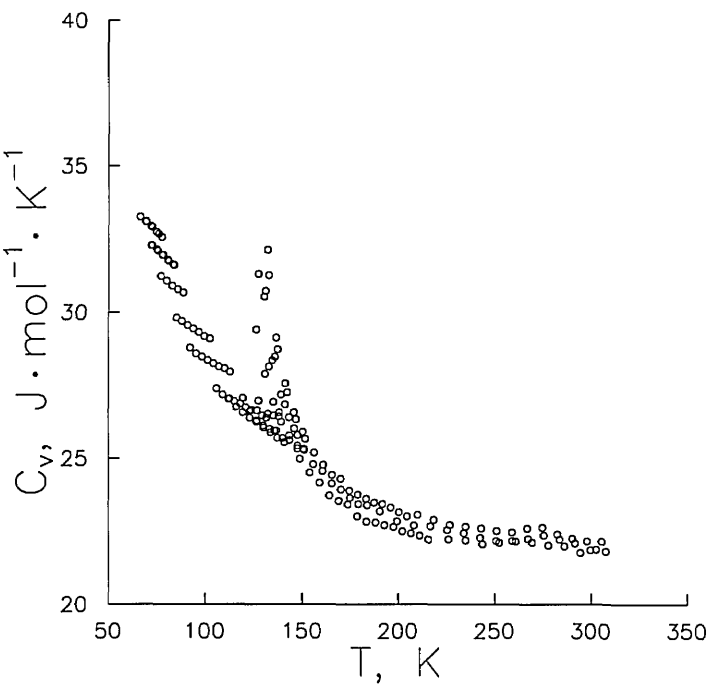

Figure 7. One-phase heat capacity C_v at fourteen filling densities.

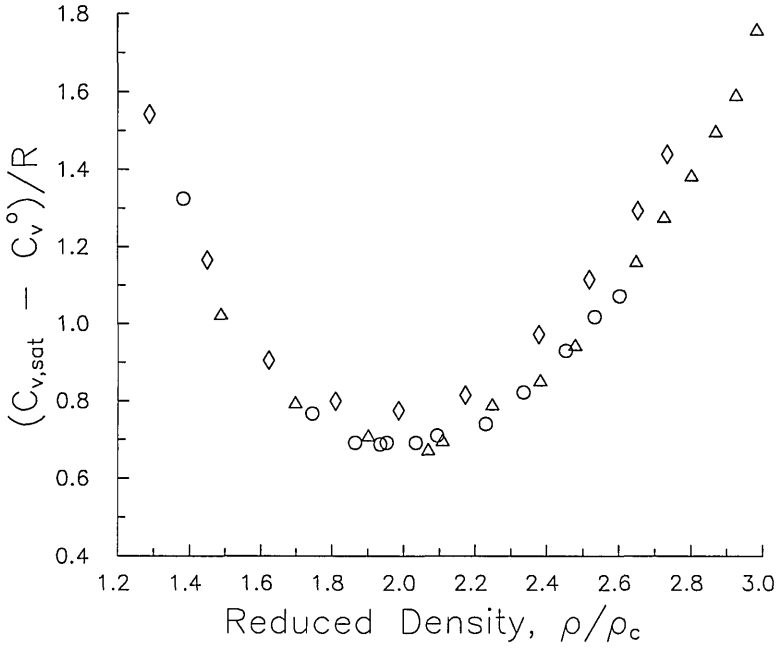

Figure 8. Reduced residual heat capacity evaluated at saturation plotted against reduced density; Ar (O) Ref. [14]; O_2 (Δ) Ref. [14]; N_2 (◇) this work.

explanation of this phenomenon based on firmly grounded theory. Further study is expected to lead to new insight and understanding of the behavior of liquid heat capacities.

4. Analysis of Errors

Uncertainty in C_v arises from several sources. Primarily, the accuracy of this method is limited by how accurately we can measure the temperature rise. The platinum resistance thermometer has been calibrated on the IPTS-68 by NIST, with an uncertainty of ±0.002 K due to the calibration. Other factors, including gradients on the bomb, radiation to the exposed head of the thermometer, and time-dependendent drift of the ice point resistance lead to an overall uncertainty of $\sigma_t = \pm 0.03$ K for the absolute temperature measurement. Uncertainty estimates of the relative temperature, however, are derived quite differently. The temperatures assigned to the beginning (T_1) and to the end (T_2) of a heating interval are determined by extrapolation of a linear drift (approximately −0.0005 K min^{-1}) to the midpoint time of the interval. This procedure leads to an uncertainty of ±0.002 K for T_1 and T_2, and consequently ±0.004 K for the temperature rise, $\Delta T = T_2 - T_1$. For a typical experimental value of ΔT of 4 K, this corresponds to an uncertainty of ±0.1%. The energy applied to the calorimeter is the integral of the product of the applied potential and current from the initial to the final heating time; its uncertainty is ±0.01%. The energy applied to the empty calorimeter has been measured in repeated experiments and fitted to a function of temperature; the estimated uncertainty is ±0.02%. However, the adjustment is considerably larger for vapor than for liquid. For low density vapor the ratio Q_0/Q is as large as 0.89, while for the highest density liquid it is as low as 0.27 . This leads to considerably larger (approximately 10 times) uncertainty propagated to the heat capacity measurements for vapor states. The number of moles of each sample was determined within ±0.2%. A correction for PV work on the bomb leads to an additional ±0.02% uncertainty. For pressures, the uncertainty due to the piston gauge calibration (±0.05% max.) is added to the cross term $[(\sigma_t)(dP/dT)_\rho]$ to yield an overall maximum probable uncertainty which varies from ±0.06 to ±0.8%, increasing steadily with the slope of the $P(\rho, T)$ isochore to a maximum at the highest density and lowest pressure of the study. However, the pressure uncertainty does not appreciably contribute to the overall uncertainty for molar heat capacity. By combining the various sources of experimental uncertainty, I estimate the maximum uncertainty in C_v which ranges from ±2.0% for vapor to ±0.5% for liquid.

5. Appendix 1. Calorimeter Volumes

A knowledge of the volumes of connecting tubing, couplings, valves, and so on is a valuable aid when deducing certain adjustments to raw measurements. The bomb volume is the same as reported in detail by Goodwin and Weber [9] and is given as a function of temperature and pressure by

$$V_{\text{bomb}} = V_r(1.0 + 3.0(C_1 + C_2 T_r)e^{\alpha(1-1/T_r)} + kT_r^{1/3}P) \quad (10)$$

where

$V_r = 72.657$ cm^3, $T_r = T/100$, $C_1 = -2.1461 \times 10^{-4}$, $C_2 = 5.9455 \times 10^{-4}$, $\alpha = 1.01062$, and $k = 1.09548 \times 10^{-4}$ MPa^{-1}. The appropriate units to be used with Eq. (10) are temperature in K and pressure in MPa.

For this apparatus, all elements of volume except for the bomb are called noxious volumes. Extensive changes were made to the noxious volumes prior to this work. In Fig. 1, the bomb is connected to the pressure transducer with a 71 cm length of fine bore (ID = 0.015 cm) capillary tubing, which passes vertically from the cryostat. Of this length, 62.5 cm is outside the adiabatic zone of the calorimeter. This volume (0.01295 cm^3) is combined with contributions from a three-port valve (0.008 cm^3), an additional 8.79 cm length of medium bore (ID = 0.051 cm) capillary (0.0178 cm^3), and the pressure transducer (0.0745 cm^3) for a total noxious volume of 0.1132 cm^3. In the worst case, the total noxious volume is only about 0.15% of the bomb volume. These last three volumes are thermostatted in an aluminum block oven, and maintained by a proportional controller at 320.0 ± 0.05 K. This oven serves two purposes. It provides a stable environment for the internal electronics of the pressure transducer and it fixes the temperature of the upper end of the 71 cm long capillary at a temperature sufficient to drive the vapor-liquid meniscus down to near the guard ring. Since only vapor resides in most of the noxious volumes, the ratio of the number of moles in these volumes to those in the bomb ranges from 1 part in 10^4 for vapor to 1 part in 10^6 for liquid.

Acknowledgments

I thank J. E. Mayrath for fitting the empty calorimeter heat capacity data. I have benefitted from numerous discussions with L. A. Weber, R. D. Goodwin, D. E. Diller, B. A. Younglove, H. M. Roder, R. A. Perkins, J. F. Ely, and W. M. Haynes.

6. References

[1] A. V. Voronel, V. G. Gorbunova, Yu. R. Chashkin, and V. V. Shchekochikhina, Sov. Phys. JETP **23**, 597–601 (1966).
[2] L. A. Weber, J. Chem. Thermodyn. **13**, 389–403 (1981).
[3] W. F. Giauque and J. O. Clayton, Am. Chem. Soc. **55**, 4875–4889 (1933).
[4] R. Wiebe and J. M. Brevoort, J. Am. Chem. Soc. **52**, 622 (1930).
[5] R. D. Goodwin, J. Res. Natl. Bur. Stand. (U.S.) **65C**, 231–243 (1961).
[6] H. M. Roder, J. Res. Natl. Bur. Stand. (U.S.) **80A**, 739–759 (1976).
[7] J. E. Mayrath, unpublished data, 1990.
[8] R. T. Jacobsen, R. B. Stewart, and M. Jahangiri, J. Phys. Chem. Ref. Data **15**, 735–909 (1986).
[9] R. D. Goodwin and L. A. Weber, J. Res. Natl. Bur. Stand. (U.S.) **73A**, 1–24 (1969).
[10] J. G. Hust, B. J. Filla, and D. R. Smith, J. Thermal Ins. **11**, 102–107 (1987).
[11] J. E. Mayrath and J. W. Magee, J. Chem. Thermodyn. **21**, 499–513 (1989).
[12] C. N. Yang and C. P. Yang, Phys. Rev. Lett. **13**(9), 303–305 (1964).
[13] R. D Goodwin, J. Res. Natl. Bur. Stand. (U.S.) **73A**, 487 (1969).
[14] B. A Younglove, J. Res. Natl. Bur. Stand. (U.S.) **78A**, 401–410 (1974).

About the author: J. W. Magee is a chemical engineer in the Thermophysics Division of the NIST Chemical Science and Technology Laboratory at Boulder.

Volume 96, Number 6, November–December 1991
Journal of Research of the National Institute of Standards and Technology

[J. Res. Natl. Inst. Stand. Technol. 96, 741 (1991)]

A Standard Reference Material for Calibration of the Cup Furnace Smoke Toxicity Method for Assessing the Acute Inhalation Toxicity of Combustion Products

Volume 96 | Number 6 | November–December 1991

Barbara C. Levin, Maya Paabo, and Susannah B. Schiller

National Institute of Standards and Technology,
Gaithersburg, MD 20899

A standard reference material (SRM 1048) has been developed for use with the cup furnace smoke toxicity method. This SRM is to be used to calibrate the apparatus and to enable the user to have confidence that the method is being conducted in a correct manner and that the equipment is functioning properly. The toxicological results from this SRM should not be used to compare with those of other materials (i.e., to determine if the combustion products of a test material are more or less toxic than those from this SRM). SRM 1048 is an acrylonitrile-butadiene-styrene (ABS) and is the same as SRM 1007B which is used for calibrating the flaming mode of the Smoke Density Chamber test method (ASTM E-662 and NFPA 258). For the purposes of calibrating the cup furnace smoke toxicity method, LC_{50} and N-Gas values plus their respective 95% confidence limits have been determined and certified for two combustion modes (flaming and nonflaming) and two observation periods (for the 30 min exposure only and for the 30 min exposure plus a 14 d post-exposure period). The certified LC_{50} values plus 95% confidence intervals (in g/m^3) are 27 ± 3 (30 min, flaming); 25 ± 3 (30 min + 14 d, flaming); 58 ± 15 (30 min, nonflaming); and 53 ± 12 (30 min + 14 d, nonflaming). The certified N-Gas values plus 95% confidence intervals are 1.4 ± 0.2 (30 min, flaming); 1.5 ± 0.2 (30 min + 14 d, flaming); 1.2 ± 0.2 (30 min, nonflaming); and 1.4 ± 0.2 (30 min + 14 d, nonflaming). It is recommended that this SRM be used with the N-Gas approach to calibrate the cup furnace smoke toxicity method rather than to determine the complete LC_{50} values. The N-Gas approach has the advantage of providing information on the gases responsible for the lethalities as well as the toxic potency of the smoke. In addition, the N-Gas approach reduces the number of experimental animals, the time necessary to complete the calibration, and the expense.

Key words: ABS; acrylonitrile-butadiene-styrene; combustion; combustion products; cup furnace; inhalation; SRM; standard reference material; toxicity tests.

Accepted: August 2, 1991

1. Introduction

The United States has one of the worst fire lethality rates in the industrialized world [1]. Eighty percent of these fire deaths are caused, not by burns, but by the inhalation of toxic smoke (gases plus particulates) [2]. The past decade has seen the development of a number of methods to measure the toxic potency of the combustion atmospheres produced from the thermal decomposition of materials [3]. In the United States, two of these methods have been used more extensively than the others. The first, known as the cup furnace smoke toxicity method [4,5], was developed at the Center for Fire Research (CFR), National Bureau of Standards (NBS), now the Building and Fire Research

Laboratory (BFRL), National Institute of Standards and Technology (NIST). The second was developed at the University of Pittsburgh under a grant from NIST and is called the University of Pittsburgh smoke toxicity method [6]. Neither the cup furnace smoke toxicity method nor the University of Pittsburgh smoke toxicity method have been accepted as standardized tests by ASTM or any other national or international scientific or technical society designed to develop standard test procedures. At the present time, the development of other smoke toxicity methods is still being actively pursued.

The number of smoke toxicity test apparatus users has increased. New York State has passed legislation requiring the testing of various materials before permitting their use in buildings [7]. Several other states are considering similar legislation. The test required by New York State is the one developed by the University of Pittsburgh. The U.S. Navy has recently specified the use of the cup furnace smoke toxicity apparatus for testing materials being considered for use in submarines [8]. A number of Federal agencies, industrial laboratories and testing companies are capable of conducting both test procedures.

Since the results of these smoke toxic potency tests, along with the results of other material flammability tests, are to be used in the decision making process regarding material selection and overall fire hazard, it is necessary to assure that such testing devices are installed and employed properly both by those laboratories currently conducting these tests and by new laboratories which enter the field. To help assure the reproducibility of results between laboratories, NIST has developed a SRM which can be used by all laboratories to calibrate the cup furnace smoke toxicity method. *It is important to note that this SRM was not selected to represent the toxic potency of the combustion products of an "average" material and is not designed to be used for the comparison of the relative toxic potency of the combustion products of test materials. In other words, the toxic potency of the smoke from a test material should not be compared to the toxic potency of the smoke from this SRM.*

The following criteria were used in the selection process of this SRM:

1. The material should have reproducible burning characteristics, regardless of the nature of the furnace (i.e., the material must be homogeneous and thus man-made).
2. The material should produce combustion products whose toxic potency values are within the range where the values for most materials are found.
3. Upon combustion, toxic gases in addition to CO should be generated and contribute to the lethal atmospheres.
4. The selected material should generate combustion products which cause deaths during the exposures or within 24 h following the exposures, since post-exposure deaths beyond this time are much less reproducible.

This report documents the research and development of a SRM for calibration of the overall test procedure and to assure that the cup furnace smoke toxicity apparatus is being used correctly. An acrylonitrile-butadiene-styrene (ABS) polymer whose characteristics fit the above criteria was selected. To perform this calibration, each laboratory would: 1. determine the LC_{50} values and compare them with the published certified LC_{50} values or 2. determine the N-Gas values (at the published certified LC_{50} values) and compare them with the certified N-Gas values. In the N-Gas approach, one or two animal tests are conducted at the certified LC_{50} values to assure that some percentage (not 0 and not 100%) of the animals respond. The calibration is conducted under two combustion modes (flaming and nonflaming) and two observation periods (a 30 min exposure and a 30 min exposure plus a 14 d post-exposure period). If the experimental values obtained by the laboratory fall within the 95% confidence intervals of the published certified values of this SRM, the investigator can be confident that the method is being conducted correctly.

2. Materials and Methods

2.1 Materials

A number of materials were screened before the decision to use an ABS polymer was made. The initial ABS that was selected for testing was standard reference material SRM 1007A used for calibrating the flaming mode in the ASTM E-662 and NFPA 258 test method to determine smoke density [9,10]. We found that this material exhibited suitable characteristics and fit the above criteria. However, during the experimental phase of this study, the stock of SRM 1007A was depleted. To conserve expense, the decision was made to obtain an ABS

material suitable for SRMs for both the cup furnace smoke toxicity procedure and the smoke density chamber.

Three different ABS samples (ABS 2, ABS 3, and ABS 4) with formulations believed to be similar to SRM 1007A were sequentially prepared by a commercial manufacturer and tested in both the toxicity and smoke density apparatuses. Only ABS 4 proved to be suitable for both systems, and the manufacturer was asked to prepare a production lot, designated ABS 5 in this paper, for certification and sale as an SRM. ABS 4 and ABS 5 were thus presumably the same. In addition to acrylonitrile-butadiene-styrene, formulations 4 and 5 contained 6% titanium dioxide by weight. The ABS 5 was prepared by the manufacturer in sheets that were 254×254 mm (10×10 in) with a measured nominal thickness of 0.762 mm (0.030 in). The thickness was an important factor for the ASTM E-662 and NFPA 258 Smoke Density Chamber tests. The sheets of the production lot of ABS 5 were randomly numbered when received by NIST. The final cup furnace smoke toxicity SRM certified for sale is designated SRM 1048.

2.2 Gases

The cup furnace smoke toxicity method includes the chemical analysis of the following gases: CO, CO_2, HCN, O_2, HCl, and HBr. (The latter two halogen gases should be monitored if the material is known or suspected of generating these gases when thermally decomposed. The ABS samples tested for this SRM do not generate any HCl or HBr.) If the instrumentation is available, the concentration of NO_x (both NO and NO_2) may also be measured when nitrogen-containing materials, such as ABS, are being tested.

The calibration gases (CO, CO_2, HCN) utilized in the research and development of this SRM were commercially supplied in various concentrations in nitrogen. The concentrations of HCN in the commercially supplied cylinders were routinely checked by silver nitrate titration [11], since it is known that the concentration of HCN stored under these conditions will decrease with time. Nitric oxide (NO) in nitrogen, a standard reference material, was obtained from the Gas and Particulate Science Division, NIST.

Carbon monoxide and carbon dioxide were measured continuously during each test by non-dispersive infrared analyzers. Oxygen concentrations were measured continuously with a paramagnetic analyzer. Syringe samples (100 μl) of the chamber atmosphere were analyzed for HCN approximately every 3 min with a gas chromatograph equipped with a thermionic detector [12]. The concentration of NO_x was measured continuously by a chemiluminescent NO_x analyzer with a sampling rate of 25 ml/min. All combustion products and gases (except HCN and NO_x) that were removed for chemical analysis were returned to the chamber. The CO, CO_2, O_2, and NO_x data were recorded by an on-line computer every 15 s.

The presence of HCN in the combustion atmospheres interfered with the NO_x analysis when the chemiluminescent analyzer was equipped with a stainless steel converter. A change of the stainless steel converter to a molybdenum (Mo) converter (set at 375 °C) prevented this interference from HCN. The amounts of NO and NO_2 in the NO_x can be distinguished by allowing the sample gas to pass through the converter (gives results for total NO_x) or to bypass the converter (gives only NO results). The amount of NO_2 is calculated from the difference of the two signals.

For each experiment, the reported gas concentrations are the time-integrated average exposure values which were calculated by integrating the area under the instrument response curve and dividing by the exposure time (i.e., (ppm×min)/min or, in the case of O_2, (%×min)/min). The calculated CO and CO_2 concentrations are accurate to within 100 and 500 ppm, respectively. The calculated HCN concentrations are accurate to 10% of the HCN concentration. The calculated NO_x concentrations are accurate to 10% of the NO_x concentration.

2.3 Animals

Fischer 344 male rats, weighing 200–300 g, were obtained from Taconic Farms (Germantown, NY).[1] They were allowed to acclimate to our laboratory conditions for at least 10 d prior to experimentation. Animal care and maintenance were performed in accordance with the procedures outlined in the National Institutes of Health's "Guide for the Care and Use of Laboratory Animals." Each rat was housed individually in suspended stainless steel cages and provided with food (Ralston Purina Rat Chow 5012) and water *ad libitum*. Twelve

[1] Certain commercial equipment, instruments, or materials are identified in this paper to specify adequately the experimental procedure. Such identification does not imply recommendation or endorsement by the National Institute of Standards and Technology, nor does it imply that the materials or equipment identified are necessarily the best available for the purpose.

hours of fluorescent lighting per day were provided using an automatic timer.

2.4 Cup Furnace Smoke Toxicity Procedure

All exposures were conducted using the combustion system, the chemical analysis system, and the animal exposure system that were designed for the cup furnace smoke toxicity method [4]. Figures 1 and 2 are a diagram and schematic drawing of the experimental arrangement, respectively. The cup furnace is shown in Fig. 3. The samples were decomposed in the cup furnace located directly below the animal exposure chamber such that all the combustion products from the test sample evolved directly into the chamber. To prepare the test samples, the ABS sheets were cut into pieces approximately 2.54 cm^2 (1 in^2). Multiple squares were used to obtain the desired test concentration (defined as grams of material placed into the furnace divided by the exposure chamber volume in meters, i.e., g/m^3 or mg/l).

Tests were conducted in both flaming and nonflaming modes. The autoignition temperature of ABS was determined according to the procedure described in the cup furnace smoke toxicity method [4] and the furnace was set approximately 25 °C below or above this autoignition temperature for the nonflaming or flaming modes, respectively. In the flaming tests, a sparker was also used to ensure that the ABS sample would flame as early as possible. This sparker was not used in the determination of the autoignition temperature.

The cup furnace smoke toxicity method is a closed design in which all the gases and smoke are kept in a 200 L rectangular chamber for the duration of the experiment. Six rats are exposed in each experiment. Each animal is placed in a restrainer and inserted into one of six portholes located along the front of the exposure chamber such that only the heads of the animals are exposed. In the experiments conducted to determine LC_{50} values, animal exposures started when the weighed sample was dropped into the preheated cup and continued for 30 min. The quartz cup which fits into the furnace and test specimen were weighed before and after the exposure to determine the mass of material consumed.

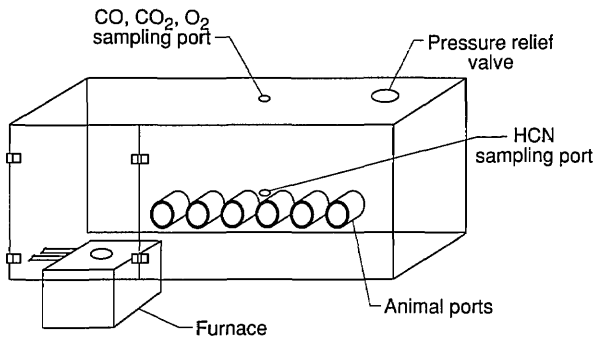

Fig. 1. Cup furnace smoke toxicity exposure chamber.

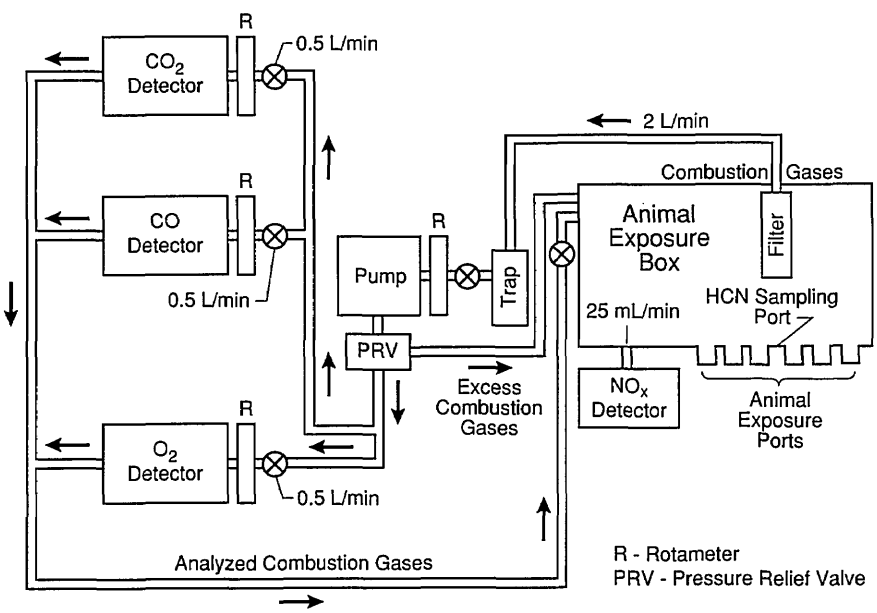

Fig. 2. Schematic of cup furnace smoke toxicity exposure chamber with attached analytical equipment.

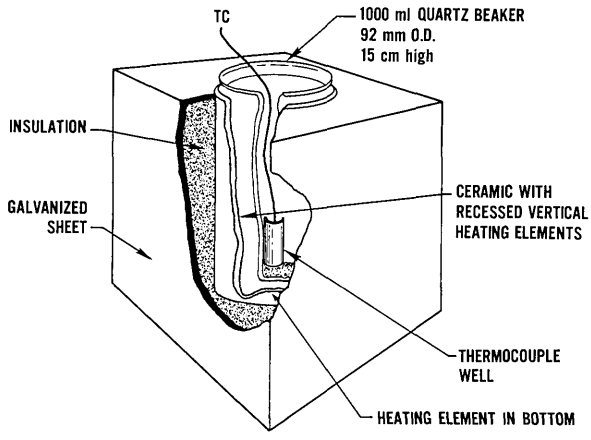

Fig. 3. Cup furnace.

The toxicological endpoint was death, which occurred either during the 30 min exposures or the 30 min exposure plus 14 d post-exposure observation period.[2] The percentage of animals dying at each fire effluent concentration was plotted to produce a concentration-response curve from which LC_{50} values were calculated for both the 30 min exposures and for the 30 min plus 14 d post-exposure observation period. The LC_{50} in these cases is defined as the mass of material placed in the furnace divided by the exposure chamber volume (g/m^3) which caused 50% of the animals to die during the exposure only or during the exposure plus the 14 d post-exposure observation period. The LC_{50} values and their 95% confidence limits shown in Tables 2 through 6 were calculated by the statistical method of Litchfield and Wilcoxon [13]. The LC_{50} values provided in Tables 7 and 8 were calculated using probit analysis as described in Finney [14]. All animals (including the controls) were weighed daily from the day of arrival until the end of the 14 d post-exposure observation period.

[2] Under our experimental conditions, the rats exposed to the combustion products of ABS 5 died either during the exposure or within 24 h. However, we routinely use a 14 d post-exposure observation period. If animals were to die during the 13 d period after the first 24 h following exposure to the ABS 5 smoke, it may be indicative that something in addition to the smoke exposure was affecting the animals (e.g., the animals may be harboring an unknown pathogen). This could be important information to prevent misinterpretation of one's data when similar deaths occur following exposures to the smoke from other materials.

2.5 N-Gas Model Prediction

The current N-Gas Model [15–18] equation is based on the studies at NIST of the toxicological interactions of six gases, CO, CO_2, HCN, reduced O_2, HCl, and HBr, and is used to estimate the amount of material (either loaded or consumed) necessary to produce an LC_{50} for a 30 min exposure or a 30 min exposure plus a 14 d post-exposure period. LC_{50} values for other exposure times can also be used. The model prediction is based on the following empirical mathematical relationship:

$$\text{N-Gas Value} = \frac{m[\text{CO}]}{[\text{CO}_2]-b} + \frac{[\text{HCN}]}{LC_{50}\,\text{HCN}} + \frac{21-[\text{O}_2]}{21-LC_{50}\,\text{O}_2} + \frac{[\text{HCl}]}{LC_{50}\,\text{HCl}} + \frac{[\text{HBr}]}{LC_{50}\,\text{HBr}} \qquad (1)$$

where the numbers in brackets are time-integrated average atmospheric concentrations during a 30 min exposure period [(ppm × min)/min or for O_2 (% × min)/min]. We have found that CO_2 acts synergistically with all toxic gases tested to date. However, empirically, we found that the CO_2 term can be used in the equation only once. Therefore, the CO_2 effect is utilized with the CO factor since CO is found in all fires and we have the most data on the CO and CO_2 synergism [19]. As the concentration of CO_2 increases [up to 50,000 ppm (5%)], the toxicity of CO increases. Above 50,000 ppm, the toxicity of CO starts to decrease again. The terms m and b define this synergistic interaction and equal -18 and 122000, if the CO_2 concentrations are 50,000 ppm or less. For studies in which the CO_2 concentrations are above 50,000 ppm, m and b equal 23 and -38600, respectively. The LC_{50} concentration of HCN is 200 ppm for 30 min exposures or 150 ppm for 30 min exposures plus 14 d post-exposure deaths. The 30 min exposure with or without the 14 d post-exposure LC_{50} value for O_2 is 5.4%. Ideally, when this equation is unity, 50% of the animals should die. Examination of our animal lethality data for the three and four gas combinations indicate that the mean N-Gas value where animal deaths occur is 1.1 with a standard deviation of ±0.1. We have found in the pure gas work that one half of the animals are likely to die when the N-Gas value is approximately 1.1, no animals usually die below 0.9 and all the animals usually die above 1.3.

The N-Gas Model has been developed into an N-Gas Method for predicting the concentration of material which would produce an LC_{50} [15,16]. This

method reduces the time necessary to evaluate a material and the number of test animals needed for the toxic potency determination. It also indicates whether the toxicity is usual (i.e., the toxicity can be explained by the measured gases) or is unusual (i.e., additional gases are needed to explain the toxicity). The N-Gas approach has been shown to work well under different combustion systems (radiant as well as convective heat sources; bench-scale as well as full-scale room tests) [20–23].

To measure the toxic potency of a given material with this N-Gas Method, a sample is combusted under the conditions of concern (e.g., nonflaming or flaming) and the principal gaseous components (CO, CO_2, HCN, reduced O_2, HCl, and HBr) of the smoke measured. Based on the results of the chemical analytical tests and the knowledge of the interactions of the measured gases, an estimated LC_{50} value is calculated. If the N-Gas approach is to be used as a screening test, then in one or two further tests, six rats are exposed to the smoke from a sample of such size that the smoke should produce an atmosphere in which the N-Gas value would be less than or equivalent to 0.8. The deaths of some of the animals indicates the presence of one or more unknown toxicants. If more accuracy is needed, a detailed LC_{50} can be determined. An N-Gas value (at the LC_{50}) above 1.3 suggests that a toxicological antagonism is occurring.

The screening test, however, is not appropriate if one wants to use the N-Gas approach with the ABS SRM 1048 to calibrate the cup furnace smoke toxicity method. In this case, N-Gas values equivalent to the actual LC_{50}s for the ABS SRM are provided in the SRM certificate. A sample mass equal to the certified LC_{50} value is combusted under the conditions of concern (e.g., nonflaming or flaming) and the principal gaseous components (CO, CO_2, HCN, and reduced O_2) of the ABS smoke measured. Equation (1) is then used to determine if this mass of material produced the gas concentrations necessary to achieve N-Gas values equivalent to those listed on the certificate. Finding N-Gas values within the 95% confidence limits of the certified values indicates the same concentration of material decomposes to produce a similar chemical atmosphere. To test if the toxicity is correct, the same mass of material (i.e., equal to the certified LC_{50}) is now used in one or two animal tests (N-Gas values are determined for these tests, too) in which the deaths of some percentage of the animals (not 0 and not 100%) indicates that the results of the laboratory are close to that of the certified SRM. Four N-Gas values (i.e., flaming, 30 min exposure; flaming, 30 min exposure plus 14 d post-exposure observation period; nonflaming, 30 min exposure; nonflaming, 30 min exposure plus 14 d post-exposure observation period) and their equivalent LC_{50} values are provided on the certificate and in Table 8. If the values found by the investigator fall within the 95% confidence limits of the certified values, the equipment can be assumed to be working correctly.

2.6 Comparison Factors in the Development of this SRM

2.6.1 Autoignition Temperatures In the intralaboratory evaluation of the various ABS formulations, the autoignition temperatures were independently determined for each formulation and before each new series of experiments designed to determine an LC_{50} value. Autoignition temperatures were also determined for ABS SRM 1007A by each of the participants in the interlaboratory evaluation.

2.6.2 Interlaboratory Evaluation In the process of selecting the SRM, it was necessary to examine the reproducibility of results across laboratories using a comparable material. Therefore, three laboratories (in addition to NIST) were asked to participate in an interlaboratory evaluation of ABS 1007A using the cup furnace smoke toxicity method. The laboratories which tested this material were Mobay (Stilwell, KS), NIST (Gaithersburg, MD), Southwest Research Institute (San Antonio, TX), and U.S. Testing (Hoboken, NJ). They agreed to determine the autoignition temperatures and LC_{50} values (30 min exposures and 14 d post-exposure observation period) for both the flaming and nonflaming modes. The interlaboratory evaluation was designed and conducted before we realized that the supply of ABS 1007A was limited. Since the interlaboratory results on ABS 1007A showed good reproducibility and ABS 1007A and ABS 5 were considered comparable materials, an additional interlaboratory evaluation of ABS 5 was not considered necessary.

2.6.3 Intralaboratory Comparison NIST examined the repeatability of the LC_{50} values (for both within the 30 min exposures and for within the 30 min exposures plus the 14 d post-exposure observation period). Enough tests were conducted to calculate three separate LC_{50} values for each of the flaming and nonflaming modes of ABS 5 (the final selected SRM), two LC_{50} values for each of the flaming and nonflaming modes of ABS sample 1007A, two LC_{50} values for the flaming mode of

ABS 4, one LC_{50} value for the nonflaming mode of ABS 4, and one LC_{50} value for the nonflaming mode of ABS 3. Since ABS 2 and 3 were found to be unsuitable for the Smoke Density Chamber, complete LC_{50} values were not determined for every combustion mode.

2.6.4 N-Gas Values In the development of this SRM, both LC_{50}s and N-Gas values were obtained for each series of experiments. N-gas prediction values at the LC_{50} concentrations were calculated as follows: first, the N-Gas value was determined for each experiment using Eq. (1). Then these N-gas values were plotted against their respective mass loading/chamber volumes. The best fit to the points was obtained by a least squares linear regression analysis. The N-Gas value at the LC_{50} was then determined from the mass loading/chamber volume equivalent to the experimentally determined LC_{50}.

2.6.5 Statistical Analysis All of the data from the 71 experiments that were conducted with ABS 5 were submitted to the Statistical Engineering Division in the Computing and Applied Mathematics Laboratory at NIST. The following measurements for each experiment were examined: the concentration of smoke [i.e., mass loading/chamber volume (g/m^3)] in the chamber, the number of rats that died during each 30 min exposure, the total number of rats that died during the 30 min exposures plus the post-exposure period of 14 d,[3] and the N-Gas values for the 30 min exposures and for the 30 min exposures plus the post-exposure period. Although more chemical analytical data was available, the "summary statistic" of the N-Gas values was sufficient to meet the goals of the analysis. The 30 min within-exposure and the 30 min within exposure plus post-exposure data were analyzed separately for both the flaming and nonflaming experiments.

Probit analysis as described in Finney [14] was used to determine the LC_{50} values, the concentration at which 50% of the animals in such an experiment should die. Individual fits were done for each of the three series of experiments and the LC_{50} values for each series was determined. N-Gas computations were also done on a series-by-series basis. A straight line through the origin was fit to the N-Gas values as a function of the concentration (i.e., mass of material loaded into the furnace per chamber volume) for each series. Then the N-Gas value at the LC_{50} for that series was calculated. Thus, three observations (one for each series) of the N-Gas value at the LC_{50} for each combustion mode and observation period were obtained.

[3] All deaths occurred within the first 24 h following exposure, but surviving animals were kept and weighed for the full 14 d to assure no further deaths occurred.

3. Results

3.1 Autoignition Temperature

The autoignition temperatures were determined for each tested formulation of ABS and three times for ABS 5 (once before each of the multiple series of tests on ABS 5) to examine the within laboratory repeatability (Table 1). Reproducibility between laboratories was tested only with ABS 1007A (Table 1). The interlaboratory evaluation was completed before we realized the stock of ABS SRM 1007A was limited.

Table 1. Autoignition temperatures

ABS designation	Laboratory	Autoignition temperatures (°C)		
		Series 1[a]	Series 2[a]	Series 3[a]
1007A	NIST	550		
1007A	#4	532–544		
1007A	#5	515		
1007A	#3	500		
ABS 2	NIST	575[b]		
ABS 3	NIST	550		
ABS 4	NIST	550		
ABS 5	NIST	550	550	550

[a] When the final ABS formulation was chosen, three series of separate experiments were conducted to examine the repeatability of results.

[b] In the determination of the autoignition temperatures, 1 g samples are tested to determine the temperature range. Then, an 8 g sample is tested to see if the higher loading will reduce the temperature. In the case of ABS 2, the amount of sample was limited, so the 8 g sample was not tested. ABS 2 proved to be unsuitable for the Smoke Density Chamber, so further testing was not pursued.

In the interlaboratory evaluation of ABS 1007A, NIST found an autoignition temperature of 550 °C which was the same as that found by NIST for all the other ABS samples except #2 (see Table 1). The other laboratories, however, found autoignition temperatures ranging from 500 °C to 544 °C for ABS 1007A. Although the autoignition temperatures were different, the LC_{50} values that were determined by the other laboratories were in the same range (except for one laboratory in the flaming combustion mode) (see Table 2). The reasons for the differences in autoignition temperatures from

the separate laboratories are unknown, but may be due to variations in furnace design, thermocouple placement, or the reference voltage of the thermocouple. Since the experiments are conducted at 25 °C above and below the autoignition temperature of the SRM (i.e., the temperature of the experiments are normalized by the material), comparable toxicological data were obtained. This aspect of the interlaboratory evaluation indicated that the autoignition temperature should not be one of the certified values of this SRM, but rather each user should determine their own autoignition temperature of the SRM according to the procedure specified in Ref. [4]. In other words, the SRM should be tested in the flaming and nonflaming modes which are, respectively, 25 °C above and below the autoignition temperature individually determined by each laboratory.

3.2 Interlaboratory Evaluation

All the toxicological and chemical data provided by the participants in the interlaboratory evaluation of ABS 1007A were analyzed by NIST and the LC_{50}s, N-Gas values, and gas concentrations at the calculated LC_{50}s are given in Tables 2, 3, and 4. Each of these values are the result of multiple experiments.

Table 2. Interlaboratory evaluation of ABS 1007A. Toxicological data

Laboratory	LC_{50} values[a] (g/m³)	
	Nonflaming	Flaming
NIST #1	40 (33–49)[b]	25 (21–29)
NIST #2	37 (32–43)	26 (24–29)
Laboratory #3	34 (24–47)	≈25[c][22.5[d]–25[e]]
Laboratory #4	29 (25–33)	26 (23–30)
Laboratory #5	38[f](33–43)	41[f](38–44)

[a] Calculated based on deaths within the 30 min exposure plus the 14 d post-exposure observation period.
[b] 95% confidence limits, computed using the method of Litchfield and Wilcoxon [13].
[c] Estimated from range of values, see footnotes d and e.
[d] No animals died at this concentration.
[e] Five out of the six exposed animals died at this concentration.
[f] These values were calculated at NIST in same manner as all other values in this table. Calculations by Laboratory # 5 resulted in slightly lower values. (Nonflaming was 34 g/m³ with 95% confidence limits of 30–38; flaming was 38 g/m³ with 95% confidence limits of 32–41.)

Table 3. Interlaboratory evaluation of ABS 1007A. Nonflaming mode chemical data[a]

Lab #	LC_{50}[b] (g/m³)	CO (ppm)	CO_2 (ppm)	HCN (ppm)	O_2 (%)	N-Gas value
NIST #1	40 (33–49)[c]	450 (370–550)[d]	2960 (2610–3410)	170 (140–200)	20.5 (20.5–20.4)	1.2[e] (1.0–1.5) 1.2[f]
NIST #2	37 (32–43)	440 (380–580)	3800 (3340–4350)	180 (150–210)	20.4 (20.5–20.3)	1.3[e] (1.1–1.5) 1.3[f]
Lab #3	34 (24–47)	NDP[h]	NDP	NDP	NDP	NDP
Lab #4	29 (25–33)	710 (610–800)	7410 (6520–8300)	150 (130–170)	20.0 (20.1–19.9)	1.2[e] (1.1–1.3) 1.1[f]
Lab #5	38 (33–44)	420 (360–490)	2270 (2140–2440)	NM[i]	20.5 (20.5–20.4)	NC[j]

[a] Time-integrated average concentration over the 30 min exposure period calculated at the LC_{50} value. Based on the least squares analysis of the average 30 min gas concentrations at each mass loading tested.
[b] Based on deaths which occurred within- and post-exposure.
[c] 95% confidence limits on LC_{50} value, computed using the method of Litchfield and Wilcoxon [13].
[d] The gas concentrations calculated at the low and high 95% confidence limits of the LC_{50}.
[e] Based on a least squares analysis of the N-Gas values for each experiment as a function of the mass loading. N-Gas value is that found at the LC_{50}.
[f] Based on gas concentrations provided in this table.
[h] NDP—no data provided.
[i] NM—not measured.
[j] NC—not calculated due to lack of HCN data.

Table 4. Interlaboratory evaluation of ABS 1007A. Flaming mode chemical data[a]

Lab #	LC_{50}[b] (g/m^3)	CO (ppm)	CO_2 (ppm)	HCN (ppm)	O_2 (%)	N-Gas value
NIST #1	25 (21–29)[c]	1600 (1300–1800)[d]	28800 (24500–33300)	120 (100–130)	17.3 (17.9–16.8)	1.2[e] (0.9–1.5) 1.3[f]
NIST #2	26 (24–29)	1700 (1500–1900)	31100 (28800–34700)	110 (100–120)	17.0 (17.2–16.5)	1.3[e] (1.1–1.4) 1.3[f]
Lab #3	25 (23–25)	NDP[h]	NDP	NDP	NDP	NDP
Lab #4	26 (23–30)	2200 (1900–2100)	36400 (32800–41200)	90 (80–100)	17.8 (18.1–17.4)	1.3[e] (1.2–1.5) 1.3[f]
Lab #5	41 (38–44)	2500 (2300–2700)	42100 (39100–45000)	NM[i]	18.6 (18.7–18.4)	NC[j]

[a] Time-integrated average concentration over the 30 min exposure period calculated at the LC_{50} value. Based on the least squares analysis of the average 30 min gas concentrations at each mass loading tested.
[b] Based on deaths which occurred within- and post-exposure.
[c] 95% confidence limits on LC_{50} value, computed using the method of Litchfield and Wilcoxon [13].
[d] The gas concentrations calculated at the low and high 95% confidence limits of the LC_{50}.
[e] Based on a least squares analysis of the N-Gas values for each experiment as a function of the mass loading. N-Gas value is that found at the LC_{50}.
[f] Based on gas concentrations provided in this table.
[h] NDP—no data provided.
[i] NM—not measured.
[j] NC—not calculated due to lack of HCN data.

This evaluation of SRM 1007A showed (with one exception) that there was good reproducibility of results across laboratories (i.e., the LC_{50} values from the different laboratories were within the 95% confidence limits of the other laboratories). These results agree with our prior and much more extensive interlaboratory evaluation that was conducted on the cup furnace smoke toxicity method [5]. Although this interlaboratory evaluation was conducted with ABS SRM 1007A prior to the realization that the supply was limited, it was not considered necessary to repeat the interlaboratory evaluation with the new material, since the new material chosen to replace ABS SRM 1007A was designed to have a similar formulation.

3.3 Intralaboratory Evaluation

Six series of experiments were conducted at NIST on ABS 5 to examine the repeatability of results. Three series were in the nonflaming combustion mode and three were in the flaming combustion mode. Each series consisted of multiple experiments (designated by (n) in Tables 5 and 6). The LC_{50} values were determined for each series for the deaths occurring during the 30 min exposures and for the deaths that occurred during the 30 min exposures plus the 14 d post-exposure observation period. The within-exposure results are given in Table 5 and the within plus post-exposure results are given in Table 6. The chemical analytical results for each gas were plotted against the concentration of material loaded into the furnace [mass loading/chamber volume (g/m^3)] and the gas concentrations at the LC_{50} values were determined by a least squares linear regression analysis of the data. Tables 5 and 6 provide the calculated LC_{50} values, the calculated gas concentrations at the LC_{50}s, and two sets of N-Gas values at the LC_{50}s; one set of N-Gas values was determined from a least squares linear regression analysis of the data from the individual experiments and the other set of N-Gas values was calculated from the gas concentrations presented in Tables 5 and 6. The data shown in Tables 5 and 6 indicate the good repeatability of results obtained with ABS 5.

Table 5. Intralaboratory evaluation of ABS 5. Within-exposure NIST Chemical data[a] at the LC_{50} value

Series # (n)[f]	LC_{50} (g/m^3)	CO (ppm)	CO_2 (ppm)	HCN (ppm)	O_2 (%)	NO_x (ppm)	NO (ppm)	NO_2 (ppm)	N-Gas value
				Nonflaming mode					
1 (6)	62(53–71)[b]	420(360–480)[c]	3490(3060–3910)[c]	220(190–250)[c]	20.4(20.5–20.3)[c]	NM[g]	NM	NM	1.2[d](1.0–1.5) 1.2[e]
2 (5)	54(49–60)	420(380–470)	3800(3500–4170)	210(190–240)	20.3(20.4–20.3)	ND[h]	ND	ND	1.1(1.1–1.2) 1.2
3 (4)	60(56–64)	440(410–460)	3400(3210–3590)	220(200–230)	20.4(20.4–20.3)	NM	NM	NM	1.2(1.1–1.3) 1.2
				Flaming mode					
1 (7)	29(28–31)	1900(1840–2030)	32200(31100–34300)	160(150–170)	16.7(16.8–16.4)	130(130–140)[c]	110(110–120)[c]	17(17–19)	1.5(1.4–1.6) 1.5
2 (6)	28(26–30)	1900(1760–2030)	34200(31800–36600)	150(140–160)	16.5(16.9–16.2)	120(120–130)	110(110–120)	18(16–19)	1.3(1.3–1.4) 1.4
3 (7)	27(26–28)	1780(1710–1840)	33700(32500–34900)	150(150–160)	16.5(16.7–16.3)	120(120–130)	100(95–100)	18(17–19)	1.4(1.4–1.4) 1.4

[a] Time-integrated average concentration over the 30 min exposure period calculated at the LC_{50} value. Based on the least squares analysis of the average 30 min gas concentrations at each mass loading tested.
[b] Values in parenthesis are the 95% confidence limits of the LC_{50} value.
[c] Values in parenthesis are the gas concentrations calculated at the low and high 95% confidence limits of the LC_{50}s.
[d] Based on least squares analysis of N-Gas values at each of the mass loadings.
[e] Based on gas concentrations provided in this table.
[f] (n)—number of experiments in each series of tests.
[g] NM—not measured.
[h] ND—not detected based on two experiments.

Table 6. Intralaboratory evaluation of ABS 5. Within plus post-exposure NIST chemical data[a] at the LC_{50}

Series # (n)[f]	LC_{50} (g/m^3)	CO (ppm)	CO_2 (ppm)	HCN (ppm)	O_2 (%)	NO_x (ppm)	NO (ppm)	NO_2 (ppm)	N-Gas value
				Nonflaming mode					
1 (6)	60(55–66)[b]	410(370–450)[c]	3390(3160–3670)[c]	210(190–230)[c]	20.4(20.4–20.3)[c]	NM[g]	NM	NM	1.5[d](1.3–1.8) 1.5[e]
2 (5)	50(48–53)	390(380–420)	3560(3440–3740)	200(190–210)	20.4(20.4–20.4)	ND[h]	ND	ND	1.4(1.3–1.4) 1.4
3 (4)	56(52–60)	410(380–440)	3210(3020–3400)	200(190–220)	20.4(20.5–20.4)	NM	NM	NM	1.4(1.3–1.6) 1.4
				Flaming mode					
1 (7)	26(24–29)	1700(1570–1900)	29000(26800–32200)	140(130–160)	17.1(17.4–16.7)	120(110–130)[c]	100(90–110)[c]	16(14–17)[c]	1.6(1.5–1.7) 1.5
2 (6)	25(24–26)	1690(1630–1760)	30600(29400–31800)	130(130–140)	17.0(17.2–16.9)	110(110–120)	100(100–110)	16(15–16)	1.5(1.5–1.5) 1.5
3 (7)	25(23–27)	1640(1510–1770)	31200(28800–33700)	140(130–150)	16.9(17.2–16.5)	110(100–120)	90(80–100)	16(15–18)	1.6(1.6–1.6) 1.5

[a] Time-integrated average concentration over the 30 min exposure period calculated at the LC_{50} value. Based on the least squares analysis of the average 30 min gas concentrations at each mass loading tested.
[b] Values in parenthesis are the 95% confidence limits of the LC_{50} value.
[c] Values in parenthesis are the gas concentrations calculated at the low and high 95% confidence limits of the LC_{50}s.
[d] Based on least squares analysis of N-Gas values at each of the mass loadings.
[e] Based on gas concentrations provided in this table.
[f] (n)—number of experiments in each series of tests.
[g] NM—not measured.
[h] ND—not detected based on two experiments.

3.4 Statistical Analysis

The Computing and Applied Mathematics Laboratory conducted a statistical analysis of the data from ABS 5 which is to be certified and sold by the Standard Reference Materials Program. Individual probit analysis fits were done for each series of experiments. (Three series were conducted to examine the repeatability of the LC_{50} values.) The LC_{50} value was calculated for each series, resulting in three observations of the LC_{50} for each combustion mode and observation time. N-Gas computations were also done on a series-by-series basis. It was important to examine the data on a series-by-series basis since there appeared to be systematic differences between the series for both the probits and the N-Gas values. For example, Fig. 4, which shows the three series of experiments for the within exposures to the nonflaming combustion mode, indicates that one series has a different relationship between the N-Gas values and the mass loading/chamber volume than the other two series (this can be seen by the fact that the slopes of the fitted lines are different for each series). If such systematic differences exist between series, one grand fit to all the data for a given mode and observation period might produce a biased estimate of the LC_{50} value or the corresponding N-Gas value.

The results of this statistical analysis are presented in Table 7 and in Figs. 4 through 7. In these figures, a straight line through the origin was fit by least squares linear regression analysis of the N-Gas values as a function to the mass loading/chamber volume for each series. Then the N-Gas value at the LC_{50} value for that series was determined resulting in three observations of the N-Gas value at the LC_{50} (one for each series) for each combustion mode and observation period.

Table 7. Statistical analysis of LC_{50} values and N-Gas values for ABS 5

Combustion mode	Observation time	Test series	LC_{50} values (g/m³)	N-Gas values
Flaming	WE[a]	1	28	1.4
		2	26	1.3
		3	28	1.4
	WE & PE[b]	1	26	1.6
		2	25	1.4
		3	24	1.5
Nonflaming	WE	1	62	1.2
		2	51	1.1
		3	60	1.2
	WE & PE	1	57	1.5
		2	48	1.3
		3	55	1.4

[a] WE—deaths occurred within the 30 min exposure.
[b] WE & PE—combined deaths that occurred either within the 30 min exposure and/or the 14 d post-exposure observation period.

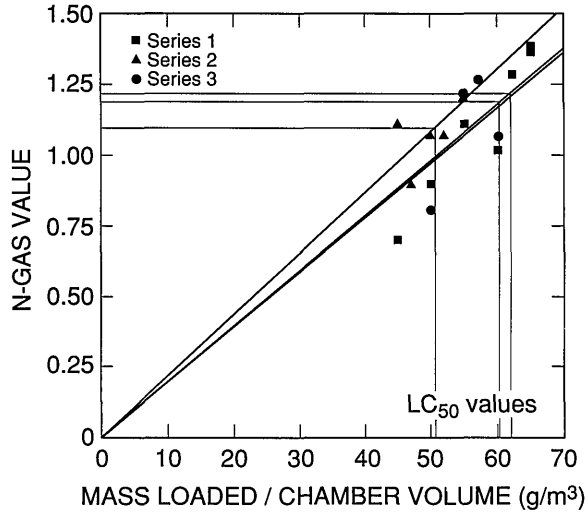

Fig. 4. N-Gas values as a function of concentration [i.e., mass of material loaded into the cup furnace divided by the exposure chamber volume (g/m³)] for the three separate series of tests on ABS 5. Nonflaming mode, within exposure effects.

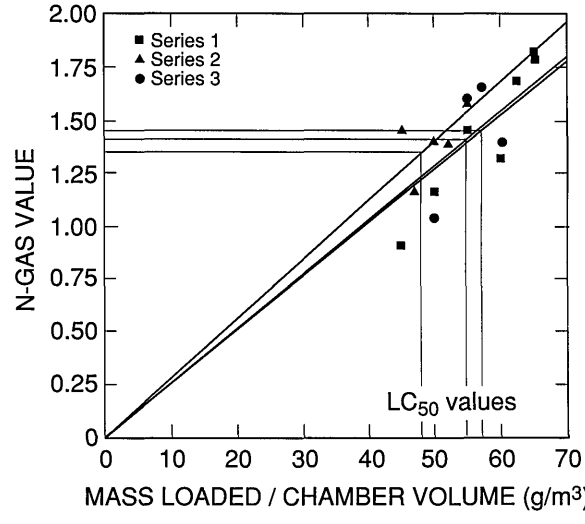

Fig. 5. N-Gas values as a function of concentration [i.e., mass of material loaded into the cup furnace divided by the exposure chamber volume (g/m³)] for the three separate series of tests on ABS 5. Nonflaming mode, within plus post-exposure effects.

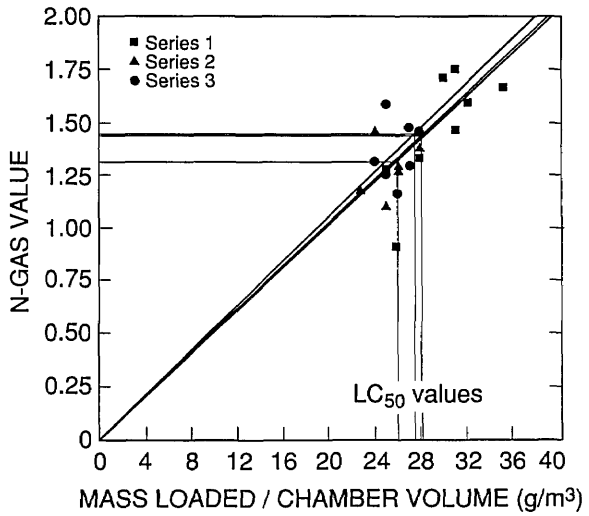

Fig. 6. N-Gas values as a function of concentration [i.e., mass of material loaded into the cup furnace divided by the exposure chamber volume (g/m^3)] for the three separate series of tests on ABS 5. Flaming mode, within exposure effects.

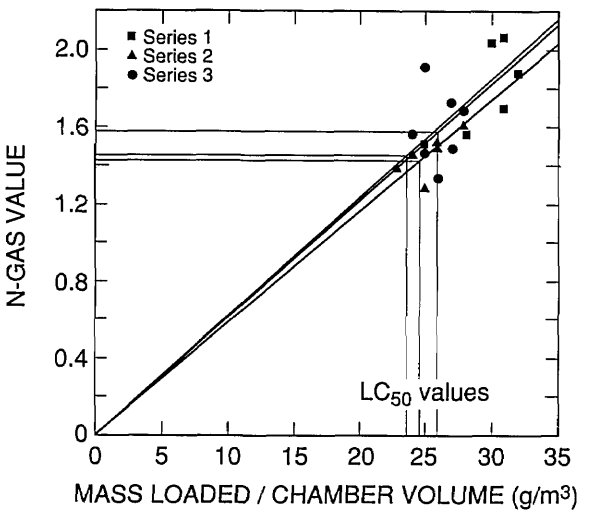

Fig. 7. N-Gas values as a function of concentration [i.e., mass of material loaded into the cup furnace divided by the exposure chamber volume (g/m^3)] for the three separate series of tests on ABS 5. Flaming mode, within plus post-exposure effects.

The variation in the three observations incorporates both the uncertainty with each fit and the differences between series. Therefore, the mean and a confidence interval for the mean based on the three observations for each combustion mode and observation period summarize the LC_{50} and N-Gas values, giving the user of the SRM our best estimates of the true values for the material and how well we know them (Table 8). The intervals provided in Table 8 are the 95% confidence intervals based on two degrees of freedom. The LC_{50} and N-Gas values shown in Table 8 are the values that will be provided on the SRM certificate.

4. Discussion

An acrylonitrile-butadiene-styrene (ABS) has been evaluated and submitted for certification for use as a standard reference material (SRM 1048) for the cup furnace smoke toxicity method. An interlaboratory evaluation conducted by four laboratories on a comparable ABS material indicated good reproducibility of LC_{50} values (with one exception in the flaming mode) and N-Gas values across laboratories. This interlaboratory evaluation showed that the determination of the autoignition temperature of the test material was variable, but that if the experiments are conducted 25 °C above (flaming) and below (nonflaming) the individually determined autoignition temperatures, the chemistry and toxicity results were comparable between laboratories. These results indicate that the autoignition temperature should be determined by each laboratory and should not be included in the certified values of the SRM. In other words, the temperatures at which the experiments are conducted are normalized by the material and not by the temperature reading which could vary due to furnace construction, thermocouple placement or other differences between laboratory equipment.

Table 8. Mean LC_{50} and N-Gas values plus their 95% confidence limits for ABS 5

Observation time	Combustion mode	$LC_{50} \pm 95\%$ CL[a] (g/m^3)	N-Gas value ± 95% CL
WE[b]	Flaming	27± 3	1.4±0.2
	Nonflaming	58±15	1.2±0.2
WE & PE[c]	Flaming	25± 3	1.5±0.2
	Nonflaming	53±12	1.4±0.2

[a] CL—95% confidence limits.
[b] WE—within the 30 min exposure.
[c] WE & PE—within the 30 min exposure plus the 14 d post-exposure observation period.

Both the mean LC_{50} values and the N-Gas values ± their respective 95% confidence limits are provided in Table 8 and can be used with this SRM to calibrate the method and assure the user that the data that they obtained with this procedure is within the expected bounds. Since the N-Gas values were determined at the LC_{50}s, the N-Gas values can be used instead of determining the complete LC_{50} value for each combustion mode (flaming or nonflaming) and observation period (within the exposure or within plus the post-exposure period). Utilization of the N-Gas values rather than determination of each LC_{50} value for comparison with the certified LC_{50} values has the advantages of reducing the number of needed experimental animals, the time necessary to complete the calibration tests, and the expense.

It is left to the user's discretion whether complete LC_{50} values should be determined or if the N-Gas approach should be used. We recommend the latter approach. In the N-Gas approach, both the chemical (N-Gas values) and toxicological results (actual lethalities at the certified LC_{50} values) are compared to the certified values. To use the N-Gas approach, one needs to decompose the SRM at the certified LC_{50} values in either the flaming or nonflaming mode, measure the concentrations of pertinent gases, namely, CO, CO_2, HCN, and O_2, and determine the N-Gas value. Comparison of this value with the N-Gas value provided in the SRM certificate will show if the chemical results agree with the certified results. To determine if the toxicological results are comparable, the mass of material equivalent to the certified LC_{50} is decomposed in the presence of the rats as described in Ref. [4]. One or two experiments should indicate if the animals respond as expected (i.e., two to five rats die either within the 30 min exposure or within the 30 min exposure plus the 14 d post-exposure period, depending on which observation period is of interest).

It should be noted that with this particular material, the N-Gas values at the LC_{50} values are higher than unity, especially in the flaming mode. N-Gas values lower than unity indicate that toxic gases other than CO, CO_2, HCN, and O_2 may be contributing to the toxic atmospheres (i.e., making the combustion atmosphere more toxic than predicted). N-Gas values higher than unity indicate that one or more gases may be acting as a toxicological antagonist (i.e., making the combustion atmosphere less toxic than predicted). In our studies at NIST, we have found N-Gas values are higher than expected in those cases where the material produces a significant amount of HCN. Our recent data (to be published) indicates that in these cases, NO_x is also formed. As expected, NO_x was found in the combustion atmospheres of the ABS tested for this SRM (Tables 5 and 6). Our studies with NO_2 indicate that exposure to NO_2 increases the methemoglobin levels in the blood [24]. It is well known that methemoglobin acts as an antidote for cyanide poisoning by binding the CN^- and preventing it from being transferred to the tissues where the toxic insult occurs. We believe, therefore, that the N-Gas values at the LC_{50} values of this ABS are higher than expected because NO_x causes the formation of methemoglobin which acts as an antidote for the HCN (i.e., an antagonistic effect occurs). An N-Gas equation including NO_2 is being tested, but for the purposes of the use of this SRM is not necessary. The user can employ the certified N-Gas values and thus, will not be required to monitor NO_x which requires additional analytical equipment that might not be readily available in many laboratories.

With SRM 1048, an investigator can calibrate both the chemical (based on the certified N-Gas values) and toxicological results (based on the certified N-Gas or LC_{50} values) from two combustion modes (flaming and nonflaming) in the cup furnace smoke toxicity method. If the experimental values fall within the 95% confidence limits of the certified values of this SRM, investigators can be confident that they are using the equipment properly.

5. Conclusions

A standard reference material ABS SRM 1048 has been developed to calibrate the cup furnace smoke toxicity method. The SRM material chosen is an acrylonitrile-butadiene-styrene (ABS) which is the same material used for SRM 1007B that has been recently certified for calibration of the flaming mode of the ASTM E-662 and NFPA 258 Smoke Density Chamber methods. Certified values plus their 95% confidence limits are provided for both the LC_{50} values and the N-Gas values for two combustion modes (flaming and nonflaming) and two observation periods (within the 30 min exposure or within the 30 min exposure plus a 14 d post-exposure period). The certified LC_{50} values plus 95% confidence intervals (in g/m^3) are 27 ± 3 (30 min, flaming); 25 ± 3 (30 min + 14 d, flaming); 58 ± 15 (30 min, nonflaming); and 53 ± 12 (30 min + 14 d, nonflaming). The certified N-Gas values plus 95% confidence intervals are 1.4 ± 0.2 (30

min, flaming); 1.5±0.2 (30 min+14 d, flaming); 1.2±0.2 (30 min, nonflaming); and 1.4±0.2 (30 min+14 d; nonflaming). It is recommended that the users conserve experimental animals, time and expense by using the N-Gas approach to calibrate their system rather than conducting the complete determination of the LC_{50} values.

Acknowledgments

The authors acknowledge the help of Mr. J. R. Lawson, who worked with the manufacturer to assure that the ABS materials would meet the necessary specifications. We also wish to acknowledge Mr. Richard Seward, now retired from the Office of Standard Reference Materials, who provided invaluable advice during the initial phases of this work. Ms. Nancy Eller is also acknowledged for her expert technical assistance in these experiments. The participation of Mobay Corporation, Southwest Research Institute, and the U.S. Testing Company, Inc. in the interlaboratory evaluation is greatly appreciated.

6. References

[1] Fire in the United States, Second Ed., Federal Emergency Management Agency, FEMA 22 (July 1982).
[2] M. M. Birky, B. M. Halpin, Y. H. Caplan, R. S. Fisher, J. M. McAllister, and A. M. Dixon, Fire fatality study, Fire Mater. 3, 211–217 (1979).
[3] H. L. Kaplan, A. F. Grand, and G. E. Hartzell, Combustion Toxicology, Principles and Test Methods, Technomic Publishing Co., Inc., Lancaster, PA (1983).
[4] B. C. Levin, A. J. Fowell, M. M. Birky, M. Paabo, A. Stolte, and D. Malek, Further development of a test method for the assessment of the acute inhalation toxicity of combustion products. NBSIR 82-2532, Natl. Bur. Stand. (U.S.), Gaithersburg, MD (1982).
[5] B. C. Levin, M. Paabo, and M. M. Birky, An interlaboratory evaluation of the National Bureau of Standards Test Method for assessing the acute inhalation toxicity of combustion products. NBSIR 83-2678, Natl. Bur. Stand. (U.S.), Gaithersburg, MD (1983).
[6] Y. C. Alarie and R. C. Anderson, Toxicologic and acute lethal hazard evaluation of thermal decomposition products of synthetic and natural polymers. Tox. Appl. Pharm. 51, 341–362 (1979).
[7] New York State Uniform Fire Prevention and Building Code, Article 15, Part 1120, Combustion toxicity testing and regulations for implementing building materials and finishes; fire gas toxicity data file. New York State, Department of State, Office of Fire Prevention and Control, Albany, NY 12231 (December 16, 1986).
[8] Navy Military Standard, Fire and toxicity test methods and qualification procedure for composite material systems used in hull, machinery applications inside naval submarines. MIL-STD-2031(SH), prepared by the Naval Sea Systems Command, (Project 19GP-N007) (March 10, 1988).
[9] Annual Book of ASTM Standards, Volume 4.07, E 662-83, Specific optical density of smoke generated by solid materials. ASTM, Philadelphia, PA (1988).
[10] NFPA 258, Smoke Generation of Solid Materials, National Fire Protection Association, Quincy, MA (1989).
[11] I. M. Kolthoff and E. B. Sandell, Textbook of Quantitative Inorganic Analysis, Second Ed., MacMillan Co., New York, p. 546 (1953).
[12] M. Paabo, M. M. Birky, and S. E. Womble, Analysis of hydrogen cyanide in fire environments. J. Comb. Tox. 6, 99–108 (1979).
[13] J. T. Litchfield and F. Wilcoxon, A simplified method of evaluating dose-effect experiments. J. Pharmacol. Exp. Therapeut. 96, 99–113 (1949).
[14] D. J. Finney, Probit Analysis, 3rd Ed., London Cambridge Press (1971).
[15] B. C. Levin and R. G. Gann, Toxic potency of fire smoke. Chapter 1, Fire and Polymers, Hazards Identification and Prevention, G. L. Nelson, ed., ACS Symposium Series 425, American Chemical Society, Washington, DC (1990).
[16] B. C. Levin, M. Paabo, J. L. Gurman, and S. E. Harris, Effects of exposure to single or multiple combinations of the predominant toxic gases and low oxygen atmospheres produced in fires, Fundamental Appl. Toxicology 9, 236–250 (1987).
[17] B. C. Levin, J. L. Gurman, M. Paabo, L. Baier, and T. Holt, Toxicological effects of different time exposures to the fire gases: carbon monoxide or hydrogen cyanide or to carbon monoxide combined with hydrogen cyanide or carbon dioxide, Proceedings of the Ninth Meeting of the U.S.-Japan Panel on Fire Research and Safety, Norwood, MA, May 1987. NBSIR 88-3753, Natl. Bur. Stand. (U.S.), Gaithersburg, MD, pp. 368–384 (April, 1988).
[18] B. C. Levin, M. Paabo, J. L. Gurman, H. M. Clark, and M. F. Yoklavich, Further studies of the toxicological effects of different time exposures to the individual and combined fire gases—carbon monoxide, hydrogen cyanide, carbon dioxide and reduced oxygen, Polyurethane 88, Proceedings of the 31st SPI Conference, Philadelphia, PA, pp. 249–252 (October 1988).
[19] B. C. Levin, M. Paabo, J. L. Gurman, S. E. Harris, and E. Braun, Toxicological interactions between carbon monoxide and carbon dioxide. Toxicology 47, 135–164 (1987).
[20] V. Babrauskas, R. H. Harris, R. G. Gann, B. C. Levin, B. T. Lee, R D. Peacock, M. Paabo, W. Twilley, M. F. Yoklavich, and H. M. Clark, Fire hazard comparison of fire-retarded and non-fire-retarded products. NBS Special Publication 749, Natl. Bur. Stand. (U.S.), Gaithersburg, MD (1988).
[21] E. Braun, S. Davis, J. H. Klote, B. C. Levin, and M. Paabo, Assessment of the fire performance of school bus interior components. NISTIR 4347, Natl. Inst. Stand. Technol., Gaithersburg, MD, July 1990.
[22] E. Braun, R. G. Gann, B. C. Levin, and M. Paabo, Combustion product toxic potency measurements: comparison of a small-scale test and "real-world" fires. J. Fire Sci. 8, 63–79 (1990).

[23] V. Babrauskas, R. H. Harris, Jr., E. Braun, B. C. Levin, M. Paabo, and R. G. Gann, The role of bench-scale test data in assessing real-scale fire toxicity. NIST Technical Note 1284, Natl. Inst. Stand. Technol., Gaithersburg, MD, January 1991.

[24] B. C. Levin, M. Paabo, L. Highbarger, and N. Eller, Synergistic effects of nitrogen dioxide and carbon dioxide following acute inhalation exposures in rats. NISTIR 89-4105, Natl. Inst. Stand. Technol., Gaithersburg, MD, June 1989.

About the authors: Barbara C. Levin is a project leader and toxicologist in the Fire Toxicity Measurement Group, Fire Measurement and Research Division, Building and Fire Research Laboratory. Maya Paabo is an analytical chemist who recently retired from the National Institute of Standards and Technology. Susannah B. Schiller is a statistician in the Computing and Applied Mathematics Laboratory.

Volume 96, Number 6, November–December 1991
Journal of Research of the National Institute of Standards and Technology

[J. Res. Natl. Inst. Stand. Technol. 96, 757 (1991)]

Investigation of the Interaction of Sodium Chloride and Two Amino Sulfonic Acids, HEPES and MOPSO, by EMF Measurements

Volume 96 | Number 6 | November–December 1991

Y. C. Wu, Daming Feng, and W. F. Koch

National Institute of Standards and Technology,
Gaithersburg, MD 20899

Ionic interactions in the two systems NaCl-HEPES (N-2-hydroxyethylpiperazine-N'-2-ethanesulfonic acid) and NaCl-MOPSO (3-(N-Morpholino)-2-hydroxypropanesulfonic acid) have been studied in terms of their mutual influence on the respective activity coefficients of each component. Activity coefficients for each component of the two systems and for corresponding buffers are calculated from emf measurements of solutions containing NaCl, the aminosulfonic acid, and its conjugate base in a NaISE/solution/AgCl-Ag cell at 5, 15, 25, and 37 °C.

Key words: activity coefficient; amino acid; emf; HEPES; MOPSO; salt interaction; sodium chloride.

Accepted: August 20, 1991

1. Introduction

The interaction between an amino acid and a neutral salt in solution can be described in terms of the activity coefficients of the components [1]. In this laboratory, when we decided to establish HEPES(N-2-hydroxyethylpiperazine-N'-2-ethanesulfonic acid) as a pH Standard Reference Material (SRM) for physiological application, we needed to know the effect of HEPES on the activity coefficient of NaCl. Since there were no relevant data in the literature, we had to assume that the influence of HEPES on the activity coefficient of NaCl was the same as that of glycine on NaCl [2]. Even though the effect was small, it was necessary to verify our assumption. MOPSO(3-[N-Morpholino]-2-hydroxypropanesulfonic acid) is another candidate for an SRM in the physiological pH range. The influence of MOPSO on the activity coefficient of NaCl is also not known. The purposes of this investigation were to determine the mutual influence between NaCl and HEPES, and between NaCl and MOPSO, and to provide the data needed to calculate the activity coefficients for NaCl, HEPES, and MOPSO in the respective mixed solutions. The determination of the activity coefficient of amino acids and NaCl in their mixed solutions may be done by potentiometry. One approach using a sodium amalgam electrode has been reported [3]. However, it was found that the amino acids decomposed sodium amalgam and evolution of hydrogen gas was observed. For this reason, the sodium ion-selective electrode (NaISE) provided a more convenient approach to this type of determination.

2. Experimental

2.1 The Apparatus

The cells studied were of the type

$$\text{NaISE/ NaCl}(m_1)\,/\,\text{AgCl-Ag} \qquad \text{(I)}$$

for the pure NaCl solution, and

NaISE/ NaCl(m_1), HEPES(m_2), NaHEPESate(m_3)/AgCl-Ag (II)

NaISE/ NaCl(m_1), MOPSO(m_2), NaMOPSOate(m_3)/AgCl-Ag (III)

for the two-component systems ($m_3=0$) and three-component systems for HEPES (II) and MOPSO (III). A glass NaISE (13-620-500, Fisher Scientific)[1] was used for the measurements for solutions containing HEPES. However, in solutions containing MOPSO the emf readings drifted continually and were not reproducible. It appeared that the MOPSO coated the glass surface of the electrode. Thus, it was necessary to use a PVC membrane neutral carrier-based NaISE (provided by Prof. W. Simon, Zürich, Switzerland [4]) for the MOPSO system. The silver-silver chloride reference electrodes were identical with those used previously in this laboratory [2]. emfs were measured using an Orion 701A pH meter with a sensitivity of 0.1 mV. Measurements were made at various temperatures in a bath controlled to ±0.01 °C [2]. The electrodes were calibrated daily using NaCl solutions in cell (I). Activity coefficients of NaCl were taken from the literature [5]. The observed (Nernstian) slopes k for both glass and PVC membrane NaISEs were constant for each calibration with a standard deviation of 0.05 mV for the whole range of temperatures in this study. The values are shown in Tables 1 and 2. They were about 1 mV lower than the theoretical Nernstian slopes; hence, the electrodes were not thermodynamically reversible, but were still useful for the purpose of this study. The selectivity of the two NaISEs toward the hydrogen ion requires that the pH of the solutions should be between 4.5 and 10 at the NaCl concentration of 0.01-0.1 m [4,6]. In this study, the pH of the solutions was 5.5-7.5, which was well within the range of requirement.

2.2 Materials

NaCl was ACS reagent grade and was dried at 110 °C for 4 h before use. HEPES and MOPSO (Sigma Co., St. Louis, MO) were recrystallized from 80% and 70% ethanol/water solutions respectively , and were dried in a vacuum oven at 50 °C overnight. Their sodium salt solutions were made by neutralizing the acid solutions with standard sodium hydroxide. Stock solutions were prepared by weight. All mass measurements were made with an accuracy to 0.03 mass percent and air buoyancy corrections were applied for all masses used. The laboratory distilled water used in this experiment was passed through a deionizing column and had a conductivity of less than 1 μS/cm.

[1]Certain commercial equipment, instruments, or materials are identified in this report to specify adequately the experimental procedure. Such identification does not imply recommendation or endorsement by the National Institute of Standards and Technology, nor does it imply that the materials or equipment identified are necessarily the best available for the purpose.

3. Results

The emfs of cells (II) and (III) can be empirically expressed as an equation similar to the Nernstian equation:

$$E = E_0 - k\log(m_{Na} m_{Cl} \gamma_1^2) \quad (1)$$

where γ_1 is the mean molal activity coefficient of NaCl and m is the molal concentration, E_0 is an extrapolated constant, and k(in mV) is another constant.

For pure NaCl solutions in cell (I), the emf is expressed as

$$E_p = E_0 - 2k\log(m_1 \gamma_1^\circ) \quad (2)$$

where γ_1° denotes the mean molal activity coefficient for pure NaCl solution. E_0 and k can be obtained from this equation by using a least square fitting procedure. For the HEPES-NaCl and MOPSO-NaCl two-component systems, if the concentrations of NaCl in cells (II) and (III) are the same as that in the pure NaCl solutions, then we can combine Eqs. (1) and (2) to obtain

$$\log(\gamma_1/\gamma_1^\circ) = (E_p - E)/2k \quad (3)$$

where E_p is the emf for pure NaCl solution from cell (I). All the emfs and $\log(\gamma_1/\gamma_1^\circ)$ values are listed in Tables 1 and 2 together with k values at four temperatures. All the molalities in Tables 1 and 2 are accurate to better than 0.1%.

3.1 Influence of HEPES and MOPSO on the Activity Coefficient of NaCl

The values of $\log(\gamma_1/\gamma_1^\circ)$ at 25 °C from Tables 1 and 2 were plotted against the molality of HEPES and MOPSO in Figs. 1 and 2, respectively. The trend of the behavior of $\log(\gamma_1/\gamma_1^\circ)$ was similar to that for other amino acids [1]. HEPES and MOPSO diminished the activity coefficients of

Table 1. The emfs of the cell: NaISE/NaCl(m_1), HEPES(m_2), NaHEPESate(m_3)/AgCl,Ag and the log(γ_1/γ_1 °) values

t °C			5		15		25		37	
m_1	m_2	m_3	E, mV	$-\log(\gamma_1/\gamma_1$ °)	E	$-\log(\gamma_1/\gamma_1$ °)	E	$-\log(\gamma_1/\gamma_1$ °)	E	$-\log(\gamma_1/\gamma_1$°)
0.01	0	0	58.3		68.6		76.3		87.2	
0.02	0	0	27.7		36.3		42.8		52.1	
0.02	0.05	0					43.5	0.0060		
0.02	0.08	0					44.1	0.0111		
0.02	0.1	0					44.5	0.0145		
0.02	0.12	0					44.9	0.0179		
0.05	0	0	−13.1		−6.1		−1.0		6.9	
0.05	0.05	0					−0.4	0.0051		
0.05	0.08	0					0.2	0.0102		
0.05	0.1	0					0.5	0.0128		
0.05	0.12	0					1.0	0.0171		
0.08	0	0	−34.1		−27.6		−22.7		−16.3	
0.08	0.05	0	−33.5	0.0055	−27.0	0.0053	−22.1	0.0051	−15.7	0.0049
0.08	0.08	0	−33.0	0.0101	−26.5	0.0097	−21.6	0.0094	−15.2	0.0090
0.08	0.1	0	−32.6	0.0138	−26.1	0.0132	−21.3	0.0120	−14.9	0.0115
0.08	0.12	0	−32.2	0.0175	−25.7	0.0167	−20.9	0.0154	−14.6	0.0139
0.1	0	0	−42.6		−37.4		−33.3		−27.3	
0.1	0.05	0					−32.8	0.0043		
0.1	0.08	0					−32.3	0.0085		
0.1	0.1	0					−32.0	0.0111		
0.1	0.12	0					−31.7	0.0137		
0.08	0.08	0.08	−47.1		−41.1		−36.3		−30.1	
	k (mV)		54.2		56.7		58.5		61.2	

Table 2. The emfs of the cell: NaISE/NaCl(m_1), MOPSO(m_2), NaMOPSOate(m_3)/AgCl,Ag and the log (γ_1/γ_1 °) values

t °C			5		15		25		37	
m_1	m_2	m_3	E, mV	$-\log(\gamma_1/\gamma_1$ °)	E	$-\log(\gamma_1/\gamma_1$ °)	E	$-\log(\gamma_1/\gamma_1$ °)	E	$-\log(\gamma_1/\gamma_1$°)
0.01	0	0	−19.8		−10.0		−2.5		10.5	
0.02	0	0	−51.2		−43.2		−36.0		−24.9	
0.02	0.05	0					−35.6	0.0034		
0.02	0.08	0					−35.2	0.0068		
0.02	0.1	0					−34.9	0.0094		
0.02	0.12	0					−34.5	0.0128		
0.02	0.15	0					−34.0	0.0171		
0.05	0	0	−91.8		−85.4		−79.5		−70.6	
0.05	0.05	0					−79.1	0.0034		
0.05	0.08	0					−78.7	0.0068		
0.05	0.1	0					−78.4	0.0094		
0.05	0.12	0					−78.0	0.0128		
0.05	0.15	0					−77.5	0.0171		
0.08	0	0	−112.7		−106.9		−101.8		−93.7	
0.08	0.05	0	−112.2	0.0046	−106.5	0.0035	−101.4	0.0034	−93.3	0.0032
0.08	0.08	0	−111.7	0.0092	−106.0	0.0080	−101.0	0.0068	−93.0	0.0057
0.08	0.1	0	−111.4	0.0120	−105.7	0.0106	−100.7	0.0094	−92.7	0.0081
0.08	0.12	0	−111.1	0.0147	−105.4	0.0133	−100.4	0.0119	−92.4	0.0105
0.08	0.15	0	−110.6	0.0193	−104.9	0.0177	−99.9	0.0162	−91.9	0.0146
0.1	0	0	−121.3		−116.8		−112.2		−105.2	
0.1	0.05	0					−111.8	0.0034		
0.1	0.08	0					−111.5	0.0060		
0.1	0.1	0					−111.2	0.0085		
0.1	0.12	0					−110.9	0.0111		
0.1	0.15	0					−110.4	0.0153		
0.05	0.05	0.05	−112.8		−104.0		−96.0		−83.7	
0.08	0.08	0.08	−132.2		−124.7		−117.2		−106.3	
	k(mV)		54.4		57.0		58.6		61.7	

NaCl; the effect of HEPES was more pronounced than that of MOPSO. An increase in the NaCl concentration decreased the effect of amino acids. The values of $\log(\gamma_1/\gamma_1^\circ)$ at 25 °C can be represented by the following equations:

HEPES-NaCl solution,

$$-\log(\gamma_1/\gamma_1^\circ) = (0.11 - 0.42m_1)m_2 + (0.45 - 0.44m_1)m_2^2 \quad (4)$$

MOPSO-NaCl solution,

$$-\log(\gamma_1/\gamma_1^\circ) = (0.05 + 0.04m_1)m_2 + (0.51 - 1.4m_1)m_2^2 . \quad (5)$$

The temperature effect is shown in Figs. 3 and 4 at $m_2 = 0.08$. In our previous paper [2], we used the following equation for HEPES-NaCl solutions at $m_{NaCl} = 0.08$ and assumed that it was temperature-independent:

$$-\log(\gamma_1/\gamma_1^\circ) = 0.125\, m_{HEPES} . \quad (6)$$

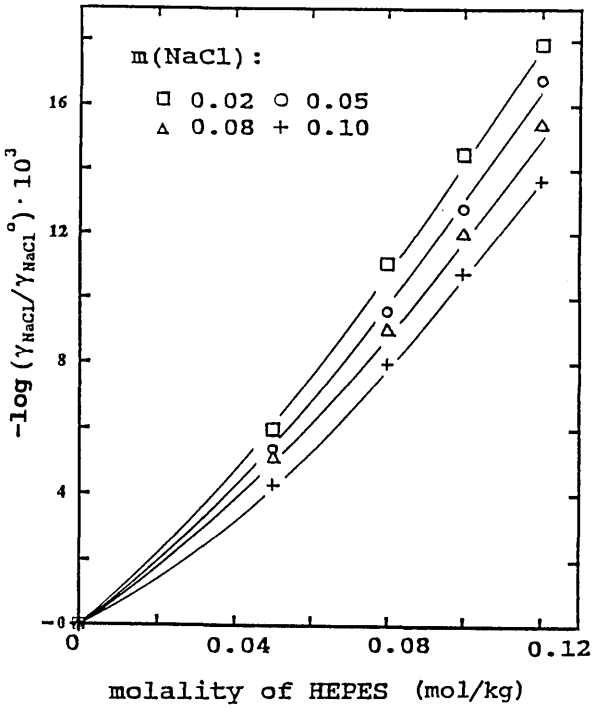

Figure 1. Influence of HEPES on activity coefficient of NaCl at 25 °C.

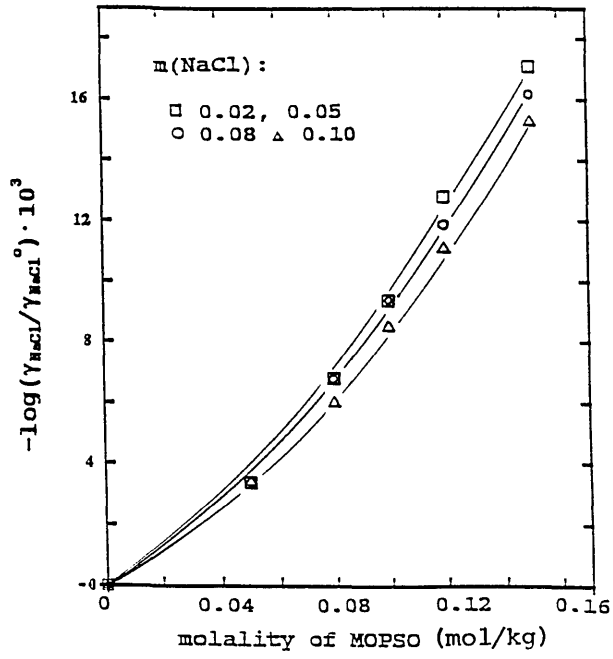

Figure 2. Influence of MOPSO on activity coefficient of NaCl at 25 °C.

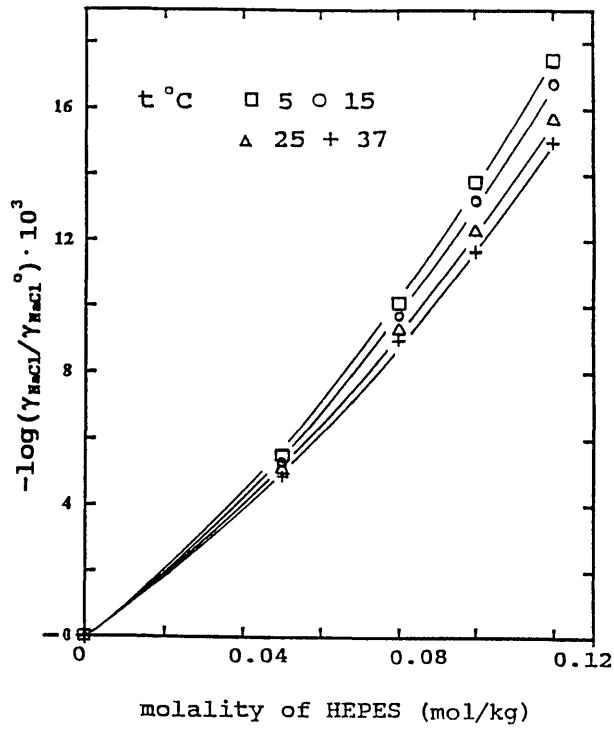

Figure 3. Influence of HEPES on activity coefficient of NaCl at different temperatures, m(NaCl) = 0.08.

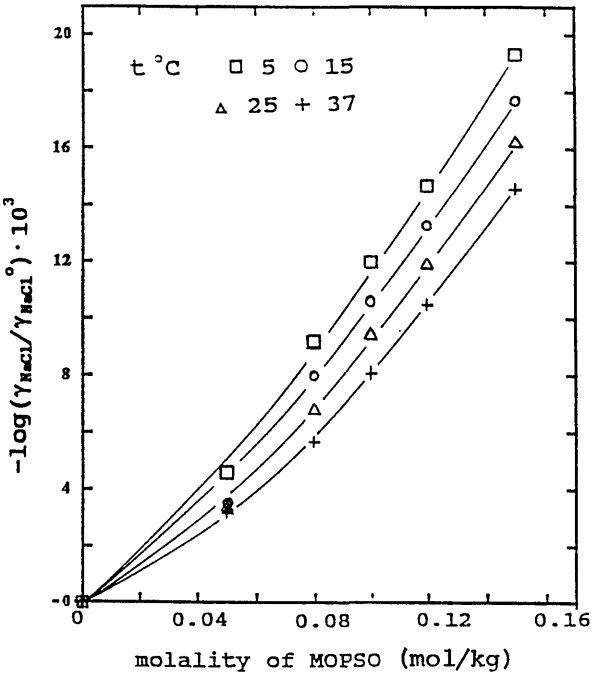

Figure 4. Influence of MOPSO on activity coefficient of NaCl at different temperatures, m(NaCl) = 0.08.

The $\log(\gamma_1/\gamma_1^\circ)$ values calculated from Eq. (6) and observed experimentally (cf. Table 1) are listed in Table 3. The difference is within the experimental uncertainty.

Table 3. Comparison of $\log(\gamma_1/\gamma_1^\circ)$ at $m_2 = 0.08$

	$-\log(\gamma_1/\gamma_1^\circ)$	
t °C	Observed	Calculated from Eq. (6)
5	0.0101	0.010
15	0.0097	0.010
25	0.0094	0.010
37	0.0090	0.010

3.2 The Activity Coefficient of NaCl in MOPSO-NaMOPSOate-NaCl Buffer Solutions

Data for the activity coefficients of NaCl are needed in the determination of the pH of three-component MOPSO-NaMOPSOate-NaCl buffer solutions. In this work, $\log\gamma_{NaCl}$ in 0.05 and 0.08 m equimolal MOPSO-NaMOPSOate-NaCl solutions was directly determined by using cell (III). For this cell,

$$\log\gamma_1 = 1/2[(E_0 - E)/k - \log(m_1 + m_3)m_1] \quad (7)$$

where E_0 and k were obtained from the measurements of cell (I). The results, listed in Table 4, are used for the determination of the pH values in these buffer solutions.

Table 4. Determination of γ_{NaCl} in MOPSO-NaMOPSOate-NaCl solutions

	$-\log\gamma_{NaCl}$	
t °C	0.05 m (equimolal)	0.08 m (equimolal)
5	0.039	0.064
15	0.070	0.091
25	0.096	0.119
37	0.132	0.153

3.3 Activity Coefficients of HEPES and MOPSO

According to the Gibbs-Duhem equation, the activity coefficient of an amino acid in an amino acid-NaCl two-component solution can be calculated from the activity coefficient of NaCl in the same solution [1]:

$$\log(\gamma_2/\gamma_2^\circ) = 2\int_0^{m_1} \partial\log\gamma_1/\partial m_2)\partial m_1 \quad (8)$$

where γ_2 is the activity coefficient of the amino acid in the mixed solution and γ_2° is that for an isomolal solution without NaCl, γ_1 is the activity coefficient of NaCl in this mixed solution. By substituting Eqs. (4) and (5) into Eq. (8), $\log(\gamma_2/\gamma_2^\circ)$ can be evaluated. $\log\gamma_2^\circ$ for HEPES at 25 °C was calculated from emf measurements of the following cell,

$$H_2(g, 1\ atm)/HEPES,NaHEPESate,NaCl/AgCl,Ag(s) \quad (IV)$$

as described in our previous paper [2], in which $\gamma_{Z\pm}$ represented γ_{HEPES}:

$$-\log\gamma_{HEPES}^\circ = 0.20 m_{HEPES}. \quad (9)$$

Analogous measurements were carried out for MOPSO at 25 °C [7] and the following result was obtained:

$$-\log\gamma_{MOPSO}^\circ = 0.10 m_{MOPSO}. \quad (10)$$

Thus, from Eqs. (8), (9) and (10), the activity coefficients of HEPES and MOPSO at 25 °C are expressed as follows:

$$\log\gamma_{HEPES} = (-0.22 m_{NaCl} + 0.42 m_{NaCl}^2) - (0.20 + 1.8 m_{NaCl} - 0.88 m_{NaCl}^2) m_{HEPES} \quad (11)$$

$$\log\gamma_{MOPSO} = (-0.10m_{NaCl} - 0.04m_{NaCl}^2) - (0.10 + 2.0m_{NaCl} - 2.8m_{NaCl}^2)m_{MOPSO} \quad (12)$$

Taking the first-order terms as an approximation, the following simpler forms result. For comparison, the analogous expression for glycine [1] is also shown:

$$\log\gamma_{HEPES} = -0.20m_{HEPES} - 0.22m_{NaCl} \quad (13)$$

$$\log\gamma_{MOPSO} = -0.10m_{MOPSO} - 0.10m_{NaCl} \quad (14)$$

$$\log\gamma_{Glycine} = -0.10m_{Glycine} - 0.28m_{NaCl}\,. \quad (15)$$

4. Discussion

All the parameters used for Eqs. (4), (5), (13), and (14) are empirical. They are derived from the least square fitting of the experimental data and are only valid within the range of the concentrations in this work. According to Cohn and Edsall [1], at low NaCl concentrations, most amino acids diminish the activity coefficients of NaCl, and NaCl in turn diminishes the activity coefficients of amino acids. The present work demonstrates a similar phenomenon in the NaCl-HEPES and NaCl-MOPSO systems.

Because of the relatively high input impedance of the NaISE, a pH meter was used to measure the emfs of cells (I), (II), and (III). The resolution of this pH meter was 0.1 mV. This corresponds to an uncertainty of 0.0017 in $\log(\gamma_1/\gamma_1^\circ)$. Each emf value reported in Tables 1 and 2 represents the mean of two separate measurements. The differences between each pair of emf values never exceeded 0.1 mV. Therefore, the overall uncertainty of $\log(\gamma_1/\gamma_1^\circ)$ is estimated to be $0.0017/\sqrt{2} = 0.0012$. The trend of the influence of the amino acid on the activity coefficients of NaCl, as indicated by $\log(\gamma_1/\gamma_1^\circ)$ and shown in Figs. 1-4, is more evident at higher concentrations of the two amino acids. As the concentration becomes lower, the influence diminishes. In the lowest concentration region, the differences in the $\lg(\gamma_1/\gamma_1^\circ)$ values at different NaCl concentrations or temperatures are within the limit of uncertainty and in some cases the $\log(\gamma_1/\gamma_1^\circ)$ values practically overlap. The curves drawn in this region are merely to show the trend of the influence.

Acknowledgment

The authors are grateful to Prof. W. Simon for kindly providing the PVC membrane NaISE.

5. References

[1] E. J. Cohn and J. T. Edsall, Proteins, Amino Acids and Peptides, Chapt. 11, Hafner Publishing Co., New York (1965).
[2] D. Feng, W. F. Koch, and Y. C. Wu, Anal. Chem. **61**, 1400 (1989).
[3] N. R. Joseph, Biol. Chem. **111**, 489 (1935).
[4] T. Maruizumi, D. Wegmann, G. Suter, D. Ammann, and W. Simon, Mikrochim. Acta I, 331 (1986).
[5] W. J. Hamer and Y. C. Wu, J. Phys. Chem. Ref. Data **1**, 1047 (1972), for 25 °C; R. A. Robinson and R. H. Stokes, Electrolyte Solutions, Butterworths Scientific Publications, London (1959) for other temperatures.
[6] Fisher Scientific, Manual of sodium ion-selective electrodes, part No. 69491 (1987].
[7] To be published.

About the authors: *Yung C. Wu and William F. Koch are chemists with the Inorganic Analytical Research Division, National Institute of Standards and Technology. Daming Feng is guest scientist from Guangzhou Research Institute of Non-ferrous Metals, China.*

Volume 96, Number 6, November–December 1991
Journal of Research of the National Institute of Standards and Technology

Conference Report

ISO/IEC WORKSHOP ON WORLDWIDE RECOGNITION OF OSI TEST RESULTS Gaithersburg, MD May 6–8, 1991

Report prepared by

Stephen Nightingale

U.S. GOSIP Testing Program,
National Institute of Standards and Technology,
Gaithersburg, MD 20899

1. Reasons for the Workshop

The testing of Open Systems Interconnection (OSI) products is expensive and time consuming. Hence there is a great desire on the part of the suppliers of such products to have their products tested only once. At the same time, clients are seeking assurances that newly acquired OSI products will interwork with their existing systems. These two points of view cannot currently be reconciled in the absence of global arrangements on the recognition of the results of testing OSI products. In order to identify a way to proceed, the Information Technology Resources Support Group (ITRSG) recommended that the International Organization for Standardization (ISO) and the International Electrotechnical Commission (IEC) should organize an International Workshop on the Worldwide Recognition of OSI Test Results.

The Workshop, which was carefully planned by a Program Committee in which most of the interested parties from North America, Europe, and "the rest of the world," i.e., Australasia, were represented was held at the National Institute of Standards and Technology (NIST) from May 6–8, 1991.

2. Summary of the Workshop

The workshop was attended by almost 150 participants and there were 25 speakers coming from a wide range of organizations worldwide, with a variety of stakes in the OSI Test Results issues. On the first day, the objectives were presented by Dr. D. Rayner of the U.K. National Physical Laboratory, and tutorials were given on the state of the art in testing, Laboratory accreditation, and certification, followed by government, industry and commercial user positions on objectives. The second day, which was chaired by Mr. Y. Yokoyama of Japanese INTAP explored current practices in testing, laboratory accreditation, and certification, in the different regions throughout the world. Reports on the European scene, including the European Infrastructure, were presented by the chairmen of ECITC (the European Committee on Information Technology Testing and Certification), OSTC (Open Systems Testing Consortium, An Example of a Recognition Arrangement), and the manager of ACERLI—a French laboratory within the European scheme. The North American scene was represented by talks from NIST, Corporation for Open Systems (COS), and CIGOS—the Canadian Interest Group on Open Systems. The "rest of the world" comprised talks from Japan, Korea, Australia and from the World Federation of MAP/TOP User Groups.

The third day was intended to digest the information from the previous 2 days and provide plans for the future. The workshop was chaired on the third day by Kevin Mills of NIST, who provided a provocative introduction and expanded the scope of the "One Stop World" to encompass: standardization, production and maintenance of standards; harmonization, mutual recognition, validation and equivalence of test systems; accreditation of conformance testing laboratories; certification of conformance tested products; and finally, the role of interoperability testing. Discussions, led by previous speakers, followed a number of strawman proposals.

3. Test Methodology Equivalence

Fundamental to the harmonization of test reports is the harmonization of standardized profiles. This work is already underway in the Regional Workshop Coordinating Committee, which mediates the efforts of the Asian and Oceanic Workshop (AOW), the European Workshop for Open Systems (EWOS), and the OSI Implementors' Workshop (OIW).

A single set of test suites for OSI conformance testing is necessary. In the past, OSI standards have been produced without accompanying means of verifying that implementations can conform. This led to the ad hoc and fragmented production of tests of varying quality, which is the situation as it exists today. The ISO/IEC workshop recognized the need to stimulate and coordinate nonduplicative efforts in filling the gaps left by the formal standardization process. The recent history of funding for conformance testing is that the "public" tests and the test system development efforts have been predominantly European in origin. The workshop noted that funding for test specification development is an issue for each region. The workshop also noted that for future protocol developments, progress should include test suites with, not after, protocol specifications.

In considering the application of quality controls to test system developments, there are different philosophical approaches from different schemes in the world today: the European scheme requires maintaining equivalent test tools and executable test suites to produce equivalent test reports. This would be fine in a world where the test suites are finalized and the test technology is mature. The NIST approach to test system acceptance criteria is more pragmatic—realizing that existing test technology is not mature and test coverage is not 100% of the features of each protocol, we set a baseline for acceptable coverage, and registered those test systems which were above the line. The baseline is increased periodically, to encourage improvements in the testing technology, until the level of full coverage of the protocol features is reached. In this scheme, test report equivalence is reached when a full coverage test suite has been developed, but not in the interim period. The theory behind this approach is that allowing some variation between "acceptable" test systems provides the freedom to stimulate improvements in competing test technologies, which is more important in the short term than maintaining a rigid equivalence of a small sample of the possible tests. The question of harmonizing test system acceptance criteria, to include a reasonable, staged, interim approach was not well explored in the workshop, but the clear message is that this is one of the issues to be handled by the conformance testing special interest group (SIG) of each of the regional implementors' workshops.

4. Mutual Recognition of Accreditation

Perhaps the easiest area to consider harmonizing is that of accreditation, although there was some friction here between the accreditation bodies and the OSI community. The accreditation bodies such as the National Voluntary Laboratory Accreditation Program (NVLAP) in the United States, the National Measurement Accreditation System (NAMAS) in England and Reseau Nationale d'Essais (RNE) in France, and their mediating body the International Laboratory Accreditation Conference (ILAC), have a way of recognizing each others' programs by bilateral agreements. Traditionally this has been "across the board," i.e., independent of any particular test method. The network of bilateral agreements in place at the moment is rather sparse. The OSI, and wider Information Technology (IT) communities make the claim that an IT specific interpretation of ISO Guide 25, covering the conduct of laboratory accreditations, is required, and hence wish to influence the accreditation bodies to make sector specific agreements. The principal issue in this case is that the concept of calibration, central to most specimen testing laboratories, is not applicable in IT. Instead, in software testing, the concept of validation of software test systems against a canonical, or a notional model is in force. This "sector specific" movement is being most pointedly

driven by the Europeans, who have produced a document entitled "Interpretation of Accreditation Requirements for Information Technology Test Laboratories for OSI Test Services." It was decided by the workshop that, (a) the accreditation bodies are the responsible parties for bilateral and/or multilateral agreements, whether they are across the board or sector specific; and (b) a harmonized OSI—or more general IT—interpretation of accreditation requirements, is a necessary component of any such agreements. The development of that interpretation is the province of the OSI/IT communities, and the European document may already provide much of the input.

5. Certification

The discussions on certification were perhaps the most confusing and the least generative of a solution. Principal among the questions were: What is certification? and, Who wants it? Of course manufacturers worldwide would prefer first party certification, i.e., a "Manufacturer's Declaration of Conformity," in accordance with ISO Guide 22. Indeed, this may be adopted as a component of more independent product quality assurance schemes, however IT users seem to be unanimous in rejecting it in its raw, unequivocal "trust me" form. In Europe, the testing establishment is taking the lead in requirements setting, and hence the naturally favored solution is a third party certificate, from an independent testing organization, widely recognized by all buyers of OSI technology. Within the United States, the Corporation for Open Systems also favors the third party certificate approach, in the form of the COS Mark. NIST, in the United States, has established a testing program which has as a goal the development of a Register of Conformance Tested Products. In this case a register entry, based on review of an acceptable conformance test report, is raised, with no particular intention to generate a certificate. This difference in philosophy arises perhaps from the fact that NIST is not primarily acting as a third party certifier, but is representing and protecting the interests of the Federal Agencies as procurement authorities. The message which is conveyed in this case is that registered products have passed a basic set of qualification tests and can be considered for Federal procurement. There is no question of NIST, or the Federal Government, certifying or providing a warranty for products tested. Since the registers are public, other interested parties outside the government are free to use the information as they see fit.

6. Outlook

There are many problems to be solved before Worldwide Recognition of OSI Test Results can be achieved: adoption of common protocol specifications, development of complete test suites, harmonization of test system quality assurance methodologies, mutual recognition of accreditation schemes, and agreements on how all these components should fit together to provide assurance that an OSI product tested in one laboratory will be considered for procurement by any purchaser, anywhere in the world. An important outcome of this workshop is that consciousness has been raised over a wide international audience, of what the pitfalls are. The workshop also provided a stimulus to harmonizing test validation methodologies, and for the accreditation agencies to explore bilateral and multilateral agreements.

In conclusion, a report on the proceedings of the workshop will be presented to the ITRSG, and the workshop's program committee has agreed to maintain contact in order to monitor progress on the above initiatives.

Volume 96, Number 6, November–December 1991
Journal of Research of the National Institute of Standards and Technology

Conference Report

SIXTH INTERNATIONAL CONFERENCE ON THE APPLICATION OF STANDARDS FOR OPEN SYSTEMS Gaithersburg, MD October 2–4, 1990

Report prepared by

Shirley M. Radack

Computer Systems Laboratory,
National Institute of Standards and Technology,
Gaithersburg, MD 20899

1. Introduction

Worldwide interest in advancing open computing systems was highlighted at the Sixth International Conference on the Application of Standards for Open Systems. Held in the United States for the first time, the conference was co-sponsored by the IEEE Computer Society, the Institute of Electrical and Electronics Engineers, and the National Institute of Standards and Technology. An exhibit of technical and educational products related to open systems was organized by the Corporation for Open Systems.

Chaired by Kevin Mills, Chief of the Systems and Network Architecture Division at the Computer Systems Laboratory, the conference featured papers and discussion on key issues affecting the implementation of open systems including policy development, international collaboration, trade issues, implementation, conformance, and security.

The conference committee included Allan Maclean of Australia, William McCrum of Canada, Michel Audoux of the European Community, Bernard Gondran and Claude Mahy of France, Hideaki Okino of Japan, George Sidey of the United Kingdom, James H. Burrows of the United States, and Wolfram Berger and Heinrich Wortmann of West Germany.

2. Requirements for Open Systems

Requirements for open systems are being driven by users who want to move away from proprietary systems to standard interfaces and interoperable software, hardware, and communications products that are developed by different vendors. No single vendor can supply systems to meet the diversity of many user requirements, or respond to enterprise-wide needs for common application architectures, communications, and networks. Users need flexible and modular systems that can be acquired and added to with equipment supplied by a variety of vendors in an open competitive market, and that can support the portability of software applications.

3. Opening the Conference

In welcoming the conference participants, James H. Burrows, Director of the Computer Systems Laboratory, said that "the cooperative efforts of users, governments and industry have taken us down the road toward open systems," and that efforts must be maintained to continue to build on

these achievements and to augment open systems standards and applications. Mr. Burrows cited the need for standards to protect the confidentiality, integrity, and availability of information transmitted in global networks for electronic mail, business data interchange and other strategic business functions.

Robert White, Under Secretary of Commerce for Technology, delivered the keynote address. In his talk, Dr. White said that new alliances will be needed to unify and to present user requirements for open systems to industry and to standards organizations. He announced that the U.S. Government was forming the Federal Open System Users Council comprising senior-level government executives. The council will develop common architectural frameworks for open systems to meet government requirements for interconnection and interoperation of systems from different vendors and for the portability of software. The Council will work with users and vendors to promote better understanding of common requirements.

Dr. White said that open systems, based on standards, will integrate software and hardware components, and provide standard interfaces to application programs and to the user. But, these systems must be based on industry-wide standards, be commercially available, and be capable of being extended or modified. A consensus based process for decisions regarding definitions, specifications and other issues must be available.

Calling for an integrated world market for open systems, Dr. White said that these markets would allow for competition based upon price, performance, and added value. Such competition helps buyers by lowering prices and improving quality. He also stated that the development of tests was essential to give users confidence that systems conform to standards and will interoperate. International cooperation among standards groups, technical organizations, and governments is needed to achieve mutual recognition of tests, testing methods, and test results. Such efforts will be effective in minimizing regional differences, reducing the need for multiple product testing cycles, and getting products to users more quickly and cheaply, he said.

4. Conference Papers

The proceedings of the Sixth International Conference on the Application of Standards for Open Systems were published by the IEEE Computer Society Press, 10662 Los Vaqueros Circle, P.O. Box 3014, Los Alamitos, CA 90720-1264. Most of the presentations referenced below are included in the proceedings.

New Open Systems Interconnection (OSI) Policies

Johansson, B., OSI Strategies for Scandinavian Governments
Statskontoret
Sweden

Okino, H., Japanese Activities for Promoting OSI
Ministry of Trade and Industry
Japan

Ramakrishnam, S., OSI Policy in India
Department of Electronics
India

Houser, W., Implementing GOSIP in VA
Department of Veterans Affairs
United States

International Collaboration

Hartmann, U., Open Systems Standards: Status of International Harmonization and European Activities
ZVEI (Siemens)
Federal Republic of Germany

Read, C., Global Harmony, The Delivery of Proof
Digital Equipment Co., Ltd.
United Kingdom

Therrien, J., International Collaboration in the Public Sector
Treasury Board Secretariat
Canada

Free Trade and Standards

Mills, K., Standards and Trade: What's the Connection?
National Institute of Standards and Technology
United States

Cameron, P., Impact of Trade Agreements on Standardization
Canadian General Standards Board
Canada

Wilkinson, C., Economic Implications of Standardization:
OECD
GATT
CEC, DGXIII
Belgium

Applications

Tunstall, J., Using OSI for the Exchange of Information between Financial Institutions
Association for Payment Clearing Services
United Kingdom

Pinson, P.H., Business Case for Open Systems
Dupont
United States

Ochiai, T., Numura OSI: An Example of the OSI-Based Transaction Processing
Nomurs Research Institute, Ltd.
Japan

Volume 96, Number 6, November–December 1991
Journal of Research of the National Institute of Standards and Technology

Volume 96, Number 6, November–December 1991
Journal of Research of the National Institute of Standards and Technology

News Briefs

General Developments

Inquiries about News Briefs, where no contact person is identified, should be referred to the Managing Editor, Journal of Research, National Institute of Standards and Technology, Administration Building, A635, Gaithersburg, MD 20899; telephone: 301/975-3572.

THREE COMPANIES WIN BALDRIGE QUALITY AWARD

President Bush on October 9 announced three U.S. electronics firms as the winners of the 1991 Malcolm Baldrige National Quality Award. The winners are Solectron Corp. (San Jose, CA) and Zytec Corp. (Eden Prairie, MN) in the manufacturing category and Marlow Industries (Dallas, TX) in the small business category. The award, managed by NIST with the active involvement of the private sector, was established by legislation in August 1987 to raise awareness about quality management and to recognize U.S. companies that have a world-class system for managing their operations and people and for satisfying their customers. A maximum of two awards may be given annually in each of three categories: large manufacturers, large service companies, and small businesses. The 1991 winners were honored at a ceremony in Washington, DC, on October 29.

TECH PROGRAMS ANNOUNCED FOR RURAL INDUSTRY

NIST and the Extension Service (ES) of the U.S. Department of Agriculture have announced an agreement to help improve the access of small, rural manufacturers to technology assistance resources provided by NIST. "This agreement promotes our collaboration with the Cooperative Extension System specialists and agents who are an unparalleled resource for reaching parts of the country where manufacturing operations are in rural localities," said Donald Johnson, director of NIST Technology Services. Under the agreement, NIST will furnish ES agents and specialists with technology-related materials and information and training in technology assistance, problem identification, and referral to appropriate resources. NIST also will provide the Cooperative Extension System with advice and assistance in solving technological problems.

STUDY HIGHLIGHTS IMPACT OF AWARD-WINNING RESEARCH

One of NIST's primary goals is to help U.S. industry develop commercial technology. Among the barometers for gauging how well the agency does this are R&D 100 Awards, given yearly by Research and Development Magazine to recognize 100 technical innovations with commercial potential. Now, a new report shows that NIST has a strong track record both for winning the award and transferring technology of the winners to the private sector. According to the 40-page report, NIST has won 71 R&D 100 Awards (note: the agency scored two more awards after the report went to press), ranking it third among all-time winners. As for the commercial potential of technology behind the awards, the report cites eight winners responsible for millions of dollars in products. For example, companies have developed and marketed a NIST cone calorimeter to the tune of $6 million. The device, a 1988 winner, predicts fire hazard from a small sample of material such as upholstery. For a free copy of NIST R&D 100 Awards—A Technology Transfer Study, send a self-addressed mailing label to Dale Hall, A525 Administration Building, NIST, Gaithersburg, MD 20899.

PARTNERSHIP TO IMPROVE ACCURACY IN GRAIN TRADE

U.S. weights and measures officials and the U.S. Department of Agriculture's Federal Grain Inspection Service (FGIS) have formed a partnership to improve the accuracy of grain measurements in trade. The 1990 Farm Bill authorized FGIS to work with the National Conference on Weights and Measures (NCWM) and NIST to establish standards for the evaluation and performance of commercial grain inspection equipment. To carry out the effort, NCWM has established two new sectors for grain equipment under its National Type Evaluation Program Technical Committee. Membership will be limited to one representative from a company or industry association, but participation in the meetings will be open to all interested parties. For information, contact Carroll S. Brickenkamp, P.O. Box 4025, Gaithersburg, MD 20885, 301/975-4005, fax: 301/926-0647.

CONSORTIUM PROPOSED TO IMPROVE POLYMER PROCESSING

Producers of plastic and rubber products and instrument manufacturers are invited to join a consortium sponsored by NIST to improve the processing and quality of polymer materials by developing new measurement technology. The goal is to develop in-line measurement technology based on optical methods to monitor important processing conditions. These new measurement tools will enable processors to make critical in-process measurements not now possible. The proposed consortium will be based on an ongoing NIST research program in fluorescence spectroscopy to monitor various processing steps in the production of advanced polymers. Participation in the consortium will require a $10,000 annual contribution for the 4 year program. NIST will provide research facilities, including new processing equipment to test measurement technologies developed under the program. For information, contact Anthony J. Bur, B320 Polymer Building, NIST, Gaithersburg, MD 20899, 301/975-6748.

AGREEMENT ON SOFTWARE DEVELOPMENT SIGNED

The Center for Advanced Research in Biotechnology (CARB) and IBM are joining forces to develop a user-friendly portable software system for computational structural biology. CARB will merge several of its own software packages to IBM's RISC 6000 Workstation in a new cooperative research and development agreement with IBM. As part of the agreement, CARB will design a system that can execute more than 20 biotechnology application programs. These programs perform a variety of jobs from computing protein structural data to modeling protein molecules. Most of the programs are public domain software written by CARB/NIST scientists. The software system would make computer studies of biological molecules much faster and easier. The agreement also calls for CARB to provide software for testing at other laboratories. CARB was established in 1984 by NIST, the University of Maryland, and Montgomery County, MD, as a unique center for government, academic, and industry scientists.

VALIDATION SERVICE STARTED FOR MUMPS

NIST recently began a validation service to test compilers for the MUMPS programming language to see if they conform to Federal Information Processing Standard (FIPS) 125, MUMPS. MUMPS—Massachusetts General Hospital Utility Multiprogramming System—is a high-level interactive computer programming language for use in developing and effecting interactive information systems with shared databases. FIPS are standards, guidelines, and technical methods issued for government-wide use. The MUMPS validation capability was developed by NIST. For technical information, contact L. Arnold Johnson, 301/975-3247.

PHASE-NOISE PROBLEM RESOLVED FOR FIBER-OPTIC NET

NIST researchers have helped resolve an important phase-noise problem for a new, fiber-optic telecommunications system called SONET. Members of an American National Standards Institute subcommittee were having difficulty defining the amount of phase noise to be tolerated by SONET. Phase noise is a random variation or "jitter" in phase of an otherwise regular signal, which enters between the nodes of a telecommunications link and must be characterized and controlled to achieve synchronization in the overall system. NIST scientists analyzed noise data collected from SONET, made recommendations on useful phase-noise measures, and served as the focal point for clarifying new network phase noise specifications.

GAS STANDARD HELPS REGULATORS ENFORCE CLEAN AIR ACT

The Environmental Protection Agency and California Air Resources Board are using a NIST gas standard to measure the success of their clean air

efforts. The new standard helps both agencies comply with the requirements for improved measurements of hydrocarbons from industry and auto emissions mandated by the Clean Air Act of 1990. Ongoing uses of the standard include establishing baseline levels of hydrocarbons in polluted areas, assessing the effectiveness of pollution reduction efforts over time, and maintaining a long-term, highly accurate measurement record. The gas standard contains minute amounts of 15 different hydrocarbons found in car exhaust. Under specific conditions, these hydrocarbons can lead to crop damage and lung irritation. The levels in the standard are low, around 5 parts in 10^9 (i.e., 5 parts per billion), to correspond to what laboratories would actually find in city air. NIST scientists developed the gas standard specifically for the EPA and California, but hope to expand its application for other laboratories by certifying it as a Standard Reference Material.

FIVE TECHNOLOGIES DOMINATE BIDS FOR ATP GRANTS

Proposals to develop key technologies in electronics or materials science make up roughly half of the 271 applications submitted by the September 25 deadline for 1991 grants under the NIST Advanced Technology Program (ATP). A significant number of proposals also came from the fields of manufacturing, information technology, and energy. Other technologies represented in the applications include biotechnology, environmental technology, agriculture/food technology, and transportation. NIST expects to award between $20 million and $25 million in ATP grants to help U.S. industry develop generic, commercially important technologies. The awards will be announced in early spring, 1992.

DEVELOPMENT OF HARDNESS STANDARD UNDER WAY

NIST has launched a program to establish a U.S. national hardness standard. Under the program, certified hardness calibration test blocks will be produced to calibrate machines to perform various property measurements such as the Rockwell hardness test. Industry will be provided with uniform hardness standards to measure and characterize hardness indenters. The U.S. standard is expected to be compatible with those maintained by other national authorities worldwide. Development of the NIST facility is being carried out in collaboration with the Instituto di Metrologie "G. Colonetti" (IMGC), Turin, Italy. IMGC will supervise the construction of a duplicate of their dead weight hardness calibration machine, which is presently used to maintain hardness standards in Europe. IMGC also will assist NIST in establishing a traceable national hardness standard through calibrations, intercomparisons, and selected measurements. For information, contact John H. Smith, B261 Materials Building, NIST, Gaithersburg, MD 20899, 301/975-5960.

STRUCTURE OF SUGAR-TRANSPORT PROTEIN SOLVED

Scientists at the Center for Advanced Research in Biotechnology (CARB) have solved the three-dimensional structure of a key protein that is indispensable for transporting sugar from the environment into the bacterial cell. The enzyme, known as the IIA domain of glucose permease (previously known as Enzyme III), is one link in a chain of proteins that enable the transport of glucose into the cell. The IIA domain interacts with a second protein, the membrane channel domain, and opens the gate for sugar transport. With the structure of the sugar transport protein in hand, pharmaceutical companies may be able to design new antibiotics that would prevent sugar transport and thereby starve infectious bacteria by cutting off their energy supply. Researchers from NIST and two universities collaborated on these studies at CARB. A paper describing the new protein structure appears in the Oct. 8, 1991, issue of Biochemistry. CARB was established in 1984 by NIST, the University of Maryland, and Montgomery County, MD, as a unique center for government, academic, and industry scientists.

REPORT FEATURES ELECTRONIC MESSAGE HANDLING

A timely report, Electronic Data Interchange in Message Handling Systems (NISTIR 4608), introduces the Message Handling System (MHS), the carrier service for Electronic Data Interchange (EDI) data, and the Interpersonal Messaging Service, the only standardized MHS application, and the model for the EDI Messaging Service. With the MHS, users can transfer EDI data between compatible EDI applications found on different computer systems. The MHS service would advance the interchange of EDI data using Open Systems Interconnection protocols and standards. A detailed review of the EDI messaging recommendations follows introductory material. EDI identifies a family of standards used for the electronic transmission of business-oriented data—invoices and purchase orders, for example. For

technical information, contact Paul Markovitz, 301/975-3606. Available from the National Technical Information Service, Springfield, VA 22161. Order by PB #91-216622 for $15 prepaid, $8 for microfiche.

PRECISE MEASUREMENTS MADE OF CLADDING DIAMETER

NIST researchers, using an in-house developed contact micrometer, have measured the cladding diameter of an optical fiber within 40 nm, one of the most accurate measurements ever made of any such macroscopic object. Cladding is the glass sheath surrounding the fiber core. Precise measurements of the cladding diameter are required by the Telecommunications Industry Association so that single-mode fibers can be connected together with low loss and little manual adjustment. The moving part of the micrometer (spindle) rides on an air bearing and its position is measured by an interferometer. Measurements are performed by closing the spindle against the fiber and using the wavelength of light as a ruler. The fiber deforms slightly and a correction is applied to account for the deformation. As a check on the micrometer, NIST scientists measured the diameters of six optical fiber specimens with the micrometer and a scanning confocal microscope, which confirmed the original measurements. They hope to improve the measurement process by using silica instead of steel contacts to reduce surface roughness. Two papers (#33-91) outlining their findings are available from Jo Emery, Division 104, NIST, Boulder, CO 80303, 303/497-3237.

PROPOSALS SOUGHT FOR PRECISION MEASUREMENT GRANTS

NIST is seeking project proposals for its 1993 Precision Measurement Grants. The grants range from $30,000 to $40,000 for 1 year and may be renewed for up to two additional years. Prospective candidates must submit summaries of their proposed projects and biographical information to NIST by Feb. 1, 1992, to be considered for the current grants, which will run from October 1992 through September 1993. NIST's Precision Measurement Grants are awarded each year to scientists in U.S. academic institutions for work in determining values for fundamental constants, investigating related physical phenomena, or developing new, fundamental measurement methods. For information, contact Barry N. Taylor, B160 Physics Building, NIST, Gaithersburg, MD 20899, 301/975-4220.

NEW SYSTEM IMPROVES FLAW DETECTION IN COMPOSITES

NIST and industry researchers have developed a low-frequency, ultrasonic system for detecting flaws and characterizing properties in composite materials, such as the polymer-matrix compounds used in the automotive, marine, and aerospace industries. Traditional ultrasonic instruments are designed for flaw detection only, operate at frequencies which are too high, and have a dynamic range which is too low for accurate evaluation of these materials. Researchers at NIST and private industry have solved the problem by designing an automated, computer-controlled measurement system which operates over the 50 kHz to 5 mHz range. The new system provides accurate measurements even on highly attenuating material, supplies data for both attenuation and velocity studies, and performs analyses rapidly. A paper (#34-91) describing the new system is available from Jo Emery, Division 104, NIST, Boulder, CO 80303, 303/497-3237.

WANTED: PARTNERS TO STUDY POLYMER X-RAY SCATTERING

NIST seeks researchers from industry, academia, or other government labs interested in pursuing advanced studies on x-ray scattering from polymers and polymer composites. Facilities at NIST include a 10 m digital small-angle x-ray scattering camera with a two-dimensional position-sensitive detector and a texture diffractometer for transmission measurements of pole figures (used to study crystalline orientation in materials). The facility supports in situ heating and deformation of samples. NIST researchers have used the facility in studies of the microstructure of blown films, fibers, engineering plastics, magnetotactic bacteria, and polymer blends and composites; and in the development of improved methods to analyze three-dimensional microstructure or to interpret the orientation texture of crystalline and semicrystalline materials. The facilities are available for both proprietary and collaborative research. Interested researchers should contact John D. Barnes, B210 Polymer Building, NIST, Gaithersburg, MD 20899, 301/975-6786 or fax 301/869-3239.

NEW MICROSCOPE TIP IMAGES MICROMAGNETIC FORCES

NIST researchers have developed a new technique that may simplify the detection of the magnetic field structure of a computer disk's surface. The

technique, known as tunneling stabilized magnetic force microscopy (TSMFM), modifies a scanning tunneling microscope—a device that uses tunneling current to map surface features—by replacing a rigid magnetic tip with a flexible one. As the tip is scanned across a sample, it is deflected by changes in magnetic forces. The resulting images show a combination of disk surface topography and magnetic field variations. NIST has used this probe on a magnetic medium to image recorded data and to create submicron magnetic records. TSMFM offers a relatively inexpensive method for detecting potential disk failure, making it a practical diagnostic tool for the magnetic recording industry. A patent application on the flexible tip filed by NIST is pending. For information, contact Paul Rice, Division 814.05, NIST, Boulder, CO 80303, 303/497-3841.

DIAL UP SYSTEM STARTED FOR GOSIP TESTING PROGRAM

NIST has begun operating an online database developed for the U.S. GOSIP (Government Open Systems Interconnection Profile) Register Database. It provides information for a list of registers, including: U.S. GOSIP Abstract Test Suites; Assessed Means of Testing; National Voluntary Laboratory Accreditation Program Accredited Test Laboratories; Conformance Tested GOSIP Products; Interoperability Test Suites for Means of Testing Assessment; Interworking GOSIP Products; and Interoperability Test and Registration Services. There are two ways to connect to the database: (1) use the Internet address 129.6.48.100, or (2) use a modem to dial 301/869-0096 using 1200/2400-8-N-1. Log in for both with the user name gosip-db (no password necessary). Address questions, problems, or comments on the database to John J. Garguilo, B141 Technology Building, NIST, Gaithersburg, MD 20899, 301/975-3623. Direct questions on the U.S. GOSIP Testing Program to Stephen Nightingale (same address as Garguilo), 301/975-3616.

SUMMARY OF CALS PROGRAM SUPPORT ISSUED

A new 25-page report, NIST Support of the CALS Program: 1990 Synopsis, (NISTIR 4609) summarizes overall Computer-aided Acquisition and Logistic Support (CALS) program management, technical support, and administration provided by NIST to the Department of Defense. A 1990 precis is offered in each of the general technical support areas: electronic data interchange, document standards, raster compression, data management, security, and data communication. This report also offers the titles and brief abstracts of published reports as well as titles and abstracts for NIST CALS documents published in previous years. Most of the NIST reports delivered to the CALS office have already been published for easier access by the CALS community. For technical information, contact Sharon J. Kemmerer, 301/975-3287. The publication is for sale by the National Technical Information Service, Springfield, VA 22161 for $17 prepaid. Order by PB 91-193821.

REPORT EXAMINES NIST ELECTRIC ENERGY RESEARCH

A review of several projects aimed at improving electrical power measurements is now available from NIST. The document, one of an ongoing series of progress reports prepared for the Department of Energy, describes four major NIST research projects. One program is creating methods to evaluate and calibrate instruments that gauge magnetic and electric fields near utility power lines or in simulated laboratory setups. Another project is examining the behavior of compressed-gas insulators (dielectrics) used in high-voltage power systems. Understanding the breakdown of liquid dielectrics, such as the oils used to insulate power transformers, is the goal of a third project. NIST is studying the propagation of electrical "streamers," which are precursors of total insulating fluid breakdown. A fourth project aims to improve the measurement of fast transient pulses such as lightning and power line surges. The report, Research for Electric Energy—An Annual Report, is free from Electronics and Electrical Engineering Laboratory, B344 Metrology Building, NIST, Gaithersburg, MD 20899, 301/975-2432.

NEW EDITION OF INTERNATIONAL METRIC GUIDE AVAILABLE

NIST has issued a new edition of the standard reference and guide to the International System of Units, the modernized metric system. The 1991 edition of The International System of Units (SI) (NIST Special Publication 330), incorporates the complete English-language translation of the 1991 edition of Le Système International d'Unités (SI), the definitive reference produced by the International Bureau of Weights and Measures. The text includes the full technical definitions of the official SI units, historical notes on the development of the present-day definitions, brief descriptions of the practical realization of the definitions of some

important units, and, in the NIST edition, special notes concerning U.S. metric usage. Single copies are available from Carolyn Stull, C210 Radiation Physics Building, NIST, Gaithersburg, MD 20899, 301/975-5607.

FIVE SBIR CONTRACTS ISSUED FOR 1991

NIST's Small Business Innovation Research (SBIR) program, which designates 1.25 percent of the institute's extramural research and development budget to fund research by small businesses, has awarded five contracts for 1991. Phase 1 contracts (up to $35,000 for feasibility studies), for evaluation of new ultraviolet and vacuum ultraviolet radiometric standards; a prototype system to measure robot positioning accuracy; the study of improved crystals for fiber-optic magnetic-field sensors; and design of an improved, large-format real-time x-ray imaging system. A Phase 2 contract (up to $200,000 for major research and development) was awarded for design and construction of an add-on x-ray concentrator for analytical instruments using an x-ray interference mirror to enhance x-ray output. For information on the SBIR program, contact Edward Tiernan, NOAA, CS/RT, Suitland Professional Center, Room 307, Suitland, MD 20233, 301/763-4240.

PRODUCT DATA EXCHANGE INITIATIVE LAUNCHED

Corporations, industry and trade associations, and government agencies have begun to join the National Initiative for Product Data Exchange that calls for the acceleration and coordination of all relevant product data exchange (PDE) development and deployment efforts. PDE technology, or the ability to express in computerized or standardized digital format all useful information about a given product, is considered a key to effective computer-integrated manufacturing and concurrent engineering. The development of a PDE standard is expected to dramatically enhance product design, manufacturing, and support processes. Under the initiative implementation plan, developed by an industry-led task force and announced Nov. 12 by Commerce Under Secretary for Technology Robert M. White, all organizations and industry programs involved in PDE activities are invited to develop a coordination program that incorporates agreed-upon priorities and schedules. The IGES/PDES Organization (IPO), which has 550 industrial, governmental, and academic participants engaged in all phases of PDE, has appointed a general manager for the initiative office; this office will begin operations at NIST in January 1992. Initiative programs will address standards development, testing, software development and deployment, and education and training. For more information or a copy of the plan, contact the PDES/CALS Office, A319 Metrology Building, NIST, Gaithersburg, MD 20899, 301/975-3986, fax 301/926-8730.

MEASURING THE ROLE OF VITAMIN C IN CANCER, ARTHRITIS

A new procedure developed by NIST and the National Cancer Institute (NCI) for measuring vitamin C is helping scientists study links between the vitamin and two diseases, cancer and arthritis. In cooperation with NCI, a NIST scientist created the new method to stabilize vitamin C in frozen plasma for extended periods (up to 18 months in current studies), allowing its level to be accurately measured over time. Using this method, NIST helped an NCI researcher assess the performance of laboratories participating in NCI studies on the role of vitamin C in cancer. In another study, NIST worked with a physician at the Children's National Medical Center in Washington, DC, to measure vitamin C levels in children with a crippling form of arthritis. The new NIST/NCI measurement method enabled the doctor to correlate vitamin C levels with disease severity.

CHANGES ANNOUNCED IN WEIGHTS AND MEASURES BOOKS

Two NIST handbooks have been revised and a supplement has been issued to reflect changes adopted at the July 1991 Annual Meeting of the National Conference on Weights and Measures (NCWM). Established in 1905, NCWM is an organization of state, county, and city weights and measures enforcement officials, along with associated business and consumer representatives. NCWM receives technical support from NIST, a nonregulatory agency, through the institute's Office of Weights and Measures.

NIST Handbook 44-1991, Specifications, Tolerances, and Other Technical Requirements for Weighing and Measuring Devices, now contains a Tentative Code for Mass Flow Meters that establishes tolerances for measuring the mass of liquids or vapors. When the tentative code is adopted by NCWM as a full code, requirements for mass flow meters that appear in other codes will be deleted. The Hydrocarbon Gas Vapor-Measuring Devices Code also was revised to recognize devices that measure compressed natural gas when sold as a motor fuel.

Handbook 130-1991, Uniform Laws and Regulations, includes a revision to the NCWM recommendation for motor fuel labeling to provide consumers with information on whether or not oxygenates such as methyl-t-butyl ether (MTBE) or ethanol exist in a product. If adopted by the states, the regulation will require pumps to be labeled when the level of oxygenates, or combinations of them, is at least 1 percent by volume.

Supplement 2, 1991, to Handbook 133-Third Edition, 1988, Checking the Net Contents of Packaged Goods, and the 1990 Supplement, contains the latest revisions to inspection procedures for meat and poultry products. Handbook 133 and the supplements have been adopted by the U.S. Department of Agriculture's Food Safety Inspection Service for compliance testing of net weight labeling of packaged meat and poultry. They will take effect Jan. 2, 1992, and cover approximately 8,000 processing facilities in the United States and overseas.

Copies of the handbooks are available from the Superintendent of Documents, U.S. Government Printing Office, Washington, DC 20402. Order Handbook 44-1992 by stock No. 003-003-03114-3, $12 prepaid; Handbook 130-1992 by stock No. 003-003-03105-4, $11 prepaid; Handbook 133-Third Edition, 1988, by stock No. 003-003-02855-1, $16 prepaid; NIST Handbook 133-Third Edition, 1990 Supplement by stock No. 003-003-03049-0, $3.25 prepaid; and NIST Handbook 133-Third Edition, 1991 Supplement 2 by stock No. 003-003-03111-9, $1.50 prepaid.

BALDRIGE AWARD CONFERENCE SET FOR FEBRUARY

A conference featuring the 1991 winners of the Malcolm Baldrige National Quality Award will take place Feb. 3–5, 1992, at the Washington Hilton Hotel in Washington, DC. The Quest for Excellence IV will highlight the quality improvement strategies of the 1991 winners: Solectron Corp. (San Jose, CA), Zytec Corp. (Eden Prairie, MN), and Marlow Industries (Dallas, TX). All three are small to medium-sized electronics firms. Executives from the companies will discuss in detail their winning strategies and the results achieved through quality improvement initiatives. The conference is being sponsored by NIST in conjunction with the American Society for Quality Control (ASQC) and the Association for Quality and Participation. Questions on registration should be directed to ASQC at 414/272-8575. General information questions should be referred to the NIST Conference Program, 301/975-2774.

SURVEY FEATURES RESEARCH ON ALTERNATIVE REFRIGERANTS

A comprehensive survey of worldwide research on the thermophysical properties of alternative refrigerants to fully halogenated chlorofluorocarbons (CFCs) has been published by NIST. CFC refrigerants are major contributors to ozone depletion. The survey reports on the thermodynamic, transport, and phase equilibria properties of 13 fluids, as well as their dielectric constants and refractive indices. A copy of the publication, A Survey of Current Worldwide Research on the Thermophysical Properties of Alternative Refrigerants (NISTIR 3969), is available from the National Technical Information Service, Springfield, VA 22161. Order by PB 92-112366; the price is $19.

NIST SINGLE-FLUX-QUANTUM ADVANCES RESULT IN OPERATING DEVICES AND SIMULATION METHODS, CONTRIBUTING TO NATIONAL PROGRAM TO DEVELOP SFQ LOGIC

NIST scientists have designed, fabricated, and successfully operated at first attempt a shift register and a binary counter based on single-flux-quantum (SFQ) principles and developed simulation methods that predict the operating margins of SFQ logic devices. SFQ logic refers to the representation of the binary states of one and zero by the presence or absence of a single magnetic flux quantum trapped in a direct-current superconducting quantum interference device (SQUID). Each SQUID is an inductive loop element incorporating two Josephson junctions.

The current high interest in SFQ is driven by (1) switching speeds in the 100 GHz range that flip-flop circuits incorporating SQUIDs potentially can provide and (2) feasibility of fabrication from the new high-critical-temperature superconductors. SQUID circuits perform best with non-hysteretic Josephson junctions, the only type of junction that has been made successfully with high-T_c materials. The limitations posed in the past by the narrow range of operating parameters that fabrication methods provide for superconducting electronic circuits typically have restricted the range of devices that can be implemented. The NIST researchers devised simulation methods which they applied to show that the margins for operating parameters for an important class of SFQ logic devices should be usefully large—as much as 30 percent. This class of devices includes AND gates, OR gates, exclusive-OR gates, and full adders.

NIST MAKES SOFTWARE AVAILABLE TO SUPPORT ANTENNA NEAR-FIELD PLANAR SCANNING RESEARCH

NIST scientists have developed a personal computer software package for the study of planar near-field measurements that offers a previously unavailable high degree of power, modularity, and flexibility. The package is part of an overall effort to develop software for use on personal computers that incorporates dedicated modules that can be combined to investigate computational tasks involving real or simulated data for research and error analysis in antenna metrology.

NIST invented the near-field method and then pioneered in the application of antenna near-field scanning as a practical measurement tool for determining the performance of antennas. In this method, measurements of phase and amplitude are made with a calibrated probe physically close to an antenna (in its near field) at a large number of points over a defined surface, for example, a plane. The resulting near-field data are processed to yield the desired antenna far-field pattern through NIST algorithms that incorporate estimates of the uncertainty associated with the pattern. Virtually all satellite and phased-array antennas now are measured with near-field methods; NIST calibrates the probes and provides support to organizations seeking to establish near-field ranges. Some 30 U.S. companies and a number of government agencies are using the method in a total of 54 near-field ranges. This large and growing body of users has led to an interest on the part of others in conducting research in near-field scanning and a request that NIST provide computer code for the near-field algorithms that is more accessible to users outside NIST. The new software package consists of a number of FORTRAN modules that can be called from DOS to achieve a wide variety of computational tasks. Personal Computer Codes for Analysis of Planar Near Fields (NBSIR 3970) describes this package.

TUNNELING-STABILIZED MAGNETIC FORCE MICROSCOPY APPLIED TO VERTICAL BLOCH LINE MEMORIES IN COLLABORATIVE RESEARCH WITH JPL

At the request of Jet Propulsion Laboratory (JPL) NIST scientists are applying the NIST tunneling-stabilized magnetic force microscope (TSMFM) to the study of domain walls in magnetic garnet as part of the JPL program to develop practical Vertical Bloch Line (VBL) memories. The TSMFM provides image information on the magnetic fields arising from very small regions of the surface of magnetic materials, for example, from individual bits on magnetic storage media. A VBL memory element consists of a thin film of magnetic garnet, patterned with various permalloy structures, used to control the magnetic domains and walls in the garnet. NIST initially is using the TSMFM to provide the highest resolution images available from any source of the domain walls of bulk specimens from JPL, providing information useful for JPL's development of VBL memory. Later, JPL is expected to provide specimen memory elements for examination.

The concept of VBL memories is exciting because of the potential to provide fast access, high packing density, and the capability of retaining stored data even when the system of which they are a part is turned off. Most fast-access computer memory currently is restricted to powered memory chips. Another attractive feature of VBL memories is that the data they hold can be actively manipulated rather than having to be rewritten. Magnetic garnet exhibits strong perpendicular anisotropy which defines narrow domain walls. Since these walls are transitions between domains, the direction of magnetization in the wall can be reversed. The point where the two magnetization directions meet is called a Bloch line. In contrast to conventional disk-based memory, which stores data statically with domain magnetization, the Bloch lines themselves store data in VBL memories.

NIST HELPS INDUSTRY AND NASA SOLVE ROBOT STABILITY PROBLEM

NIST scientists have been supporting the NASA Goddard Space Flight Center in the development of the Flight Telerobotic Servicer (FTS), the two-armed robot that will build and maintain Space Station "Freedom." Recently, the prime contractor for the space qualified version of the FTS, experienced a curious instability in their robot control algorithm. They found that the robot was stable when in contact with some environmental stiffnesses, but unstable for others. As NIST researchers delved deeply into the problem, an important and fundamental set of design criteria for robot control systems emerged. Analysis showed that the control system could become unstable when passivity is violated. In order to stabilize the system, the frequency at which passivity is violated must be greater than the torque loop resonant frequency. These results were then verified empirically on a seven degree-of-freedom robot at NIST. Based on this work, a paper will be

published in the Proceedings of the IEEE Robotics and Automation Conference in 1992. These results could have significant impact on industry outside of space applications. Private industry can use these results in another project, the Next Generation Controller, where the controllers for robots, machine tools, and coordinate measurement machines are coalesced into the same standard structure.

WAY PREPARED FOR 0.01 PERCENT RADIOMETRIC CALIBRATIONS

A core problem in radiometric physics is to reference optical power measurements to SI units. NIST is now preparing to do this 10 times better than ever before. Over the years, many physical principles have been employed, such as the power spectra from hot bodies (Planckian radiation) and accelerating charges (synchrotron radiation), as well as the solid-state physics of silicon photodiodes. The latest technique, which promises the best accuracy over the greatest spectral range, is cryogenic radiometry. It is a refinement of electrical substitution radiometry, whereby optical power absorbed in a black cavity is balanced against electrical resistive heating. Both raise the temperature of the cavity, as compared to a stabilized reference temperature. The cryogenic aspect of the radiometer reduces systematic errors, such as cavity reradiation and convective cooling, and provides favorable operating conditions, such as a low specific heat and high thermal conductivity of the cavity.

The high-accuracy cryogenic radiometer (HACR) provides an absolute measure of optical power at about 1mW, referenced to the volt and ohm, with a design accuracy of better than 100 parts per million. An intensity-stabilized laser light source is alternately measured by the radiometer and the detector under test. These detectors include transfer standards, such as silicon photodiodes combined in the "trap" arrangement, which have comparable precision to the HACR and are portable. Using these, the HACR becomes the root of all detector-based calibration at NIST, as well as a facility for specialized customer needs.

This newly completed cryogenic radiometer is the second one at NIST. The first is dedicated to the low-background infrared radiometer facility and was optimized for use at the low power levels encountered in aerospace work.

PHASES OF X-RAY DIFFRACTION DATA FROM BIOLOGICAL MACROMOLECULES BY MAXIMUM ENTROPY

The development by scientists at NIST and the Chalmers University of Technology (Gothenburg, Sweden) of methods for applying the principle of maximum entropy to the determination of the phases of x-ray diffraction data has greatly expanded capabilities for determining the structures of biological molecules such as proteins. A computer program that makes extensive use of fast Fourier transform (FFT) techniques and exploits space group symmetries to make further reductions in necessary computational resources has been written. It has already been used to explore a variety of strategies for determining phases for large data sets (tens of thousands of reflections) starting from a minimum of prior information, possibly no more than the two to four phases that may be chosen arbitrarily to define an origin and an enantiomorph. FFT routines for a wide range in the number of grid points per period enable the study of the effect of resolution on the quality of the resulting density map.

The technique has been applied to diffraction data from the protein bovine heart creatine kinase, in collaboration with scientists from the Center for Advanced Research in Biotechnology (CARB), to produce an electron density map in which features of secondary protein structure such as α-helices and β-sheets are clearly visible. Application to structure studies of other proteins is proceeding in collaboration with scientists at the Naval Research Laboratory and the University of California at San Diego.

ASPHALT CHEMISTRY ADVANCEMENT BASED ON NIST RESEARCH

The results of research performed at NIST for the Strategic Highway Research Program (SHRP) have been instrumental in the development of a new model of asphalt structure, which explains the mechanical performance characteristics of asphalt binders and cements. NIST researchers have shown that the "micellar" model of asphalt, widely used as a description of asphalt microstructure, is inconsistent with recent measurements. Asphalt samples are difficult to characterize owing to their complex chemical composition. Employing the technique of solid-state nuclear magnetic resonance, the NIST researchers were able to determine upper limits for the minimum-length dimension across domains of like chemical substances in heterogeneous asphalt. This upper limit

of typically 4 nm is too small to be consistent with micellar structure. Other researchers participating in a coordinated SHRP program on asphalt chemistry and performance have used this insight for developing an alternative model, which can explain asphalt behavior. SHRP expects the research to enable manufacturers to modify asphalts to improve performance.

GLASSES FOR PROTECTION OF EYES FROM LASER DAMAGE

University researchers have shown that certain glasses prepared by NIST can reduce the intensity of a laser beam in an optical system to below that at which retinal damage may occur. The operating principle is thermal lensing in which the change of refractive index with temperature, dn/dT, is so strong that the heating due to an impinging laser beam will automatically defocus the beam, thus reducing the intensity reaching the eye of an observer. NIST scientists prepared a series of borate, phosphate, germanate, and silicate glasses, which university scientists tested. Sufficient understanding was obtained to prepare another group of glasses, which were also tested. The best glasses turned out to be silicates with high contents of lead and some europium. These glasses have combinations of high dn/dT and low thermal diffusivity and thermal conductivity, the latter two properties being important for ensuring that the heating of the glass by the laser beam is sufficiently rapid to activate the thermal lensing. The ready formability and relative low cost of the silicate glasses suggest that they will find considerable use in industrial and military applications.

NEW PUBLICATION FOCUSES ON SECURITY IN ISDN

In the 1990s, ISDN (Integrated Services Digital Network) standards will provide worldwide digital communications service and will play a key role in the transition to electronic documents and business transactions. Government and business are increasingly concerned with security in ISDN. NIST Special Publication 500-189, Security in ISDN, discusses the standards needed to implement user security. ISDN security standards should take advantage of, and be compatible with, emerging standards for Open Systems Interconnection security, including confidentiality, access control, authentication, data integrity, and non-repudiation. The publication provides a broad discussion of user security needs and suggests possible solutions.

NIST PUBLISHES COMPUTER SECURITY BULLETIN BOARD USER'S GUIDE

NISTIR 4667, Computer Security Bulletin Board User's Guide, assists users in accessing and utilizing the many features of this electronic bulletin board which focuses on computer security issues. Examples of posted information include an events calendar, software reviews, publications, bibliographies, lists of organizations, and other government bulletin board numbers. The bulletin board operates 24 hours a day, charges no fee, and is accessible to anyone who has a computer or terminal with a modem or network connection. The bulletin board numbers are (301) 948-5717 for 300, 1200, or 2400 baud modems; (301) 948-5140 for 9600 baud modems.

HIGH-INTEGRITY WORKSHOP PROCEEDINGS ISSUED

NIST Special Publication 500-190, Proceedings of the Workshop on High Integrity Software; Gaithersburg, MD, Jan. 22-23, presents the results of a Workshop on the Assurance of High Integrity Software sponsored by NIST. Workshop participants addressed techniques, costs, and benefits of assurance, controlled and encouraged practices, and hazard analysis. The workshop prepared a preliminary set of recommendations and proposed future directions for NIST to coordinate a comprehensive set of standards and guidelines for the assurance of high-integrity software.

Volume 96, Number 6, November–December 1991
Journal of Research of the National Institute of Standards and Technology

Calendar

February 18–19, 1992
CHESAPEAKE AREA FOCUS USERS' SYMPOSIUM

Location: National Institute of Standards and Technology Gaithersburg, MD

Purpose: To provide an opportunity for networking and information exchange among members of Baltimore FUSE, DC FUSE, and Richmond FUSE and the Government Special Interest Group.
Topics: Business Problems/Business Solutions, USDA—National Finance Center Presentation, Interfaces to Relational Databases, IBI's Future Directions.
Format: Symposium. Audience: Users of FOCUS software.
Sponsors: NIST, Baltimore FUSE, DC FUSE, Richmond FUSE and The Government Special Interest Group.
Contact: Rebecca Umberger, Information Builders, Inc., 1655 N. Ft. Myer Drive, Suite 510, Arlington, VA 22209, 703/525-5888 or Leslie Piwowarczyk, NIST, A735 Administration Building, Gaithersburg, MD 20899, 301/975-2286.

February 25–28, 1992
NORTH AMERICAN ISDN USERS' FORUM (NIU-FORUM)

Location: National Institute of Standards and Technology Gaithersburg, MD

Purpose: To develop user-defined applications, implementation agreements for existing standards, and tests needed for transparent, ubiquitous, and user-driven integrated services digital network (ISDN).
Topics: ISDN-related subjects.
Format: Tutorials, users' and implementors' workshops, and working group meetings.
Audience: ISDN users, implementors, and service providers.
Sponsor: NIST.
Contact: Dawn Hoffman, B364 Materials Building, NIST, Gaithersburg, MD 20899, 301/975-2937.

March 9–13, 1992
NIST/OSI IMPLEMENTORS' WORKSHOP

Location: National Institute of Standards and Technology Gaithersburg, MD

Purpose: To develop implementation specifications from international standards design specifications for computer network protocols.
Topics: Open systems interconnection.
Format: Workshop sessions.
Audience: Computer and communications users, vendors, and suppliers.
Sponsor: NIST and the IEEE Computer Society.
Contact: Brenda Gray, 301/975-3664 or Tim Boland, 301/975-3608, B217 Technology Building, NIST, Gaithersburg, MD 20899.

Volume 96, Number 6, November–December 1991
Journal of Research of the National Institute of Standards and Technology

Subject Index to Volume 96

Numbers in parenthesis after the page number are the issue numbers

No. 1 January-February
No. 2 March-April
No. 3 May-June
No. 4 July-August
No. 5 September-October
No. 6 November-December

F

G

H

I

L

M

N

O

P

Volume 96, Number 6, November–December 1991
Journal of Research of the National Institute of Standards and Technology

Author Index to Volume 96

Numbers in parenthesis after the volume number are the issue numbers

No. 1 January-February
No. 2 March-April
No. 3 May-June
No. 4 July-August
No. 5 September-October
No. 6 November-December

L

M

N

P

R